Beiträge aus der Informationstechnik

Manu Viswambharan Thayyil

Analysis and Design of Silicon based Integrated Circuits for Radio Frequency Identification and Ranging Systems at 24 GHz and 60 GHz Frequency Bands

VOGT

Dresden 2023

Bibliografische Information der Deutschen Nationalbibliothek
Die Deutsche Nationalbibliothek verzeichnet diese Publikation in der Deutschen Nationalbibliografie; detaillierte bibliografische Daten sind im Internet über http://dnb.dnb.de abrufbar.

Bibliographic Information published by the Deutsche Nationalbibliothek
The Deutsche Nationalbibliothek lists this publication in the Deutsche Nationalbibliografie; detailed bibliographic data are available on the Internet at http://dnb.dnb.de.

Zugl.: Dresden, Techn. Univ., Diss., 2023

Die vorliegende Arbeit stimmt mit dem Original der Dissertation „Analysis and Design of Silicon based Integrated Circuits for Radio Frequency Identification and Ranging Systems at 24 GHz and 60 GHz Frequency Bands“ von Manu Viswambharan Thayyil überein.

© Jörg Vogt Verlag 2023
Alle Rechte vorbehalten. All rights reserved.

Gesetzt vom Autor

ISBN 978-3-95947-067-4

Jörg Vogt Verlag
Niederwaldstr. 36
01277 Dresden
Germany

Phone: +49-(0)351-31403921
Telefax: +49-(0)351-31403918
e-mail: info@vogtverlag.de
Internet : www.vogtverlag.de

Technische Universität Dresden

Analysis and Design of Silicon based Integrated Circuits for Radio Frequency Identification and Ranging Systems at 24 GHz and 60 GHz Frequency Bands

M.Sc.
Manu Viswambharan Thayyil

der Fakultät Elektrotechnik und Informationstechnik
der Technischen Universität Dresden

zur Erlangung des akademischen Grades

Doktoringenieur

(Dr.-Ing.)

genehmigte Dissertation

Vorsitzender:	Prof. Dr.-Ing. habil. Wolf-Joachim Fischer
Gutachter:	Prof. Dr. sc. techn. habil. Dipl. Betriebswiss. Frank Ellinger
	Prof. Dr.-Ing. habil. Alexander Kölpin

Tag der Einreichung:	09. Januar 2023
Tag der Verteidigung:	08. Juni 2023

What I cannot create, I do not understand.

Richard P. Feynman

Original Publications

Original work already published by this author under the copyright of publishers like IEEE and IET are reused in this document. Any text extract, tables or figures used from previously published documents with minor or no modifications are marked using the notation: *[*reference*]©YYYY, Publisher

Acknowledgements

First and foremost I would like to thank Prof. Dr. sc. techn. habil. Frank Ellinger for the trust bestowed in me and providing the opportunity to do the doctoral work at the chair for circuit design and network theory, TU Dresden.

My special thanks to Dr. Niko Joram for mentorship through his actions and timely directions. His work on local positioning systems has always been an inspiration to acquire the multidisciplinary skills required for building reliable systems and has gone a long way into the making of this thesis. I would also like to appreciate his effort in reviewing this work and other publications which have remarkably improved their quality. I would also like to give a special thanks Dr. Stefan Schumann for support in the laboratory.

I am grateful for having shared an office with wonderful colleagues like Songhui Li - the Shifu, Amirali Taghavi, Dr. Adrian Figueroa, Florian Protze and Marco Gunia. Thanks to them for creating a stimulating and open work atmosphere. I would also like to thank other colleagues and students whom I was privileged to collaborate with: Seyyedmohsen Seyyedrezaei, Mengqi Cui, Jan Pliva, Dr. Tilo Meister, Sujay Charania, Dr. Naglaa Elagroudy, Dr. Hatem Ghaleb, Dr. Belal Al-Quidsi, Zoltán Tibenszky and Katharina Isaack.

A humbling thank you goes to all those who have inspired, provided opportunity, been kind, respectful and considerate to pave me small steps along the way in this journey, including: Vinodkumar A.N., Marykutty T., Dr. Kasyap T.V., Bella Jacob, Vishnu Mohan, Prince V. Thachil, Biju Mathew, Dr. M. V. Rajesh , Dr. T.K. Mani, Shalu Thomas, Dr. Kurian Polachan, Kurian John, B. Manojkumar, Vinodh Rakesh, Anil K. S. Dr. Thirukumar Vethanayagam and Frank Dolzmann.

Last but not the least, boundless gratitude to my family for lending me their valuable time and support so that I could realize this work.

Dresden, im Januar 2023 *Manu Viswambharan Thayyil*

Abstract

This scientific research work presents the analysis and design of radio frequency (RF) integrated circuits (ICs) designed for two cooperative RF identification (RFID) proof of concept systems. The first system concept is based on localizable and sensor-enabled superregenerative transponders (SRTs) interrogated using a 24 GHz linear frequency modulated continuous wave (LFMCW) secondary radar. The second system concept focuses on low power components for a 60 GHz continuous wave (CW) integrated single antenna frontend for interrogating close range passive backscatter transponders (PBTs).

In the 24 GHz localizable SRT based system, a LFMCW interrogating radar sends a RF chirp signal to interrogate SRTs based on custom superregenerative amplifier (SRA) ICs. The SRTs receive the chirp and transmit it back with phase coherent amplification. The distance to the SRTs are then estimated using the round trip time of flight method. Joint data transfer from the SRT to the interrogator is enabled by a novel SRA quench frequency shift keying (SQ-FSK) based low data rate simplex communication. The SRTs are also designed to be roll invariant using bandwidth enhanced microstrip patch antennas. Theoretical analysis is done to derive expressions as a function of system parameters including the minimum SRA gain required for attaining a defined range and equations for the maximum number of symbols that can be transmitted in data transfer mode. Analysis of the dependency of quench pulse characteristics during data transfer shows that the duty cycle has to be varied while keeping the on-time constant to reduce ranging errors. Also the worsening of ranging precision at longer distances is predicted based on the non-idealities resulting from LFMCW chirp quantization due to SRT characteristics and is corroborated by system level measurements.

In order to prove the system concept and study the semiconductor technology dependent factors, variants of 24 GHz SRA ICs are designed in a 130 nm silicon germanium (SiGe) bipolar complementary metal oxide technology (BiCMOS) and a partially depleted silicon on insulator (SOI) technology. Among the SRA ICs designed, the SiGe-BiCMOS ICs feature a novel quench pulse shaping concept to simultaneously improve the output power and minimum detectable input power. A direct antenna drive SRA IC based on a novel stacked transistor cross-coupled oscillator topology employing this concept exhibit one of the best reported combinations of minimum detected input power level of −100 dBm and output power level of 5.6 dBm, post wirebonding. The SiGe stacked transistor with base feedback capacitance topology employed in this design is analyzed to derive parameters including the SRA loop gain for design optimization. Other theoreti-

cal contributions include the analysis of the novel integrated quench pulse shaping circuit and formulas derived for output voltage swing taking bondwire losses into account. Another SiGe design variant is the buffered antenna drive SRA IC having a measured minimum detected input power level better than −80 dBm, and an output power level greater than 3.2 dBm after wirebonding. The two inputs and outputs of this IC also enables the design of roll invariant SRTs. Laboratory based ranging experiments done to test the concepts and theoretical considerations show a maximum measured distance of 77 m while transferring data at the rate of 0.5 symbols per second using SQ-FSK. For distances less than 10 m, the characterized accuracy is better than 11 cm and the precision is better than 2.4 cm. The combination of the maximum range, precision and accuracy are one of the best reported among similar works in literature to the author's knowledge.

In the 60 GHz close range CW interrogator based system, the RF frontend transmits a continuous wave signal through the transmit path of a quasi circulator (QC) interfaced to an antenna to interrogate a PBT. The backscatter is received using the same antenna interfaced to the QC. The received signal is then amplified and downconverted for further processing. To prove this concept, two optimized QC ICs and a downconversion mixer IC are designed in a 22 nm fully depleted SOI technology. The first QC is the transmission lines based QC which consumes a power of 5.4 mW, operates at a frequency range from 56 GHz to 64 GHz and occupies an area of 0.49 mm^2. The transmit path loss is 5.7 dB, receive path gain is 2 dB and the tunable transmit path to receive path isolation is between 20 dB and 32 dB. The second QC is based on lumped elements, and operates in a relatively narrow bandwidth from 59.6 GHz to 61.5 GHz, has a gain of 8.5 dB and provides a tunable isolation better than 20 dB between the transmit and receive paths. This QC design also occupies a small area of 0.34 mm^2 while consuming 13.2 mW power. The downconversion is realized using a novel folded switching stage down conversion mixer (FSSDM) topology optimized to achieve one of the best reported combination of maximum voltage conversion gain of 21.5 dB, a factor of 2.5 higher than reported state-of-the-art results, and low power consumption of 5.25 mW. The design also employs a unique back-gate tunable intermediate frequency output stage using which a gain tuning range of 5.5 dB is attained. Theoretical analysis of the FSSDM topology is performed and equations for the RF input stage transconductance, bandwidth, voltage conversion gain and gain tuning are derived. A feasibility study for the components of the 60 GHz integrated single antenna interrogator frontend is also performed using PBTs to prove the system design concept.

Kurzfassung

In dieser wissenschaftlichen Forschungsarbeit werden die Analyse und der Entwurf von integrierten Schaltungen (integrated circuits, ICs) für zwei kooperative Radiofrequenzidentifikationssysteme (RFID systems) vorgestellt, die als Konzeptnachweis dienen. Das erste Systemkonzept basiert auf ortbaren und sensorfähigen superregenerativen Transpondern (SRTs), die mit einem 24 GHz-Sekundärradar mit linearer frequenzmodulierter Dauerstrichwelle (linear frequency modulated continuous wave, LFMCW) abgefragt werden. Das zweite Systemkonzept konzentriert sich auf Komponenten mit geringem Stromverbrauch für ein integriertes 60 GHz-Frontend zur Abfrage von passiven Transpondern (passive backscatter transponders, PBTs).

Bei dem 24 GHz SRT-System sendet ein LFMCW-Abfrageradar ein hochfrequentes Rampensignal, um SRTs abzufragen, die auf dafür optimierten Verstärkerschaltungen (super-regenerative amplifiers, SRA) basieren. Die SRTs empfangen das Rampensignal und senden es phasenkohärent und verstärkt zurück. Die Entfernung zu den SRTs wird dann nach der Round-Trip-Time-of-Flight-Methode geschätzt. Die gleichzeitige Datenübertragung vom SRT zum Abfragesystem wird durch eine neuartige Frequenzmodulation (SRA quench frequency shift keying, SQ-FSK) mit niedriger Datenrate ermöglicht. Die SRTs sind mit Hilfe von bandbreitenerweiterten Mikrostreifen-Patchantennen auch rollinvariant konzipiert. Durch eine theoretische Analyse werden mathematische Zusammenhänge in Abhängigkeit der Systemparameter abgeleitet, einschließlich der minimalen SRA-Verstärkung, die zum Erreichen einer bestimmten Reichweite erforderlich ist, sowie Gleichungen für die maximale Anzahl von Symbolen, die im Datenübertragungsmodus übertragen werden können. Die Analyse der Quenchpulse während der Datenübertragung zeigt, dass das Tastverhältnis variiert und die Einschaltdauer konstant gehalten werden muss, um Fehler bei der Abstandsmessung zu reduzieren. Auch die Verschlechterung der Entfernungsgenauigkeit bei größeren Entfernungen auf der Grundlage der ermittelten Nicht-Idealitäten vorhergesagt. Diese ergeben sich aus der Quantisierung des Rampensignals aufgrund der SRT-Eigenschaften. Die Theorie wird durch Systemtests bestätigt.

Um das Systemkonzept zu prüfen und die von der Halbleitertechnologie abhängigen Faktoren zu untersuchen, wurden Varianten der 24 GHz-SRA-ICs in einer 130nm Silizium-Germanium-Technologie (SiGe) mit komplementärem Metalloxidhalbleiter (complementary metal oxide semiconductor, CMOS) und einer 45nm-Silizium-auf-Isolator-Technologie (silicon on insulator, SOI) realisiert.

Unter den entworfenen SRA-ICs zeichnen sich die SiGe-BiCMOS-ICs durch ein neuartiges Quench-Pulse-Shaping-Konzept aus, das gleichzeitig die Ausgangsleistung und die minimale detektierbare Eingangsleistung verbessert. Ein SRA-IC mit direkter Antennensteuerung, der auf einer neuartigen kreuzgekoppelten Oszillatortopologie mit gestapelten Transistoren basiert und dieses Konzept anwendet, weist eine der besten Kombinationen von minimalem detektiertem Eingangsleistungspegel von -100 dBm und einem Ausgangsleistungspegel von 5,6 dBm nach dem Drahtbonden auf. Die genannte Topologie verwendet eine Rückkopplungskapazität an der Basis. Sie wird theoretisch analysiert, um Parameter einschließlich der SRA-Schleifenverstärkung für eine Entwurfsoptimierung abzuleiten. Weitere theoretische Beiträge umfassen die Analyse der neuartigen integrierten Pulsformungsschaltung für die Quench-Pulse und Formeln für den Ausgangsspannungshub unter Berücksichtigung der Bonddrahtverluste. Eine weitere SiGe-Design-Variante ist der gepufferte SRA-IC mit Antennentreiber mit einem gemessenen minimalen detektierten Eingangsleistungspegel von weniger als -80 dBm und einem Ausgangsleistungspegel von mehr als 3,2 dBm nach dem Drahtbonden. Die zwei Ein- und Ausgänge dieses ICs ermöglichen, in Kombination mit der entworfenen Patchantenne, den Aufbau rollinvarianter SRTs. Laborexperimente zur Überprüfung der Konzepte und theoretische Überlegungen zeigen eine maximal gemessene Reichweite von 77 m bei einer Datenübertragungsrate von 0,5 Symbolen pro Sekunde mit SQ-FSK. Bei Entfernungen von weniger als 10 m ist die gemessene Genauigkeit besser als 11 cm und die Präzision besser als 2,4 cm. Die Kombination aus maximaler Reichweite, Präzision und Genauigkeit ist nach Kenntnis des Autors eine der besten, die unter ähnlichen Arbeiten in der Literatur zu finden sind.

Beim entworfenen 60-GHz-CW-Abfragesystem für den Nahbereich sendet das HF-Frontend ein Dauerstrichsignal über einen Quasizirkulator (quasi circulator, QC) im Sendepfad. Dieser ist mit einer Antenne verbunden, um einen PBT abzufragen. Die Rückstreuung wird über den Zirkulator mit der gleichen Antenne empfangen. Das empfangene Signal wird dann verstärkt und zur weiteren Verarbeitung heruntergemischt. Um dieses Konzept zu prüfen, wurden zwei dafür optimierte QC-ICs und ein Abwärtsmischer-IC in einer 22 nm SOI-Technologie realisiert. Der erste auf Streifenleitungen basierende QC benötigt eine Versorgungsleistung von 5,4 mW, arbeitet in einem Frequenzbereich von 56-64 GHz und nimmt eine Chipfläche von 0.49 mm^2 ein. Der Verlust im Sendepfad beträgt 5,7 dB, die Verstärkung im Empfangspfad 2 dB und die abstimmbare Isolation zwischen Sende- und Empfangspfad liegt zwischen 20 dB und 32 dB. Der zweite QC basiert auf konzentrierten Elementen, arbeitet in einer

relativ schmalen Bandbreite von 59,6 GHz bis 61,5 GHz, hat eine Verstärkung von 8,5 dB und bietet eine abstimmbare Isolation von mehr als 20 dB zwischen dem Sende- und Empfangspfad. Dieser QC-Entwurf benötigt außerdem nur eine kleine Fläche von 0.34 mm^2 und hat eine Leistungsaufnahme von 13,2 mW. Das Abwärtsmischen wird mit einer neuartigen Topologie mit gefalteten Schaltstufen (folded switching stage down conversion mixer, FSSDM) realisiert. Die Topologie ist so optimiert, dass sie eine maximale Spannungsverstärkung von 21,5 dB bei nur 5,25 mW Leistungsaufnahme erreicht. Es handelt sich dabei nach Kenntnis des Autors um eine der besten Kombinationen aus Spannungsverstärkung und Leistungsaufnahme in der aktuellen Literatur. Die Spannungsverstärkung der Schaltung ist um den Faktor 2,5 höher als der Stand der Technik.

Der Entwurf verwendet auch eine einzigartige, durch das Backgate abstimmbare Zwischenfrequenz-Ausgangsstufe, mit der ein Verstärkungsabstimmungsbereich von 5,5 dB erreicht wird. Die theoretische Analyse der FSSDM-Topologie wird durchgeführt, und es werden Gleichungen für die Transkonduktanz der Eingangsstufe, die Bandbreite, die Spannungsumwandlungsverstärkung und den Verstärkungsabstimmungsbereich abgeleitet. Um den Systementwurf zu überprüfen wird eine Machbarkeitsstudie für die Komponenten des 60 GHz-Abfragefrontends mit Einzelantennen unter Verwendung von PBTs durchgeführt.

Contents

1 Introduction **1**
1.1 Motivation and Related Work 1
1.2 Scope and Functional Specifications 4
1.3 Objectives and Structure 5

2 Features and Fundamentals of RFIDs and Superregenerative Amplifiers **9**
2.1 RFID Transponder Technology 9
2.1.1 Chipless RFID Transponders 10
2.1.2 Semiconductor based RFID Transponders 11
2.1.2.1 Passive Transponders 11
2.1.2.2 Active Transponders 13
2.2 RFID Interrogator Architectures 18
2.2.1 Interferometer based Interrogator 19
2.2.2 Ultra-wideband Interrogator 20
2.2.3 Continuous Wave Interrogators 21
2.3 Coupling Dependent Range and Operating Frequencies 25
2.4 RFID Ranging Techniques 28
2.4.0.1 Received Signal Strength based Ranging 28
2.4.0.2 Phase based Ranging 30
2.4.0.3 Time based Ranging 30
2.5 Architecture Selection for Proof of Concept Systems 32
2.6 Superregenerative Amplifier (SRA) 35
2.6.1 Fundamentals 35
2.6.2 Modes of Operation 42
2.6.3 Frequency Domain Characteristics 45
2.7 Semiconductor Technologies for RFIC Design 48
2.7.1 Silicon Germanium BiCMOS 48
2.7.2 Silicon-on-Insulator 48

3 24 GHz Superregenerative Transponder based Identification and Ranging System **51**
3.1 System Design 51
3.1.1 SRT Identification and Ranging 51
3.1.2 Power Link Analysis 55
3.1.3 Non-idealities 59
3.1.4 SRA Quench Frequency Shift Keying for data transfer . . . 61
3.1.5 Knowledge Gained 63

3.2 RFIC Designs 64
3.2.1 Low Power Direct Antenna Drive CMOS SRA IC 66
3.2.1.1 Circuit analysis and design 66
3.2.1.2 Characterization 69
3.2.2 Direct Antenna Drive SiGe SRA ICs 71
3.2.2.1 Stacked Transistor Cross-coupled Quenchable Oscillator 72
3.2.2.1.1 Resonator 72
3.2.2.1.2 Output Network 75
3.2.2.1.3 Stacked Transistor Cross-coupled Pair and Loop Gain 77
3.2.2.2 Quench Waveform Design 85
3.2.2.3 Characterization 89
3.2.3 Antenna Diversity SiGe SRA IC with Integrated Quench Pulse Shaping 91
3.2.3.1 Circuit Analysis and Design 91
3.2.3.1.1 Crosscoupled Pair and Sampling Current 94
3.2.3.1.2 Common Base Input Stage 95
3.2.3.1.3 Cascode Output Stage 96
3.2.3.1.4 Quench Pulse Shaping Circuit 96
3.2.3.1.5 Power Gain 99
3.2.3.2 Characterization 102
3.2.4 Knowledge Gained 103
3.3 Proof of Principle System Implementation 106
3.3.1 Superregenerative Transponders 106
3.3.1.1 Bandwidth Enhanced Microstrip Patch Antennas 108
3.3.2 FMCW Radar Interrogator 114
3.3.3 Chirp Z-transform Based Data Analysis 116

4 60 GHz Single Antenna RFID Interrogator based Identification System 121
4.1 System Design 121
4.2 RFIC Designs 125
4.2.1 Quasi-circulator ICs 125
4.2.1.1 Transmission Lines based Quasi-Circulator IC . . 126
4.2.1.2 Lumped Elements WPD based Quasi-Circulator . 130
4.2.1.3 Characterization 134
4.2.1.4 Knowledge Gained 135
4.2.2 Folded Switching Stage Downconversion Mixer IC 138
4.2.2.1 FSSDM Circuit Design 138
4.2.2.2 Cascode Transconductance Stage 138
4.2.2.3 Folded Switching Stage with LC DC Feed 142
4.2.2.4 LO Balun 145

4.2.2.5 Backgate Tunable IF Stage and Offset Correction 146
4.2.2.6 Voltage Conversion Gain 147
4.2.2.7 Characterization 150
4.2.2.8 Knowledge Gained 151
4.3 Proof of Principle System Implementation 154

5 Experimental Tests 157
5.1 24 GHz System 157
5.1.1 Ranging Experiments 157
5.1.2 Roll Invariance Experiments 158
5.1.3 Joint Ranging and Data Transfer Experiments 158
5.2 60 GHz System Detection Experiments 165

6 Summary and Future Work 167

Appendices 171

A Derivation of Parameters for CB Amplifier with Base Feedback Capacitance 173

B Definitions 177

C 24 GHz Experiment Setups 179

D 60 GHz Experiment Setups 183

References 185

List of Original Publications 203

List of Abbreviations 207

List of Symbols 213

List of Figures 215

List of Tables 223

Curriculum Vitae 225

1 Introduction

1.1 Motivation and Related Work

Throughout human history, the ability to identify objects and determine their position in space has been a skill of utmost importance. This skill was necessary for tasks including navigation of surroundings, locating objects and following animals, thus making it as essential as communication and time telling [PMvD+20]. A wide range of tools and techniques like coordinate systems, maps, references based on the motion of celestial bodies and compasses were invented in due course to master this ability. Foundations to alter those conventional paradigms beyond recognition were laid in the second half of 19th century through exponential advances in our understanding of electromagnetic (EM) radiant energy, when its existence and characteristics were predicted as fundamental laws in the seminal works of J.C. Maxwell [Max65], and conclusive proof of its existence was obtained through experiments done by H. R. Hertz [WC95, SSP14]. Building on their work, pioneers including J.C. Bose, A. Popov, G. Marconi, R. Fessenden, E.H. Armstrong, J.L. Baird and many others sought to find a diverse set of applications for electromagnetism [Eme97, Bon98, SSP14]. Their work done in that era form the building blocks upon which many fascinating and now ubiquitous technologies including radio communications, *radio detection and ranging* or radar and radio frequency identification (RFID) are based.

Originally devised for direction finding [Sch11] and prevention of ship collisions [Sko88, SSP14], the radar concept for detection of objects and range estimation based on the reflection of EM waves evolved independently across multiple countries in the early 20th century, with significant contributions from inventors including C. Hülsmeyer with the spark-gap based *telemobiloskop* [Sko88], R. Watson-Watt with the 22 MHz Chain Home [SSP14] and U. Tiberio with the radar equation for the linear frequency modulated continuous wave (LFMCW) radar *radiotelemetro* at 200 MHz [Gal14]. Since then, radar technology has been used in a diverse range of systems including precise localization systems, imaging systems and also as interrogators in RFID systems.

In RFID systems, a cooperating target [SFS11] also called a transponder or tag communicates with an interrogating radar using backscatter [Lan05]. These systems, which originated as identify friend or foe (IFF) systems and grew from the works of H. Stockman [Sto48], R. F. Harrington [Har64] and others, have a history which runs concurrently with radar systems research [Ros14, Lan05].

Though early radar systems operated at very high frequency (VHF) and ul-

tra high frequency (UHF), the invention of devices like Magnetron and Klystron pushed the frequencies to the microwave band where the highly directive and physically small antennas made the systems long range and more compact [Sko88]. Subsequent advances in semiconductor technology enabled the design of more compact radio frequency (RF) circuits and systems, mainly through discrete components made using III-V compound semiconductor technologies like gallium-arsenide and indium-phosphide [MBG+96, GRB+00]. But recent progress in the highly scalable and integratable silicon based technologies like silicon-germanium bipolar complementary metal oxide semiconductor (SiGe-BiCMOS) [RHW+10a] and fully depleted silicon on insulator (FDSOI) [OLC+18] are making the realization of high performance radio frequency integrated circuits (RFICs) and systems operating at microwave, millimeter-wave (mmWave) and beyond, a reality. These state-of-the-art technologies offer fast transistors, passives like capacitors, inductors and transmission lines with a relatively high quality factor. Additional advantages of such technologies also include the possibility to integrate baseband circuits including filters and analog to digital converters (ADCs), powerful microcontrollers (µCs) and efficient digital signal processing hardware for the implementation of smart algorithms.

These advances have resulted in the miniaturization and scaling of both secondary radar interrogators and RFID transponders, and the creation of ingenious civilian and humanitarian applications like search and rescue, logistics, transportation, public infrastructure, automotive systems. Of particular interest for active transponder based systems are civilian automotive applications and wireless sensor node (WSN) nodes for internet of things (IoT), catering to diverse uses cases from automotive safety systems for parking, lane switching and vehicle tagging [RBK+19], to toll collection, livestock tracking and inventory management.

In such recent applications combining fundamental concepts of radar and RFID transponders, it is becoming increasingly necessary for the transponders to interface with sensors and to be localizable at short to medium distances [SFS11], in addition to the basic functionality of identification and communication using backscatter. These transponders can be either another radar sensor node like in secondary radars [GHZ+11, JWSE12], or backscatter transponders [SFS11, Weh10, SCW+13b, NEAE18, MMW+19]. Fig. 1.1 illustrates a general overview of the components of such a system, where a static element called a reader or interrogator sends transmit command signals to a number of low power remote elements called transponders in the forward-link [FM10]. The transponders which interface to various sensors responds to the interrogation signal and sends data back to the interrogator through the return-link. As will be discussed in detail

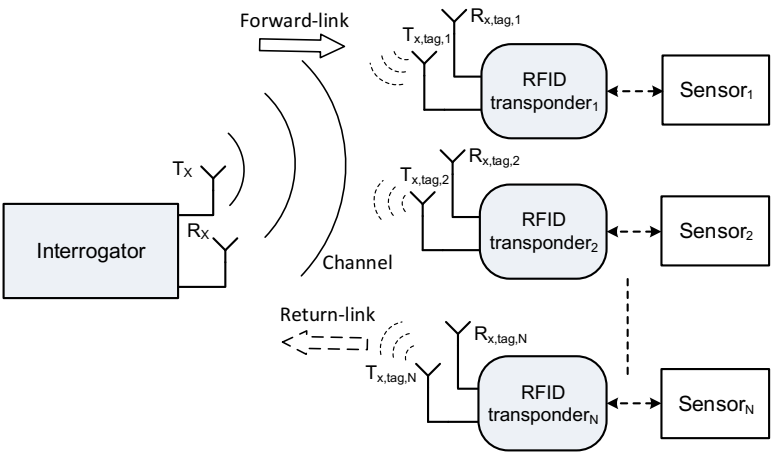

Figure 1.1: System overview showing the components of an RFID system, including an interrogator, antennas and passive or active transponders interfacing sensors.

in Chapter 2, the interrogator and transponders can be implemented in different architectures, technologies and topologies, depending on the usage scenario.

Of the recent RFID transponder based systems and solutions reported for various applications in literature, each has its own unique advantages and also disadvantages. Conventional short range radio and secondary radar based systems like [GHZ+11, JWSE12] where both interrogator and transponders use the same hardware, report location information with high precision, accuracy and long range. They also have communication and multiple sensor interface capabilities. But they are expensive, bulky, consume relatively high power, pose challenges in large scale deployment and operate at relatively low frequencies. Systems based on passive or semi-passive backscatter transponders using Schottky or PIN diodes [MMW+19, MDG12, KPRVH13] are also used for identification and sensor interface at large scale [Lan05]. Though they are inexpensive and consume low power, they operate at near field and are without localization capabilities. Secondary radar interrogator based systems where superregenerative transponders (SRTs) [SFS11, VG08, SCW+13b] are used as cooperative coherent transponders [Bid02] provide a trade-off between the two systems with relatively high precision, accuracy and moderate range. They are also implementable as custom integrated

circuits (ICs), making them suitable for mass deployment at moderate costs. But they do not report identification and sensor interfacing capabilities. An important challenge with interrogator frontends operating at frequencies above 24 GHz is that they are bistatic with separate transmit and receive antennas [SCW+13a, MMW+19]. Solutions like transmit (T_x) / receive (R_x) switches are not optimum for RFID and discrete circulators are expensive. Interrogator implementations at such higher frequencies also use discrete commercial components [PD11, SCW+13a, MMW+19] and older technologies with longer minimum feature length, thereby occupying a relatively large area and consume high power [FHB+21, KPRVH13, PKK+11, VHPM+08].

1.2 Scope and Functional Specifications

This work is basic scientific research investigating novel IC topologies and hardware level system design for radio frequency identification and ranging.

The key research questions posed in this thesis are:

Is it possible to reduce energy consumption of integrated microwave RFID transponders that are jointly identifiable and localizable at long ranges? Are such transponders analyzable and implementable using superregenerative amplifier theory?

Are monolithic IC based components consuming very low power at mmWave frequency bands feasible for implementing single antenna RFID interrogators? Is it possible to analyze and understand the characteristics of these components?

To answer these questions, the scope of this work is constrained by the following functional requirement specifications, characteristic of interrogator-transponder systems:

- Proximity, sensitivity & read range: Design of backscatter transponders operating in the range of at least 50 m and within the limits set by the effective isotropic radiated power (EIRP) of the respective frequency bands pose an interesting research problem. This also requires the transponders to have a very high sensitivity to the interrogation signal.

- Localization: Many novel WSN applications require the location of the RFID transponder, preferably with centimeter level accuracy.

- Small form factor: The objects on which transponders are attached should ideally be oblivious to the transponder, and therefore transponders are required to occupy a small area. The same requirement is also applicable for components of the interrogator.

- Low energy consumption: Reducing energy consumption is a key sustainability goal. Hence both transponders and interrogators should be optimized for low power consumption. In particular, the transponders should consume very low energy so that operation from a battery for at least 8 hours is possible.
- Sensor interface, data storage and communication: The transponders should interface with sensors to acquire data of physical parameters, store the data in on-board memory and send the data to the interrogator to emulate WSN nodes.
- Orientation tolerance: It is desirable to have robust detection and localization even if the transponder orientation changes by rolling.
- Interference tolerance & robustness: Interrogators shall detect and measure the distance to transponders with a high degree of robustness showing resilience to interfering frequencies.
- Frequency tolerance: The system should operate in the unlicensed microwave and mmWave frequency bands so that experimental testing is possible without interference with existing off-the-shelf systems.
- Scalability: Scalability and integration are one of the key requirements for all research done in the information era. It is particularly relevant to RFID transponders.

1.3 Objectives and Structure

This thesis presents two system concepts based on RFICs aimed at seeking answers to the key questions posed in Section 1.2 and to create new knowledge in the field of RFID transponders and interrogators. The main focus is on the analysis, design and characterization of two system concepts for identification and ranging at 24 GHz and 60 GHz. The designed systems include a medium range, locatable SRT based system concept at 24 GHz, and a close range, low area, low power interrogator and semi-passive transponder based system concept at 60 GHz.

For the 24 GHz system concept, the emphasis is on the design of custom RFICs in a SiGe-BiCMOS technology for the SRTs. The SRTs are interrogated using a LFMCW secondary radar based interrogator implemented mainly using commercial off-the-shelf (COTS) components and a custom power amplifier (PA) IC

for range extension. Exploiting specific characteristics of superregenerative amplifier (SRA) operation, makes the SRTs localizable and sensor-enabled. The SRTs also feature roll invariance using custom bandwidth enhanced microstrip patch antennas.

The 60 GHz system concept focuses on RFICs for an unmodulated continuous wave (CW) radar interrogator frontend. In the CW interrogator frontend of this system, a quasi circulator (QC) IC with an integrated low noise amplifier (LNA) is used to interface both the T_x and R_x signal paths to a single antenna. Novel low power topologies are devised to implement custom QC variants and a down-conversion mixer IC in a FDSOI technology. A passive transponder using custom passive and active elements is used to test this system concept.

Though algorithms are designed for data analysis and range estimation, the focus of this thesis is the analysis, design and characterization of the two systems at hardware level and key RF components at circuit level.

The key contributions from this work are the following:

- System level design: System level requirements are derived from analytic expressions of parameters for both the LFMCW and CW interrogators. Theoretical considerations include minimum SRA gain required for achieving a particular maximum range, and models for simultaneous data transfer and ranging using novel SRA quench frequency shift keying (SQ-FSK). Equations to determine key parameters including the maximum number of symbols that can be transmitted in data transfer mode and SRA gain required to achieve a particular maximum range as a function of system parameters. Parameters serving as requirement specifications for both circuit design are also derived *[TFJE23].

- Integrated circuit design: Circuit analysis, design and characterization of RFICs meeting the system level requirement specifications using novel topologies. The novel designs operating at 24 GHz include SRAs variants with integrated quench pulse shaping to simultaneously maximize the output power, minimize the detected input signal and provide multiple inputs and outputs to implement roll-invariance *[TLJE18, TGJE18, TJE20]. Also implemented is a PA with novel bandwidth extension technique *[TLJE19]. The designs operating at 60 GHz include two low power, low area QCs with single antenna interface *[TPC+21] and a folded switching stage down-conversion mixer (FSSDM) with a high conversion gain to power consumption ratio *[TSJE21].

- Experimental tests: The parameters of the designed RFICs are character-

ized independently. The RFICs meeting the requirement specifications are employed along with discrete components to implement the two proof of concept systems involving interrogators, SRTs and antennas *[TTCE18]. Measured system level parameters like range and position estimates, data transfer and roll-invariance are analyzed using programs employing a chirp z-transform (CZT) based algorithm and results are compared against simulations and theory.

The rest of this work is organized as follows:

Chapter 2 presents the features and classification of the RFID transponders and interrogators reported in the literature. Key system level specifications are identified to compare and identify the optimum transponder topology and interrogator architecture. Also included are the fundamentals of SRA operation and a brief overview of the semiconductor technologies used for design.

Chapter 3 is dedicated to the design of K-band SRT and LFMCW radar based identification and ranging system. This chapter includes the system level design and derivation of requirement specifications for circuit design, along with the introduction of key design parameters for the use of SRA in range enhanced SRTs. The chapter then proceeds with sections on analysis, design and characterization of the various 24 GHz RFICs used in the system concept, followed by the implementation details of the components of the proof of concept system. These include sections on the SRT, LFMCW secondary radar interrogator, bandwidth enhanced patch antennas and the data analysis algorithm.

Chapter 4 has a similar structure as Chapter 3, and starts with the system level design, and moves on to the analysis, design and characterization of various 60 GHz RFICs and a 60 GHz passive transponder. The chapter ends with sections on the proof of concept system implementation based on passive transponder and CW interrogator operating at V-band.

Chapter 5 follows with the experimental tests of both the proof of concept systems and the corresponding results from laboratory measurements.

Chapter 6 wraps up this thesis with a summary of main results and key contributions, outlook into the future and an overview of open research questions and interesting challenges that lies ahead in the exciting fields of RFICs, RFID transponders and interrogators.

2 Features and Fundamentals of RFIDs and Superregenerative Amplifiers

In this chapter, an overview and classification of the different RFID transponder technologies and interrogator architectures are presented with a focus on the principle of operation, components and key features relevant to the selection of optimum system architecture. Also discussed are the fundamentals of SRAs and their characteristic specifications which makes them attractive as RFID transponders. The last section of this chapter gives a brief overview of the semiconductor technologies used for IC based transponder and interrogator design.

There are multiple ways to do the classification of RFID systems and its components. Fig. 2.1 lists one possibility based on the transponder technology, interrogator architecture, interrogation EM field regions and localization methods. The interrogation EM field regions and the communication modes employed also determines the EM field coupling mechanisms used in the system.

2.1 RFID Transponder Technology

The basic RFID transponder consists of a coupling element like a capacitor, coil or antenna to interact with the interrogator and a passive or active element. The passive or active element can *tran*smit data to the interrogator and re*spond* to the interrogation signal to receive data [FM10, Par10]. There are numerous variants of RFID transponders reported in literature [SPB$^+$21, MGAC19, KPRVH13, FM10, Par10, Weh10]. The choice of a particular transponder technology depends on a combination of parameters to meet the requirement specifications and demands of the respective application in which the RFID system is used.

The left half of Fig. 2.1 shows one possible classification of RFID transponders. Based on the technology used for implementation, they can be broadly categorized as chipless transponders and semiconductor IC based transponders. They can also be classified based on the type of EM field coupling, and whether the tag operates in the near of far field interrogation zones. Another differentiating specification of advanced RFID transponders are the capability to be localized. To estimate the distance to tags, different localization techniques based on amplitude, phase and time of flight of the scattered signal are employed. Key features of aforementioned methods are briefly discussed in the following subsections.

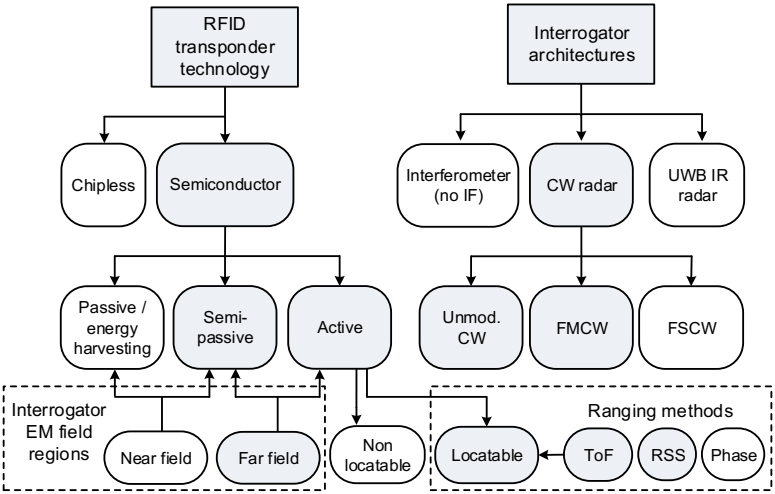

Figure 2.1: Classification of relevant RFID transponder technologies and interrogator architectures. The areas covered by this work are highlighted in gray.

2.1.1 Chipless RFID Transponders

They are based on passive structures that do not constitute a semiconductor device or ICs, and are constructed using inductive components, magnetic materials, and reflective or absorptive EM materials, which encode specific data [HPMCM19]. Depending on the encoding method, these transponders can be categorized as time domain encoding based, frequency domain encoding based or hybrid transponders [HPMCM19]. When placed in the interrogation zone, these transponders receive the interrogation signal using an antenna and depending on the implementation, temporal or frequency signatures can be detected [MGAC19, HPMCM19].

Chipless transponders employing time domain encoding methods are based on time domain reflectometry (TDR) [HPMCM19, FK15] and typically employ surface acoustic wave (SAW) resonators [WV65], loaded transmission lines [MGAC19], or pulse position modulation (PPM)[GNC10, Cri66]. Frequency domain chipless RFID transponders are implemented using an array of antennas or resonant elements tuned at different frequencies within a frequency band swept by the interrogation signal [PBKS08, PK10, JR05]. Hybrid transponders like [VPT11, VPT12b]

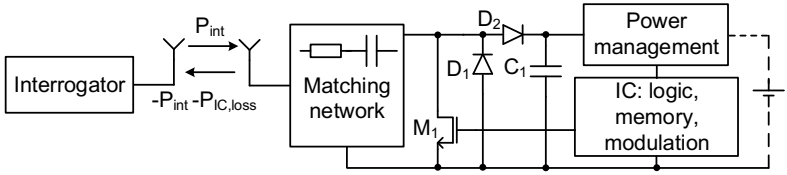

Figure 2.2: Schematic of a typical semiconductor based passive transponder.

combine two or more encoding methods to assign more than two logic states to a single element. This multi-state behavior is achieved by encoding information in the frequency [VPT12b] or by encoding information in the amplitude level of the transmission zeroes introduced by the resonant elements [HPMC+17] or by using polarization diversity to increase the information density and bandwidth as reported in [VPT12a].

Chipless RFID transponders are small form factor, low cost solutions [MGAC19], but some approaches also require narrower interrogation pulses to minimize overlap between pulses [HPMCM19, MGAC19]. Such requirements, increase the size of the transponders, reduce the number of data bits that can be encoded, and require high bandwidth interrogator frontends [HPMCM19, MGAC19]. Though recently reported chipless transponders achieve high information density and carry up to 100 bits of data, they operate at very short ranges, with a maximum reported range of 150 cm, and report no localization capability [HPMCM19].

2.1.2 Semiconductor based RFID Transponders

Semiconductor based RFID transponders use components like diodes or ICs and are either passive or active. Passive transponders are either batteryless using energy harvesting or battery assisted, while active transponders are typically battery assisted.

2.1.2.1 Passive Transponders

The international standards organisation (ISO) standard ISO 19762 defines passive RFID transponders as those devices which receive the typically unmodulated forward-link radiation from the interrogation signal and send reply signals back to the interrogator by deflecting or modulating in a passive way, without using any on-board active transmitter [Par10]. The return-link communication is either in the half duplex or full duplex mode.

Passive load modulation: passive load modulation (PLM) is the most common RFID backscattering method found in literature [FM10, Par10, CF11]. Fig. 2.2 illustrates the schematic of a typical passive transponder. The interrogation signal is received by the antenna and the received signal power is transferred to the rest of the transponder using a matching network. The N-channel metal oxide semiconductor (NMOS) transistor M_1 is periodically switched between cut-off and saturation regions by on-off keying (OOK) modulation signal generated by the semiconductor based IC. This modulation causes a change in termination impedance and thereby reflection coefficient of the antenna, and thereby a change in the radar cross section (RCS) of the transponder, and is called passive load modulation. Interrogators detect this variation in σ_{ant} and decode the data sent by the transponder. Such transponders can be remotely powered by the interrogation signal, or can be battery assisted.

Battery-less passive transponders: These are remotely powered or energy harvesting transponders where power is drawn from the magnetic or EM field of the interrogator [Par10, FM10]. In Fig. 2.2 the diodes D_1 and D_2, together with capacitor C_1 function as a halfwave rectifier to rectify and store a part of the interrogation signal energy in C_1. The potential difference across C_1 is then regulated by a power management circuit to power the transponder IC. In addition to generating the modulation signal , the transponder IC may include logic, memory for data storage and other functionalities. The received signal power is then used to communicate data back to the interrogator through the return-link.

Another class of battery-less transponders in which antenna arrays are used to reflect the incident signal towards the direction of the source without any prior knowledge about the direction of the source are called retrodirective or Van Atta arrays [MSU+11, SPB+21]. There are also passive directional coupler based transponders reported in [AD19]. These transponders achieve medium range and good accuracy, but they function as reflectors and do not report data transfer.

Battery-assisted passive transponders: These devices, also called semi-passive trans-ponders include on-board batteries to power the ICs in the RFID device, instead of harvesting energy from the interrogating signal using the rectifier signal. They do not include RF transmitters to generate high frequency signals on their own. They typically include more complex circuitry for storage and faster data processing, which require on-board batteries. They also operate at short to medium ranges [Par10]. They have higher sensitivity compared to battery-less passive transponders, and their maximum range is limited by interrogator sensitivity. Recently semi-passive transponders are also reported at mmWave frequencies at 60 GHz [SFS11, KPRVH13].

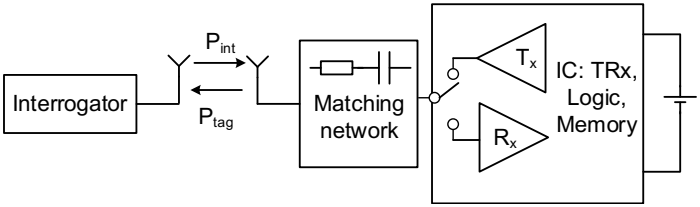

Figure 2.3: Illustration of a active transponder functionality.

Passive transponders are intended to replace traditional barcode technology and are inexpensive and light weight. Maximum range of passive RFID systems are limited by transponder sensitivity. Most passive RFID have a limited communication range of around 1 m to 2 m due to very low reflected power. They are smaller, lighter and cost less than active transponders and also their data storage capacity is much lower than active transponders [FM10, Par10].

2.1.2.2 Active Transponders

Active RFID transponders (ARTs) are defined as RFID devices having an ability to produce RF signals on its own, according to the ISO 19762-3 [Par10]. As illustrated in Fig. 2.3, active transponders typically have an on-board RF transmitter or transceiver capable of providing much stronger return link power to the interrogator [Par10]. They also utilize a local power source like a battery or a solar cell, periodically transmitting their ID and data over return link [Par10, FM10].

The on-board transmitter reduces the interrogator transmit power required for the same distance compared to passive RFID transponders and requires a smaller antenna aperture [FM10]. This also enables active RFID transponders with high sensitivity to cover distances in the range of tens of meters from the RFID interrogator [FM10]. Active RFIDs can be used for localization easily embedded in the tracking objects but they typically do not achieve sub-centimeter accuracy. They are also not readily available on portable user devices and require maintenance through battery replacement [Par10].

In literature, numerous ARTs can be found [Xue08, BMM12, SFS11, Weh10, DHV17b]. Their key differentiating parameters include operation frequency, transmit power, the extend of integration, input receiver sensitivity, localization capability and data transfer rate. Based on the operation principle, they can be categorized as short range radio devices, reflection amplifiers, active retrodirective Van Atta array transponders, active load modulation transponders, pulsed

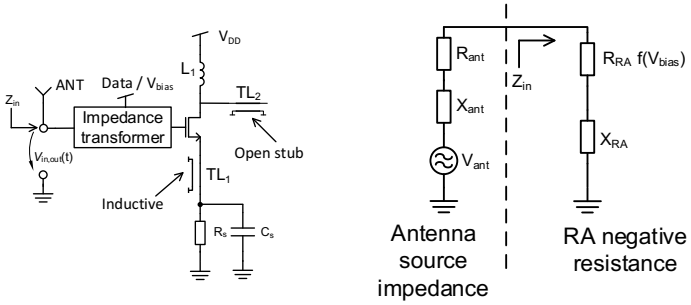

(a) (b)

Figure 2.4: (a) Schematic of a unilateral reflection amplifier based ART. (b) Corresponding small signal model.

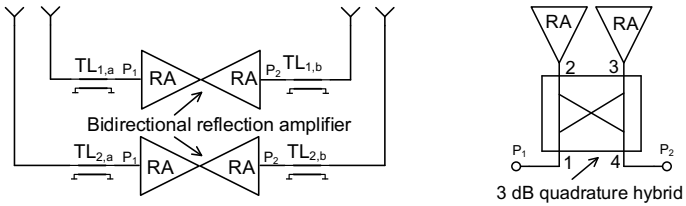

(a) (b)

Figure 2.5: Schematic of (a) active retrodirective Van Atta array. (b) Bidirectional reflection amplifier.

oscillators and SRAs based transponders.

Short range radio devices: Short range radio devices are a class of active transponders where data from the interrogator is amplified and downconverted to decode the data in the receive mode as shown in Fig. 2.3. In the transmit mode, the transmitter with its own oscillator and power amplifier is turned on and connected to the antenna using a transmit-receive switch. The antenna radiates an EM field without backscatter modulation to send data back to the interrogator [FM10].

Due to the methods employed, SRDs can operate with the maximum possible output power in the allowed frequency bands to cover the maximum possible range, typically several hundred meters [FM10] and employ limited localization and ranging capabilities. But these devices are complex, occupy a large footprint and consume relatively large power.

Reflection amplifiers: One of the simplest approaches to implement active RFID transponders is by using reflection amplifiers to amplify the backscattered signal [VMCV02, CF06, BMM12, KGCT14, FKSE17]. Reflection amplifiers are one-port narrowband circuits that presents an input impedance with a negative real part that makes the input reflection coefficient larger than one [VMCV02]. They are implemented using devices like transistors, Gunn diodes or tunnel diodes [FKSE17].

Fig. 2.4 shows a reflection amplifier implementation using a common drain amplifier using transistor M_1 at the core [CF06]. L_1 is an RF choke to supply V_{DD} to the transistor. R_s controls the biasing and C_s is a RF bypass capacitor. The microstrip transmission line TL_1 with an equivalent inductive impedance between the source and R_s sets amplifier closer to the region of instability. The transmission line TL_2 at the drain of M_1 is an open stub used for frequency selectivity. Both TL_1 and TL_2 are optimized to provide a negative input resistance at the operating frequency. An impedance transformer is also used to transform the impedance to a real part as close to $-50\,\Omega$ as possible. When an input transmission line of characteristic impedance $Z_o = 50\,\Omega$ is terminated on a reflection amplifier with input impedance $Z_{in} = R_{in} + jX_{in}$, the magnitude of voltage reflection coefficient Γ_{in} at the input of the circuit is given by [KGCT14]

$$|\Gamma_{in}| = \left|\frac{Z_{in} - Z_o}{Z_{in} + Z_o}\right|. \tag{2.1}$$

In a reflection amplifier (RA), the real part of input impedance is negative according to $\mathfrak{Re}(Z_{in}) = -R_{in}$, resulting in $|\Gamma_{in}| > 1$ as,

$$|\Gamma_{in}| = \left|\frac{-R_{in} + jX_{in} - Z_o}{-R_{in} + jX_{in} + Z_o}\right|. \tag{2.2}$$

The resulting return power gain of $|S_{11}|$ in decibel given by

$$|S_{11}| = 10\log|\Gamma_{in}|^2\,\text{dB} = 20\log\frac{R_{in} - jX_{in} + Z_0}{R_{in} - jX_{in} - Z_0}\,\text{dB}, \tag{2.3}$$

In oscillator designs, the condition

$$R_{in} + Z_o < 0 \tag{2.4}$$

is used and the imaginary part is designed to be zero at the frequency of oscillation, whereas in a reflection amplifier, the real part is designed to have a small negative value to result in an increased gain, while the imaginary part is a value higher than zero in magnitude so that undesired oscillations are damped. The input

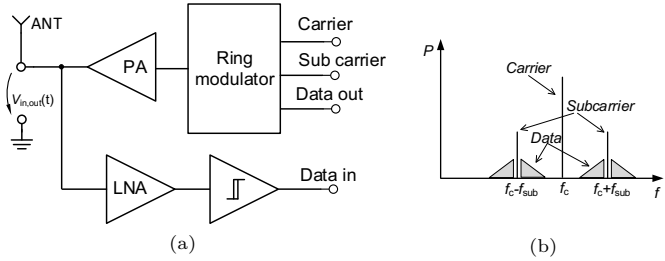

Figure 2.6: Schematic of (a) active load modulation transponder. (b) illustration of corresponding amplitude spectrum.

reflection coefficient varies from a positive real part to a negative real part as a function of V_{DD} and hence data to be transmitted to the interrogator is encoded as a function of V_{DD} to generate amplitude modulation (AM) or OOK signals.

Another RA based design variant is reported in [BMM12]. This design is based on a differential cross-coupled core interfaced to a dipole antenna and a varactor for phase modulation. The circuit uses microwave reflections to amplify and re-radiate the incident interrogation signal at 4 GHz, and is implemented in a 130 nm CMOS technology.

Reflection amplifier based ARTs are capable of generating amplified backscatter in operating frequency bands from UHF to K band, with return gains up to 8 dB over a an interrogation range up to 2 m while consuming very low power [CF06, FKSE17]. But no demonstration of ranging or localization is reported in literature.

Active retrodirective Van Atta arrays:

The Van Atta array uses paired antennas connected by transmission lines with equal lengths or difference in lengths equal to multiples of the guided wavelength, ensuring that the transmission lines do not contribute extra phase difference to the incident waves [CCL03, CF11, SPB$^+$21]. Each antenna functions as both a receiving and transmitting antenna, and the two antennas of each pair are located symmetric with respect to the center fo the array. Each antenna receives a wave, and the pairing antenna reflects the wave back after it is delayed by a connecting transmission line. Each antenna and its pair is connected in a mirror symmetric configuration, resulting in relative phase reversal for the reflected wave compared to the incident wave [SPB$^+$21]. Therefore the reradiation field phase distribution becomes reversed producing a reradiation beam in the incident wave direction. In a passive Van Atta array, the reflected wave intensity is proportional to the

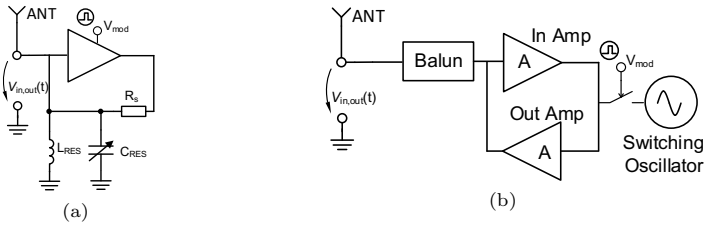

Figure 2.7: Schematic of pulsed oscillator based transponder (a) The implementation from [Weh10] and (b) [SCW+13b].

number of antennas in the array. An active Van Atta array on the other hand either uses a unilateral amplifier or a bidirectional amplifier.

A bidirectional amplifier based Van Atta array is shown in the schematic of Fig. 2.5(a). This implementation results in increased radiated field intensity by a factor of the gain of the amplifier G_{VA}, which is 6 dB higher than the unilateral amplifier based arrays [CCL03]. The bidirectional amplifier is typically implemented using two reflection amplifiers and a quadrature hybrid as illustrated in Fig. 2.5(b).

Active load modulation: Active load modulation tries to improve the range and data transmission capabilities of the transponder by generating a signal with the same spectral characteristics as that of conventional passive transponder based load modulation devices [Fin11, GWMC12, SRS+21]. Transponders utilizing the active load modulation principle employ either OOK or binary phase shift keying (BPSK). As shown in Fig. 2.6(a), the typical OOK active load modulation transponder includes a ring modulator which modulates the carrier signal and sub-carrier based on the data to be transmitted. The generated frequency spectrum consists of the carrier and two sidebands separated by a fixed frequency, similar to double side band (DSB) modulation as illustrated in Fig. 2.6(a). A PA drives this signal and transmits through an antenna. The transponder receives data using the same antenna, which is amplified using a LNA, and digitized using a Schmitt trigger.

BPSK modulator based transponder architectures employ relatively complex architectures consisting of LNA, BPSK modulator, detector and a variable gain amplifier (VGA). IC implementations of such transponders are reported at a wide range of frequencies including 77 GHz [DHV17b].

The reported works report extend the range, chip level detection and communication capabilities, but no distance measurement capability is reported [Fin11,

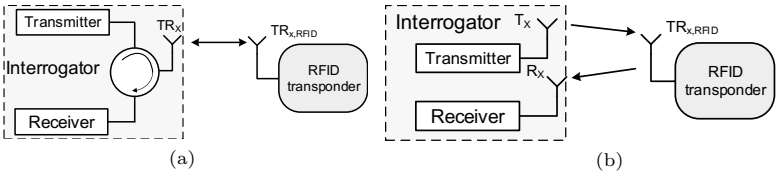

Figure 2.8: Illustration of (a) Monostatic interrogation and (b) bistatic interrogation principle.

DHV17b].

Pulsed oscillators and superregenerative amplifiers: Another interesting ART class based on a pulsed oscillator is reported in [Weh10]. A similar architecture is also reported with the nomenclature switched injection locked oscillator (SILO) in [VG08, SCW$^+$13b]. As shown in Fig. 2.7(a), these transponders are based on frequency tunable narrowband oscillators which can be switched ON and OFF using a modulation signal [Weh10]. Some implementations [VG08, SCW$^+$13b] also use a LNA and PA based architecture as illustrated in Fig. 2.7(b). Such modulated backscatter transponders perform phase coherent amplification of the interrogation signal based on the startup characteristics of oscillators. They also enable the measurement of distance between interrogator and transponder using the round trip time of flight (RToF) principle [VG08, SCW$^+$13b]. Active pulsed reflector operates with an accuracy of 33 cm [Weh10] [SFS11].

Active pulsed oscillator based ARTs have better clutter performance, can measure distance to transponder, have low complexity and consume low power. But these works report only ranging at short distance and not communication for data transfer. Active pulsed oscillator based RFIDs find roots in a class of circuits known as SRAs as discussed in detail in Section 2.6.

2.2 RFID Interrogator Architectures

RFID interrogators, also called RFID readers are full duplex RF frontends which transmit an interrogation signal and receive the backscattered or load modulated signal at the same time. RFID interrogators are similar to radar frontends, though not all radar architectures fit the purpose. Similar to conventional radars, depending on the location of transmit and receive antenna, RFID interrogators are classified as monostatic and bistatic radar systems. As shown in Fig. 2.8(a), the monostatic interrgator interfaces the transmit and receive frontends using a single antenna. This is done either with the help of transmit-receive switches

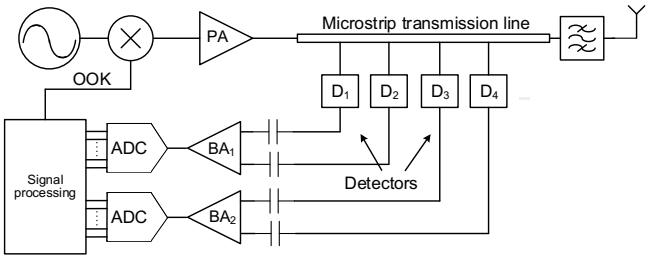

Figure 2.9: Illustration of an interferometer based interrogator.

or circulators. Bistatic interrogators on the other hand have separate transmit and receive antennas as illustrated in Fig. 2.8(b). The definition holds in conventional systems operating at lower frequencies when the separation between the two antennas are significantly greater than the wavelength. In systems operating at microwave and millimeter wave frequencies, due to the shorter wavelength, the separation is quite small so that both transmitter and receiver can be located in the same module, and considered essentially monostatic. In the following sections, some architectures like interferometers are strictly monostatic, while others like the ultra-wideband (UWB) interrogators and CW radar interrogators are used in both monostatic and bistatic configurations.

Depending on the down conversion and data analysis methods used, RFID interrogators can be broadly classified into those utilizing time domain and frequency domain methods. While architectures like interferometers and UWB utilize the time domain properties of the received signal to detect the presence of a transponder, continuous wave architectures like frequency stepped and frequency modulated continuous wave employ frequency domain techniques for transponder identification, detection and ranging.

2.2.1 Interferometer based Interrogator

Interferometers are no-intermediate frequency (IF) full-duplex time-domain interrogators which detect the backscatter based on the interference of the transmitted signal and received backscatter signal [ZXLW04]. They are implemented using an array of envelope detectors to eliminate blind spots and do not require a receiver side mixer. [ZXLW04] reports the design of a non-IF interrogator where 4 detectors with a spacing of $\lambda/8$ are placed along a $50\,\Omega$ microstrip transmission line and

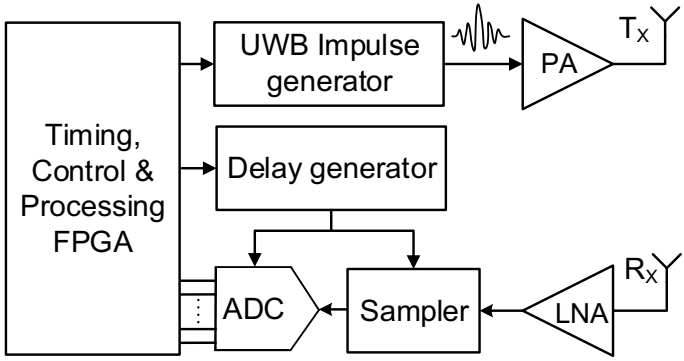

Figure 2.10: Illustration of a IR-UWB interrogator.

length greater than $3\lambda/4$, but less than λ. The transmitted traveling wave and the received traveling wave superimpose along the microstrip transmission line, forming a standing wave. The envelope detectors are zero-bias Schottky diode based rectifiers with AC filtering capacitors at the cathode output. The detector output has the characteristics of a harmonic voltage source, and the output voltage is digitized by ADC to decode the OOK data transmitted by the transponder.

Interferometer based interrogator have low complexity, moderate sensitivity and consume low power, but they are not suitable for measuring the distance to the transponder.

2.2.2 Ultra-wideband Interrogator

Fig. 2.10 depicts one of the state-of-the-art architectures of a ultra-wideband impulse radio (UWB-IR) system [GSP+15]. The core of this interrogator is a pulse generator which generates short duration n^{th} order Gaussian pulses [WS98], typically less than 1 ns, amplified by a PA and radiated using the T_x antenna. The pulse generator is implemented using delay elements and charge pumps. The transponder shapes the signal and reflects it back to the interrogator. The received signal at the interrogator R_x antenna is amplified by the LNA and undergoes a delayed sampling process using a sampler circuit [GSP+15, WTLH18]. The sampled signal is digitized by an ADC, and the data is processed, typically by a field programmable gate array (FPGA) to retrieve the signal sent by the transponder using the equivalent time algorithm [GSP+15]. The impulse generator, the tunable delay generator, the sampler and the ADC are controlled and synchronized

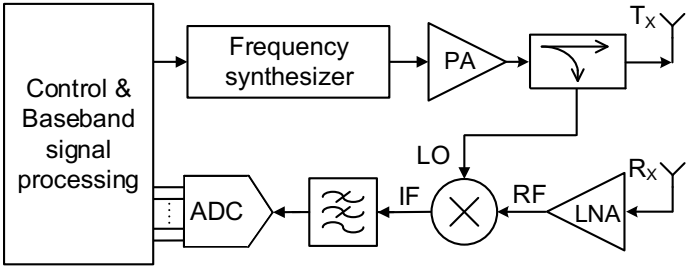

Figure 2.11: Generic architecture of bistatic CW radar interrogators.

by the FPGA.

They consume very low power due to low duty cycle operation, have high tolerance to interference and multipath compared to narrow band and also have high object penetration depths [LDBL07, DDR+10]. The short Gaussian pulses used for interrogation are also beneficial for precise ToA and ToF based localization, but require multiple optimally located interrogators and time synchronization between them, increasing the complexity of the system [LDBL07]. However, due to the short duration pulses, the interrogator requires high bandwidth RF components and expensive radiating elements like horn antennas or moderate gain Vivaldi antennas that operate in the frequency bands from 3.1 GHz to 10.6 GHz [DDR+10].

2.2.3 Continuous Wave Interrogators

CW secondary radars are one of the widely used interrogators for identifying backscatter RFID transponders. Their advantages include low transmit power requirements, high sensitivity and low complexity [Sko80, PMFT+17]. They can be broadly divided into two categories, namely unmodulated single-carrier CW radar interrogators and modulated CW interrogators. Interrogator architectures like pulse radars and interferometry CW radars fall under the single-carrier CW unmodulated CW radar category and operate based on time domain signal processing principles. Modulated radar systems like stepped frequency continuous wave (SFCW) and LFMCW on the other hand operate based on frequency domain signal processing principles [PMFT+17].

Most CW bistatic radar systems typically employ a single channel homodyne, direct conversion or low-IF architecture as depicted in the simplified architecture

of Fig. 2.11. Here the frequency synthesizer is typically a voltage controlled oscillator (VCO) controlled either by a digital to analog converter (DAC) or a phase locked loop (PLL), or a direct digital synthesizer (DDS). The generated signal is amplified using a PA and transmitted using the T_x antenna. The backscattered signal received from the transponder is received using the R_x antenna, and amplified before it is fed to the RF port of the downconversion mixer. The LO port of this mixer is fed with a a part of the transmitted power using a coupler or power divider. The downconverted IF signal is then low pass filtered and digitized by an ADC to decode the demodulated data from the transponder. In the case of monostatic interrogators using a single antenna, the separation of the received backscatter signal from the transmit signal is done using a circulator.

The characteristics of the transmitted signal are controlled by the frequency synthesizer, which is able to generate unmodulated CW, SFCW or LFMCW signals by varying the VCO tuning voltage as a function of the required modulation characteristics [GPSH19].

Unmodulated single-carrier continuous wave radar: One of the earliest interrogator architectures used single carrier CW [Sto48, KDF75]. They operate using a single-frequency CW to obtain phase accumulation of targets [PMFT+17]. In the more recent interrogator architectures similar to that illustrated in Fig. 2.11, the synthesizer generates a constant amplitude single frequency signal by controlling the tuning voltage of the VCO. The transmitted CW signal is backscattered by the transponder. The backscattered signal is an amplitude modulated CW signal and is demodulated and digitized by the receive frontend to detect the presence of the transponder. CW radars also enable the measurement of range to transponder, albeit ambiguity after a distance of one wavelength. The transmitted wave traveling through the channel accumulates the phase and when the received wave is compared with the transmitted wave, the range R_{CW} is calculated as [Sko80]

$$R_{\mathrm{CW}} = \lambda \left(\frac{\theta_{\mathrm{CW}}}{2\pi} + n_{\mathrm{CW}} \right), \tag{2.5}$$

where the wavelength $\lambda = C_{\mathrm{o}}/f_{\mathrm{CW}}$, f_{CW} is the transmitted carrier frequency, θ_{CW} is the measured phase difference between transmitted and received signal varying from 0 to 2π, and n_{CW} is an integer denoting the wave cycle. (2.5) says that the estimated range is ambiguous because the receiver measured only θ_{CW} and not n_{CW}.

Single carrier CW radars have the simplest architecture, and hence relatively low power consumption. They can identify transponders based on backscatter, provide high precision displacement and unambiguous velocity measurements of single targets [PMFT+17]. However, they are not suitable for measuring the ab-

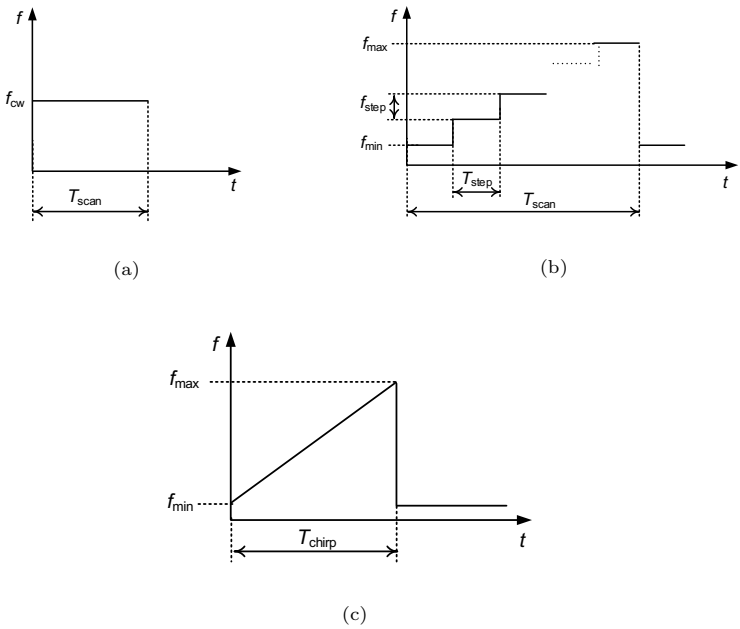

Figure 2.12: Illustration of the frequency domain representation of CW transmit signals. (a) single-carrier CW (b) SFCW and (c) FMCW.

solute distance to targets and transponders [PMFT+17]. Also since the interrogator only uses a single frequency, these systems are not resilient against multipath effects at lower frequencies, but is seen as a suitable candidate for low power close-coupling system applications at mmWave frequencies [VHPM+08].

Stepped frequency continuous wave radar: SFCW radars [LDBI96] are wideband interrogators where the frequency synthesizer output in the simplified architecture of Fig. 2.11 is stepped as discrete frequency steps illustrated in Fig. 2.12(b). In the depicted bistatic configuration, the instantaneous frequency f_{i} of the VCO is varied in discrete steps of duration T_{step} by a DAC, and transmitted after amplification using a PA [LZA09, LAE+11, AWM09]. The instantaneous frequency is given by

$$f_{\mathrm{i}} = f_{\mathrm{min}} + k * f_{\mathrm{step}}, \tag{2.6}$$

where integer $k = 0, 1, 3, ..N_{\mathrm{SFCW}}$ and N_{SFCW} is the number of steps within a

scan period T_{scan} given by

$$T_{\text{scan}} = N_{\text{SFCW}} T_{\text{step}}. \tag{2.7}$$

For each stepped frequency value, the backscattered EM wave from transponder is received by the homodyne receiver. The received baseband signal is the sum of scattered signals from all the targets [IF83] and transponders present within the interrogator coverage area, and a discrete Fourier transform (DFT) is be used to retrieve the scattering coefficients from individual targets [LDBI96, IF83] to identify and detect the transponders. The range resolution of the SFCW radar using N_{SFCW} steps of δf_{step} is determined as [LDBI96]

$$\delta R_{\text{SFCW}} = \frac{C_{\text{o}}}{2B_{\text{SFCW}}}, \tag{2.8}$$

where C_{o} is the free space propagation velocity of EM waves, and bandwidth $B_{\text{SFCW}} = N_{\text{SFCW}} \delta f_{\text{step}}$. Range resolution is one of the most important parameter of radars that measure range to target. It is the ability of a radar system to unambiguously distinguish between two or more targets placed in the same direction, but at different ranges. In other words, if two targets are placed closer than δR_{SFCW} in the same angular direction, the radar system will not be able to distinguish between the two targets, and represent both of them as a single target.

The corresponding maximum range $R_{\text{SFCW,max}}$ for unambiguous range measurement is given by [LDBI96]

$$R_{\text{SFCW,max}} = \left(\frac{N_{\text{SFCW}}}{2} - 1 \right) \delta R_{\text{SFCW}} \tag{2.9}$$

SFCW radar is advatageous in applications where a lower operating frequency band is required along with high resolution and low system noise. Their main drawback is the longer scan time T_{scan}, especially when long range performance is desired. The T_{scan} in (2.7) determines how fast a sweep can be done. For a given loop bandwidth or settling time of the DAC, T_{step} is generally set to a minimum. But in order to detect transponders at a long range, N_{SFCW} should be increased, and this proportionately increases T_{scan} according to (2.7).

Frequency modulated continuous wave radar: LFMCW radars are an extension of SFCW radar, and operate based on frequency domain principles [Sko80]. The main advantage of LFMCW radar compared to unmodulated CW is that the unambiguous absolute range can be determined. When compared to SFCW radar, instead of using discrete frequency steps, the instantaneous frequency is varied

linearly from a minimum frequency $f_{\min}$ to a maximum $f_{\max}$ to generate a chirp with period T_{chirp} as illustrated in Fig. 2.12(c). Due to this, they are able to interrogate transponders at longer distances faster as the maximum range is not dependent on the number of frequency steps. More details are described in Section 3.1.1. Since they use a wide spectral bandwidth similar to UWB, LFMCW based radar based interrogators also offer high degree of multipath immunity and accuracy compared to unmodulated CW and SFCW.

2.3 Coupling Dependent Range and Operating Frequencies

The physical coupling between interrogator and transponders is possible using electric, magnetic and EM fields [FM10]. Electric fields are employed by capacitively coupled systems, magnetic fields by inductively coupled systems and EM fields by backscatter systems. Depending on the operation range, these systems can be classified as follows:

Close-coupling or close range systems: These are systems typically operating at ranges below 1 cm, and hence used in applications allowing close contact between the interrogator and transponder, like electronic door locking or point of sale contactless smart cards [FM10]. Such systems operate with either magnetic coupling using inductors or electric field coupling using capacitors at frequencies less than 30 MHz and does not rely on radiative fields. Typically the transponders are passive, and the short interrogation range facilitates the transfer of relatively large amounts of power from the interrogator to the transponder.

Remote-coupling or short range systems: These are RFID systems with an interrogation range less than 1 m. They employ either inductive coupling using coils and operate at frequencies below low frequency (LF) at 135 kHz or high frequency (HF) at 13.56 MHz. This enables such systems to be employed in applications like industrial automation and animal tagging. Recent millimeter-wave identification (MMID) systems at millimeter-wave frequencies operating at 60 GHz are relatively short range and could come under this category.

Long range systems: When the interrogator range is much larger than 1 m, the RFID systems operate in the ultra high frequency (UHF) at 433 MHz or 868 MHz and 915 MHz and microwave frequency ranges at 2.45 GHz, 5.8 GHz and 24 GHz [LDBL07, FM10]. Passive backscatter transponders generally achieve a range of around 3 m, while active backscatter transponders achieve a range greater than 15 m [FM10]. The operating frequency range implies communication and power transfer is done using antennas. These antennas receive the RF power from the interrogator and transfer the power to the ICs in the transponder with minimal

losses. The optimum design of the antenna is essential to maximize the reflected or reradiated incident power in backscatter modulation. Common antenna designs include dipole antennas and microstrip patch antennas.

Frequency of operation: RFID systems are governed by numerous standards, and operates at standard frequency bands. Table 2.1 compares the operation frequency, coupling methods, data rate and storage capacity, maximum range and applications corresponding to those frequency bands [FM10, Par10].

Table 2.1: RFID transponder frequency bands and coupling methods

Frequency band	Frequency range	Coupling	Data rate	Data storage capacity	Range	Applications
LF	125 to 134 kHz	Inductive	Low	small (16 bits)	10 cm	Access control, Animal tagging etc.
HF	13.56 MHz	Inductive	Medium	small to medium	< 1 m	Smart cards, case tagging etc.
VHF	433 MHz	EM	High	Large	< 100 m	Asset & container tracking etc.
UHF	860 to 960 MHz	EM	High	Medium	< 12 m	Case level tagging, railroads etc.
Microwave	2.45 GHz, 5.4 GHz	EM	High	Medium	< 2 m	802.11 WLAN, Bluetooth standards
Microwave	24 GHz	EM	High	Large	< 100 m	Automotive
mmWave	60 GHz	EM	High	Medium	< 10 m	Automotive, Lane switching etc.

2.4 RFID Ranging Techniques

When an RF signal propagates through a channel, the three key characteristics of the signal including amplitude, time and phase undergoes transformation. RF localization and ranging techniques rely on the fact that geometric parameters like distance or direction of the transponder can be estimated from these transformed parameters [YZL13, BSRS10]. There are multiple ranging methods [NR08, SR92, MBN21] reported in literature which exploit each of the three signal characteristics, but there are key differences in the localization of RFID transponders as compared to traditional wireless local positioning systems [MEK+11]. Traditional wireless local position systems rely on a network of spatially distributed interrogators or transponders, and do localization based on multilateration and multiangulation. RFID localization is mainly centered around bilateral ranging and direction finding, typically based on radar principles [MEK+11]. What follows is a brief discussion of a few important ranging techniques and the suitability of a particular technique to locate RFID transponders.

2.4.0.1 Received Signal Strength based Ranging

The amplitude of an RF signal propagating through a channel undergoes attenuation. The magnitude of this attenuation is proportional to the distance travelled as described by the Friis' path loss equation [Sko80].

$$\mathrm{PL_d} = \left(\frac{4\pi d}{\lambda}\right)^n \tag{2.10}$$

where d is the distance between the interrogator and transponder antennas, λ is the wavelength of the interrogating signal, and $n = 4$ for passive transponders and $n = 2$ for active or semi-passive transponders.

In a typical RFID system, the interrogator transmits a power level P_{TX}. The transponder backscatters or transmits back the signal and d is estimated based on the received signal strength (RSS) or received signal power level P_{RX} at the interrogator as [NR08],

$$d = \frac{\lambda}{4\pi}|H| \sqrt[n]{\frac{P_{\mathrm{TX}}}{P_{\mathrm{RX}}} G_{\mathrm{TX}}^2 G_{\mathrm{RFID}}^2 K \chi^2} \tag{2.11}$$

G_{TX} and G_{RFID} are the antenna gains for the interrogator and transponder respectively. χ is the coefficient of polarization matching , and K is the coefficient of backscattering. H represents the complex channel response, which equals to 1 for line of sight (LoS) interrogation.

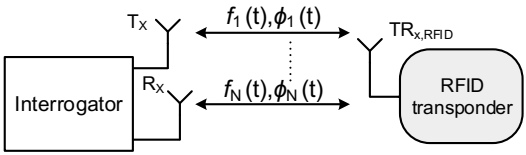

Figure 2.13: Illustration of frequency domain phase difference of arrival technique.

RSS in indoor environments is affected by multipath fading and shadowing. To estimate the distance to transponder from interrogator under such conditions, a mean path loss exponent p is defined in [SR92]. The distance between interrogator and transponder is then estimated by using the measured absolute mean path loss $\overline{\mathrm{PL}}_{\mathrm{d}}$ defined in the distance dependent path loss model from [SR92] given by,

$$d = d_0 10^{\frac{\overline{\mathrm{PL,dB}}_{\mathrm{d,dB}} - \mathrm{PL}_{\mathrm{d}_0,\mathrm{dB}} - X_{\sigma,\mathrm{dB}}}{10p}}, \tag{2.12}$$

where d_0 is a reference distance and $\mathrm{PL}_{\mathrm{d}_0}$ is the path loss measured at d_0. $p = 2$ for free space, and in indoor environments with multipath signals $p > 2$ is empirically determined. $X_{\sigma,\mathrm{dB}}$ is a zero mean log-normally distributed random variable with a standard deviation of σ in decibels. The characteristics of (2.12) result in a linear variation of received signal power with distance in a log-log plot.

RSS based localization and ranging is easy to implement, cost efficient and can be used with a number of technologies including RFID. However, since RSS depends on the received signal power, the signal to noise ratio degrades with distance, degrading the distance estimation accuracy more than other techniques [ZGL19]. Also received signal power is not a highly sensitive function of distance and antenna radiation [NMR+10]. Additionally, multipath fading and shadowing from objects in the environment further attenuate the signal power through absorption, reflection, scattering and diffraction [YZL13, ZGL19], especially at lower frequency of operation and therefore the path loss exponent is difficult to determine analytically and us usually determined using statistics [NR06]. Accuracy is also affected by other factors including transponder orientation, receiver sensitivity in the case of active or semi-passive transponders, antenna radiation pattern and channel characteristics [ZGL19]. So RSS is often combined with other techniques to improve ranging accuracy [MBN21].

2.4.0.2 Phase based Ranging

RFID systems in which interrogators employ in-phase and quadrature (IQ) demodulators with coherent detectors have the capability to extract the phase of the backscattered signal along with RSS [MBN21]. The phase of the backscattered signal is given by [NMR+10],

$$\phi = \frac{4\pi d}{\lambda} + \phi_0 + 2\pi\omega_\phi \tag{2.13}$$

where λ is the wavelength of the interrogating signal, d is the distance between interrogator and transponder, ω_ϕ is the phase noise and ϕ_0 is a constant phase offset that depends on multiple variables including interrogator components, tag characteristics and orientation. The main limitation of this approach as is evident from (2.13) is the phase-ambiguity above 2π radians. Several phase unwrapping techniques to solve this problem are reported in [SK08, TMS+19, MNM+18, BMN+19], but often with time consuming calibration requirements. Alternative approaches like frequency domain frequency domain phase differene of arrival (FD-PDoA) estimates the transponder range [NMR+10] without phase unwrapping. This technique is similar to LFMCW radar or harmonic radar [NMR+10]. Here phases of the transponder signal at two or more frequencies are measured. Then the derivative of the phase with respect to frequency is calculated to estimate the range to the transponder as [NMR+10],

$$d = -\frac{c}{4\pi}\frac{\partial\phi}{\partial f}. \tag{2.14}$$

(2.14) assumes a physically static transponder with constant phase offset and transponder backscatter phase that do not vary with frequency.

Phase based localization techniques have better localization accuracy because they are more tolerant to the effects of multipath propagation than RSS based approaches [NR08]. However, phase based approaches have degraded accuracy in the absence of LoS, and have to be used in conjunction with other techniques like RSS or ToF to improve overall accuracy. Also phase based ranging is employable only for passive or semi-passive RFID transponders which do not employ local oscillators [NR08].

2.4.0.3 Time based Ranging

The conventional time based ranging and positioning techniques reported in literature include time of arrival (ToA), time difference of arrival (TDoA) and RToF based methods [LDBL07]. ToA and RToF methods utilize the fundamental char-

acteristics of a propagating EM waves that the distance traveled is directly proportional to the propagation time from an interrogator to the transponder. In the ToA technique, the absolute one-way propagation time is measured with respect to interrogators located at a minimum of three reference points, and is typically used for two dimensional positioning systems. In RToF based ranging, the two-way propagation time is measured. In a typical system, the interrogator transmits a signal, which is received by the transponder and transmitted back to the interrogator with a delay which corresponds to twice the distance between the interrogator and transponder. The estimate of the distance d_{RToF} using RToF of the transmit signal is then calculated according to

$$d_{\mathrm{RToF}} = \frac{c_0 \cdot (t_{\mathrm{RToF}} - t_{\mathrm{d}})}{2}, \tag{2.15}$$

where c_0 is the free space propagation velocity, and t_{d} is the additional delay introduced by the transponder and signal processing by the interrogator. This processing delay defines the minimum measurable range and limits the close range accuracy of the system.

TDoA is another technique mainly employed in positioning systems. In TDoA, the time difference of the received signal is measured by interrogators positioned at two reference points to estimate the relative position of the transponder [BSRS10]. For each TDoA measurement, the transponder is assumed to lie on a hyperboloid with a constant range difference between the two reference interrogators, and distance is calculated using techniques like nonlinear regression [LDBL07].

Both ToA and TDoA techniques require multiple interrogators, often requiring clock synchronization to determine the range and position of the transponder. Also it is not possible to do high accuracy and unambiguous ranging of the distance between interrogator and transponder by using the ToA or TDoA approach.

In the RToF based approach, the measured range resolution is proportional to the bandwidth of the system as will be seen in Section 3.1.1. The communication channel bandwidth of commercial UHF-RFID systems is relatively limited to around 100s of kHz and this bandwidth is not always sufficient to make accurate measurements. But advances in semiconductor technology makes it possible to design RFID systems at frequency bands like the 24 GHz ISM band, which has a higher allocated bandwidth of 250 MHz, and thus significantly improving the range resolution.

2.5 Architecture Selection for Proof of Concept Systems

The choice of a particular combination of transponder technology, interrogator architecture or field regions are determined by the application and operation constraints. In order to evaluate the suitability of a particular method, for the implementation of a state-of-the-art RFID system, several differentiating specifications should be considered. Key among these are the frequency of operation, the method for physical coupling and the minimum and maximum interrogation range.

Operating frequency band selection depends on several factors including the frequency dependent specific absorption rate of atmospheric water molecules, and better object penetration [Sey05, FM10]. Traditional RFID frequency bands like LF and HF are used for low data rate, inductively coupled short range applications and the components occupy a relatively large area. UHF and the lower microwave frequency band of 2.4 GHz are relatively congested. Higher operating frequencies also have several advantages for the interrogating radar. Even though an increase in frequency results in shorter range due to larger attenuation and more vulnerable to atmospheric effects, it results in higher resolution due to larger available bandwidth, narrower beamwidth for the same physical dimensions of the antenna and miniature antennas. The use of small antennas enables the implementation of roll invariant techniques to achieve polarization diversity. So the designs in this work employ the 24 GHz ISM band for the long range system and 60 GHz ISM band for the remote-coupling short range system.

Table 2.2 shows state-of-the-art RFID systems operating at microwave frequencies utilizing a combination of the different interrogator and transponder technologies discussed so far. In the interferometer and backscatter system employed by [ZXLW04], data transfer is possible, but localization is difficult due to the limitations of the technique and hence not reported. An LFMCW radar based interrogator and a SILO based transponder is reported in [SCW+13a]. This system operates at 34 GHz, and achieves a good localization accuracy of 7 cm and a moderately long range of 11.5 m. However, the system does not feature data transfer. The first system designed in this work, operating at 24 GHz is based on [SCW+13a], but integrates data transfer functionality at lower power, and at a much longer distance. Not many RFID systems with low power IC RFID transponders with large data storage capacity operating in the microwave and mmWave frequency bands are reported that demonstrate data transfer at long ranges and high accuracy bilateral ranging [DHV17b].

Due to the suitability of the LFMCW radar principle discussed in Section 2.2.3 for long range multipath tolerant detection and localization, a LFMCW radar

based system is implemented for interrogating transponders at 24 GHz. The unmodulated single carrier system also discussed in Section 2.2.3 has low complexity and offers the lowest power consumption, and hence is used for the short range system at 60 GHz.

In a LFMCW radar based interrogator system, the signal from the ART received at the radar is mixed with the original chirp to obtain baseband beat frequencies which are directly proportional to the distance to the reflector [Sko80] as discussed in Section 2.2. Though the active reflector ICs discussed in Section 2.1 have the advantage of squaring the maximum range of the radar compared to passive reflectors, the amplitude of the beat frequency signal is often submerged in the noise floor of the low frequency part of the baseband spectrum as will be shown in Fig. 3.4. This results in degradation of the signal to noise ratio (SNR) of the system due to artifacts from static clutter, low frequency close-in noise, DC offsets, frequency pulling, and RF or local oscillator (LO) to IF leakage from mixers of the interrogating radar. The typical solution employed involves the use of a high pass filter in baseband at the radar downconverter output [JAW+13], but it sets a limitation on the minimum measurable distance.

Due to the abovementioned reasons, a modulated transponder based on SRAs which shifts the baseband frequencies of interest towards the higher end of the spectrum is chosen as the topology for a robust long range RFID transponder operating at 24 GHz. For the proof of concept system at 60 GHz a close range passive load modulation based battery-assisted transponder discussed in Section 2.1.2.1 is chosen due to its low implementation complexity.

Table 2.2: Features of state-of-the-art RFID interrogator and transponder systems

	[RLG13]	[ZXLW04]	[MMW+19]	[SPB+21]	[DHV17b]	[SCW+13b]
Interrogator tech.	UWB-ISM	Interferometer	FSCW	FMCW	FMCW	FMCW
Transponder tech.	PIN diode	Schottky diode	Schottky diode	Van Atta array	BPSK IC	SILO IC
Frequency (GHz)	3.1-10.6 / 2.4	0.915	5.8	77	77	34
Bilateral Localization tech.	No	No	PoA	RToF	N.A.	RToF
Range (m)	8.5	10	1.5	< 100	5	11.5
Ranging accuracy (cm)	N.A.	N.A	$< 10\%$	56	-	7
Coupling	Radiative	Radiatve	Radiative	Radiative	Radiative	Radiative
Power cons. (mW)	75 uA			0.003	25	122
Transponder data storage			N.A.	N.A.		N.A
Data rate	10 Mbps	Moderate	> 10 Hz	N.A.		N.A.

2.6 Superregenerative Amplifier (SRA)

The superregeneration principle was invented by E. Armstrong in 1922 [Arm22] and one of the first detailed theoretical treatments of the principle traces back to E. Whitehead's work from 1950 [Whi50]. Many early works like [Mac48, Rie49] followed and focused on the original application of this principle in vacuum tube based communication receivers. As will be seen in detail in Section 2.6.1, the concept is based on the regenerative sampling principle, where a signal present across the resonator of an oscillator is amplified when the oscillations are periodically quenched at a frequency much lower than the resonator natural frequency, but higher than twice the input signal modulation frequency [Whi50].

Though SRA based receivers were of relatively low complexity, consumed low power and had high gain, the natural oscillations of the resonator resulted in back-radiation, which caused significant interference with other receivers [Whi50, Lee03] and were soon replaced by architectures like superheterodyne receivers [Lee03]. Though back-radiation is detrimental for communication circuits, SRAs operated in the logarithmic step-controlled mode named as SILO proposed in [VG08] take advantage of this radiated power, the circuit's sensitivity to input signals and high gain amplification to implement RFID transponders for localization. Section 3.1.1 extends the work of [VG08] and describes how the otherwise detrimental back radiation of the SRA can be put to good use in combined RF identification, communication and localization.

In literature SRAs are also called superregenerative oscillators by some authors because structurally, the circuit is an oscillator as discussed in Section 2.6.1. However, from the behavioral model perspective, the circuit does phase coherent amplification of an input signal. So, by following conventions in the well established Gajski-Kuhn Y-chart [GK83, LS20], the terminology for SRAs also employed in works like [BMCD09] is used throughout this work.

2.6.1 Fundamentals

The basic superregeneration principle can be understood with the help of the circuit model illustrated in Fig. 2.14(a). Here, L_{res} and C_{res} represents the inductance and capacitance respectively of a frequency selective bandpass parallel resonant network. The effective loss of the resonator is represented by the time-invariant transconductance G_{p}, which is the parallel combination of the losses due to the source resistance $R_{\mathrm{s}} = 1/G_{\mathrm{s}}$ and the resonator loss $R_{\mathrm{res}} = 1/G_{\mathrm{res}}$, yielding $G_{\mathrm{p}} = G_{\mathrm{s}} + G_{\mathrm{res}}$. The sinusoidal input signal, typically received using an antenna is $i_{\mathrm{in}}(t) = \hat{I}_{\mathrm{in}}\sin(\omega_{\mathrm{in}}t + \phi_{\mathrm{in}})$ and the output voltage is v_{out}. $i_{\mathrm{f}}(t)$ is the modeled

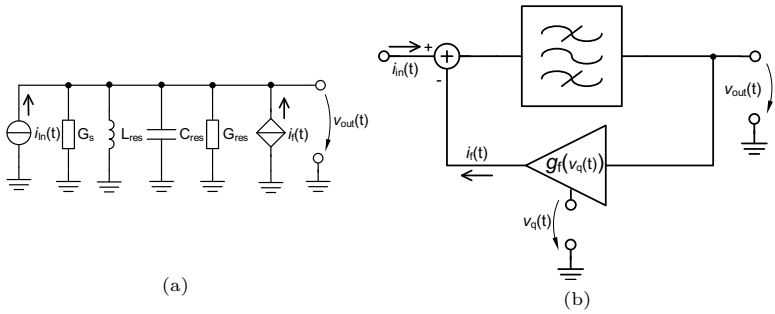

Figure 2.14: (a) Circuit model for illustrating the superregeneration principle. (b) Feedback loop based system model used for analysis.

time-variant feedback current component, and is defined as,

$$i_{\mathrm{f}}(t) = g_{\mathrm{f}}(t) v_{\mathrm{out}}(t), \tag{2.16}$$

where $g_{\mathrm{f}}(V_{\mathrm{q}}(t))$ is the time-varying transconductance which controls the damping of the network, and is varied periodically using the quench signal voltage $V_{\mathrm{q}}(t)$.

In order to understand this principle analytically, the equivalent time varying feedback system model of Fig. 2.14(b) is considered [BMCD09]. From Fig. 2.14(b), the impedance Z_{res} of the the bandpass resonant tank network can be written as [BMCD09],

$$\underline{Z}_{\mathrm{res}} = \frac{\underline{V}_{\mathrm{out}}(s)}{\underline{I}_{\mathrm{in}}(s)} = \frac{Z_{\mathrm{c}}\omega_{\mathrm{res}} s}{s^2 + 2\zeta_0\omega_{\mathrm{res}} s + \omega_{\mathrm{res}}^2}. \tag{2.17}$$

Where $\omega_{res} = 1/(\sqrt{L_{res}C_{res}})$ is angular resonant frequency of tank. Z_{c} is the characteristic impedance defined according to,

$$Z_{\mathrm{c}} = \sqrt{\frac{L_{\mathrm{res}}}{C_{\mathrm{res}}}}. \tag{2.18}$$

ζ_0 is the quiescent damping factor given by,

$$\zeta_0 = \frac{G_{\mathrm{p}}}{2C_{\mathrm{res}}\omega_{\mathrm{res}}} = \frac{G_{\mathrm{p}} Z_{\mathrm{c}}}{2}. \tag{2.19}$$

If the variation of $g_{\mathrm{f}}(t)$ compared to ω_{res} is small, then the system can be considered quasi-static [BMCD09], and the time-varying transfer function for the

feedback loop illustrated in Fig. 2.14(b) is given by [BMCD09],

$$\underline{Z}_{\mathrm{SRA,LTV}}(s,t) = \frac{\underline{V}_{\mathrm{out}}(s,t)}{\underline{I}_{\mathrm{in}}(s)} = \frac{\underline{Z}_{\mathrm{res}}(s)}{1 - g_{\mathrm{f}}(t)\underline{Z}_{\mathrm{res}}(s)}. \tag{2.20}$$

On substituting (2.17) and rewriting (2.20) we get [BMCD09],

$$\underline{Z}_{\mathrm{SRA,LTV}}(s,t) = \frac{Z_{\mathrm{c}}\omega_{\mathrm{res}}s}{s^2 + 2\zeta(t)\omega_{\mathrm{res}}s + \omega_{\mathrm{res}}^2}. \tag{2.21}$$

(2.21) looks structurally similar to (2.17), with the only difference being the time invariant ζ_0 is replaced by the time-variant instantaneous damping or quench function $\zeta(t)$ as the coefficient of first degree term in the denominator. $\zeta(t)$ is defined in a circuit designer friendly form as,

$$\zeta(t) = \zeta_0(1 - \frac{g_{\mathrm{f}}(t)}{G_{\mathrm{p}}}) = \frac{G_{\mathrm{p}} - g_{\mathrm{f}}(t)}{2}\sqrt{\frac{L_{\mathrm{res}}}{C_{\mathrm{res}}}}\,. \tag{2.22}$$

When $g_{\mathrm{f}}(t) > -G_{\mathrm{p}}$, the system is a frequency selective second order band pass filter. When $g_{\mathrm{f}}(t) \leq -G_{\mathrm{p}}$, the circuit is an oscillator in which the oscillations build up with a random initial phase and grows with an exponential envelope. When $G_{\mathrm{p}} + g_{\mathrm{f}}(t)$ transitions from a positive to negative value, oscillations would still build up with an exponential amplitude envelope, but interestingly $v_{\mathrm{out}}(t)$ is phase coherent to $i_{\mathrm{in}}(t)$ which has an initial phase ϕ_{in}.

With reference to Fig. 2.14(a), this system can described using a second order non-homogeneous differential equation with time varying coefficients given by,

$$\begin{aligned} v''_{\mathrm{out}}(t) + 2\zeta(t)\omega_{res}v'_{\mathrm{out}}(t) \\ + \omega_{res}^2 v_{\mathrm{out}}(t) = \frac{1}{C_{\mathrm{res}}}i'_{\mathrm{in}}(t)\,. \end{aligned} \tag{2.23}$$

Using the solution exhaustively treated in [BMCD09] and [MPM05], we can write the output voltage $v_{\mathrm{out}}(t)$ as the product of Z_{c}, the time dependent gain term $A_{\mathrm{SRA}}(t)$ and the filtering term $h(t)$ according to,

$$v_{\mathrm{out}}(t) = Z_{\mathrm{c}}A_{\mathrm{SRA}}(t)h(t). \tag{2.24}$$

where the gain term $A_{\mathrm{SRA}}(t)$ reaches a maximum at $t = T_{\mathrm{q,on}}$, and is defined as,

$$A_{\mathrm{SRA}}(t) = e^{-\omega_{\mathrm{res}}\int_{T_{\mathrm{samp}}}^{t}\zeta(x)dx}, \tag{2.25}$$

and the filtering term is the product of the derivative of the input signal and

the sensitivity function $\mu(t)$ according to

$$h(t) = \int_{T_{\mathrm{q,st}}}^{t} i'_{\mathrm{in}}(\tau)\mu(\tau)\sin\omega_0(t-\tau)d\tau, \tag{2.26}$$

with

$$\mu(t) = e^{\omega_{\mathrm{res}}\int_{T_{\mathrm{samp}}}^{t}\zeta(x)dx} \tag{2.27}$$

where T_{samp} is the time at which the resonator losses are equal to the time varying negative resistance and $\zeta(t)$ is defined as positive in the time interval $T_{\mathrm{q,st}} \leq t < T_{\mathrm{samp}}$ and negative in the interval $T_{\mathrm{samp}} \leq t \leq T_{\mathrm{q,on}}$ as illustrated in Fig. 2.15(a),Fig. 2.15(b) and Fig. 2.15(c). $T_{\mathrm{q,st}}$ is the starting time instant of the quench signal and $T_{\mathrm{q,on}}$ is the duration of quench signal for which $\zeta(t)$ is negative, with

$$T_{\mathrm{q}} = T_{\mathrm{q,on}} - T_{\mathrm{q,st}}. \tag{2.28}$$

Though (2.24) gives insight into the SRA operation, it does not reveal the circuit design parameters. In order to optimize circuit design parameters, the v_{out} derived using a frequency-domain model with a convolution approximation of $h(t)$ in [BMCD09] can be used, and is given by

$$v_{\mathrm{out}}(t) = A_0 A_{\mathrm{s}} A_{\mathrm{r}}(t)\sin(\omega_{\mathrm{res}}t + \phi_{\mathrm{in}})\,. \tag{2.29}$$

(2.29) shows that, with a sinusoidal input current, the output voltage is a sinusoidal signal with frequency ω_{res} set by the resonator elements, and phase coherent to the input signal phase ϕ_{in}. The amplitude of the voltage signal is determined by two time invariant gain terms A_0 and A_{s}, and a time variant gain term $A_{\mathrm{r}}(t)$. The time invariant gain A_0 is given by [BMCD09]

$$A_0 = \frac{I_{\mathrm{in}}}{2}\sqrt{\frac{L_{\mathrm{res}}}{C_{\mathrm{res}}}}\frac{\omega_{\mathrm{in}}\sqrt{2\pi}}{\sqrt{(\omega_{\mathrm{res}}k_{\mathrm{q}})}} = \frac{I_{\mathrm{in}}Z_{\mathrm{c}}}{2}\frac{\omega_{\mathrm{in}}\sqrt{2\pi}}{\sqrt{(\omega_{\mathrm{res}}k_{\mathrm{q}})}}\,. \tag{2.30}$$

(2.30) shows that the the output signal amplitude is directly proportional to the input current amplitude, the characteristic impedance, and the input signal frequency, while it is inversely proportional to the slope of the ramp or sawtooth quenching function, k_{q} with units s^{-1} [BMCD09].

A_{s} is the superregenerative gain component which determines the frequency selectivity of the SRA, and is given by [BMCD09]

$$A_{\mathrm{s}} = e^{-\frac{(\omega_{\mathrm{res}}-\omega_{\mathrm{in}})^2}{2\omega_{\mathrm{res}}k_{\mathrm{q}}}}. \tag{2.31}$$

(2.31) shows that the SRA acts as a band-pass filter with a Gaussian frequency response centered around ω_{res}, and attains a maximum value of 1. From (2.31), an equation for the filter 3 dB bandwidth can be derived by equating $A_{\mathrm{s}} = \frac{1}{\sqrt{2}}$ as

$$\omega_{\mathrm{in,BW}} = \omega_{\mathrm{res}} \pm \sqrt{\omega_{\mathrm{res}}k_{\mathrm{q}}\ln(2)}. \tag{2.32}$$

From (2.32), we can see that the frequency response curve and bandwidth of the filter can be controlled by varying the slope k_{q}. A higher k_{q} corresponds to larger bandwidth and poor selectivity, whereas a lower k_{q} results in increased selectivity. Another interesting factor to consider here is that selectivity in frequency domain corresponds to the sensitivity function in time domain, and is defined in [BMCD09] as,

$$\mu(t) = e^{-\frac{\omega_{\mathrm{res}}k_{\mathrm{q}}}{2}(t-T_{\mathrm{samp}})^2}. \tag{2.33}$$

(2.33) shows that $\mu(t)$ is a Gaussian function in time domain with a peak value of one, at the sampling instant T_{samp}.

The third gain term is the time dependent regenerative gain $A_{\mathrm{r}}(t)$ which describes the exponential oscillation build up in the linear mode, and is a function of k_{q} as given by,

$$A_{\mathrm{r}}(t) = e^{\frac{\omega_{\mathrm{res}}k_{\mathrm{q}}}{2}(t-T_{\mathrm{samp}})^2}. \tag{2.34}$$

$A_{\mathrm{r}}(t)$ increases with the duration of quench pulse width till the SRA enters the logarithmic mode regime with steady state oscillations. Due to this, there is an inverse relationship between maximum achievable regenerative gain, quenching frequency and data rate. The linear and logarithmic modes are discussed further in Section 2.6.2.

As plotted in Fig. 2.15(d), Fig. 2.15(e) and Fig. 2.15(f), the maximum of $v_{\mathrm{out}}(t)$ envelope in (2.29) occurs when $g_{\mathrm{f}}(t) \geq G_{\mathrm{P}}$ at $t = T_{\mathrm{q,on}}$. Beyond $T_{\mathrm{q,on}}$, till the beginning of next quench cycle, there are no oscillations. The maximum of the $v_{\mathrm{out}}(t)$ envelope $V_{\mathrm{out,env,max}}$ can be written as,

$$V_{\mathrm{out,env,max}} = A_0 A_{\mathrm{s}} A_{\mathrm{r}}(T_{\mathrm{q,on}}). \tag{2.35}$$

The key inferences that can be made from (2.29) to (2.35) are as follows:

- (2.29) indicates that the output signal oscillates with a frequency equal to

the $L_{\text{res}}C_{\text{res}}$ tank network resonant frequency ω_{res}, but coherent to the phase of the input signal ϕ_{in}.

- It can be inferred from (2.30) that the rate at which the output voltage increases is directly proportional to the amplitude of input signal and characteristic impedance of the resonant tank in the linear mode of operation as illustrated in Fig. 2.15(d), Fig. 2.15(e) and Fig. 2.15(f) for three different input current signal amplitudes.

- (2.30) also indicates that the output signal is directly proportional to a constant gain term which is a function of input signal frequency and the quenching function.

- (2.31) shows that the SRA functions as a bandpass filter with a Gaussian frequency response centered around the resonant frequency of the network, and with a filter bandwidth not only dependent on the resonator elements, but also the slope of the quench signal k_{q}. This implies that a high selectivity can be achieved even with a resonator with low Q_{res}.

- The input signal sensitivity of the SRA is a Gaussian function in time domain, centered around the sampling instant T_{samp}.

- The output voltage grows with an exponential envelope with a time squared exponent that is dependent on σ_{s} according to (2.34).

- Also it can bne deduced that unlike in conventional amplifiers where the gain bandwidth product is a constant, SRAs have gain and logarithm of bandwidth product constant.

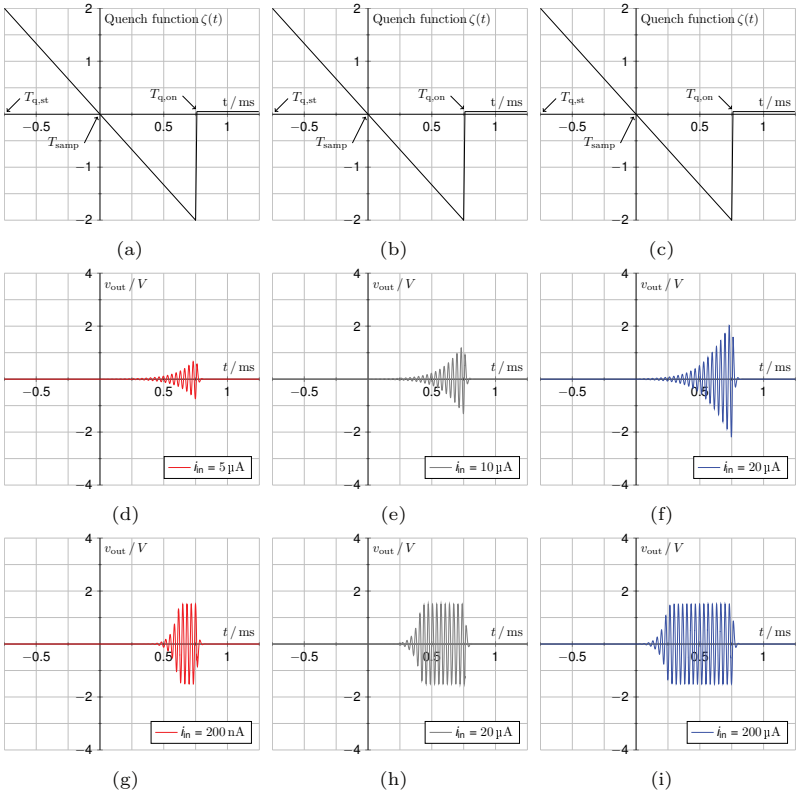

Figure 2.15: (a), (b) and (c) shows the SRA quenching function. (d), (e) and (f) shows the SRA linear quench mode in which the output voltage amplitude build up is directly proportional to the input current signal. (g),(h) and (i) shows the SRA logarithmic quench mode output in which the time dependent output voltage signal area is proportional to the input current signal. (Partly reused from *[TFJE23] ©2023 IET).

2.6.2 Modes of Operation

The SRA can operate in four different modes, and combinations thereof [Whi50]. Based on how the output amplitude is restricted, the SRA can be operated in either linear mode or logarithmic mode. Also based on the characteristics of the quenching function, the SRA can be operated in either slope-controlled mode or step-controlled mode.

Linear mode: (2.35) derived using a linear model says that the peak of the envelope of the output signal amplitude increases with input signal amplitude and scaled by the superregenerative gain as shown in the plots of Fig. 2.15(d), Fig. 2.15(e) and Fig. 2.15(f). This is a valid model at low input power levels and the SRA operates in the linear mode [Whi50].

Logarithmic mode: Like most practical nonlinear systems, beyond a certain input power level, the output amplitude increase ultimately saturates as plotted in Fig. 2.15(g), Fig. 2.15(h) and Fig. 2.15(i). This behavior of the SRA is called the logarithmic mode of operation in which the peak of the output signal amplitude envelope defined in (2.35) remains constant, while the area under the envelope, within each quenching period defined in (2.29) is directly proportional to input signal amplitude [Whi50].

Of particular interest is the input power level $P_{\mathrm{i,N}}$ annotated in Fig. 2.16(a), at which the transition from linear to logarithmic mode occurs. In the linear mode, input power $P_{\mathrm{in}} < P_{\mathrm{N}}$, and the approximate output signal envelope power level $P_{\mathrm{lin,env,max}}$ is given by [SSE+14]

$$P_{\mathrm{lin,env,max}} = D_{\mathrm{q}} \frac{V_{\mathrm{out}}^2 P_{\mathrm{in}}}{2 R_{\mathrm{P}} P_{\mathrm{in,N}}} \tag{2.36}$$

where $R_{\mathrm{P}} = 1/G_{\mathrm{P}}$ and the duty cycle D_{q} is defined as

$$D_{\mathrm{q}} = \frac{T_{\mathrm{q,on}}}{T_{\mathrm{q}}}. \tag{2.37}$$

c is given by

$$P_{\mathrm{in}} = I_{\mathrm{in}}^2 R_{\mathrm{P}} \tag{2.38}$$

and the input referred noise power level $P_{\mathrm{in,N}}$ is given by,

$$P_{\mathrm{in,N}} = \frac{4 \mathrm{k_B} T f_{\mathrm{res}}}{Q_{\mathrm{res}}}, \tag{2.39}$$

where $\mathrm{k_B}$ is the Boltzmann constant, T is the absolute temperature in Kelvin and Q_{res} is the quality factor of the resonator determined as

$$Q_{\mathrm{res}} = R_{\mathrm{P}}\sqrt{\frac{C_{\mathrm{res}}}{L_{\mathrm{res}}}}. \tag{2.40}$$

From (2.36) through (2.40), it can be deduced that $P_{\mathrm{out,lin,env,max}}$ in the linear mode of operation is linearly dependent on P_{in} as illustrated in Fig. 2.16(a).

In the logarithmic mode, $P_{\mathrm{in}} \geq P_{\mathrm{i,N}}$, and the power level of the output signal envelope $P_{\mathrm{log,env,max}}$ reaches a maximum that is independent of P_{in} as depicted in Fig. 2.16(a) and is given by [SSE+14]

$$P_{\mathrm{log,env,max}} = D_{\mathrm{q}}\frac{V_{\mathrm{out}}^2}{2R_{\mathrm{P}}}. \tag{2.41}$$

As annotated in Fig. 2.16(a), $P_{\mathrm{in,N}}$ is the intersection point of the linear mode output power and logarithmic mode output, and can be derived by equating (2.41) and (2.36) to yield

$$P_{\mathrm{in}} = P_{\mathrm{in,N}} \tag{2.42}$$

The minimum input signal power level $P_{\mathrm{i}} < 10$ for phase coherent amplification can also be determined using the standard deviation of phase defined in [SSE+14] as

$$\sigma_{\phi,\mathrm{SRA}} = \frac{10}{4\pi}\log_{10}\frac{10P_{\mathrm{in,N}}}{P_{\mathrm{i}}} \tag{2.43}$$

and the corresponding minimum input power level $P_{\mathrm{i,min}}$ is given by

$$P_{\mathrm{in,min}} = \frac{4K_{\mathrm{B}}Tf_{\mathrm{res}}}{Q_{\mathrm{res}}}\frac{1}{D_{\mathrm{q}}}. \tag{2.44}$$

According to (2.44), $P_{\mathrm{in,min}}$ is directly proportional to f_{res} and inversely proportional to Q_{res}. So in order to improve the input sensitivity of the SRA, it is desirable to operate at lower frequencies and have the resonator optimized for higher Q_{res} as is evident from the plots in Fig. 2.16(b).

Slope-controlled mode: The analysis so far has been based on the fact that the quenching signal is a linear function of time as is evident from (2.22) and as depicted in the plots Fig. 2.15(a), Fig. 2.15(b) and Fig. 2.15(c). This operation mode of the SRA, where $\zeta(t)$ is a periodically repeating linear function like a sawtooth waveform is called the slope controlled mode. In this mode, if $\zeta(t)$ slowly varying so that multiple periods of input signal can occur within the Gaussian sensitivity function window defined in (2.33), the SRA can achieve better sensitivity and selectivity [Whi50].

Step-controlled mode: In this mode, $\zeta(t)$ changes from positive ζ_{pos} to negative

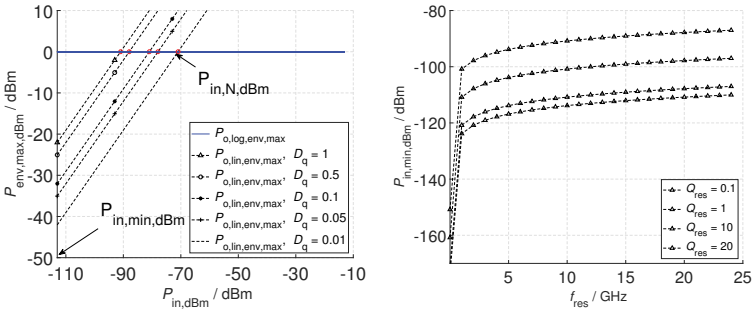

(a) (b)

Figure 2.16: (a) SRA output power level versus input power level for different resonator quality factor values (b) SRA minimum input power level required for phase coherent amplification at different resonator quality factor values, T=290K and $D_{\mathrm{q}} = 0.1$.

ζ_{neg} abruptly when using a quench signal similar to that depicted in Fig. 2.17(a), and defined as

$$\zeta_{\mathrm{step}}(t) = \begin{cases} \zeta_{\mathrm{pos}} & \text{if } t < T_{\mathrm{q,samp}} \\ \zeta_{\mathrm{neg}} & \text{if } t > T_{\mathrm{q,samp}} \end{cases} . \tag{2.45}$$

The quenching signal in this case can be a square waveform or duty cycled pulses. In this mode, SRA sensitivity is an exponential function of time with a discontinuity at $T_{\mathrm{q,samp}}$, and is defined according to

$$\mu_{\mathrm{step}}(t) = \begin{cases} e^{\omega_{\mathrm{res}}\zeta_{\mathrm{pos}}t} & \text{if } t < T_{\mathrm{q,samp}} \\ e^{-\omega_{\mathrm{res}}\zeta_{\mathrm{neg}}t} & \text{if } t > T_{\mathrm{q,samp}} \end{cases} . \tag{2.46}$$

Though $\mu_{\mathrm{step}}(t)$ is not as good as in the slope-controlled mode [Whi50, BMCD09], the SRA can be quenched at a higher frequency, and maintains a phase coherent relationship with input signal as shown in Fig. 2.17(b). Also some interesting frequency domain characteristics of step-controlled mode makes it attractive to RFID systems as will be seen in Section 2.6.3 and Section 3.1.1.

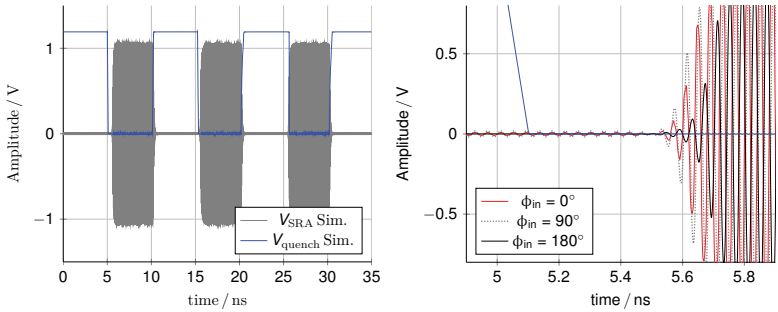

(a) (b)

Figure 2.17: (a) Time domain characteristics of SRA operating in the step controlled mode. (b) Phase coherence of the SRA output signal when input signal phase is varied.

2.6.3 Frequency Domain Characteristics

When operating in the step-controlled mode with the quench signal as a pulse train as illustrated in Fig. 2.17, the time domain output response $s_{\text{out}}(t)$ of the SRA in response to a CW input signal

$$s_{\text{in}}(t) = A_{\text{in}} \cos \omega_{\text{in}} t \tag{2.47}$$

with amplitude A_{in} and frequency ω_{in} can be represented from a signal theory perspective as [VG08, SCW+13b],

$$s_{\text{out}}(t) = \sum_{n=-\infty}^{\infty} A_{\text{res}} \cos(\omega_{\text{res}}(t - nT_{\text{q,on}}) + \omega_{\text{in}} n T_{\text{q}}) \cdot \text{rect}\left(\frac{t - nT_{\text{q}} - 0.5T_{\text{q,on}}}{T_{\text{q,on}}}\right) \tag{2.48}$$

where $n = 0, 1, 2, ...$ is an integer representing the pulse number and rect is the rectangle or normalized boxcar function and ω_{res} is the free-running frequency of the resonator. T_{q} is the quench signal time period and $T_{\text{q,on}}$ is the duration for which oscillations build up, with $T_{\text{q,on}} \leq T_{\text{q}}$. A_{res} is the amplitude of the output signal.

The Fourier transform $S_{\text{out}}(f)$ can then be calculated as the convolution of Fourier transforms of the cosine term and rect term in (2.48) and can be simplified as [SCW+13b]

$$\begin{aligned} S_{\text{out}}(f) =& K_1 \sum_{n=-\infty}^{\infty} \exp^{-j2\pi(f-f_{\text{in}})nT_{\text{q}}} \\ &+ K_2 \sum_{n=-\infty}^{\infty} \exp^{-j2\pi(f+f_{\text{in}})nT_{\text{q}}} \end{aligned} \tag{2.49}$$

where the envelope terms $K_{1,2}$ are defined by

$$\begin{aligned} K_1 =& \frac{A_{\text{res}}T_{\text{q,on}}}{2} \text{sinc}\left[\pi T_{\text{q,on}}(f-f_{\text{res}})\right] \exp^{j\pi(f-f_{\text{res}})T_{\text{q,on}}} \\ K_2 =& \frac{A_{\text{res}}T_{\text{q,on}}}{2} \text{sinc}\left[\pi T_{\text{q,on}}(f+f_{\text{res}})\right] \exp^{j\pi(f+f_{\text{res}})T_{\text{q,on}}} \end{aligned} \tag{2.50}$$

The terms in (2.50) corresponds to a Dirac impulse train known as the Sha function denoted by Ш, and the magnitude spectrum of $S_{\text{out}}(f)$ is determined as [SCW+13b]

$$\begin{aligned} |S_{\text{out}}(f)| =& \frac{A_{\text{res}}D_{\text{q}}}{2} \text{sinc}\left[\pi T_{\text{q,on}}(f+f_{\text{res}})\right] \left[\text{Ш}(f+f_{\text{in}})T_{\text{q}}\right] \\ &+ \frac{A_{\text{res}}D_{\text{q}}}{2} \text{sinc}\left[\pi T_{\text{q,on}}(f-f_{\text{res}})\right] \left[\text{Ш}(f-f_{\text{in}})T_{\text{q}}\right] \end{aligned} \tag{2.51}$$

The two Ш function terms in (2.51) are non-zero at the linear combination of frequencies $f_{\text{in}} \pm nf_{\text{q}}$, and therefore track f_{in} as illustrated in Fig. 2.18(a) where $f_{\text{in}} = f_{\text{res}}$ and in Fig. 2.18(b) where $f_{\text{in}} = f_{\text{res}} + 2.5f_{\text{q}}$. Fig. 2.18(a) and Fig. 2.18(b) also depicts the magnitude envelope $|S_{\text{out,env}}|$ of $|S_{\text{out}}(f)|$, which is the sinc function in (2.51) with a maximum value at the free running frequency f_{res}. Also the frequency span of each side lobe in the magnitude spectrum of $|S_{\text{out}}(f)|$ is determined by $T_{\text{q,on}}$. The smaller the $T_{\text{q,on}}$, the larger the span and vice versa as illustrated in the plots in Fig. 2.18.

(2.51) is derived without considering the noise in the system. When AWGN with a variance corresponding to an SNR of 20 dB is added to the $|S_{\text{out}}(f)|$, noise is also modulated by the sinc function as illustrated in Fig. 2.18(c).

Another parameter of interest to system design are the bounds on SRA quench frequency f_{q} when a modulated CW signal is used as the input. If $s_{\text{in,m}}(t)$ is a modulated signal with a modulation frequency f_{m}, the maximum quench frequency $f_{\text{q,max}}$ and the minimum quench frequency $f_{\text{q,min}}$ is constrained by the Nyquist sampling theorem with with $f_{\text{m}} << f_{\text{res}}$ as [Whi50]

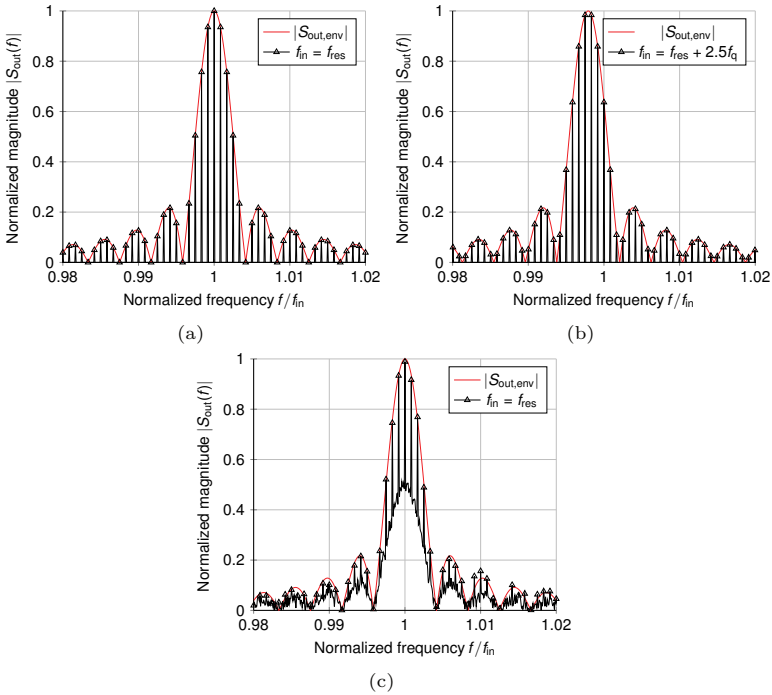

Figure 2.18: Modeled frequency domain characteristics of SRA with normalized amplitude plotted as a function of frequency normalized to f_{in}: (a) shows the spectral lines and peak of envelope align when $f_{\mathrm{in}} = f_{\mathrm{res}}$, (b) shows that the spectral line corresponding to f_{in} is greater the peak of the envelope corresponding to f_{res} by 2.5 times f_{q} and (c) shows the effect of AWGN corresponding to 20 dB SNR in (a).

$$\begin{aligned} f_{\mathrm{q,min}} &= 2f_{\mathrm{m}} \\ f_{\mathrm{q,max}} &= \frac{f_{\mathrm{res}}}{2} \end{aligned} \tag{2.52}$$

$f_{\mathrm{q,max}}$ is also dependent on the minimum quench time required so that the sampled input signal phase at each quenching instant is not affected by the signal phase of the previous sampling period. This phenomenon is also called the history or memory effect, and is relatively benign at low f_{q} [Whi50, PSBDdAL+20].

2.7 Semiconductor Technologies for RFIC Design

A brief overview of the features of semiconductor technologies used for RFIC design are presented in this section. All 24 GHz circuits except one SRA variant are implemented in a 130 nm SiGe-BiCMOS technology. One SRA variant is implemented in a 45 nm partially depleted silicon on insulator (PDSOI) technology and the 60 GHz circuits are implemented in a 22 nm FDSOI technology.

2.7.1 Silicon Germanium BiCMOS

The SiGe-BiCMOS circuits designed in this work are implemented in a 130 nm SiGe-BiCMOS technology. The key features of this technology are [RHW+10b, RS18]:

- High performance heterojunction bipolar transistors (HBTs) with f_t up to 240 GHz and f_{max} up to 330 GHz.
- The HBTs have a break down voltage of 1.6 V [RHW+10b, RS18].
- 7-layer back end of line (BEOL) with two thick copper layers at the top
- Two thick copper top layers for implementing high Q passives including inductors and transmission lines, and five thin bottom layers for high density routing.
- A metal insulator metal (MIM) layer for high Q capacitors with high capacitance density.
- Salicided, N+ and P+ poly resistors, and metal oxide semiconductor (MOS) varactors with 3 to 1 tunability and a capacitance density of 4.5 fF / µm^2 [RHW+10b, RS18].
- The complementary metal oxide semiconductor (CMOS) core devices having a minimum gate length of 130 nm and operating at a maximum supply voltage of 1.2 V. A peak f_t of 80 GHz is reported for N-channel field effect transistors (nFETs) and 40 GHz for P-channel field effect transistors (pFETs).

2.7.2 Silicon-on-Insulator

The designs in this work also use a 45 nm PDSOI and a 22 nm FDSOI technology. The transistors available in these technologies use an ultra-thin buried oxide layer

between the substrate and a very thin silicon layer forms the channel [OLC+18]. The ultra-thin oxide layer significantly reduces leakage currents to substrate, and short channel effects like drain induced barrier lowering [OLC+18]. The short channel lengths result in higher intrinsic gain and lower capacitances compared to bulk CMOS technology. The channel can also be controlled by a backgate enabling the charge carrier flow through both the top and bottom surfaces of the channel, which provides a knob to tune the threshold voltage of the transistors [OLC+18].

The key features of this technology reported in literature [OLC+18] are:

- High performance nFETs with a maximum $f_\mathrm{t}/f_\mathrm{max}$ 347 GHz/371 GHz, and strained SiGe channel pFETs with a $f_\mathrm{t}/f_\mathrm{max}$ up to 275 GHz/299 GHz.
- The low voltage transistors have a maximum operating voltage of 0.8 V ± 10 %.
- Of the many BEOL flavors available, the one with 10 metal layers including two thick copper layers at the top are used for the designs in this work.
- One aluminium layer and two thick copper top layers for implementing high Q passives including inductors and transmission lines, and five thin bottom layers for high density routing.
- Passive components include high density alternate polarity metal-oxide-metal (APMOM) capacitors, accumulation mode MOS varactors and different types of polysilicon and diffusion resistors.

3 24 GHz Superregenerative Transponder based Identification and Ranging System

This chapter begins with a discussion on the system design aspects of detecting and ranging SRT using a LFMCW secondary radar interrogator. This is followed by the derivation of SRA IC design requirement specifications and the theory of novel SQ-FSK modulation for identification and data transfer. Also presented are the analysis, design, experimental characterization outcomes and knowledge acquired from the designed SRA IC variants. The last section of the chapter presents the details of the proof of concept system implemented using two SRTs with bandwidth enhanced microstrip patch antennas, a LFMCW radar interrogator and data analysis using a CZT based algorithm to improve the accuracy of distance estimates.

3.1 System Design

3.1.1 SRT Identification and Ranging

The illustration in Fig. 3.1 depicts a RToF, based RFID transponder range measurement system using a LFMCW interrogating secondary radar. In this system, interrogation is done by sending a sequence of LFMCW chirps, each with a sequence number $i = 0, 1, .., N_\mathrm{c} - 1$, with the total number of chirps in the sequence N_c as shown in Fig. 3.2. For each chirp i in the sequence, the transmitted signal $s_{\mathrm{T_x},i}(t)$ has a starting angular frequency $\omega_\mathrm{min} = 2\pi f_\mathrm{min}$, bandwidth f_chirp, chirp duration T_chirp, periodically repeats in the interval T_rep and can be written as

$$\begin{aligned} s_{\mathrm{T_x},i}(t) = A_{\mathrm{T_x},i}\mathrm{rect}\left(\frac{t - iT_\mathrm{rep} - 0.5T_\mathrm{chirp}}{T_\mathrm{chirp}}\right) \\ \cdot \cos(\omega_\mathrm{min}(t - iT_\mathrm{rep}) + \pi\mu(t - iT_\mathrm{rep})^2 + \phi_{\mathrm{tx},i}), \end{aligned} \tag{3.1}$$

where $A_{\mathrm{T_x},i}$ is the voltage amplitude and $\phi_{\mathrm{tx},i}$ is the starting phase of the transmitted chirp signal. The gradient of each LFMCW chirp μ is given by

$$\mu = \frac{f_\mathrm{chirp}}{T_\mathrm{chirp}}. \tag{3.2}$$

The chirp propagates through the channel with speed of light in free space C_o and a passive or active reflector present reflects or re-transmits this chirp back. For each chirp i in the sequence, the interrogator frontend receives the chirp delayed by the RToF τ_i and attenuated by α as $s_{\mathrm{R_x},i}(t) = \alpha s_{\mathrm{T_x},i}(t - \tau_i)$ and mixes it

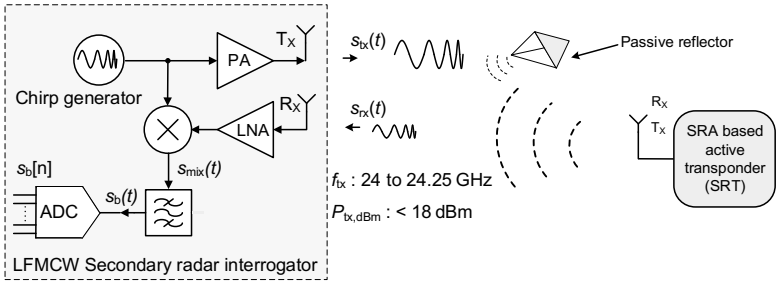

Figure 3.1: LFMCW radar based ranging using passive reflector and a SRT. (Partly adapted from *[TFJE23] ©2023 IET).

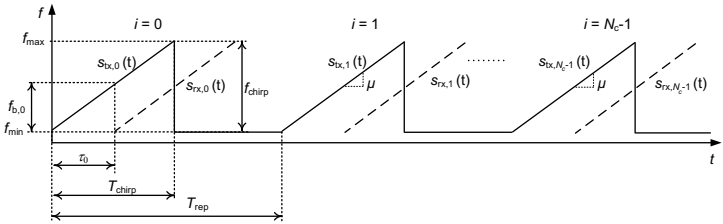

Figure 3.2: Illustration of interrogating chirp sequence sent by the LFMCW radar.

with the original chirp $s_{\mathrm{T_x},i}(t)$, resulting in $s_{\mathrm{mix},i}(t)$. τ_i is directly proportional to the distance to target d_i according to [Sko80]

$$\tau_i = \frac{2d_i}{\mathrm{c}_0} \tag{3.3}$$

where c_0 is the free space propagation velocity of EM waves. For passive targets, the attenuation is proportional to $\alpha \propto \lambda^{-4}$, whereas for active targets, $\alpha \propto \lambda^{-2}$ [Sko80]. With a conventional static, active or passive, unmodulated target like a repeating amplifier or the illustrated corner reflector, the baseband spectrum of the lower sideband of $s_{\mathrm{mix},i}(t)$ for each chirp in the sequence i contains a single beat frequency $f_{\mathrm{b,i}}$

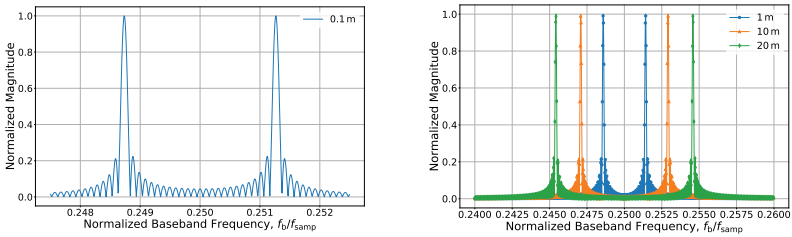

(a) (b)

Figure 3.3: SRT baseband signal magnitude spectrum: (a) The plot of (3.8) for a distance of 0.1 m. (b) shows the variation of the baseband frequency for different values of distance between interrogator and static transponder. (Reused from *[TFJE23] ©2023 IET).

$$f_{\mathrm{b,i}} = \mu \tau_i, \tag{3.4}$$

and the corresponding distance to target d_i is estimated as

$$d_i = \frac{\mathrm{c}_0}{2\mu} \cdot f_{\mathrm{b,i}}. \tag{3.5}$$

On the other hand, when a cooperating coherent static transponder like an SRT is used as illustrated in Fig. 3.1, the received chirp is transmitted back with phase coherent amplification using the SRA. The SRA which operates in the step-controlled mode described in Section 2.6.2 at a free running frequency of ω_{res} is periodically quenched with a signal having angular frequency ω_{q} and phase ϕ_{q}. The interrogator receives back the chirp $s_{\mathrm{R_x},i}(t)$ which is amplified and modulated by the SRA, but attenuated by α and delayed by τ_i due to the characteristics of the channel, similar to a secondary radar system. $s_{\mathrm{R_x},i}(t)$ is then amplified by the interrogator LNA and is mixed with the original transmit chirp $s_{\mathrm{T_x},i}(t)$. The resulting down conversion mixer output $s_{\mathrm{mix},i}(t)$ is a carrier-suppressed amplitude-modulated signal [VG08]. This $s_{\mathrm{mix},i}(t)$ is further bandpass filtered yielding a baseband signal $s_{\mathrm{b},i}(t)$ which is given by a modified form of the expression from [VG08] as

$$\begin{aligned} s_{\mathrm{b},i}(t) = A_{\mathrm{b},i}\cos(\omega_{\mathrm{q}}t + \phi_{\mathrm{q}}) \cdot \mathrm{sinc}\left(\frac{T_{\mathrm{q,on}}\mu t}{2}\right) \\ \cdot \cos\left(2\omega_{\mathrm{res}}\frac{d_{\mathrm{SRT},i}}{\mathrm{c}_0} + \left(2\mu\frac{d_{\mathrm{SRT},i}}{\mathrm{c}_0} + \frac{T_{\mathrm{q,on}}\mu}{2}\right)t\right) \end{aligned} \tag{3.6}$$

where $A_{\mathrm{b},i}$ is the amplitude of the baseband signal, $d_{\mathrm{SRT},i}$ is the distance from the interrogator to the SRT and $T_{\mathrm{q,on}}$ is the duration for which the SRA is turned on within a quench cycle, represented in terms of duty cycle D_{q} of the quench signal using the relation

$$D_{\mathrm{q}} = T_{\mathrm{q,on}} f_{\mathrm{q}}. \tag{3.7}$$

The frequency spectrum of $s_{\mathrm{b},i}(t)$ in (3.6) is obtained by taking the Fourier transform and can be written according to [Str14]

$$\begin{aligned} \mathcal{F}(s_{\mathrm{b},i}(t)) = S_{\mathrm{b},i}(f) = \frac{A_{\mathrm{b},i}T_{\mathrm{q,on}}f_{\mathrm{q}}}{4}\left|\mathrm{sinc}(T_{\mathrm{q,on}}f_{\mathrm{q}})\right| \\ \left[\mathrm{sinc}\big(T_{\mathrm{chirp}}\,(f - f_{\mathrm{b,l},i})\big) + \mathrm{sinc}\big(T_{\mathrm{chirp}}\,(f + f_{\mathrm{b,u},i})\big)\right]. \end{aligned} \tag{3.8}$$

From (3.8), the lower sideband $f_{\mathrm{b,l},i}$ and upper sideband $f_{\mathrm{b,u},i}$, centered around f_{q} [VG08] can be written by introducing D_{q} as,

$$\begin{aligned} f_{\mathrm{b,l},i} &= f_{\mathrm{q}} - \frac{\mu\tau}{\pi} - \frac{\mu D_{\mathrm{q}}}{4\pi f_{\mathrm{q}}} \qquad \text{and} \\ f_{\mathrm{b,u},i} &= f_{\mathrm{q}} + \frac{\mu\tau}{\pi} + \frac{\mu D_{\mathrm{q}}}{4\pi f_{\mathrm{q}}}. \end{aligned} \tag{3.9}$$

The corresponding expression for distance to SRT then becomes

$$d_{\mathrm{SRT},i} = \frac{\pi \mathrm{c}_0}{4\mu} \cdot \left(f_{\mathrm{b,u},i} - f_{\mathrm{b,l},i} - \frac{\mu D_{\mathrm{q}}}{2\pi f_{\mathrm{q}}}\right). \tag{3.10}$$

Fig. 3.3(a) shows a plot of (3.8) at a distance of 0.1 m and clearly showing the sidelobes of the *sinc* spectrum. Fig. 3.3(b) illustrates how the separation between the peaks $f_{\mathrm{b,u},i}$ and $f_{\mathrm{b,l},i}$ increases as the distance between SRT and interrogator $d_{\mathrm{SRT},i}$ increases, as defined in (3.9).

The insight from (3.10) is that, with an SRA based reflector, the range is not dependent on a single beat frequency as in (3.5), but rather on the difference between two beat frequencies higher up in the spectrum and centered around f_{q}

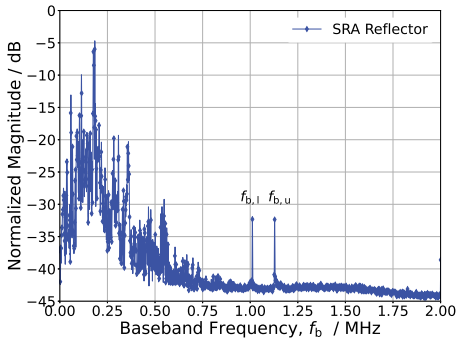

Figure 3.4: Baseband magnitude spectrum showing the frequency signature of a SRT in the presence of static clutter. (Reused from *[TFJE23] ©2023 IET).

also given by,

$$f_{\mathrm{q}} = \frac{f_{\mathrm{b,u},i} + f_{\mathrm{b,l},i}}{2}. \tag{3.11}$$

While the SRA based reflector helps in translating the frequencies of interest to the higher end of the spectrum, and away from close range clutter as depicted in Fig. 3.4, the maximum range of the reflector is mainly dependent on the minimum power level required for phase coherent amplification, and the re-transmitted output power.

3.1.2 Power Link Analysis

Considering the assumption that the antennas of interrogator and SRT have conjugate matched input and are polarization matched, the signal power $P_{\mathrm{rx,SRT}}$ received by an SRA based SRT with an antenna gain G_{SRT} can be calculated using the Friis' transmission equation [Sko80] as

$$P_{\mathrm{rx,SRT}} = \frac{P_{\mathrm{tx}} G_{\mathrm{trx}} G_{\mathrm{SRT}}}{\mathrm{FSPL}}\,, \tag{3.12}$$

where P_{tx} and G_{trx} are the output power and antenna gain respectively of the interrogating radar. FSPL is the free space path loss for secondary radar given by [Sko80]

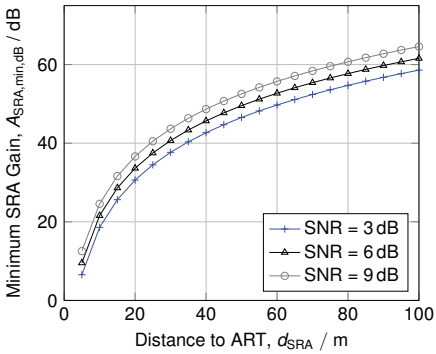

Figure 3.5: Minimum SRA gain required for covering a particular range at different SNR values. (Reused from *[TFJE23] ©2023 IET).

$$\mathrm{FSPL} = \left(\frac{4\pi d_{\mathrm{SRT},i}}{\lambda}\right)^2 . \tag{3.13}$$

Here, λ is the free-space wavelength of the maximum frequency of the interrogating chirp signal. At 24 GHz, for $d_{\mathrm{SRT},i} = 100\,\mathrm{m}$, the FSPL is around 81 dB. With $P_{\mathrm{tx,dBm}} \approx 6\,\mathrm{dBm}$, $G_{\mathrm{trx,dBi}} \approx 14\,\mathrm{dBi}$ and $G_{\mathrm{SRT,dBi}} \approx 5\,\mathrm{dBi}$, the power received by the SRT can be calculated as, $P_{\mathrm{rx,SRA,dBm}} \approx -67\,\mathrm{dBm}$, implying that the SRT minimum detected power level needs to be less than $-67\,\mathrm{dBm}$.

At distances farther from the interrogator where $P_{\mathrm{rx,SRT,dBm}}$ is relatively small, the SRA operates in the linear mode as discussed in Section 2.6.2, and does phase coherent amplification of the signal with the peak gain, A_{SRA}. The amplified signal is then transmitted back with power level

$$P_{\mathrm{tx,SRT,dBm}} = P_{\mathrm{rx,SRT,dBm}} + A_{\mathrm{SRA,dB}}. \tag{3.14}$$

Now again using the Friis' equation, the relationship between the minimum gain required for the SRA, $A_{\mathrm{SRA,min,dB}}$ and the power received back by the interrogator, $P_{\mathrm{rx,min,dBm}}$ can be determined as

$$A_{\mathrm{SRA,min,dB}} = P_{\mathrm{rx,min,dBm}} + 2\mathrm{FSPL}_{\mathrm{dB}} - P_{\mathrm{lim,dBm}}\,, \tag{3.15}$$

where

$$P_{\text{lim,dBm}} = P_{\text{tx,dBm}} + 2G_{\text{trx,dBi}} + 2G_{\text{SRT,dBi}} \,. \tag{3.16}$$

The minimum detectable power level of the interrogator $P_{\text{rx,min,dBm}}$ is determined using the receiver sensitivity equation

$$P_{\text{rx,min,dBm}} = \text{SNR}_{\text{min}} + \text{NF}_{\text{rx}} + 10\log\left(\frac{\text{k}_\text{B}\text{T}f_{\text{BW,bb}}}{1\,\text{mW}}\right)\,\text{dBm} \tag{3.17}$$

where k_B is the Boltzmann constant, T is the ambient temperature in Kelvin and SNR_{min} is the minimum SNR required at the interrogator. NF_{rx} is the receiver noise figure, and $f_{\text{BW,bb}}$ is the modulation bandwidth of the SRT.

Using (3.13) and (3.15), the distance between the interrogator and SRT in the linear mode can be calculated as

$$d_{\text{SRT,lim,n}} = \frac{\lambda}{4\pi} \cdot 10^{((P_{\text{lim,dBm}} + A_{\text{SRA,dB}} - P_{\text{rx,min,dBm}})/40)} \,, \tag{3.18}$$

Fig. 3.5 shows the plot of $A_{\text{SRA,min,dB}}$ against distance to SRT for different SNR_{min} values according to (3.15) and (3.18). For the off-the-shelf monolithic microwave integrated circuit (MMIC) based interrogator frontend as discussed in Section 3.3.2, $NF_{\text{rx}} \approx 12\,\text{dB}$, and a maximum baseband bandwidth, $f_{\text{BW,bb}} = 1.5\,\text{MHz}$. The interrogator SNR_{min} is determined from Fig. 3.5 as around 10 dB, and is set by the analog to digital converter (ADC) and post processing employed. At room temperature, the minimum input power required can then be calculated using (3.17) as, $P_{\text{rx,min,dBm}} \approx -90\,\text{dBm}$. Substituting $P_{\text{rx,min,dBm}}$ in (3.15), the SRA gain required for $d \geq 100\,\text{m}$ can be calculated as,

$$A_{\text{SRA,dB}} \geq 65\,\text{dB} \,. \tag{3.19}$$

At shorter ranges where $d_{\text{SRT},i}$ is relatively small, $P_{\text{rx,SRA}}$ is relatively high, and the SRA operates in the logarithmic mode discussed in Section 2.6.2. The SRA does phase coherent sampling of the received signal, and transmits back with saturated output signal power $P_{\text{out,sat,dBm}}$, giving $P_{\text{tx,SRA,dBm}} = P_{\text{out,sat,dBm}}$. Using the path loss equation used to determine (3.15), $P_{\text{out,sat,dBm}}$ can be determined as

$$P_{\text{out,sat,dBm}} = P_{\text{rx,min,dBm}} + \text{FSPL} - G_{\text{ANT,dBi}} \,, \tag{3.20}$$

with

$$G_{\text{ANT,dBi}} = G_{\text{trx,dBi}} + G_{\text{SRT,dBi}} \,. \tag{3.21}$$

With a $P_{\text{rx,min,dBm}}$ of $-90\,\text{dBm}$ at $24\,\text{GHz}$, for $d \leq 30\,\text{m}$, $\text{FSPL} \leq 60\,\text{dB}$, thus

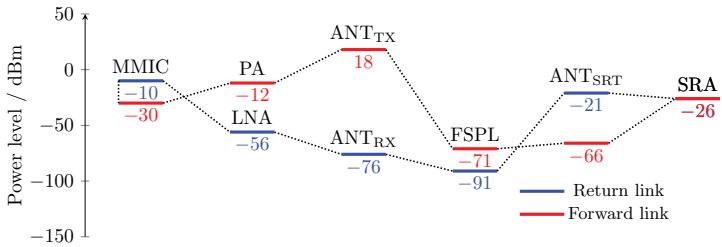

Figure 3.6: Level diagram showing the power levels at different stages in the forward link and return link of the system level implementation, with d_{SRT} of 75 m.

requiring

$$P_{\mathrm{out,sat,dBm}} \leq -20\,\mathrm{dBm}\,. \tag{3.22}$$

Also in a similar way, the maximum distance obtained for logarithmic mode operation $d_{\mathrm{SRA,lom}}$ for a given transmit power and SNR can be calculated as,

$$d_{\mathrm{SRT,lom}} = \frac{\lambda}{4\pi} 10^{((P_{\mathrm{lom,dBm}} - P_{\mathrm{rx,min,dBm}})/20)}\,, \tag{3.23}$$

where

$$P_{\mathrm{lom,dBm}} = P_{\mathrm{out,sat,dBm}} + G_{\mathrm{ANT,dBi}}. \tag{3.24}$$

It is seen from (3.18) and (3.23), that in order to maximize the distance covered, it is required to increase not just the sensitivity of the SRA, but gain and output saturated power as well. So a novel quench pulse shaping is implemented *[TLJE18, TJE20] and presented in Section 3.2.2 and Section 3.2.3.

The level diagram in Fig. 3.6 illustrates the power levels at different stages in the interrogator to SRA forward link moving left to right, marked in red and the return link moving from right to left, marked in blue. In the forward link, the interrogator MMIC generates the chirp signal with a power level of -30 dBm, which is amplified by an external PA IC *[TLJE19] to generate $P_{\mathrm{tx,dBm}} = -12\,\mathrm{dBm}$ and radiated by ANT$_{\mathrm{tx}}$ with $G_{\mathrm{trx}} = 26\,\mathrm{dBi}$. The signal received at the SRT, undergoes a FSPL of around 71 dB at 24 GHz corresponding to the interrogation distance of 100 m. The attenuated signal is received by ANT$_{\mathrm{SRT}}$ with $G_{\mathrm{SRT}} = 5\,\mathrm{dBi}$ and amplified by the SRA with a superregenerative gain of 40 dB.

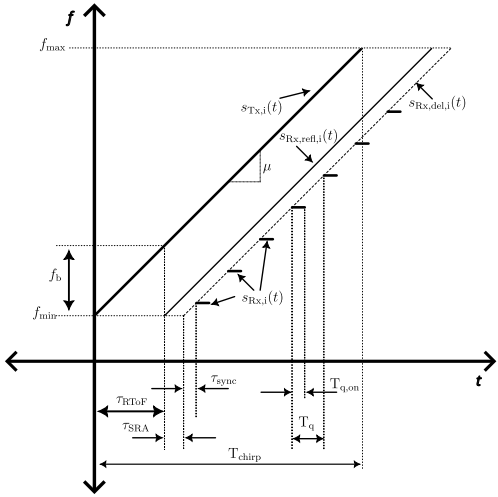

Figure 3.7: Illustration of the characteristics of a single chirp backscscattered by a corner reflector and a SRT. (Adapted from *[TFJE23] © 2023 IET).

In the return link, with a $P_{\mathrm{tx,SRA}} = -26\,\mathrm{dBm}$ the same $\mathrm{ANT_{SRT}}$ radiates an transmit power $P_{\mathrm{tx,SRT,dBm}} = -21\,\mathrm{dBm}$. This signal undergoes the same FSPL encountered in the forward link and the corresponding input power received by the $\mathrm{ANT_{rx}}$ with a gain $G_{\mathrm{trx}} = 26\,\mathrm{dBi}$ is $P_{\mathrm{rx,dBm}} = -76\,\mathrm{dBm}$. $P_{\mathrm{rx,dBm}}$ is further amplified by the gain of an LNA integrated within the MMIC to yield around $-56\,\mathrm{dBm}$ input power level, which is downconverted, further amplified and digitized to receive an equivalent base band signal power of around -10 dBm.

3.1.3 Non-idealities

Fig. 3.7 shows an illustration that details the characteristics of a single chirp backscattered by a corner reflector and an SRT. In the ideal scenario where a corner reflector is used, the transmitted signal $s_{\mathrm{T_x},i}(t)$ is delayed by the RToF τ_{RTOF} at the receive frontend of the interrogator. As described in Section 2.6, the SRA generates an output signal phase coherent to the input signal. But the input signal is regeneratively sampled only once every quench pulse period T_{q}. So when an SRT is employed, in addition to τ_{RTOF}, the signal is also delayed by the propagation delay τ_{SRA} of the SRA so that the total delay of the received signal $s_{\mathrm{Rx,refl,i}}$ at the interrogator is

$$\tau = \tau_{\mathrm{RTOF}} + \tau_{\mathrm{SRA}}. \tag{3.25}$$

τ_{SRA} arises due to the finite rise time of the SRA, and hence determines the time $T_{\mathrm{q,on}}$ required for attaining the minimum SRA output power level $P_{\mathrm{SRA,min}}$ so that the minimum detectable power level P_{min} is delivered at the interrogator. It can be determined using the relationships in (3.12) and (3.13) that

$$P_{\mathrm{min}} = \frac{P_{\mathrm{SRA,min}}}{\mathrm{FSPL}}. \tag{3.26}$$

At short distances, when the SRT is close to the interrogator, $P_{\mathrm{SRA,min}}$ is reached in the rising exponential region of the SRA output voltage signal illustrated in Fig. 2.15(f), and the corresponding τ_{SRA} can be determined approximately by substituting (3.26) in (2.36) as

$$\tau_{\mathrm{SRA}} = \frac{2T_{\mathrm{q}} R_{\mathrm{P}} P_{\mathrm{in,N}} P_{\mathrm{min}} \mathrm{FSPL}}{V_{\mathrm{out}}^2 P_{\mathrm{in}}}. \tag{3.27}$$

Since FSPL increases as distance between interrogator and SRT increases, it can be deduced from (3.27) that in order to maintain the same P_{min} as the distance increases, τ_{SRA} should increase, thereby also increasing the distance estimation error as can be deduced from (3.25) and (3.10).

Another nonideality that can be observed from the illustration of Fig. 3.7 is that, though the transmitted chirp signal $s_{\mathrm{T_x},i}(t)$ is continuous, the chirp received by the interrogator $s_{\mathrm{R_x},i}(t)$ is quantized by the SRA operation. This error manifests as τ_{sync}, and results due to the absence of synchronization between the interrogating chirp signal and the SRA quenchig signal, and manifests as a randomly varying start frequency offset error.

τ_{sync} can be considered as an approximate uniform distribution, and the corresponding probability, expectation and variance can be obtained using definitions [Kay93] according to,

$$\mathrm{P}(0 \leq t \leq \tau_{\mathrm{sync}}) = \int_0^{\tau_{\mathrm{sync}}} \frac{1}{T_{\mathrm{q}}}\, dt = \frac{\tau_{\mathrm{sync}}}{T_{\mathrm{q}}}, \tag{3.28}$$

$$\mathrm{E}(T) = \int_0^{T_{\mathrm{q}}} \frac{t}{T_{\mathrm{q}}}\, dt = \frac{T_{\mathrm{q}}}{2} \text{ and} \tag{3.29}$$

$$\mathrm{Var}(T) = \mathrm{E}(T^2) - \mathrm{E}(T)^2 = \int_0^{T_{\mathrm{q}}} \frac{t^2}{T_{\mathrm{q}}}\, dt - \left(\frac{T_{\mathrm{q}}}{2}\right)^2 = \frac{T_{\mathrm{q}}^2}{12}. \tag{3.30}$$

For ranging using a single chirp, the quantization related non-idealitites can

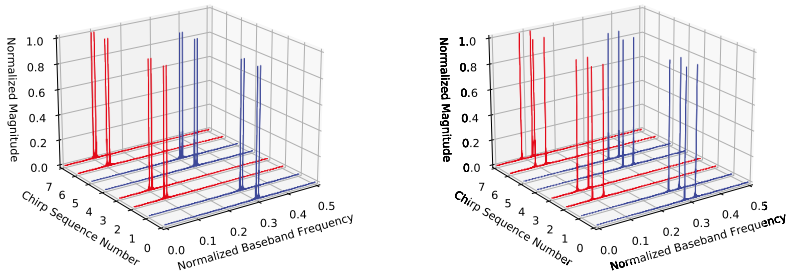

(a) (b)

Figure 3.8: Plot of modeled baseband magnitude spectrum for different chirp sequence numbers corresponding to transfer of binary data 4'b1010 using quench frequency shift keying at a distance of (a) 10 m and (b) 100 m. In this example, $K = 2$, binary zero is represented by $f_\mathrm{q}/f_\mathrm{samp} = 0.1$ and binary one represented by $f_\mathrm{q}/f_\mathrm{samp} = 0.3$. (Reused from *[TFJE23] ©2023 IET).

result in quite large errors. Hence in this work, multiple chirps forming a chirp sequence are used so that the frequencies in $s_{\mathrm{R_x},i}(t)$ are evenly distributed to approximate the frequencies in the ideal linear chirp.

3.1.4 SRA Quench Frequency Shift Keying for data transfer

The baseband spectrum $S_{\mathrm{b},i}(f)$ from (3.8), and the plots in Fig. 3.3 corresponds to a single chirp in the entire chirp sequence generated by the interrogator to locate a static SRT using a step-controlled SRA. Since the SRT is static, ideally there is no difference in the magnitude spectrum $S_{\mathrm{b},i}(f)$ for different values of i. However for the same $d_{\mathrm{SRT},i}$, if f_q is shifted while $T_{\mathrm{q,on}}$ is kept constant, the peaks in the amplitude spectrum would shift without changing the difference between the beat frequency peaks as plotted in Fig. 3.8. This property of $S_{\mathrm{b},i}(f)$ can be used for simultaneous distance measurement and data transfer from SRT to the interrogator using a SRA quench frequency shift keying (SQ-FSK) modulation scheme as illustrated in Fig. 3.9.

The data transfer feature is made possible due to two reasons. Firstly because the distance between interrogator and ART is independent of f_q if D_q is kept

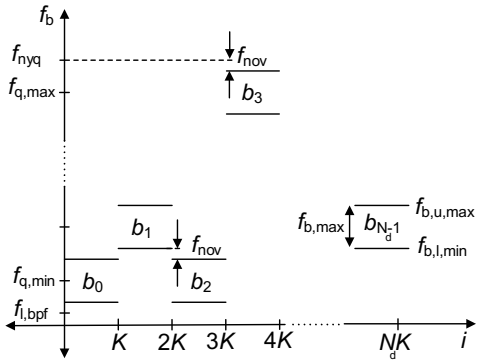

Figure 3.9: Plot of baseband frequency f_b against chirp sequence number i illustrating data transfer using quench frequency shift keying. The properties of the carrier chirp remains constant. (Adapted from *[TFJE23] © 2023 IET).

constant according to (3.10). Secondly, because f_q can be switched by a control signal over a wide frequency range bound by $f_\mathrm{q,min}$ and $f_\mathrm{q,max}$ according to

$$\begin{aligned} f_\mathrm{q,min} &= f_\mathrm{l,bpf} + f_\mathrm{nov} + \frac{f_\mathrm{b,max}}{2} \approx 410\,\mathrm{kHz} \text{ and} \\ f_\mathrm{q,max} &= f_\mathrm{nyq} - f_\mathrm{nov} - \frac{f_\mathrm{b,max}}{2} \approx 4.84\,\mathrm{MHz} \end{aligned} \tag{3.31}$$

where f_nyq is the Nyquist frequency given by $f_\mathrm{nyq} = f_\mathrm{samp}/2$ with f_samp as the sampling rate of the ADC used. $f_\mathrm{l,bpf}$ is the lower cut off frequency of the interrogating radar baseband bandpass filter, and f_nov is a small frequency offset required to ensure that there is no overlap between the maximum beat frequency $f_\mathrm{b,max}$ which is independent of the chirp sequence number i and is defined as

$$f_\mathrm{b,max} = f_\mathrm{b,u,max} - f_\mathrm{b,l,max}. \tag{3.32}$$

For a given SRA output power level and minium detected power level, the maximum distance and thereby the maxiumum beat frequency $f_\mathrm{b,max}$ is obtained by combining and rearranging (3.10), (3.12) and (3.13) in as (3.32)

$$f_\mathrm{b,max} = \frac{\mu \mathrm{D_q}}{2\pi f_\mathrm{q}} + \frac{2\mu}{\pi c} \cdot \frac{\lambda}{4\pi} \sqrt{\frac{P_\mathrm{tx} G_\mathrm{trx} G_\mathrm{ART}}{P_\mathrm{rx,SRA,min}}} \approx 300\,\mathrm{kHz}. \tag{3.33}$$

In Fig. 3.9, $f_{\mathrm{b,max}}$ and the corresponding upper and lower beat frequencies $f_{\mathrm{b,l,max}}$ and $f_{\mathrm{b,u,max}}$ are plotted against consecutive interrogator chirps with chirp sequence number i. Now, to transfer data with N digits per frame, each digit b is chosen from a set of M symbols, represented by

$$\{b \,|\, 0 \leq b < M\}, \tag{3.34}$$

where integer $m = 0, 1, ...N_{\mathrm{d}} - 1$. For example, an 8-bit binary data frame has $N_{\mathrm{d}} = 8$ and $M = 2$. Whereas an 5 digit quaternary data frame has $N_{\mathrm{d}} = 5$ and $M = 4$ and so on. The SRT shifts f_{q} once in every K chirps as a function of the digits and number system of the data to be transmitted so that,

$$f_{\mathrm{q}}(b_i) = f_{\mathrm{q,min}} + b_i(f_{\mathrm{nov}} + f_{\mathrm{b,max}}). \tag{3.35}$$

Fig. 3.9 depicts (3.35) for digits $b_{0\text{-}3}$ and $b_{N_{\mathrm{d}}-1}$ as an example, and the following correspondances can thereby be deduced

$$\begin{aligned} &f_{\mathrm{q}}(b_{0,i}) = f_{\mathrm{q}}(b_{2,i}) = f_{\mathrm{q,min}}, \\ &f_{\mathrm{q}}(b_{1,i}) = f_{\mathrm{q}}(b_{N_{\mathrm{d}}-1,i}) = f_{\mathrm{q,min}} + f_{\mathrm{nov}} + f_{\mathrm{b,max}} \text{ and} \\ &f_{\mathrm{q}}(b_{3,i}) = f_{\mathrm{q,max}}. \end{aligned} \tag{3.36}$$

Now with K chirps per symbol, a data frame consisting of N_{d} digits requires at least $N_{\mathrm{c}} = N_{\mathrm{d}}K$ chirps. Since the interrogator and ART are not synchronized, additional symbols for start and stop bits are required, and the total number of chirps in the sequence required to decode an entire data frame can go up to $N_{\mathrm{c}} = 2N_{\mathrm{d}}K$.

In order to maximize the spectrum utilization, an upper bound on the possible number of symbols M can also be determined from (3.31) and (3.35) as,

$$M \leq \frac{f_{\mathrm{nyq}} - f_{\mathrm{l,bpf}} - f_{\mathrm{nov}}}{f_{\mathrm{b,max}} + f_{\mathrm{nov}}} \approx 15.3 \tag{3.37}$$

It is interesting to note from (3.37) that M also sets the limit on the number of simultaneous SRT that can be interrrogated in a multi-transponder scenario.

3.1.5 Knowledge Gained

From Section 3.1 we can see that the SRA based RFID transponder can be used for both identification and ranging. The maximum detection range is determined by the minimum SRA gain derived as shown in (3.15) and the saturated output power in linear mode is determined according to (3.18) and logarithmic mode

derived in (3.23).

A novel data transfer scheme using SQ-FSK is envisaged shifting f_q as a function of the data to be transferred. Simultaneous ranging is also made possible by keeping $T_\mathrm{q,on} = D_\mathrm{q}/f_\mathrm{q}$ constant. Under this condition, the difference between upper and lower frequencies, and the corresponding distance estimated in (3.10) remains the same irrespective of the value of f_q. This implies that when the system is implemented, for each f_q shift, D_q has to be calibrated to keep $T_\mathrm{q,on}$ constant in order to make accurate ranging measurements along with data transfer simultaneously. Also the upper bound for the number of symbols within the baseband frequency range is derived considering the parameters of the baseband components like the bandpass filter and ADC according to (3.37).

3.2 RFIC Designs

As discussed in Section 2.6, the basic SRA is a one port network which receives the input signal across a passive resonator core. When a time varying quench signal $V_\mathrm{q}(t)$ modulates the transconductance across the resonator from positive to negative using an active device, the resonator functionally transitions from a bandpass filter to an oscillator, whose oscillations build up with an exponential amplitude and are phase coherent to the input signal. This amplified output signal is generated at the same port where the input signal is applied. Periodic quenching of the oscillation using $V_\mathrm{q}(t)$ is necessary to sustain this phase coherent amplification because the sampling and amplification occurs only during oscillator start-up. Hence the SRA design is essentially an oscillator design problem with the additional requirement of controlling the damping factor using a periodic signal. So the key structural requirements of SRA design are:

- A resonator core with an active element that can transition damping from positive to negative and back according to a quench signal.
- Interface to inject the input signal to the resonator of the circuit.
- Optimum quench pulse generation to improve input signal sensitivity and output power.
- The ability to drive $50\,\Omega$ single ended or $100\,\Omega$ differential loads presented by antennas at the system level.

The following subsections presents the design of four SRA ICs and their comparative studies. Since the core of the SRA is similar to an oscillator, the designed

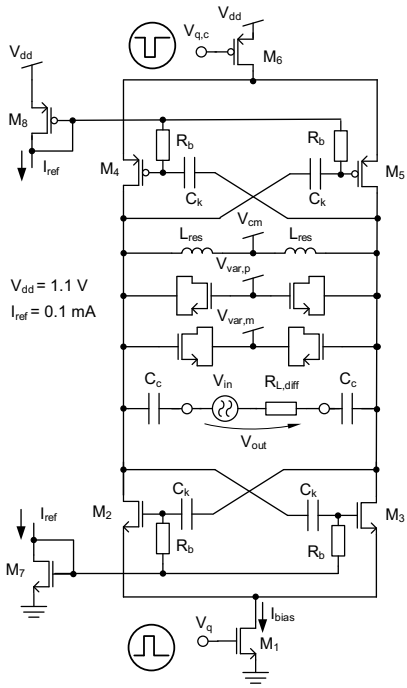

Figure 3.10: Schematic of the CMOS cross-coupled oscillator based SRA_{SOI} (Adapted from *[TGJE18] ©2018 IEEE).

SRAs use the differential cross coupled oscillator (CCO) topology because of relaxed startup condition requirements and low occupied area when compared to other differential topologies [AWVF05, MDW15, MMKN16]. The designs enable the following comparative studies:

- Technology dependence on the performance of direct antenna drive SRAs using silicon on insulator (SOI) and SiGe-BiCMOS implementations.
- Impact of quench pulse shaping on the performance of direct antenna drive SRAs.
- Performance characteristics of direct antenna drive SRA against the buffered antenna drive SRA having multiple input and output buffers.

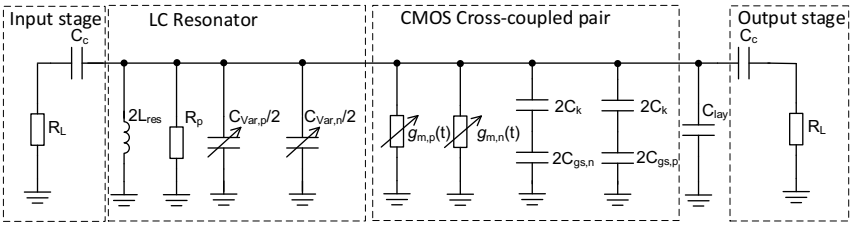

Figure 3.11: Small signal equivalent circuit of the CMOS cross-coupled oscillator based $\mathrm{SRA_{SOI}}$.

3.2.1 Low Power Direct Antenna Drive CMOS SRA IC

The first SRA design presented is a low complexity direct antenna drive CMOS SRA ($\mathrm{SRA_{SOI}}$) implemented in a 45 nm SOI technology discussed in Section 2.7.2, and is a frequency optimized variant of *[TGJE18]. $\mathrm{SRA_{SOI}}$ has two single ended ports or one differential port which directly drive the antennas without a buffer. The design is optimized for low DC power consumption, and operates around the center frequency of 24.5 GHz.

3.2.1.1 Circuit analysis and design

The schematic of the designed $\mathrm{SRA_{SOI}}$ based on a CMOS complementary CCO is shown in Fig. 3.10. The input signal V_{in} is injected and output signal V_{out} is measured at the same port across the differential load resistance $R_{\mathrm{L,diff}} = 100\,\Omega$. The quench voltage V_{q} sets the bias current and operating point of the circuit through the tail current course nFET $\mathrm{M_1}$. When V_{q} is low, the circuit is current starved and the transconductance of the crosscoupled nFET pairs $\mathrm{M_{2,3}}$ and pFET pairs $\mathrm{M_{2,3}}$ is not enough to compensate the losses of the resonator according to (2.22), resulting in neither oscillations nor superregenerative amplification. Under the conditions where the bias current I_{bias} is sufficiently large, oscillation builds up and reaches a steady state. The frequency of this natural oscillations of the resonator f_{res} is set by the resonator inductance L_{res} and the equivalent parallel capacitance determined using the small signal model drawn in Fig. 3.11 as

$$f_{\mathrm{res}} = \frac{1}{2\,\pi\,\sqrt{L_{\mathrm{res}}(C_{\mathrm{par}} + C_{\mathrm{var,p}}(V_{\mathrm{var,p}}) + C_{\mathrm{var,n}}(V_{\mathrm{var,n}})}}. \tag{3.38}$$

Where L_{res} is chosen in the sub hundred pH range and is implemented using a

differential center tapped symmetrical inductor with an unloaded quality factor $Q_{\mathrm{ul}} \approx 30$, and is optimized using EM simulations. The capacitance C_{par} is the sum of four components.

$$C_{\mathrm{par}} = C_{\mathrm{lay}} + C_{\mathrm{k,n}} + C_{\mathrm{k,p}} + 2C_{\mathrm{c,eq}}. \tag{3.39}$$

Here C_{lay} is the modeled parasitic capacitance resulting from layout. $C_{\mathrm{k,n}}$ and $C_{\mathrm{k,p}}$ are the equivalent capacitances in the feedback path of nMOS devices $\mathrm{M}_{2,3}$ and and pMOS devices $\mathrm{M}_{4,5}$ respectively according to

$$C_{\mathrm{k,n}} = \frac{C_{\mathrm{k}} C_{\mathrm{gs,n}}}{(C_{\mathrm{k}} + C_{\mathrm{gs,n}})} \tag{3.40}$$

and

$$C_{\mathrm{k,p}} = \frac{C_{\mathrm{k}} C_{\mathrm{gs,p}}}{(C_{\mathrm{k}} + C_{\mathrm{gs,p}})}. \tag{3.41}$$

$C_{\mathrm{c,eq}}$ is the equivalent capacitance presented by the output coupling capacitance C_{c} after a network transformation using the relationship

$$C_{\mathrm{c,eq}} = \frac{C_{\mathrm{c}}}{(1 + \frac{1}{Q_{\mathrm{c}}^2})}, \tag{3.42}$$

where Q_{c} is the quality factor of the input and output coupling network given by

$$Q_{\mathrm{c}} = \frac{1}{\omega_{\mathrm{res}} C_{\mathrm{c}} R_{\mathrm{L}}}. \tag{3.43}$$

$R_{\mathrm{L}} = R_{\mathrm{L,diff}}/2 = 50\,\Omega$ represents the single ended antenna impedance which also degrades the quality factor Q_{load} of the resonator and the coupling capacitor C_{C} in the few hundreds of fF range.

The effective loaded quality factor of the resonator is determined as $Q_{\mathrm{load}} \approx 5.5$ at $f_{\mathrm{res}} = 24.5\,\mathrm{GHz}$ using EM simulations. The corresponding effective parallel resistance of the resonator is

$$R_{\mathrm{p}} = \frac{1}{G_{\mathrm{p}}} = \omega_{\mathrm{res}} L_{\mathrm{res}} Q_{\mathrm{load}}. \tag{3.44}$$

The two parallel branches of thin oxide nMOS accumulator mode varactors provides a combined capacitance range of $C_{\mathrm{max}}/C_{\mathrm{min}} \approx 5.72$ and are used for differential frequency tuning. The capacitance C_{k} in the sub fifty femto Farad range is optimized to to limit the voltage swing at the gate of the transistors, and have a peak voltage swing higher than the center tap voltage V_{cm} across

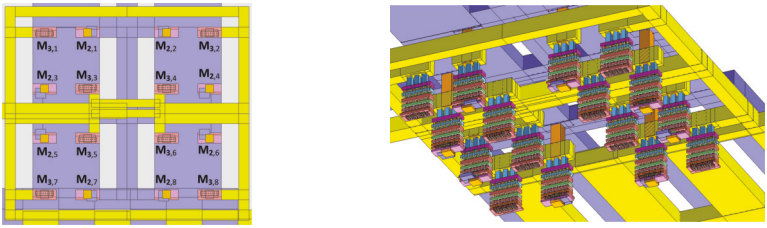

(a) (b)

Figure 3.12: Illustration of the common centroid layout and corresponding transistor interconnection for $\mathrm{SRA_{SOI}}$: (a) top view (b) perspective view showing via stack.

the inductor. In steady state, the negative resistance R_{neg} required for sustained oscillations is obtained from the transconductance $g_{\mathrm{m,n}}$ and $g_{\mathrm{m,p}}$ of the nFET pair and pFET pair respectively as

$$R_{\mathrm{neg}} \approx \frac{-2}{g_{\mathrm{m,n}} + g_{\mathrm{m,p}}}. \tag{3.45}$$

Using the rule of thumb from [Ell07] $R_{\mathrm{neg}} \approx -R_{\mathrm{p}}/3$, the value of the optimum transconductance $g_{\mathrm{m,opt}} = g_{\mathrm{m,n}} g_{\mathrm{m,p}}$ can be written using (3.45) and (3.44) as

$$g_{\mathrm{m,opt}} \approx -\frac{3}{\omega_{\mathrm{res}} L_{\mathrm{res}} Q_{\mathrm{load}}}. \tag{3.46}$$

The bias current $I_{\mathrm{bias}} = 9\,\mathrm{mA}$ corresponding to $g_{\mathrm{m,opt}}$ is set by the current mirrors transistors $\mathrm{M_7}$ and $\mathrm{M_8}$. This current also sets the peak-to-peak output voltage swing of 1.1 V, resulting in an output power $P_{\mathrm{out,dBm}} \approx 2\,\mathrm{dBm}$. The gate of switching transistor $\mathrm{M_1}$ is over-driven by the quench signal V_{q}, which swings from V_{ss} to V_{dd}, and the gate of switching transistor $\mathrm{M_6}$ is over-driven by the complementary quench voltage $V_{\mathrm{q,C}}$, generated from V_{q} using a CMOS inverter. This lets $\mathrm{M_1}$ and $\mathrm{M_6}$ operate between cut-off and triode regions to quench the oscillations on and off. A periodic V_{q} can thus vary the transconductance across the resonator from zero to the optimum transconductance $g_{\mathrm{m,opt}}$ and back resulting in superregenerative amplification of of V_{in} present across the resonator.

The circuit is implemented in the 45 nm SOI technology discussed in Section 2.7.2 using minimum length floating body transistors. Layout of transistor interconnects are done with double-gate contacts similar to that illustrated in [IMU+14]. Common centroid layout is done for transistors $\mathrm{M_{2,3}}$ and $\mathrm{M_{4,5}}$ to reduce the sensitivity to threshold voltage variations as illustrated in Fig. 3.12(a)

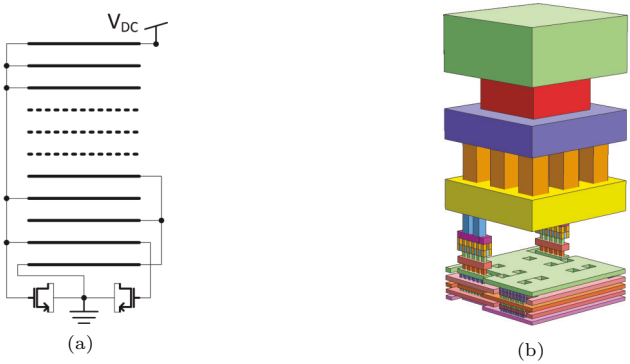

Figure 3.13: (a) Schematic of the zero-ohm transmission line unit cell used for DC bias routing. (b) Corresponding layout.

and the corresponding via stack layout is shown in Fig. 3.12(b). Routing of DC bias voltages like V_{dd}, V_{cm} and I_{ref} to pads is done using scalable custom-designed zero-ohm transmission lines unit cells shown in the schematic of Fig. 3.13(a) and the implementation in Fig. 3.13(b). These structures utilize the relatively high inter-layer capacitance of the lower metal layers in the CMOS technology to provide a high decoupling capacitance to reduce noise and are based on [TFL+15].

3.2.1.2 Characterization

The fabricated integrated circuit shown in Fig. 3.14, is characterized by microprobing. Parameters including f_{res}, the output power $P_{\mathrm{out,dBm}}$, input sensitivity $P_{\mathrm{min,dBm}}$ and bandwidth f_{BW} are characterized using the test setup consisting of a Rohde & Schwarz FSU spectrum analyzer, Keysight 8257D RF signal source, and an arbitrary waveform generator for quench waveform generation as shown in Fig. 3.14. When the quench signal V_{q} is kept high, the circuit operates in the free-running oscillator mode, and f_{res} is measured by varying the varactor voltages $V_{\mathrm{var,p}}$ and $V_{\mathrm{var,n}}$. The measured frequency variation from 24.07 GHz to 25.35 GHz is shown in Fig. 3.15(a).

In order to characterize the operation of the circuit as a SRA, the oscillator has to be quenched ON and OFF. Since the time domain measurements of regenerative sampling is not practical at the oscillation frequency, characterization is done using the spectral measurement procedure described in [SCW+13b]. When V_{q} is applied as a periodic pulse, and when input is present outside the regenerative

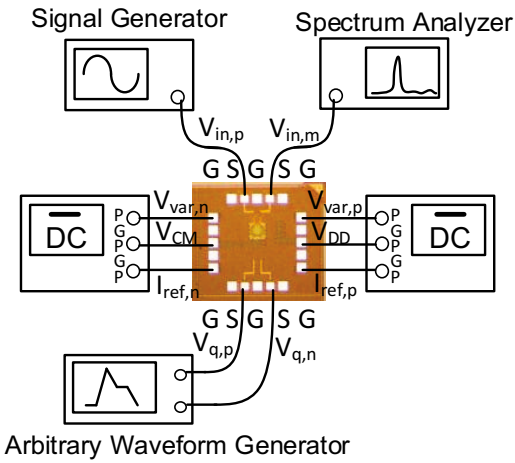

Figure 3.14: Illustration of the measurement setup around the chip micrograph of $\mathrm{SRA_{SOI}}$ measuring 820 µm × 820 µm including pads (Adapted from *[TGJE18] © 2018 IEEE).

sampling frequency range, a *sinc* spectrum can be measured as shown in the blue trace with triangle markers in Fig. 3.16(a). When V_q is applied as a periodic pulse, and an input signal is present within the regenerative sampling frequency range, the characteristic delta function peaks are observed superimposed on the *sinc* spectrum as shown in the black trace with dotted markers in Fig. 3.16(a).

Frequency response measurements are done for different input signal power levels $P_\mathrm{dBm,in}$ as shown in Fig. 3.25(b) to determine the regenerative sampling frequency range and bandwidth f_BW, which increases with increasing input power levels. In Fig. 3.25(b), the peak power spectral density measurements with a pulsed V_q are compared to measurements with a sinusoidal V_q. The delta function peaks indicating regenerative sampling start to appear from $P_\mathrm{in,dBm} = -85\,\mathrm{dBm}$, and the output power $P_\mathrm{out,dBm}$ increases linearly. With pulsed quenching, from $P_\mathrm{i,N,dBm} = -64.9\,\mathrm{dBm}$, the output power starts to saturate, as the SRA enters the logarithmic mode. With sinusoidal quenching, this power is measured to be $P_\mathrm{i,N,dBm} = -66.3\,\mathrm{dBm}$. The measured peak superregenerative gain is 48 dB. The circuit draws a current of 8.7 mA from 1.1 V power supply, consuming 9.6 mW when operating as a free-running oscillator, and 4 mW when quenched with a periodic pulse with 50% duty cycle. Measurements are done till a maximum pulse

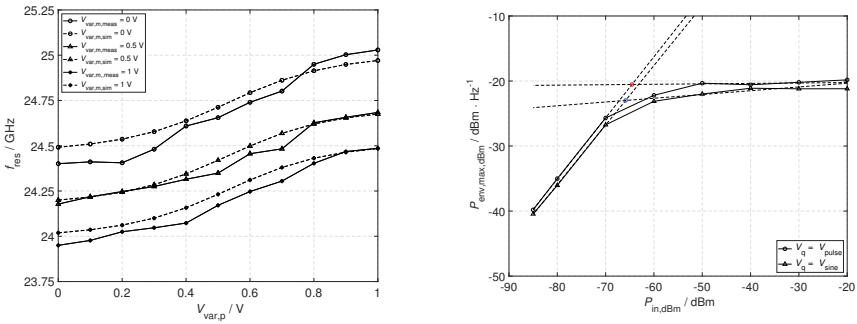

(a) (b)

Figure 3.15: (a) Simulated and measured differential tuning range of $\mathrm{SRA_{SOI}}$ in free-running mode, showing frequency tuning from 24.1 GHz to 25.4 GHz. (b) Measured peak output power spectral density vs. input power, with marking of linear mode to logarithmic mode transition points for sinusoidal and pulsed quenching.

repetitive frequency of 20 MHz.

3.2.2 Direct Antenna Drive SiGe SRA ICs

This section describes the direct antenna drive SiGe SRA ($\mathrm{SRA_{dir}}$) which is similar to $\mathrm{SRA_{SOI}}$ in the aspect of directly interfacing the resonant tank with a 100 Ω differential load representing the antenna input impedance, but uses three novel concepts to simultaneously improve the output power level and minimum detected input signal *[TLJE18]:

- The first concept is a differential stacked transistor cross-coupled quenchable oscillator topology which improves the output power of the SRA described in Section 3.2.2.1.
- The second concept is a quench waveform design which improves the P_{min} required for phase coherent amplification as described in Section 3.2.2.2.
- The third concept is the realization of the designed quench waveform characteristics using a novel quench pulse shaping circuit described in Section 3.2.3.1.

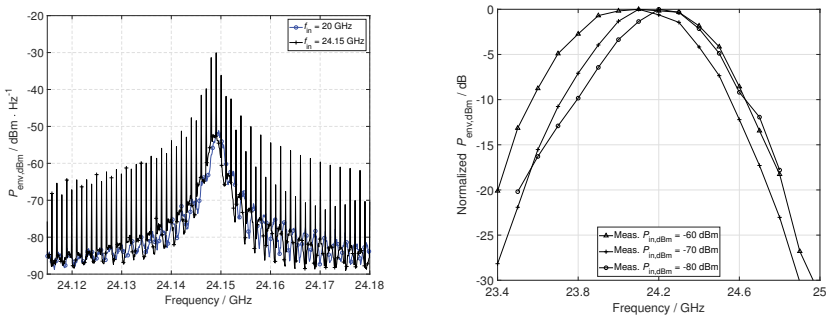

(a) (b)

Figure 3.16: (a) Measured power spectral density with $P_{\mathrm{in,dBm}} = -70\,\mathrm{dBm}$ at $f_{\mathrm{res}} = 24.148\,\mathrm{GHz}$. (b) Measured normalized frequency response for various input power levels, showing an increase in bandwidth with increase in input power from $-85\,\mathrm{dBm}$ to $-60\,\mathrm{dBm}$.

The three concepts are juxtaposed to design an improved $\mathrm{SRA_{dir,q}}$ with integrated quench pulse shaping.

3.2.2.1 Stacked Transistor Cross-coupled Quenchable Oscillator

The schematic of $\mathrm{SRA_{dir}}$ employing the stacked transistor cross-coupled quenchable oscillator (STCCO) topology *[TLJE18] is depicted in Fig. 3.17. The key subcircuits of this design are, the resonant tank formed by L_{res} and C_{var} which also drives the output load, the cross-coupled pair is formed by HBTs $\mathrm{T_{1,3}}$, with series stacked transistors $\mathrm{T_{2,4}}$, and the quenching stage implemented using $\mathrm{T_{5\text{-}8}}$ and the nFET $\mathrm{M_7}$.

3.2.2.1.1 Resonator As illustrated in Fig. 3.18, the key contributor to the inductive reactance of the $\mathrm{SRA_{dir}}$ resonator is a two turn, symmetrical center tapped differential spiral inductor with series inductance L_{res} optimized for a peak unloaded quality factor $\mathrm{Q_{uL}}$ around 24 GHz. The series inductance is slightly increased by a positive coupling coefficient k_{M} [MDW15]. Since the $\mathrm{SRA_{dir,q}}$ directly drives the antenna when included in a transponder, an additional inductance $L_{\mathrm{B,P}}$ as a result of the network transformation of the bond-wire inductance $L_{\mathrm{B}} \approx 900\,\mathrm{pH}$ also forms part of the effective resonator inductance. This equivalent parallel inductance $L_{\mathrm{B,P}}$ is derived as

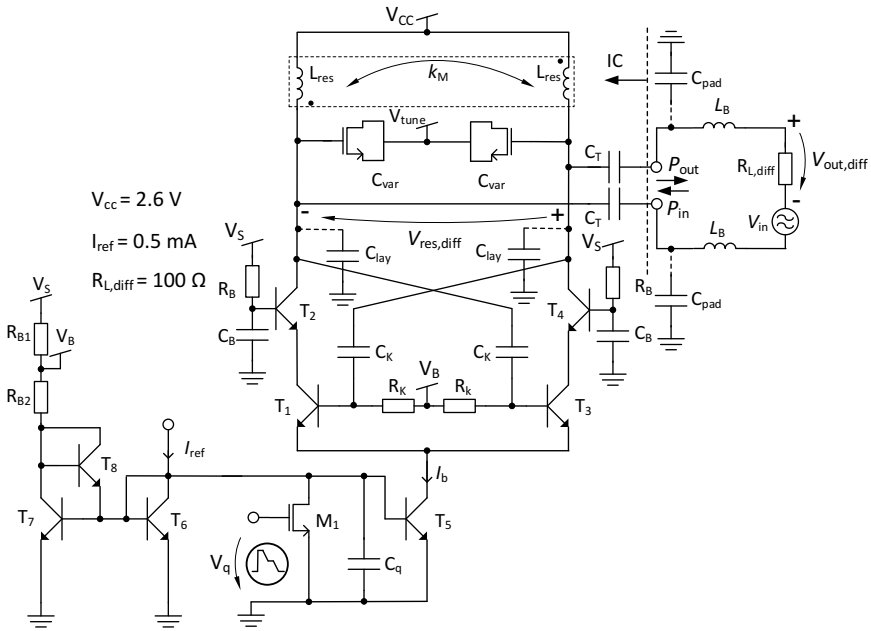

Figure 3.17: Schematic of the direct antenna interface $\mathrm{SRA_{dir}}$ (Adapted from *[TLJE18] ©2018 IEEE)

.

$$L_{\mathrm{B,P}} = \frac{L_{\mathrm{B}} \cdot (1 + Q^2_{R_{\mathrm{L}},L_{\mathrm{B}},C_{\mathrm{T}}})}{Q^2_{R_{\mathrm{L}},L_{\mathrm{B}},C_{\mathrm{T}}}} . \tag{3.47}$$

$Q_{R_{\mathrm{L}},L_{\mathrm{B}},C_{\mathrm{T}}}$ is the quality factor of the series load transfer network formed by L_{B}, the single ended load resistance R_{L} and the output stage coupling capacitor C_{T}, and is given by

$$Q_{R_{\mathrm{L}},L_{\mathrm{B}},C_{\mathrm{T}}} = \frac{\omega_{R_{\mathrm{L}},L_{\mathrm{B}},C_{\mathrm{T}}} L_{\mathrm{b}}}{R_{\mathrm{L}}} \approx 0.97 \tag{3.48}$$

The equivalent resonator capacitance C_{res} is the parallel combination of varactor capacitance C_{var}, the equivalent parallel transformed output stage capacitance $C_{\mathrm{T,P}}$ calculated as

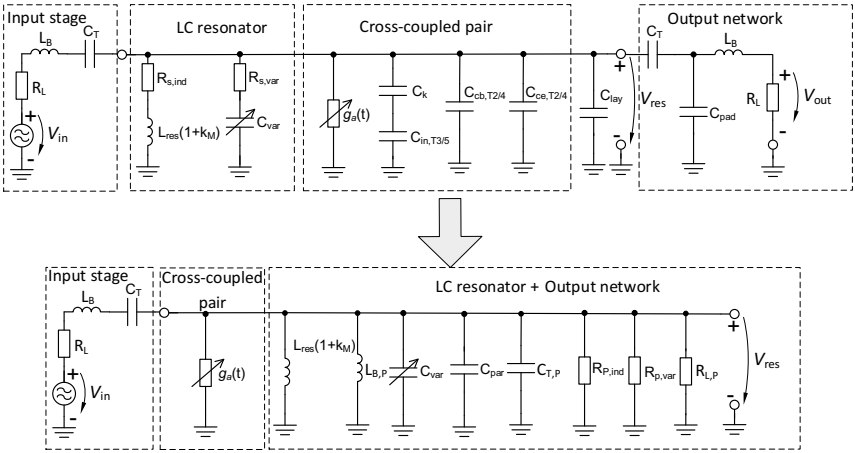

Figure 3.18: Small signal equivalent circuit of the $\mathrm{SRA_{dir}}$ resonator and output network transformation used to derive f_{res} and V_{res}.

$$C_{\mathrm{T,P}} = \frac{C_{\mathrm{T}} \cdot Q^2_{R_{\mathrm{L}},L_{\mathrm{B}},C_{\mathrm{T}}}}{(1 + Q^2_{R_{\mathrm{L}},L_{\mathrm{B}},C_{\mathrm{T}}})}, \tag{3.49}$$

and an effective fixed capacitance C_{par}. C_{par} is the equivalent capacitance which includes the base-collector capacitor of transistors $\mathrm{T}_{2,4}$ in series with C_{B}, the feedback capacitance C_{k} in series with the input capacitance of transistors $\mathrm{T}_{1,3}$, and other layout parasitic capacitances including pad capacitance C'_{lay}. Since there is no mutual coupling between L_{B} and L_{res}, the resonant frequency f_{res} is derived as,

$$f_{\mathrm{res}} = \frac{1}{2\,\pi\,\sqrt{(L_{\mathrm{res}}(1+k_{\mathrm{M}}) + L_{\mathrm{B,P}})(C_{\mathrm{par}} + C'_{\mathrm{var}}(V_{\mathrm{tune}}) + C_{\mathrm{T,P}})}}, \tag{3.50}$$

with

$$\begin{aligned} C_{\mathrm{par}} &= C_{\mathrm{cb,T2,4}} + C_{\mathrm{ce,T2,4}} + C'_{\mathrm{lay}} \\ &\quad + \frac{C_{\mathrm{k}} C_{\mathrm{in,T1,3}}}{C_{\mathrm{k}} + C_{\mathrm{in,T1,3}}}, \end{aligned} \tag{3.51}$$

where, $C_{\mathrm{cb,T1,2}}$ and $C_{\mathrm{ce,T1,2}}$ are the collector-base and collector-emitter capac-

itance of HBTs $T_{1,2}$ respectively and

$$C'_{\mathrm{var}}(V_{\mathrm{tune}}) = C_{\mathrm{var}}(V_{\mathrm{tune}})\frac{Q^2_{\mathrm{var}}}{1+Q^2_{\mathrm{var}}}. \tag{3.52}$$

C_{var} is a function of V_{tune}, and represents the capacitance of the thick oxide n-channel metal oxide semiconductor accumulation mode varactor and Q_{var} is the quality factor of the varactor with a series resitance of $R_{\mathrm{s,var}}$ and is given by

$$Q_{\mathrm{var}} = \frac{1}{\omega C_{\mathrm{var}}(V_{\mathrm{tune}})R_{\mathrm{s,var}}}. \tag{3.53}$$

f_{res} is then tuned by varying the varactor control voltage V_{tune} to change the capacitance C_{var} from $C_{\mathrm{var,min}}$ to around $1.95\,C_{\mathrm{var,min}}$. The resulting f_{res} variation is from 24.4 GHz to 25.8 GHz.

3.2.2.1.2 Output Network The small signal equivalent circuit in Fig. 3.18 also helps to calculate the output voltage swing and maximum output power generated by the circuit. At first the total loss of the circuit R_{P} is determined as the reciprocal of the conductance as

$$R_{\mathrm{P}} = \frac{1}{G_{\mathrm{P}}} = \frac{1}{G_{\mathrm{P,var}} + G_{\mathrm{P,ind}} + G_{\mathrm{L,P}}}. \tag{3.54}$$

$R_{\mathrm{P,var}}$ represents the losses in the varactors C_{var} given by

$$R_{\mathrm{P.var}} = \frac{1}{Q_{\mathrm{uV}}\omega_{\mathrm{res}}C_{\mathrm{var}}(V_{\mathrm{tune}})}, \tag{3.55}$$

where Q_{uV} is the unloaded quality factor of the varactor obtained from extracted simulations at resonator center frequency ω_{res}. $R_{\mathrm{P,ind}}$ is the equivalent parallel resistance of L_{res} with unloaded quality factor Q_{uL} and is given by

$$R_{\mathrm{P,ind}} = Q_{\mathrm{uL}}\omega_{\mathrm{res}}L_{\mathrm{res}}. \tag{3.56}$$

Also the output power is delivered to the single ended load resistance $R_{\mathrm{L}} = 50\,\Omega$ through coupling capacitors C_{T} and L_{B}. The equivalent parallel resistance $R_{\mathrm{L,P}}$ of this output network is

$$R_{\mathrm{L,P}} \;=\; R_{\mathrm{L}} \cdot \left(1 + Q^2_{R_{\mathrm{L}},L_{\mathrm{B}},C_{\mathrm{T}}}\right). \tag{3.57}$$

Now, using the effective parallel resistance just defined, the resonator loaded quality factor $Q_{\mathrm{res}} \approx 5.6$ is obtained using

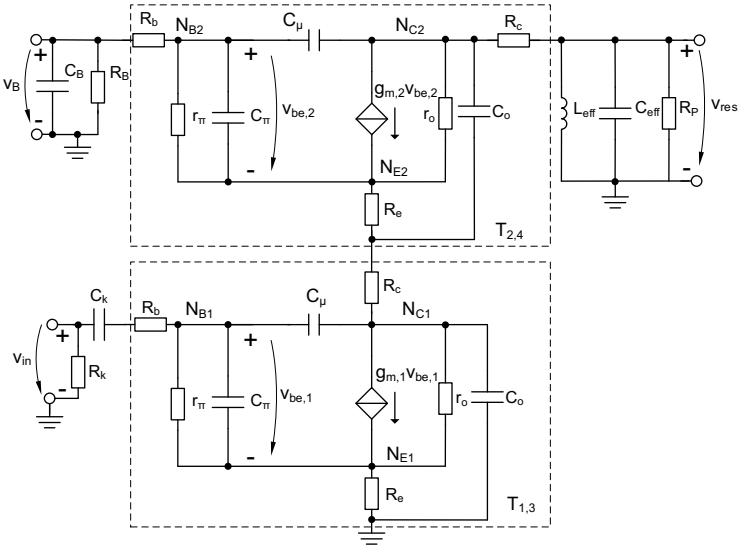

Figure 3.19: The comprehensive HBT small signal equivalent circuit of the stacked transistor CCO half cell.

$$Q_{\mathrm{res}} = \frac{R_{\mathrm{P}}}{\omega_{\mathrm{res}} L_{\mathrm{res}}}. \tag{3.58}$$

(3.58) can also be used to calculate the bandwidth of the resonator as $f_{\mathrm{BW,res}} = f_{\mathrm{res}}/Q_{\mathrm{res}} \approx 4.3\,\mathrm{GHz}$.

Defining the differential peak to peak output voltage across the load resistor $R_{\mathrm{L,diff}} = 100\,\Omega$ as $V_{\mathrm{out,pp}}$, the differential voltage peak to peak swing across the resonator as V_{res}, and the single ended peak to peak voltage swing across each HBT as $V_{\mathrm{C,T,pp}} = V_{\mathrm{res,pp}}/2$, it can be seen from the equivalent network shown in Fig. 3.18 that the output stage forms a voltage divider with,

$$\frac{|V_{\mathrm{out}}|}{|V_{\mathrm{res}}|} = \left| \frac{R_{\mathrm{L}}}{(R_{\mathrm{L}} + j(X_{L_{\mathrm{b}}} - X_{C_{\mathrm{T}}}))} \right| \approx 0.32\,, \tag{3.59}$$

where $X_{C_{\mathrm{T}}} = 1/\omega_{\mathrm{res}} C_{\mathrm{T}}$ and $X_{L_{\mathrm{b}}} = \omega_{\mathrm{res}} L_{\mathrm{b}}$. (3.59) shows that differential peak to peak voltage swing across the load resistor $V_{\mathrm{out,pp}}$ is 0.32 times the peak to peak voltage swing generated across the resonator, $V_{\mathrm{res,pp}}$. The HBTs used in this design have a a knee voltage V_{knee} of around 550 mV and a collector to

emitter breakdown voltage with base open of $V_{\mathrm{BVCEO}} \approx 1.7\,\mathrm{V}$ [RHW+10a]. But it can be seen from [CL05] that in circuits biased with relatively low values of base resistances less than $5\,\mathrm{k\Omega}$, $V_{\mathrm{BVCER}} \approx 3.5\,\mathrm{V}$ sets the safe operating area (SOA). Thus a conservative maximum collector voltage $V_{\max}$ is chosen such that $V_{\max} \approx 2\,\mathrm{V} < V_{\mathrm{BVCER}}$.

Transistor stacking is a concept used in recently reported PA designs [FWE12]. To increase the output power of the $\mathrm{SRA_{dir}}$, a similar concept is employed, and the minimum number of HBTs that need to be stacked N_{stack} can be calculated as the *ceil*ing of the ratio given by

$$N_{\mathrm{stack}} = \left\lceil \frac{V_{\mathrm{C,T,pp}}}{(V_{\max} - V_{\mathrm{knee}})} \right\rceil. \tag{3.60}$$

To operate within the SOA, two stacked transistors, $\mathrm{T_1}$ and $\mathrm{T_2}$ are used in $\mathrm{SRA_{dir}}$. This translates to peak to peak differential voltage swings of $V_{\mathrm{res,pk\text{-}pk}} \approx 5.8\,\mathrm{V}$ across the resonator and $V_{\mathrm{out,pk\text{-}pk}} \approx 1.87\,\mathrm{V}$ across R_{L}. The corresponding output power level is $P_{\mathrm{out,dBm}} \approx 6.4\,\mathrm{dBm}$. Using $V_{\mathrm{res,pk\text{-}pk}}$ from (3.59) and R_{P} from (3.54), the bias current I_{b} corresponding to the steady state power level can then be calculated as

$$I_{\mathrm{b}} = \frac{V_{\mathrm{res,pk\text{-}pk}}}{R_{\mathrm{P}}} \approx 47.5\,\mathrm{mA}. \tag{3.61}$$

The feedback capacitor C_{K} in the three quarters femto Farad range is optimized to meet the startup requirements across process, voltage and temperature corners. The bias voltages V_{B} is generated using the biasing network shown in Fig. 3.17. In addition to making the circuit less sensitive to variations in process, voltage and temperature, the biasing circuit also makes sure that the emitter base breakdown voltage $V_{\mathrm{BVEBO}} = 1.2\,\mathrm{V}$ on $\mathrm{T_3}$ and $\mathrm{T_4}$ are not exceeded when the oscillations are quenched, with the help of $\mathrm{T_9}$. All RF path capacitances are implemented using MIM capacitors from the technology process design kit (PDK).

3.2.2.1.3 Stacked Transistor Cross-coupled Pair and Loop Gain The time varying controlled transonductance $g_{\mathrm{a}}(t)$ in the equivalent circuit of Fig. 3.18 is implemented using the stacked HBT pair formed by $T_{1,2}$ and $T_{3,4}$ in the schematic of Fig. 3.17. $g_{\mathrm{a}}(t)$ can be determined by looking into the collectors of $T_{2,4}$, and is calculated according to [Lee03] as

$$g_{\mathrm{a}}(t) = \frac{-g_{m,T_{2,4}}(t)}{2}\,. \tag{3.62}$$

Since $g_{m,T_{2,4}}$ is directly proportional to the collector current $I_{\mathrm{c,T2,4}}(t)$ and since

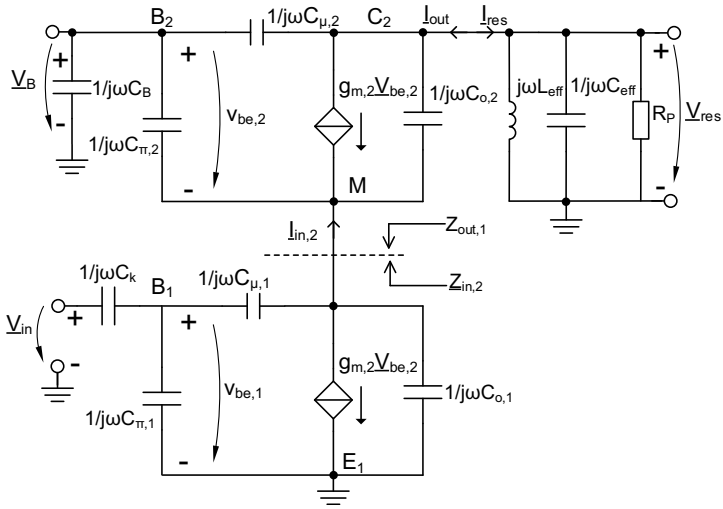

Figure 3.20: Simplified high frequency small signal equivalent circuit of the stacked transistor CCO half cell for loop gain analysis and determining the value of C_{B}.

the tail current through HBT T_5 sets the total bias current $I_{\mathrm{b}}(t) = 2I_{\mathrm{c,T2,4}}(t)$, then

$$g_{m,T_{2,4}}(t) \approx \frac{I_{\mathrm{b}}(t)}{2V_{\mathrm{T}}} \tag{3.63}$$

From (3.63) and (2.22), we can see that the optimum control of the SRA damping function can be realized by controlling $I_{\mathrm{b}}(t)$, and this property is explored more in Section 3.2.3.1 to determine the critical sampling current for maximum input signal sensitivity.

In this section, the properties of the STCCO are explored further. As seen in Fig. 3.17, the STCCO is essentially a loop back cascade of two tuned amplifier stages. Each tuned amplifier consists of a common base (CB) amplifier with base-capacitance feedback stacked on top of a common emitter (CE) amplifier. The STCCO half cell depicted in Fig. 3.19 shows the detailed small signal equivalent circuit of the half cell, which is simplified to the high frequency equivalent circuit shown in Fig. 3.20 for small signal analysis by ignoring the tranconductance delay τ, the extrinsic resistance at base R_{b}, collector R_{c} and emitter R_{e} respectively

and the output resistance r_o. This approximation is valid since the frequency of operation of 24 GHz is at least 10 times lower than f_t [Voi13].

From Fig. 3.20, the loop gain $\underline{a}_{v,loop}(j\omega)$ can be defined as the cascaded gain of the two half cell gains $\underline{a}_{v,hc,1}$ and $\underline{a}_{v,hc,2}$ according to

$$\underline{a}_{v,loop}(j\omega) = \underline{a}_{v,hc,1} \cdot \underline{a}_{v,hc,2} = \underline{a}_{v,hc}^2 \tag{3.64}$$

Assuming that both half cells are identical as $\underline{a}_{v,hc}$, the schematic of the small signal equivalent circuit shown in Fig. 3.19 can be used to analyze $\underline{a}_{v,hc}$, defined as the ratio of resonator output voltage $\underline{V}_{res}$ to the feedback input voltage $\underline{V}_{in}$ according to

$$\underline{a}_{v,hc} = \frac{\underline{V}_{res}}{\underline{V}_{in}}. \tag{3.65}$$

Since the $SRA_{dir,q}$ operates in the microwave frequency range, and also since the operation frequency f_{res} of $SRA_{dir,q}$ is around 10 times lower than transit frequency (f_t), the high frequency simplified equivalent circuit drawn in Fig. 3.20 is used for further analysis. As seen, the half cell circuit is a cascade of the CE amplifier input stage with voltage gain $\underline{a}_{v,1}(j\omega)$ and a CB amplifier with base feedback capacitor C_B, providing a transconductance $\underline{G}_{m,2}$. The output current $\underline{I}_{out}$ of the CB amplifier flows through the effective load of the resonator denoted by $\underline{Z}_{res}$, and the resulting half cell voltage gain is,

$$\underline{a}_{v,hc} = \underline{a}_{v,1}(j\omega) \cdot \underline{G}_{m,2} \cdot \underline{Z}_{res}. \tag{3.66}$$

The first parameter in the right hand side of (3.66) $\underline{a}_{v,1}(j\omega)$. From the simplified high frequency small signal equivalent circuit of Fig. 3.20, $\underline{a}_{v,1}(j\omega)$ can be written as,

$$\underline{a}_{v,1}(j\omega) = \frac{\underline{V}_{ce,1}}{\underline{V}_{in}} = \frac{-g_{m,1}\underline{V}_{be,1}(\underline{Z}_{o,1}||\underline{Z}_{in,2})}{\underline{V}_{in}}. \tag{3.67}$$

Where $g_{m,1}$ is the transconductance of the first stage HBT biased as a CE amplifier. The base to emitter voltage $\underline{V}_{be,1}$ is a potential divided version of the input signal $\underline{V}_{fb}$ according to

$$\underline{V}_{be,1} = \underline{V}_{in}\frac{C_k}{C_k + C_{in,1}} = \underline{V}_{in}\frac{1}{1 + K_{B,in}}, \tag{3.68}$$

where $K_{B,in} = C_{in,1}/C_k$ and $C_{in,1}$ is determined using the Miller relationship as,

$$C_{in,1} = C_{\pi,1} + (1 - a_{v,1}(0))C_{\mu,1}. \tag{3.69}$$

Again using the Miller relationship, the output impedance of the first stage amplifier $\underline{Z}_{\mathrm{o},1}$ is given by,

$$\underline{Z}_{\mathrm{o},1} = \frac{1}{j\omega(C_{\mathrm{o},1} + (1 - \frac{1}{a_{\mathrm{v},1}(0)})C_{\mu,1})}. \tag{3.70}$$

$\underline{Z}_{\mathrm{in},2}$ is the input impedance of the second stage HBT biased in the capacitive feedback CB topology, and is derived as,

$$\underline{Z}_{\mathrm{in},2} = \left(1 + \frac{C_{\pi,2}}{C_{\mathrm{B}} + C_{\mu,2}}\right) \frac{1}{g_{\mathrm{m},2} + j\omega\left[C_{\pi,2} + C_{\mathrm{o},2}\left(1 + \frac{C_{\pi,2}}{C_{\mathrm{B}}+C_{\mu,2}}\right)\right]}. \tag{3.71}$$

The detailed derivation of (3.71) using nodal analysis is given in Appendix A.

On defining the base feedback factor $\mathrm{K}_{\mathrm{B,fb}}$ as

$$\mathrm{K}_{\mathrm{B,fb}} = \frac{C_{\pi,2}}{C_{\mathrm{B}} + C_{\mu,2}}, \tag{3.72}$$

and multiplying the numerator and denominator of (3.71) with complex conjugate of the term in the denominator, the real and imaginary parts of (3.71) can be separated as

$$\begin{aligned}\underline{Z}_{\mathrm{in},2} = & \frac{(1 + \mathrm{K}_{\mathrm{B,fb}})g_{\mathrm{m},2}}{g_{\mathrm{m},2}^2 + \omega^2\left[C_{\pi,2} + C_{\mathrm{o},2}(1 + \mathrm{K}_{\mathrm{B,fb}})\right]^2} \\ & - j\omega\frac{(1 + \mathrm{K}_{\mathrm{B,fb}})\left[C_{\pi,2} + C_{\mathrm{o},2}(1 + \mathrm{K}_{\mathrm{B,fb}})\right]}{g_{\mathrm{m},2}^2 + \omega^2\left[C_{\pi,2} + C_{\mathrm{o},2}(1 + \mathrm{K}_{\mathrm{B,fb}})\right]^2}\end{aligned} \tag{3.73}$$

(3.71) clearly shows the effect of C_{B} on the input impedance of the stacked HBT. In a conventional cascode amplifier, $C_{\mathrm{B}} \gg C_{\pi,2}$, resulting in $K_{\mathrm{B,fb}} = 0$, and when $\omega = 0$, $\underline{Z}_{\mathrm{in},2}$ approximates to the familiar form of $1/g_{\mathrm{m},2}$. A plot of $\underline{Z}_{\mathrm{in},2}$ in Fig.xx shows the variation of the real and imaginary parts of $\underline{Z}_{\mathrm{in},2}$ for different C_{B} values and the corresponding simulations verifies the result.

Now, on substituting (3.67), (3.68) and (3.70) in (3.67), we get

$$\underline{a}_{\mathrm{v},1}(j\omega) = -g_{\mathrm{m},1}\frac{(1+\mathrm{K}_{\mathrm{B,fb}})}{(1+\mathrm{K}_{\mathrm{B,in}})} \cdot \frac{1}{g_{\mathrm{m},2} + j\omega\left[C_{\pi,2} + (1+\mathrm{K}_{\mathrm{B,fb}})(2C_{\mathrm{o}} + (1-\frac{1}{a_{\mathrm{v},1}(0)})C_{\mu,1})\right]} \tag{3.74}$$

(3.74) assumes identical output capacitor values for both HBTs, $C_{\mathrm{o},1} = C_{\mathrm{o},2} = C_{\mathrm{o}}$. By defining the imaginary part in the denominator as,

$$\mathrm{A} = C_{\pi,2} + (1+\mathrm{K}_{\mathrm{B,fb}})(2C_{\mathrm{o}} + (1-\frac{1}{a_{\mathrm{v},1}(0)})C_{\mu,1}), \tag{3.75}$$

(3.74) can also be written in a more tractable form as

$$\underline{a}_{\mathrm{v},1}(j\omega) = -g_{\mathrm{m},1}\frac{(1+\mathrm{K}_{\mathrm{B,fb}})}{(1+\mathrm{K}_{\mathrm{B,in}})} \cdot \frac{1}{g_{\mathrm{m},2} + j\omega\mathrm{A}}. \tag{3.76}$$

From (3.76), when $g_{\mathrm{m},1} \approx g_{\mathrm{m},2}$, $\mathrm{K}_{\mathrm{B,fb}} = 0$, $\mathrm{K}_{\mathrm{B,in}} = 0$ and $\omega = 0$, $\underline{a}_{\mathrm{v},1}(j\omega)$ approximates the familiar CE amplifier voltage gain $a_{\mathrm{v},1}(0) \approx -g_{\mathrm{m},1}/g_{\mathrm{m},2} \approx 1$, resulting in a very low output voltage swing at the collector of $\mathrm{T}_{1,3}$, and hence a non-symmetric distribution of the voltage swing across the $\mathrm{T}_{1,3}$ and $\mathrm{T}_{2,4}$.

However, in the stacked transistor CCO, there are two additional degree of freedoms to increase $\underline{Z}_{\mathrm{in},2}$ and $\underline{a}_{\mathrm{v},1}(j\omega)$.

- The first option is to choose C_{B} such that $C_{\mathrm{B}} \ll \frac{C_{\pi,2}}{g_{\mathrm{m},2}}$.
- The second option is dependent on the first option, and that is to have $\mathrm{K}_{\mathrm{B,fb}} \gg \mathrm{K}_{\mathrm{B,in}}$ to achieve a larger than unity $\underline{a}_{\mathrm{v},1}(j\omega)$ according to (3.74).

Both these options can be used to achieve a relatively larger voltage swing at node M, which can also be used as a design constraint and is given by,

$$\underline{V}_{\mathrm{ce},1} = |\underline{a}_{\mathrm{v},1}(j\omega)|\underline{V}_{\mathrm{in}} = \frac{\underline{V}_{\mathrm{res}}}{N_{\mathrm{stack}}}. \tag{3.77}$$

Also from (3.76), taking magnitude at right hand side (RHS) and left hand side (LHS), an expression to design and optimize C_{B} can be derived as

$$C_{\mathrm{B}} = \frac{g_{\mathrm{m},1}C_{\pi,2}}{\left[|\underline{a}_{\mathrm{v},1}(j\omega)|(1+\mathrm{K}_{\mathrm{B,in}})\sqrt{g_{\mathrm{m},2}^2 + \omega^2 A^2}\right] - g_{\mathrm{m},1}}. \tag{3.78}$$

The small signal model of the half cell in Fig. 3.20 treats the circuit as an amplifier. When the circuit functions as an oscillator according to the schematic

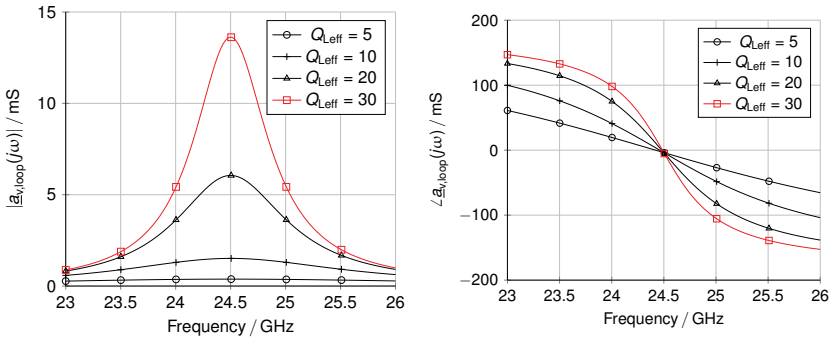

(a) (b)

Figure 3.21: (a) The magnitude of loop gain $|\underline{a}_{\mathrm{v,loop}}(j\omega)|$ and (b) phase of loop gain $\angle\underline{a}_{\mathrm{v,loop}}(j\omega)$ versus frequency for different inductor L_{eff} quality factor values.

of Fig. 3.17, in steady state $\underline{V}_{\mathrm{in}} = \underline{V}_{\mathrm{res}}$. Under this condition, using (3.77) and (3.78) a modified expression for C_{B} incorporating N_{stack} can be derived as

$$C_{\mathrm{B}} = \frac{g_{\mathrm{m},1} C_{\pi,2} N_{\mathrm{stack}}}{\left[(1+\mathrm{K}_{\mathrm{B,in}})\sqrt{g_{\mathrm{m},2}^2 + \omega^2 A^2}\right] - g_{\mathrm{m},1} N_{\mathrm{stack}}}. \tag{3.79}$$

The second parameter on the right hand side of (3.66), $\underline{a}_{\mathrm{v},1}(j\omega)$, is the transconductance $\underline{G}_{\mathrm{m},2}$ of the stacked HBTs $\mathrm{T}_{2,3}$. Using nodal analysis, we can derive $\underline{G}_{\mathrm{m},2}$ as

$$\underline{G}_{\mathrm{m},2} = \frac{\underline{I}_{\mathrm{res}}}{\underline{V}_{\mathrm{in}}} = \frac{g_{\mathrm{m},2}}{1+\mathrm{K}_{\mathrm{B,fb}}} + j\omega \frac{C_{\mu,2}\mathrm{K}_{\mathrm{B,fb}} + (1+\mathrm{K}_{\mathrm{B,fb}})C_{\mathrm{o},2}}{(1+\mathrm{K}_{\mathrm{B,fb}})}. \tag{3.80}$$

(3.80) is based on the detailed derivation in Appendix A, with the modification, $\underline{I}_{\mathrm{res}} = -\underline{I}_{\mathrm{out}}$ as required by the schematic in Fig. 3.20 to account for the direction of current flow. Also by defining the numerator of the imaginary part in (3.80) as

$$\mathrm{B} = C_{\mu,2}\mathrm{K}_{\mathrm{B,fb}} + (1+\mathrm{K}_{\mathrm{B,fb}})C_{\mathrm{o},2}, \tag{3.81}$$

and accounting for the direction of resonator output current direction, and (3.80) can be rewritten as,

$$\underline{G}_{\mathrm{m},2} = \frac{g_{\mathrm{m},2}}{1+\mathrm{K}_{\mathrm{B,fb}}} + j\omega \frac{B}{1+\mathrm{K}_{\mathrm{B,fb}}}. \tag{3.82}$$

The third parameter is $\underline{Z}_{\mathrm{res}}$ which is the effective impedance of the parallel RLC network described in section 1.

$$\underline{Z}_{\mathrm{res}} = \frac{j\omega R_{\mathrm{p}} L_{\mathrm{eff}}}{R_{\mathrm{p}}(1-\omega^2 L_{\mathrm{eff}} C_{\mathrm{eff}}) + j\omega L_{\mathrm{eff}}} \tag{3.83}$$

Now, substituting (3.76), (3.82) and (3.83) into (3.66), the cascaded half cell gain is obtained as

$$\underline{a}_{\mathrm{v,res}} = -\frac{g_{\mathrm{m,1}}}{(1+\mathrm{K_{B,in}})} \cdot \frac{g_{\mathrm{m,2}} + j\omega \mathrm{B}}{g_{\mathrm{m,2}} + j\omega \mathrm{A}} \cdot \frac{j\omega R_{\mathrm{p}} L_{\mathrm{eff}}}{R_{\mathrm{p}}(1-\omega^2 L_{\mathrm{eff}} C_{\mathrm{eff}}) + j\omega L_{\mathrm{eff}}}. \tag{3.84}$$

Assuming identical component parameters, and substituting $\underline{a}_{\mathrm{v,res}}$ from (3.84) in (3.64) yields the loop gain,

$$\underline{a}_{\mathrm{v,loop}}(j\omega) = \left[-\frac{g_{\mathrm{m,1}}}{(1+\mathrm{K_{B,in}})} \cdot \frac{g_{\mathrm{m,2}} + j\omega \mathrm{B}}{g_{\mathrm{m,2}} + j\omega \mathrm{A}} \cdot \frac{j\omega R_{\mathrm{p}} L_{\mathrm{eff}}}{R_{\mathrm{p}}(1-\omega^2 L_{\mathrm{eff}} C_{\mathrm{eff}}) + j\omega L_{\mathrm{eff}}}\right]^2. \tag{3.85}$$

Fig. 3.21(a) depicts the variation of $\underline{a}_{\mathrm{v,loop}}(j\omega)$ according to (3.85) for different values of L_{eff} quality factor, and is used to determine the optimum inductance to ensure sustained oscillations. Fig. 3.21(b) shows the plot of loop gain phase $\angle \underline{a}_{\mathrm{v,loop}}(j\omega_{\mathrm{res}})$ with a negative slope which is one of the necesary condition for sustained oscillations.

At resonance, $\omega = \omega_{\mathrm{res}}$, and $\omega_{\mathrm{res}}^2 L_{\mathrm{eff}} C_{\mathrm{eff}} = 1$, resulting in a real $\underline{Z}_{\mathrm{res}} = R_{\mathrm{p}}$. The corresponding maximum loop gain is

$$\underline{a}_{\mathrm{v,loop}}(j\omega_{\mathrm{res}}) = \left[\frac{g_{\mathrm{m,1}} R_{\mathrm{p}}}{(1+\mathrm{K_{B,in}})} \cdot \frac{g_{\mathrm{m,2}} + j\omega_{\mathrm{res}} \mathrm{B}}{g_{\mathrm{m,2}} + j\omega_{\mathrm{res}} \mathrm{A}}\right]^2. \tag{3.86}$$

$|\underline{a}_{\mathrm{v,loop}}(j\omega_{\mathrm{res}})|$ is designed to be greater than one for sustained oscillations according to Barkhausen criterion for oscillations [Voi13, Ell07]. Also the phase shift around the loop, $\angle \underline{a}_{\mathrm{v,loop}}(j\omega_{\mathrm{res}})$ is also designed to be an integer multiple of 2π.

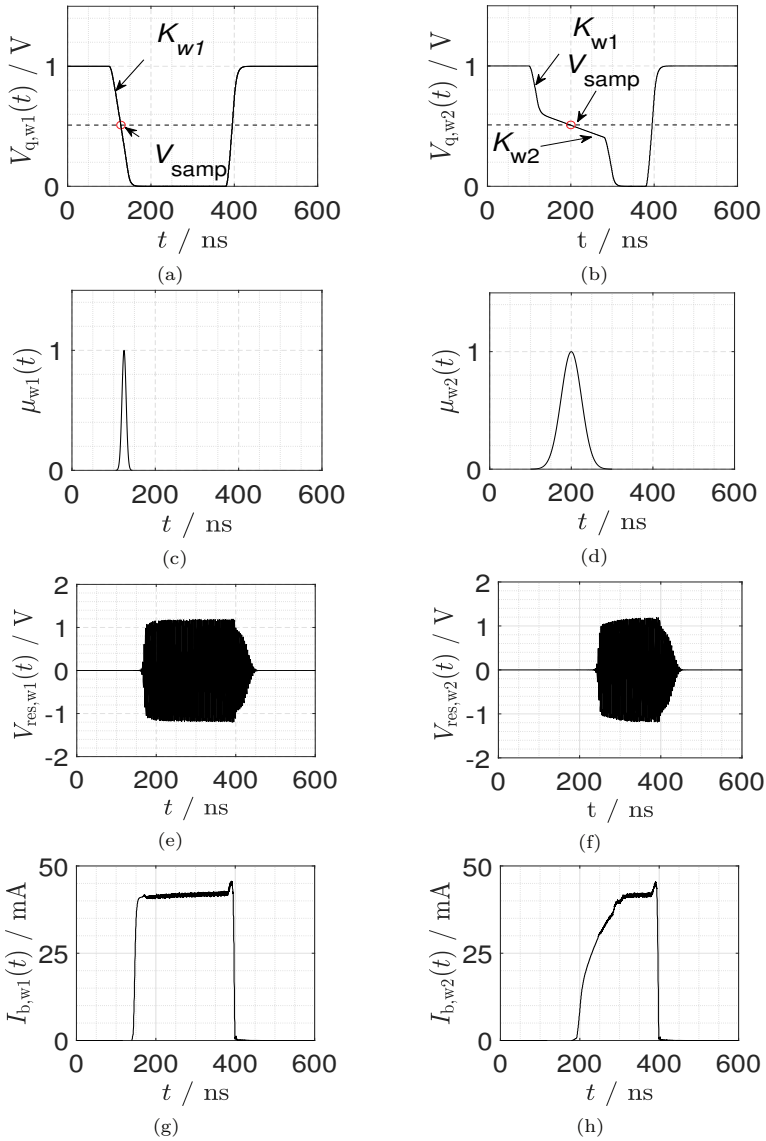

Figure 3.22: Modeled signal characteristics: (a) quench signal $V_{q,w1}(t)$, (c) normalized sensitivity curve $\mu_{w1}(t)$, (e) SRA output voltage $V_{res,w1}$ and (g) bias current $I_{b,w1}$. (b) quench signal $V_{q,w2}$, (d) normalized sensitivity curve $\mu_{w2}(t)$, (f) SRA output oscillations $V_{res,w2}$ and (h) bias current $I_{b,w2}$. (Adapted from *[TLJE18] ©2018 IEEE)

3.2.2.2 Quench Waveform Design

The SRA based ranging described in Section 3.1.1 uses the characteristics of the SRA in the step-controlled mode described in Section 2.6.2. However, the linear slope-controlled mode described in Section 2.6.2 is better for sensitivity [Whi50, BMCD09]. This difference can be understood by analyzing the characteristics of the quench signal waveform $V_{\mathrm{q,w1}}(t)$(t) illustrated in Fig. 3.22(a) which is applied at the gate of M_1 in Fig. 3.17 and its effect on the sensitivity. In Fig. 3.22(a) and the rest of the illustrations in Fig. 3.22, only a single quench cycle is considered. However, when operating as SRT, periodic quench bursts have to be generated with quench period T_{q} so that, $T_{\mathrm{samp}} = pT_{\mathrm{q}}$, where $p = 0, 1, 2, ..N_{\mathrm{burst}}$, where N_{burst} is the number of quench cycles in a given quench burst. The impact of the $V_{\mathrm{q,w1}}(t)$ on sensitivity can be visualized by revisiting the normalized Gaussian sensitivity window function $\mu(t)$ defined in (2.33) from [BMCD09], and including the parameters specific to $V_{\mathrm{q,w1}}(t)$ as

$$\mu(t) = e^{-\frac{1}{2}\frac{(t-T_{\mathrm{samp}})^2}{t_\sigma^2}} \tag{3.87}$$

where t_σ is defined as the SRA time constant given by

$$t_\sigma = \frac{\sqrt{\delta V_{\mathrm{q,w1}}(t)}}{\sqrt{\omega_{\mathrm{osc}} k_{\mathrm{w,1}}}} \tag{3.88}$$

where k_{w1} is the negative slope of the falling edge quench waveform $V_{\mathrm{q,w1}}(t)$ at time T_{samp} with units Vs^{-1} and is defined as

$$k_{\mathrm{w1}} = -\frac{dV_{\mathrm{q,w1}}}{dt}, \tag{3.89}$$

and holds the relationship with k_{q} as

$$k_{\mathrm{q}} = k_{\mathrm{w1}} \cdot \frac{1}{dV} \tag{3.90}$$

so that the quenching function $\zeta(t) = -k_{\mathrm{q}}t$ is unit less and with a negative slope. It can be deduced from (3.87) that an increase in t_σ as result of a decrease in quench signal slope K_{w1} broadens the $\mu(t)$. It is also known from [BMCD09, Whi50] that a broadening of $\mu(t)$ results in an increase in the number of input signal cycles within the Gaussian sensitivity window, and thereby results in increased SRA sensitivity. Also from (2.33) it can then be deduced that a larger k_{q} worsens sensitivity. On the other hand, (2.34) tells that a larger k_{q} and longer $T_{\mathrm{q,on}}$ is required for higher regenerative gain. But a longer $T_{\mathrm{q,on}}$ also reduces the

range and resolution of the SRA based reflector as discussed in Section 3.1.1. It can also be deduced from (2.33) that the magnitude of $\mu(t)$ is almost zero outside $T_{\text{samp}} \pm 3t_\sigma$ based on the characteristics of the Gaussian function [Kay93].

This knowledge of the quench signal characteristics of the step- and slope-controlled modes can be combined with (2.34) to design a dual slope quenching signal waveform $V_{\text{q,w2}}(t)$ that has a large slope k_{w1} outside the sensitivity time window for higher regenerative gain at the start and finish of each quench cycle similar to that for waveform $V_{\text{q,w1}}$. $V_{\text{q,w2}}(t)$ also has a smaller quench voltage slope k_{w2} within the time window $T_{\text{samp}} \pm 3t_\sigma$ *[TLJE18] as illustrated in Fig. 3.22(b). The designed dual slope quench waveform $V_{\text{q,w2}}(t)$ can hence be defined as

$$V_{\text{q,w2}}(t) = \begin{cases} -K_{\text{w1}} \cdot t & \text{if } |t - T_{\text{samp}}| > 3t_\sigma \\ -K_{\text{w2}} \cdot t & \text{if } |t - T_{\text{samp}}| \leq 3t_\sigma \ . \end{cases} \tag{3.91}$$

Such a waveform simultaneously widens the sensitivity window, and increases the peak regenerative gain $A_{\text{r}}(T_{\text{q,on}})$. Also $V_{\text{q,w2}}(t)$ improves the minimum input power level $P_{\text{min,dBm}}$ required for phase coherent amplification while maintaining a high quench f_{q} similar to that of step-controlled mode.

Fig. 3.22(c) and Fig. 3.22(d) illustrates the broadening of $\mu(t)$ between $V_{\text{q,w1}}(t)$ and $V_{\text{q,w2}}(t)$ with $K_{\text{w2}} = 0.04 \cdot K_{\text{w1}}$. Fig. 3.22(e) and Fig. 3.22(f) shows the corresponding SRA output voltage from simulations. Fig. 3.22(g) and Fig. 3.22(h) shows the respective simulated bias current characteristics $I_{\text{b,w1}}(t)$ and $I_{\text{b,w2}}(t)$.

Using the information from (3.91), a circuit level implementation to pulse shape a square wave similar signal V_{w1}(t) and transform it to an approximation of V_{w2}(t) is designed and integrated into SRA_{dir} to create $\text{SRA}_{\text{dir,q}}$ as shown in the schematic of Fig. 3.23. Section 4.2.2.1 describes the design details of the dual slope quench pulse shaping circuit, which reduces k_{w2} around T_{samp}, improving sensitivity, while keeping $T_{\text{q,on}}$ relatively short. The pulse shaping is implemented using two additional nFETs $\text{M}_{2,3}$ and capacitors $C_{\text{q},1,2}$.

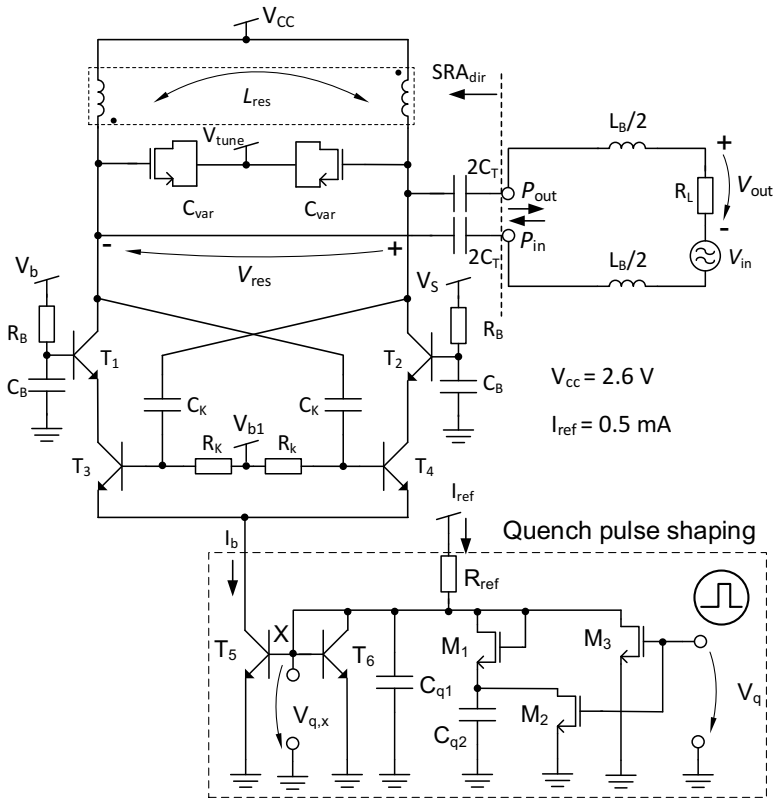

Figure 3.23: Schematic of the direct antenna interface $SRA_{dir,q}$ with integrated quench pulse shaping. (Adapted from *[TFJE23] ©2023 IET).

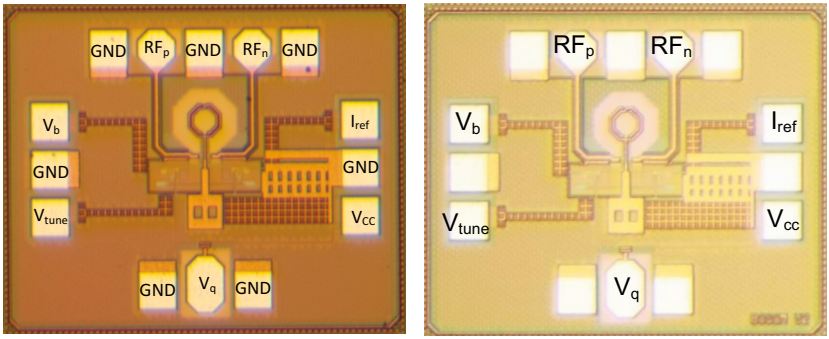

(a) (b)

Figure 3.24: Implemented direct drive SRA ICs in a 130 nm SiGe BiCMOS technology measuring 875 µm × 725 µm including pads, and having the same footprint: (a) SRA_{dir} (reused from [TLJE18] ©2018 IEEE) (b) $SRA_{dir,q}$ with integrated quench pulse shaping

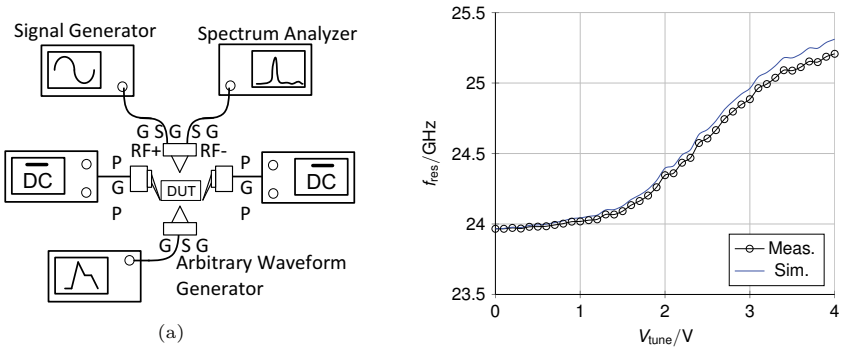

(a) (b)

Figure 3.25: (a) Illustration of the characterization setup. (b) Resonator frequency versus tuning voltage. (reused from [TLJE18] ©2018 IEEE)

3.2.2.3 Characterization

To prove the proposed $\mathrm{SRA_{dir}}$ and $\mathrm{SRA_{dir,q}}$ concept, ICs were implemented and experimental characterization is performed. The ICs shown in the micrograph of Fig. 3.24 are fabricated in a 130 nm SiGe-BiCMOS technology, and characterized by micro probing. Since time domain measurements of regenerative sampling is not practical at the frequencies of interest, frequency domain characterization is done as described in [SCW+13b]. Parameters including f_{res}, $P_{\mathrm{out,dBm}}$, $P_{\mathrm{min,dBm}}$ and bandwidth are characterized using the test setup consisting of a Rohde & Schwarz® 67 GHz spectrum analyzer, Keysight® 8257D RF power source, and an arbitrary waveform generator for quench generation as shown in Fig. 3.25(a).

At first for each IC, the SRA is powered ON with quench signal $V_q = 0\,\mathrm{V}$ to measure the free-running oscillation frequency f_{res} as 25.3 GHz for $\mathrm{SRA_{dir}}$ and 24.5 GHz for $\mathrm{SRA_{dir,q}}$ respectively. The DC power consumption is measured as $P_{\mathrm{DC}} \approx 110\,\mathrm{mW}$ for both ICs. V_{q} is then manually decreased from $V_q = 1\,\mathrm{V}$ corresponding to no oscillations, until $V_{\mathrm{q}} = V_{\mathrm{samp}} \approx 670\,\mathrm{mV}$, where V_{samp} is the voltage at which oscillations just begin to start. For $\mathrm{SRA_{dir}}$, an arbitrary waveform generator is used to shape the quench signal similar to $V_{\mathrm{q,w2}}$ and sourced with the input signal present. The corresponding *sinc* spectrum envelope, $P_{\mathrm{env,dBm}}$ with Dirac delta spectral peaks separated by the quench frequency [SCW+13b], indicating phase coherence as shown in Fig. 3.26(a) is then measured. A plot of the maximum of this spectral envelope $P_{\mathrm{env,max,dBm}}$, when $P_{\mathrm{in,dBm}}$ is varied is

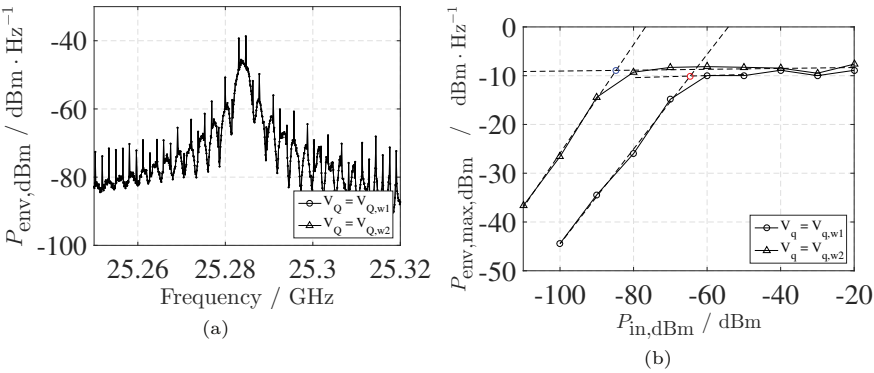

Figure 3.26: (a) Measured power spectral density with $P_{\mathrm{in,dBm}} = -100\,\mathrm{dBm}$ at $f_{\mathrm{res}} = 25.3\,\mathrm{GHz}$. (b) Plot of $P_{\mathrm{out,dBm}}$ against $P_{\mathrm{in,dBm}}$ for quench signals $V_{\mathrm{q,w1}}$ and $V_{\mathrm{q,w2}}$. (reused from *[TLJE18] © 2018 IEEE)

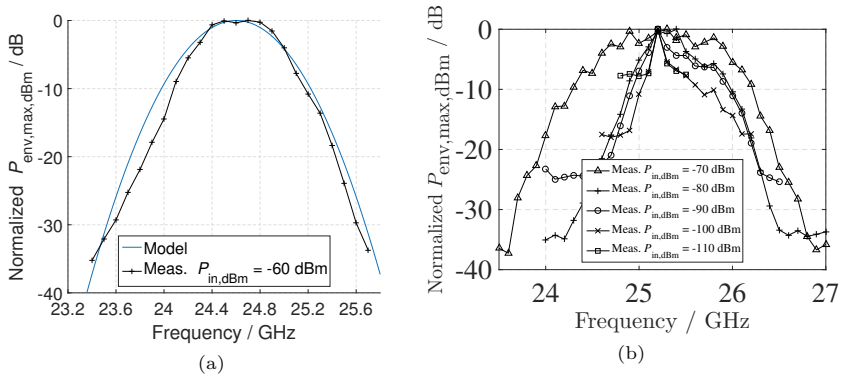

Figure 3.27: Normalized frequency response: (a) Comparison of measurement and model. (b) Characterization results at different input power levels. (reused from [TLJE18] ©2018 IEEE)

shown in Fig. 3.26(b). $V_{\text{q,w2}}$ is designed to have a $T_{\text{q,on}} \approx 180\,\text{ns}$ and a period $T_{\text{q}} \approx 600\,\text{ns}$, resulting in an average power consumption of 38 mW. The maximum quench signal frequency that can be used is 4.5 MHz. From Fig. 3.26(b), it is seen that with $V_{\text{q,w1}}$, $P_{\text{min,dBm}} = -100\,\text{dBm}$ and for $V_{\text{q,w2}}$, $P_{\text{min,dBm}} = -110\,\text{dBm}$. The slope of the curve at low input power level $P_{\text{in,dBm}}$ gives the linear mode super-regenerative gain of 66 dB with $V_{\text{q,w1}}$ and 85 dB with $V_{\text{q,w2}}$.

For higher values of $P_{\text{in,dBm}}$, the circuit enters the logarithmic mode and gain compression occurs for $P_{\text{in,dBm}} > P_{\text{i,N,dBm}}$. The parameter, $P_{\text{i,N,dBm}}$ denotes the input power level corresponding to the linear to logarithmic mode transition as described in Section 2.6.2. From the measurement data, $P_{\text{i,N,dBm}}$ is calculated as the intersection of the two extrapolated lines in Fig. 3.26(b). For $V_{\text{q,w1}}$, $P_{\text{i,N,dBm}} = -65\,\text{dBm}$, and with $V_{\text{q,w2}}$, $P_{\text{i,N,dBm}} = -85\,\text{dBm}$, clearly showing the advantage of $V_{\text{q,w2}}$. Bandwidth of the circuit is also an important parameter for LFMCW radar based interrogator as ranging resolution is directly proportional to bandwidth. The normalized frequency response when input frequency is swept over a range of values around f_{res} is shown in Fig. 3.16(b), indicating a bandwidth increase with increased input signal power. A bandwidth of at least 500 MHz is available for $P_{\text{in,dBm}}$ greater than $-90\,\text{dBm}$ as seen in Fig. 3.16(b).

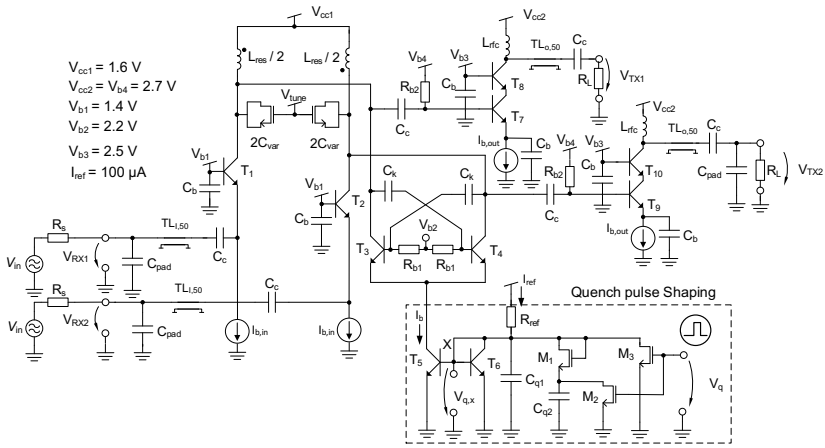

Figure 3.28: Schematic of buffered antenna interface $\mathrm{SRA_{buf,q}}$ including quench pulse shaping circuit (Adapted from *[TJE20] ©2020 IEEE).

3.2.3 Antenna Diversity SiGe SRA IC with Integrated Quench Pulse Shaping

In this section, a buffered antenna drive SiGe SRA with integrated quench pulse shaping ($\mathrm{SRA_{buf,q}}$) *[TJE20] is designed with the following features:

- Input and output buffers for better input port and output port matching and to reduce f_{res} the sensitivity to the source and load impedance variations.
- Four single ended ports or two differential ports to enable the implementation of spatial diversity SRTs.
- Integrated quench pulse shaping circuit.

3.2.3.1 Circuit Analysis and Design

The schematic of the $\mathrm{SRA_{buf,q}}$ is shown in Fig. 3.28. Drawing parallels between the generic SRA model already described in Fig. 2.14(a) and the $\mathrm{SRA_{buf,q}}$ schematic in Fig. 3.28, the resonant core consists of inductor L_{res}. The capacitance C_{res} can be calculated from the $\mathrm{SRA_{buf,q}}$ small signal model depicted in Fig. 3.29 as

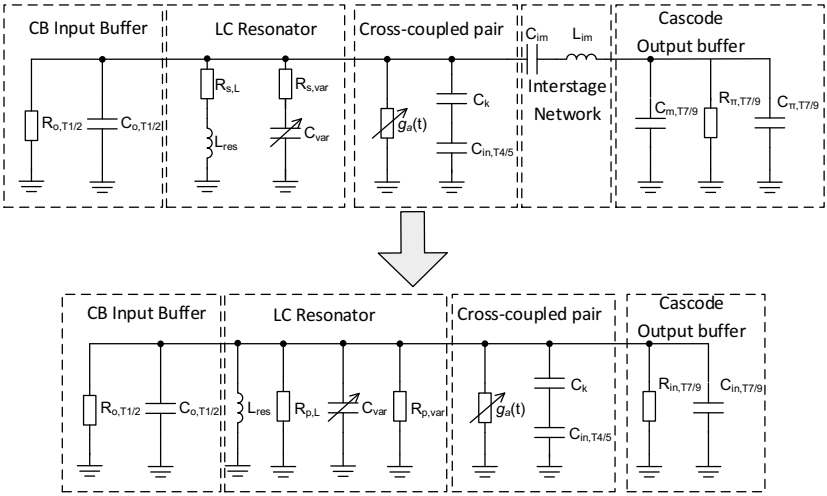

Figure 3.29: $\mathrm{SRA_{buf,q}}$ small signal equivalent circuits used for analysis.

$$C_{\mathrm{res}}(V_{\mathrm{tune}}) = C_{\mathrm{var}}(V_{\mathrm{tune}}) + C_{\mathrm{par}}, \tag{3.92}$$

with

$$\begin{aligned} C_{\mathrm{par}} &= C_{\mathrm{cb,T1/2}} + C_{\mathrm{ce,T1/2}} \\ &+ \frac{C_{\mathrm{k}} C_{\mathrm{in,T3/4}}}{C_{\mathrm{k}} + C_{\mathrm{in,T3/4}}} + \frac{C_{\mathrm{c}} C_{\mathrm{in,T7/9}}}{C_{\mathrm{c}} + C_{\mathrm{in,T7/9}}}, \end{aligned} \tag{3.93}$$

where, $C_{\mathrm{cb,T1/2}}$ and $C_{\mathrm{ce,T1/2}}$ are the collector-base and collector-emitter capacitance of HBTs $T_{1/2}$ respectively. C_{var} is a function of V_{tune}, and represents the capacitance of the thick oxide NMOS varactors. The resonant frequency can then be determined as

$$f_{\mathrm{res}} = \frac{1}{2\,\pi\,\sqrt{L_{\mathrm{res}}(C_{\mathrm{par}} + C_{\mathrm{var}}(V_{\mathrm{tune}}))}}. \tag{3.94}$$

The fixed loss conductance G_{P} in Fig. 2.14(a), is the combination of the losses in L_{res}, C_{var} and the real part of the output admittance of the common-base input stage transistors $r_{\mathrm{o,T1/2}}$, and input impedance of the output stage transistors

$T_{7,9}$, which can be calculated as

$$G_{\mathrm{p}} = \frac{C_{\mathrm{res}}(V_{\mathrm{tune}})\omega_{\mathrm{res}}}{Q_{\mathrm{res}}(V_{\mathrm{tune}})} + \frac{1}{r_{\mathrm{in,T7/9}}} + \frac{1}{r_{\mathrm{o,T1/2}}}. \tag{3.95}$$

where, $\omega_{\mathrm{res}} = 2\pi f_{\mathrm{res}}$. Hence,

$$G_{\mathrm{p}} = \frac{1}{Q_{\mathrm{ul}}\omega_{\mathrm{res}}L_{\mathrm{res}}} + \frac{1}{r_{\mathrm{o,T1/2}}} + \frac{1}{r_{\mathrm{in,T7/9}}}. \tag{3.96}$$

To implement the resonator, a symmetrical octogonal inductor is designed and optimized to obtain an L_{res} in the hundred pico Henry range and an unloaded quality factor $Q_{\mathrm{ul}} \approx 21$ and an equivalent parallel resistance $R_{\mathrm{p,L}}$ around nine times the load resistance at 25 GHz. From post layout extraction simulations, the fixed parasitic capacitance C_{par} in the hundred femto Farad range is obtained. The varactors are dimensioned for a $C_{\mathrm{var,max}}/C_{\mathrm{var,min}} \approx 2.45$ resulting in an f_{res} covering the 24 GHz ISM band according to (3.94). The varactor quality factor is also not negligible at K-band frequencies, and varies with a ratio $Q_{\mathrm{var,max}}/Q_{\mathrm{var,min}} \approx 2.79$ when V_{tune} is varied from $V_{\mathrm{tune,min}} = 0\,\mathrm{V}$ to $V_{\mathrm{tune,max}} = 4\,\mathrm{V}$. Both the varactor capacitance and quality factor variation with V_{tune} can be modeled approximately using the hyperbolic tangent function from [KG95]

$$C_{\mathrm{var}}(V_{\mathrm{tune}}) = C_{\mathrm{var,mid}}\left(1 + \frac{2\tanh(V_{\mathrm{tune,mid}} - V_{\mathrm{tune}})}{V_{\mathrm{tune,max}} - V_{\mathrm{tune,min}}}\right), \tag{3.97}$$

where $C_{\mathrm{var,mid}} = (C_{\mathrm{var,max}} + C_{\mathrm{var,min}})/2$ and $V_{\mathrm{tune,mid}} = (V_{\mathrm{tune,max}} + V_{\mathrm{tune,min}})/2$. Similarly, the varactor quality factor Q_{var} can be modeled according to [KG95] as

$$Q_{\mathrm{var}}(V_{\mathrm{tune}}) = Q_{\mathrm{var,mid}}\left(1 + \frac{2\tanh(V_{\mathrm{tune}} - V_{\mathrm{tune,mid}})}{V_{\mathrm{tune,max}} - V_{\mathrm{tune,min}}}\right), \tag{3.98}$$

where $Q_{\mathrm{var,mid}} = (Q_{\mathrm{var,max}} + Q_{\mathrm{var,min}})/2$.

From small signal simulations using the VBIC model of the HBTs, the equivalent resistance at the input of the output buffer $r_{\mathrm{in,T7/9}}$ is determined to be in the sub 1 kΩ range and at the output of the input buffer is $r_{\mathrm{o,T1/2}}$ around 10 times $r_{\mathrm{in,T7/9}}$. The respective equivalent parallel capacitances fall in the sub 50 femtofarad range with a ratio of $C_{\mathrm{in,T1/2}}/C_{\mathrm{o,T7/9}} \approx 4.5$. This enables to approximate

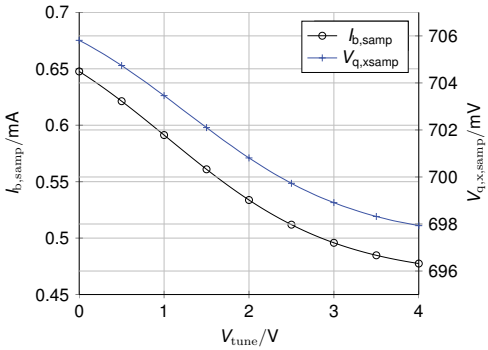

Figure 3.30: Plot of $I_{\mathrm{b,samp}}$ and $V_{\mathrm{q,x,samp}}$ as a function of varactor tuning voltage V_{tune}.

G_{p} as

$$G_{\mathrm{p}} \approx \frac{C_{\mathrm{res}}(V_{\mathrm{tune}})\omega_{\mathrm{res}}}{Q_{\mathrm{res}}(V_{\mathrm{tune}})} + \frac{1}{r_{\mathrm{in,T7/9}}}. \tag{3.99}$$

3.2.3.1.1 Crosscoupled Pair and Sampling Current The controlled transonductance $g_{\mathrm{a}}(t)$ in the equivalent circuit of Fig. 2.14(a), is implemented using the cross-coupled HBT pair $T_{3,4}$ in the schematic Fig. 3.28. The time variant input admittance, when looking into the collector of $T_{3,4}$ is calculated according to [Lee03] as

$$g_{\mathrm{a}}(t) = \frac{-g_{m,T_{3/4}}(t)}{2}\,. \tag{3.100}$$

Since $g_{m,T_{3/4}}$ is directly proportional to the collector current $I_{\mathrm{c,T3/4}}(t)$ [Lee03], and the tail current through HBT T_5 sets the total bias current $I_{\mathrm{b}}(t) = 2I_{\mathrm{c,T3/4}}(t)$, then

$$g_{m,T_{3/4}}(t) \approx \frac{I_{\mathrm{b}}(t)}{2V_{\mathrm{T}}}\,. \tag{3.101}$$

where V_{T} is the thermal voltage. Also, from (2.22), the phase coherent sampling of the input signal occurs at the sampling time T_{samp} when,

$$G_{\mathrm{p}} + g_{\mathrm{a}}(t = T_{\mathrm{samp}}) = 0\,. \tag{3.102}$$

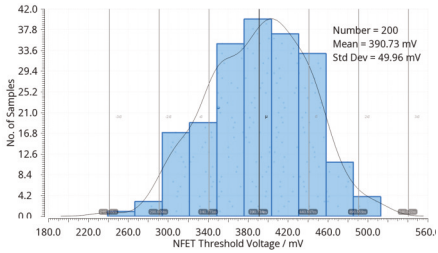

Figure 3.31: Monte Carlo simulation results for 200 iterations showing the variation of $V_{\mathrm{th,M1}}$.

Inserting (3.100) and (3.102) into (3.101), the corresponding bias current can be derived as,

$$I_{\mathrm{b}}(t = T_{\mathrm{samp}}) = I_{\mathrm{b,samp}} \approx 4V_{\mathrm{T}}G_{\mathrm{P}}\,. \tag{3.103}$$

Now, inserting G_{p} from (3.99) into (3.103), an approximate expression for the collector current through T_5, $I_{\mathrm{b,samp}}$ can be derived as,

$$I_{\mathrm{b,samp}}(V_{\mathrm{tune}}) \approx 4V_{\mathrm{T}}\left(\frac{\omega_{\mathrm{res}}C_{\mathrm{res}}(V_{\mathrm{tune}})}{Q_{\mathrm{res}}(V_{\mathrm{tune}})} + \frac{1}{r_{\mathrm{in,T7/9}}}\right). \tag{3.104}$$

It should be noted that the varactor capacitance and V_{tune} have an inverse relationship; an increase in V_{tune} reduces $I_{\mathrm{b,samp}}$ and vice-versa, as shown in the plot of Fig. 3.30.

Now, substituting the base voltage and collector current from the Ebers-Moll model approximation for HBT T_5, with forward common emitter current gain β_{F}, and reverse saturation current I_{s} in (3.104), the corresponding expression for $V_{\mathrm{qx,samp}}$ is obtained as,

$$V_{\mathrm{q,x,samp}} \approx V_{\mathrm{T}}\ln\left(\frac{4V_{\mathrm{T}}}{\beta_{\mathrm{F}}I_{\mathrm{s}}}\left(\frac{\omega_{\mathrm{res}}C_{\mathrm{res}}(V_{\mathrm{tune}})}{Q_{\mathrm{res}}(V_{\mathrm{tune}})} + \frac{1}{r_{\mathrm{in,T7/9}}}\right)\right). \tag{3.105}$$

As depicted in Fig. 3.30, $I_{\mathrm{b,samp}}$ varies by around 170 µA and $V_{\mathrm{q,x,samp}}$ only by around 10 mV for a V_{tune} variation from 0 to 4 V, corresponding to the tunable frequency range.

3.2.3.1.2 Common Base Input Stage The input stage consists of HBTs $\mathrm{T}_{1,2}$, biased as common base amplifiers. Bias currents $I_{\mathrm{b,in}} \approx 600\,\mu\mathrm{A}$ are set by current

mirrors so that the transconductance of $T_{1,2}$, $g_{m,1,2} \approx 1/R_s$, and the input impedance $\underline{Z}_{in,1\text{-}2} \approx 1/g_{m,1\text{-}2}$ across the bandwidth of interest. The capacitors $C_c = 1/(\omega_l R_s)$ at the input limits the lower cut off frequency $\omega_l/2\pi$ to around 15 GHz and also functions as a DC block. The frequency dependency of the input impedance, when looking from the emitter of $T_{1,2}$, can be analyzed using the transfer function derived as

$$A_{v,in}(s) = \frac{sC_c}{L_T C_{pad} C_m s^3 + (g_m L_T C_{pad} + R_s C_m C_{pad}) s^2}. \tag{3.106}$$

(3.106) includes the effect of probe pad capacitance C_{pad}, the input current mirror capacitances C_m, the DC block capacitance C_c, and an inductance approximation L_T of the transmission lines $TL_{o,50}$ for a small range of frequencies around the resonant frequency [HEKS10].

3.2.3.1.3 Cascode Output Stage The power generated at the resonator core is delivered into a load resistance $R_L = 50\,\Omega$ by two cascode amplifiers formed by $T_{7\text{-}10}$, biased at $I_{b,out} \approx 25\,mA$. The impedance transfer network with unity transformation ratio is formed by the parasitic capacitors of $T_{8,10}$ in combination with 320 µm long grounded coplanar waveguide (GCPW) transmission lines $TL_{o,50}$, with a characteristic impedance of $50\,\Omega$. A peak to peak voltage swing $V_{TX,1,2,pp} \approx 1.6\,V$ generates an output power $P_{TX,1,2} = V_{TX,1,2,pp}^2/(8R_L) \approx 6.5\,mW$ or 8 dBm. The output amplifiers are designed with DC block capacitors, optimized to minimize the loading of the oscillator core.

In order to simultaneously improve the sensitivity and output power of the SRA, a two slope piece wise linear implementation quench pulse shaping is implemented using nFETs $M_{1\text{-}3}$, HBT T_6 and capacitors $C_{q,1\text{-}2}$. The circuit takes advantage of the difference in threshold voltage values of the diode connected nFET M_1 and HBT T_6, and is similar to our implementation in *[TJE20]. The quench pulse shaping also enables SRA to be used with commercial clock and pulse width modulation ICs having CMOS or TTL output voltage swings.

3.2.3.1.4 Quench Pulse Shaping Circuit In the schematics of Fig. 3.28 and Fig. 3.23, when $V_{q,x}(t)$ is a linearly increasing ramp given by $V_{q,x}(t) = k_w t$, the bias current I_b flowing through T_5 can be written as,

$$I_b(t) = I_{c,\,T_5}(t) \approx \beta_F I_s e^{\frac{k_w t}{V_T}} \quad . \tag{3.107}$$

(3.107) shows that I_b and hence g_m is an exponentially increasing function with time. Also the ideal $V_{q,x}(t)$ for linear control of $I_b(t)$ is a logarithmic function of

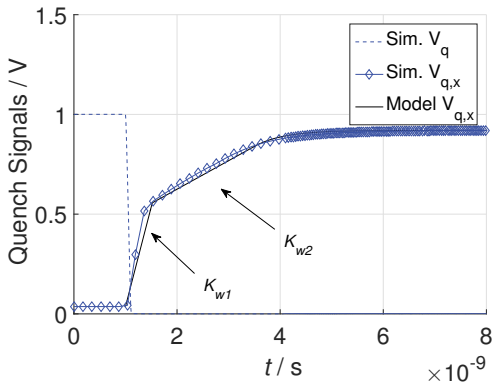

Figure 3.32: Model and simulation of shaped quench signal (reused from *[TJE20] ©2020 IEEE).

time. Since a logarithmic amplifier could be power hungry, at higher switching speeds, a simpler solution can be obtained by linearizing $I_\mathrm{b}(t)$ around T_samp. This is a valid assumption because according to (2.33), regenerative sampling sensitivity is maximum around T_samp. And the slope of I_b near $I_\mathrm{b,samp}$ is relevant. This slope can be evaluated by doing the Taylor series expansion of $I_\mathrm{b}(t)$ at T_samp. T_samp can be written as

$$T_\mathrm{samp} = \frac{V_\mathrm{T}}{k_\mathrm{w}} \ln \frac{I_\mathrm{b,samp}(V_\mathrm{tune})}{\beta_\mathrm{F} I_\mathrm{s}} \quad . \tag{3.108}$$

and the Taylor series approximation of (3.107) for the first two terms can be written as

$$I_\mathrm{b,T}(t) = \beta_\mathrm{F} I_\mathrm{s} e^{\frac{k_\mathrm{w} T_\mathrm{samp}}{V_\mathrm{T}}} + \frac{\beta_\mathrm{F} I_\mathrm{s}}{V_\mathrm{T}} e^{\frac{k_\mathrm{w} T_\mathrm{samp}}{V_\mathrm{T}}} (t - T_\mathrm{samp}) \,. \tag{3.109}$$

The slope term in the linear equation described by (3.109) helps to optimize the sensitivity of the SRA by reducing k_w. But from (2.34), it is clear that this reduces the peak regenerative gain $A_\mathrm{r}(T_\mathrm{q,on})$. This means that for low values of k_w, a higher quench time $T_\mathrm{q,on}$ is needed to generate the same output voltage. This puts a limit on the maximum possible quench frequency, translating to low data rates in communication systems [MPM05] and low range in radar systems according to (3.18).

Because sensitivity is relevant only around T_samp, and the regenerative gain

$A_{\mathrm{r}}(t)$ peaks at $T_{\mathrm{q,on}}$, a two slope piece-wise linear function is an ideal quench waveform candidate, as proposed in *[TLJE18]. The two slope piece-wise linear function is integrated using a low power pulse shaping circuit, taking advantage, of the difference in threshold voltage values for nFET and HBT simultaneously available in BiCMOS technologies. The quench pulse shaping also enables SRA to be used with off-the-shelf clock and pulse width modulation ICs having CMOS or TTL output voltage swings.

In the schematic of Fig. 3.28 and Fig. 3.23, when $V_{\mathrm{q}}(t) = 1\,\mathrm{V}$, $\mathrm{M}_{2,3}$ are in saturation, the node voltage $V_{\mathrm{q,x}}(t) = 0\,\mathrm{V}$, no current flows through T_5, and there is no oscillation. When $V_{\mathrm{q}}(\mathrm{t})$ is a pulse falling from 1 V to 0 V as shown in Fig. 3.32, the reference current I_{ref} charges C_{q1} with the slope K_{w1}. $V_{\mathrm{q,x}}(t)$ can then be written as,

$$V_{\mathrm{q,x}}(t) = K_{\mathrm{w1}} t = \frac{I_{\mathrm{ref}}}{C_{\mathrm{q1}}} t \qquad 0 \leq t \leq T_{\mathrm{samp}}\,. \tag{3.110}$$

As seen in Fig. 3.32, the linear increase of $V_{\mathrm{q,x}}(t)$ according to (3.110), occurs until $V_{\mathrm{q,x}}(t) = V_{\mathrm{th,M1}}$. Here $V_{\mathrm{th,M1}}$ is the threshold voltage of the diode-connected nFET M_1 in Fig. 3.28 and Fig. 3.23. The corresponding time is, $T_{\mathrm{samp}} = V_{\mathrm{th,M1,max}} \cdot C_{\mathrm{q1}}/I_{\mathrm{ref}}$. Monte Carlo simulation results of $V_{\mathrm{th,M1}}$, depicted in Fig. 3.31, show that $V_{\mathrm{th,M1}}$ varies from 255 mV to 520 mV with typical $V_{\mathrm{th,M1}}$ of around 400 mV. The slowest T_{trig} and best case sensitivity is when $V_{\mathrm{th,M1}} \approx 520\,\mathrm{mV}$. The fastest T_{trig} corresponding to worst case sensitivity is when $V_{\mathrm{th,M1}} \approx 255\,\mathrm{mV}$. For time $t > T_{\mathrm{trig}}$, diode connected M_1 enters triode region, so that both C_{q1} and C_{q2} are connected to node X. Now, $V_{\mathrm{q,x}}$ has a new slope,

$$V_{\mathrm{q,x}}(t) = K_{\mathrm{w2}} t = \frac{I_{\mathrm{ref}}}{C_{\mathrm{q1}} + C_{\mathrm{q2}}} t \qquad T_{\mathrm{trig}} \leq t \leq T_{\mathrm{q,on}}\,. \tag{3.111}$$

Now, $V_{\mathrm{q,x}}(t)$ increases till the threshold voltage of the diode-connected HBT T_6, $V_{\mathrm{D,T6}} \approx 0.9\,\mathrm{V}$, and eventually saturates as shown in Fig. 3.32. The quench pulse shaping circuit is implemented using MIM capacitors in the hundreds of femto Farads range with a $C_{\mathrm{q2}}/C_{\mathrm{q1}} \approx 6$, and $I_{\mathrm{ref}} = 100\,\mu\mathrm{A}$. nFET M_2 is used to keep C_{q2} discharged at the beginning of each quench cycle.

The same quench circuit also operates in a voltage controlled mode, when instead of I_{ref}, a voltage reference V_{ref} is used. Here, when $V_{\mathrm{q}}(t)$ is switching, $V_{\mathrm{q,x}}(t)$ rises due to exponential charging of $C_{\mathrm{q,1}}$ through R_{ref}. Since at the end of each cycle, M_3 goes into saturation and completely discharges $C_{\mathrm{q,1}}$, $V_{\mathrm{q,x}}(t)$ can be

written as,

$$\begin{aligned} V_{\mathrm{q,x}}(t) &= V_{\mathrm{ref}}(1 - e^{\frac{-t}{R_{\mathrm{ref}}C_{\mathrm{q,1}}}}) \qquad 0 \leq t \leq T_{\mathrm{samp}} \\ V_{\mathrm{q,x}}(t) &= V_{\mathrm{q,x}}(T_{\mathrm{samp}}) \\ &\quad + (V_{\mathrm{ref}} - V_{\mathrm{q,x}}(T_{\mathrm{samp}}))(1 - e^{\frac{-t}{R_{\mathrm{ref}}(C_{\mathrm{q,1}}+C_{\mathrm{q,2}})}}) \\ &\qquad T_{\mathrm{samp}} \leq t \leq T_{\mathrm{q,on}} \end{aligned} \tag{3.112}$$

(3.112) is particularly attractive because the function has similar shape of the logarithmic quench function, resulting in better linear control of $I_{\mathrm{b}}(t)$ through k_{w} according to (3.107).

3.2.3.1.5 Power Gain As will be described in Section 3.2.3.2, the characterization of the $\mathrm{SRA_{buf,q}}$ is done in the frequency domain, and a plot of output power against input power is used to calculate parameters like regenerative gain. The maximum value of the envelope of the output voltage in (2.29) from Section 2.6.1 can be determined by inserting (2.30) into (2.29) as,

$$V_{\mathrm{out}} = \frac{I_{\mathrm{in}}}{2}\sqrt{\frac{L_{\mathrm{res}}}{C_{\mathrm{res}}}}\frac{\omega_{\mathrm{in}}\sqrt{2\pi}}{\sqrt{(\omega_{\mathrm{res}}k_{\mathrm{q}})}}A_{\mathrm{s}}A_{\mathrm{r}}(T_{\mathrm{q,on}})\,. \tag{3.113}$$

With a common-base input stage, the input current to the resonator is equal to the current through the source. Under input matched conditions, I_{in} can be written as $I_{\mathrm{in}} = \sqrt{2P_{\mathrm{in}}/R_{\mathrm{s}}}$, where P_{in} is the input power, and R_{s} is the source resistance. At the output stage, the voltage across the resonator is amplified by the cascode amplifier, and the small signal output voltage across the load resistor R_{L} is $v_{\mathrm{out,buf}} = -g_{\mathrm{m,T8/10}}\, R_{\mathrm{L}}\, v_{\mathrm{out}}$. In terms of output power $P_{\mathrm{out,buf}}$, and the average large signal transconductance $G_{\mathrm{m,T8/10}}$, V_{out} can hence be written as,

$$V_{\mathrm{out}} = \frac{\sqrt{2P_{\mathrm{out,buf}}/R_{\mathrm{L}}}}{G_{\mathrm{m,T8/10}}}. \tag{3.114}$$

Inserting (3.114) in (3.113), the power gain of the buffered SRA in linear mode, $A_{\mathrm{SRA,buf}} = P_{\mathrm{out,buf}}/P_{\mathrm{in}}$ is,

$$A_{\mathrm{SRA,buf}}(\omega_{\mathrm{in}}) = \frac{G^2_{m,T8/10}R_{\mathrm{L}}L_{\mathrm{res}}}{2R_{\mathrm{s}}C_{\mathrm{res}}}\frac{\omega^2_{\mathrm{in}}\pi}{\omega_{\mathrm{res}}k_{\mathrm{q}}}A^2_{\mathrm{s}}A^2_{\mathrm{r}}(T_{\mathrm{q,on}})\,. \tag{3.115}$$

At $f_{\mathrm{in}} = 24\,\mathrm{GHz}$ and $T_{\mathrm{q,on}} \approx 300\,\mathrm{ns}$, using the relationships $R_{\mathrm{s}} = R_{\mathrm{L}} = 50\,\Omega$, $G_{m,T8/10} \approx 1/R_{\mathrm{s,L}}$, and with extracted values of L_{res} and C_{res}. Also, using (3.111),

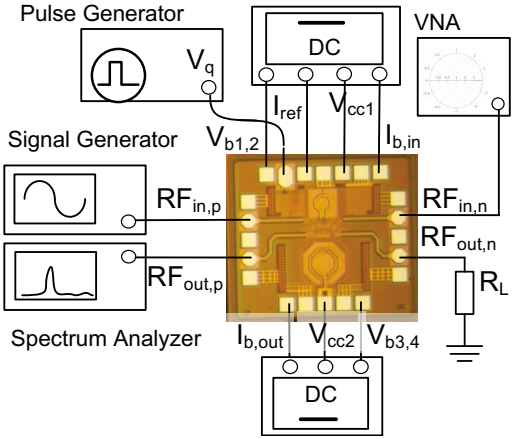

Figure 3.33: Illustration of the characterization setup around the chip micrograph of the $\mathrm{SRA_{buf,q}}$ occupying an area of 990 µm × 895 µm. including pads (Adapted from *[TJE20] © 2020 IEEE).

$k_{\mathrm{w2}} \approx 143\,\mathrm{mV\,ns^{-1}}$ and $k_{\mathrm{q}} = 143\,\mathrm{ns^{-1}}$ for $\Delta V_{\mathrm{q}} = 1\,\mathrm{mV}$. $A_{\mathrm{SRA,buf}}$ can then be calculated as $A_{\mathrm{SRA,buf,dB}} \approx 56\,\mathrm{dB}$ at $f_{\mathrm{res}} = 24\,\mathrm{GHz}$, which closely matches with the measurement result of 51 dB as depicted in Fig. 3.34(b).

The power gain $A_{\mathrm{SRA,dir}}$ of the direct antenna interface SRA can be obtained using $V_{\mathrm{out,dir}} = \sqrt{2P_{\mathrm{out}}R_{\mathrm{L}}}$ as,

$$A_{\mathrm{SRA,dir}}(\omega_{\mathrm{in}}) = \frac{L_{\mathrm{res}}}{2R_{\mathrm{s}}R_{\mathrm{L}}C_{\mathrm{res}}}\frac{\omega_{\mathrm{in}}^2\pi}{(\omega_{\mathrm{res}}k_{\mathrm{q}})}A_{\mathrm{s}}^2A_{\mathrm{r}}^2(T_{\mathrm{q,on}})\,. \tag{3.116}$$

Substituting circuit parameters from the compact model and EM simulations at $f_{\mathrm{in}} = 25\,\mathrm{GHz}$, $L_{\mathrm{res}} = 130\,\mathrm{pH}$ and $C_{\mathrm{res}} = 310\,\mathrm{fF}$. Also, with $k_{\mathrm{q}} = 143\,\mathrm{ns^{-1}}$, $T_{\mathrm{q,on}} \approx 300\,\mathrm{ns}$ and $R_{\mathrm{s}} = R_{\mathrm{L}} = 50\,\Omega$, the power gain can be calculated as, $A_{\mathrm{SRA,dir,dB}} \approx 68\,\mathrm{dB}$ at $f_{\mathrm{res}} = 25\,\mathrm{GHz}$, satisfying the minimum gain requirement for $d \geq 100\,\mathrm{m}$ derived in (3.19), and closely matching the measurement result of around 65 dB as depicted in Fig. 3.34(b). It should be noted that for a fixed $T_{\mathrm{q,on}}$ and k_{q}, the peak gain is dependent on the input signal frequency ω_{in} relative to the resonance frequency ω_{res}, as depicted in the Gaussian frequency response measurement results for different input power levels in Fig. 3.27(a).

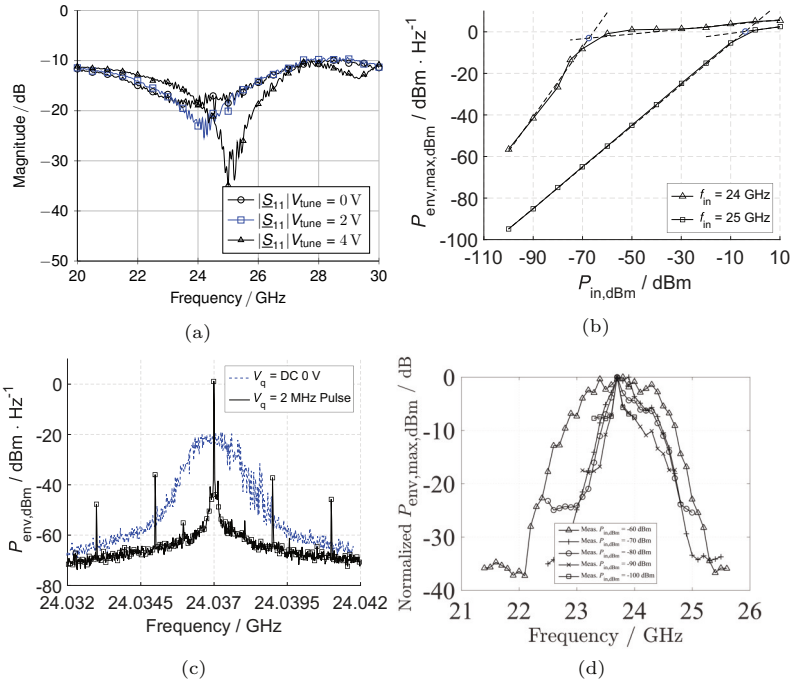

Figure 3.34: $\mathrm{SRA_{buf,q}}$ characterization results: (a) Measured magnitude of input reflection coefficient versus frequency for different V_{tune} values for $\mathrm{SRA_{buf}}$. (b) Measured and modeled peak of the envelope of output power density versus input power level for $\mathrm{SRA_{buf}}$. (c) Measured envelope of power spectral density showing the Dirac delta peaks when an input signal is applied within the bandwidth of the resonator. (d) Normalized frequency response measurements used to determine bandwidth (Adapted from *[TJE20] ©2020 IEEE).

3.2.3.2 Characterization

The implemented $\mathrm{SRA_{buf,q}}$ IC to prove the design concept occupies an area of $0.89\,\mathrm{mm}^2$ and is shown in the chip micrograph of Fig. 3.33. $\mathrm{SRA_{buf,q}}$ characterization is done using the setup illustrated in Fig. 3.33 employing methods similar to that described in Section 3.2.2. IC characterization is done on a wafer prober and pads are contacted using Infinity probes from Cascade Microtech®. Since $\mathrm{SRA_{buf,q}}$ operates in the similar frequency range as $\mathrm{SRA_{dir,q}}$ where time domain measurements of regenerative sampling are not practical, frequency domain characterization is done. The input signal is applied to $\mathrm{RF_{in,p,n}}$ using the Keysight® 8257D signal generator, and the output signal spectrum is measured at $\mathrm{RF_{out,p,n}}$ using the Rohde & Schwarz FSW67® spectrum analyzer. An arbitrary waveform generator provides the periodic input pulses to the integrated quench pulse shaping circuit.

As detailed in Section 3.2.2 and *[TJE20], when $V_\mathrm{q} = 0\,\mathrm{V}$, and with no input signal applied, the $\mathrm{SRA_{buf,q}}$ operates in the free-running oscillator mode, and measurement of the tuning range is done by varying V_tune from 0 V to 4 V, resulting in a a measured frequency variation covering the unlicensed frequency bands from 22.6 GHz to 25.6 GHz. The buffered inputs of $\mathrm{SRA_{buf,q}}$ also enable the measurement of the input reflection coefficient using the vector network analyzer Rohde & Schwarz ZVA67 ®, and the measurement results show good agreement with simulations as depicted in Fig. 3.34(a), with measured $|\underline{S}_{11}| < -10\,\mathrm{dB}$ across the frequency range from 20 GHz to 30 GHz. The DC power consumption when operated in the free-running oscillator mode is 87 mW with 1.6 V core and 2.7 V output buffer power supplies.

$\mathrm{SRA_{buf}}$ operates in the SRA mode when V_q is a periodic pulse and an input signal is applied. Characteristic Dirac delta spectral peaks superimposed with a *sinc* spectrum indicate phase coherent sampling [SCW+13b], and are proven by the measurements shown in Fig. 3.34(c). The input signal power level $P_\mathrm{in,dBm}$ is then varied to obtain the transfer characteristics of the SRA which are shown in Fig. 3.34(b). At lower input power levels, the SRA operates in the linear mode, with a regenerative gain of 51 dB till $P_\mathrm{i,N,dBm} \approx -67.4\,\mathrm{dBm}$. Further increase in input power level causes the SRA to transition from linear to logarithmic mode, where the output power level ($P_\mathrm{out,dBm}$) reaches a maximum of around 7 dBm. This is the preferred operating region for active reflector tags. The power consumption of the circuit when operating with a V_q of 50 % duty cycle is 44 mW.

3.2.4 Knowledge Gained

A comparative study of the four SRA variants discussed in Section 3.2.1 to Section 3.2.3 is now done to determine the suitability of the variants to be used as SRTs. Table 3.1 tabulated the wafer prober characterization results of the four SRA and also the state-of-the-art ICs designed for RFID transponder applications.

A reflection amplifier based design is reported in [BMM12]. Though the design reports moderate gain consuming low DC power, the transmit power is low, minimum received input signal power is high and the design occupies a relatively large area. A pulsed oscillator based design is reported in [Weh10] and [EWU+13]. [Weh10] reports a moderate transmit power and received signal sensitivity, consuming moderate DC power. On the other hand, the design in [EWU+13] reports a high bandwidth of 2.3 GHz, but with low transmit power, receiver sensitivity and relatively high DC power consumption. All three works report operation at lower frequencies below 10 GHz. Of the high frequency works in literature, implementation complexity is high in [SCW+13b],[DHV17b],[DHV17a] and [HES+13]. These designs uses multiple blocks like LNAs and PAs. [SCW+13b] reports a design called SILO which is based on a topology similar to the SRA, but operating only in the step-controlled mode. The SILO has a relatively low peak gain and consumes relatively high DC power. [DHV17b] and [DHV17a] reports a BPSK modulator based architecture which additionally employs a downconversion mixer and a VGA. [HES+13] also uses a relatively complex architecture with a transmit and receive frontend consisting of LNA, PA, VGA and a transmit / receive switch. [GJE22] uses an SRA based approach at 60 GHz with a high peak gain and moderate power consumption, but with low output power and occupying relatively large area.

Among the SRA variants from this work in Table 3.1, we can see that the $\mathrm{SRA_{SOI}}$ has an operating frequency range of 24.07 GHz to 25.35 GHz, detects input signals as low as −85 dBm, and delivers 1.1 dBm output power into a 100 Ω differential load consuming a low DC power of 10.6 mW. The $\mathrm{SRA_{SOI}}$ also has a good combination of sensitivity and output power for implementations in CMOS. Though the circuit consumes low DC power, low breakdown voltages of the SOI transistors put a limit on the maximum output power, which is required at larger ranging distance of SRTs (3.23). The output power can be increased by stacking more transistors as will be described in Section 3.2.2, but the corresponding number of transistors required for $\mathrm{SRA_{SOI}}$ to achieve the same output power is much higher than in the SiGe implementations discussed in Section 3.2.2 and Section 3.2.3. Additionally, phase compensation structures which increase area and

complexity are required to keep the current and voltage in phase at 24 GHz when stacking. The common centroid layout used to compensate for process variation in the CMOS transistors result in higher fixed parasitic output capacitance C_{par}, which along with the increased capacitance due to stacking reduces the frequency tuning range of $\mathrm{SRA_{SOI}}$ according to (3.38).

Though the $\mathrm{SRA_{SOI}}$ consumes very low DC power, the limitation on output power level and superregenerative gain results in a significantly reduced localization range according to (3.23). $\mathrm{SRA_{dir}}$ uses the SiGe-BiCMOS technology which provides the advantage of higher breakdown voltage transistors and better tolerance to variability and process mismatch, eliminating the requirement for special layout techniques. $\mathrm{SRA_{dir}}$ which uses the novel stacked transistor CCO with the quenching clearly shows improvement in the minimum input power level from which phase coherence is observed, $P_{\mathrm{min,dBm}}$ of -110 dBm and the linear to logarithmic mode transition power $P_{\mathrm{i,N,dBm}}$ of -85 dBm, combined with a high output power level of $P_{\mathrm{out,dBm}}$ of 7.8 dBm and occupies a low area.

The parameters from characterization of $\mathrm{SRA_{dir,q}}$, which integrates the quench pulse shaping circuit, are within 5% of the the results from $\mathrm{SRA_{dir}}$. The measured minimum input power level for phase coherent amplification is -100 dBm, and the linear to logarithmic mode transition power is -63 dBm, along with an output power level of 5.6 dBm. The combination of output power and minimum detectable input power from this design stands out among the other results.

While the direct antenna drive topology employed in $\mathrm{SRA_{dir}}$ and $\mathrm{SRA_{dir,q}}$ is less complex and occupies low area, it is not optimum due to the relatively high sensitivity of f_{res} to output load variations. The topology is also inherently less efficient for input and output power transfer to and from resonator core respectively. The two input and two output terminals of the $\mathrm{SRA_{buf,q}}$ enables the implementation of roll invariant SRTs as described in Section 3.3.1. $\mathrm{SRA_{buf,q}}$ shows a minimum detectable input power level of -90 dBm, the circuit has a peak regenerative gain of 51 dB. The combination of the peak gain and 7 dBm output power level for this design also stands out when compared to reported values from other works. Both $\mathrm{SRA_{dir,q}}$ and $\mathrm{SRA_{buf,q}}$ employs a novel integrated quench pulse shaping circuit to simultaneously improve the minimum detectable input power level and output power level which in turn improves the maximum range of the system.

Table 3.1: Comparison of the designed SRAs with state-of-the-art ICs suitable as RFID Transponders

Ref.	f_{res} (GHz)	$P_{out,dBm}$ (dBm)	Peak Gain (dB)	$P_{min,dBm}$ (dBm)	$P_{i,N,dBm}$ (dBm)	f_{BW} (GHz)	P_{DC} (mW)	Area (mm^2)	Topology	Tech.
[BMM12]	4	-15.2	22.3	-45.4	-	0.0003	0.004	1.12	Reflection Amp.	0.13 µm CMOS
[Weh10]	5.8	6	-	-70.0	-	0.15	54	0.85	Pulsed	0.18 µm SiGe
[EWU+13]	6.8	-4.7	-	-65.00	-	2.30	130	-	SILO	0.25 µm SiGe
[HES+13]	24.125	5.0	-	-	-	0.24	42			0.13 µm CMOS
[SCW+13b]	34.45	5	38	-80	-53	0.50	122[a]	0.83	SILO	0.25 µm SiGe
[DHV17a]	77	-14	20	-66	-	5.00	18	0.50	BPSK Mod.	45 nm SOI
[DHV17b]	78	-	19	-62.0	-	9.00	25/10.8[b]	0.50	BPSK Mod.	55 nm SiGe
[GJE22]	60	3.1	80.5	-79.5	-58	-	25	0.87	SRO	0.13 µm SiGe
SRA_{SOI}	**24.71**	**1.5**	**48**	**-85.0**	**-64.9**	**0.2**	**4/9.6[c]**	**0.67**	**SRA**	**45 nm SOI**
SRA_{dir}	**25.3**	**7.8**	**70**	**-110.0**	**-85**	**0.25**	**38/110[c]**	**0.63**	**SRA**	**0.13 µm SiGe**
$SRA_{dir,q}$	**24.6**	**8.2**	**68**	**-107.0**	**-80**	**0.25**	**43/124[c]**	**0.63**	**SRA**	**0.13 µm SiGe**
$SRA_{buf,q}$	**25.6**	**7**	**51**	**-90.0**	**-67**	**0.5**	**44/87[c]**	**0.89**	**SRA**	**0.13 µm SiGe**

[a] Includes pulse generation and interface. [b] Active / Idle. [c] Quenched (active) / DC.

3.3 Proof of Principle System Implementation

In order to perform experimental testing of the principle described in Section 3.1.1, two different SRT variants and an interrogating secondary radar is implemented. The two SRT variants operating the 24 GHz ISM band are implemented using the high gain integrated SRAs presented in Section 3.2 *[TLJE18, TJE20]. The SRTs also include printed circuit board (PCB) based bandwidth enhanced microstrip patch antennas as will be discussed in Section 3.3.1.1. The interrogating secondary radar is based mainly on off-the-shelf components, and is augmented by the custom designed PA *[TLJE19] to reduce leakage to the receive front end and improve the interrogation range.

3.3.1 Superregenerative Transponders

The core of the first SRT ($\mathrm{SRT_{dir}}$) is the direct antenna drive SRA ($\mathrm{SRA_{dir,q}}$) IC described in Section 3.2.2 and *[TLJE18]. The second SRT ($\mathrm{SRT_{buf}}$) uses the buffered superregenerative amplifier ($\mathrm{SRA_{buf,q}}$) IC described in Section 3.2.3 and *[TJE20]. $\mathrm{SRT_{buf}}$ features antenna diversity enabled by the separate inputs and output buffers of $\mathrm{SRA_{buf,q}}$.

Fig. 3.37 shows the designed SRT prototypes. Except for the SRA ICs and the number of antennas used, both tags are functionally similar. The core of each SRT is the SRA IC with integrated quench pulse shaping described in Section 3.2.2 and Section 3.2.3. The SRA ICs are wire-bonded using 17 µm bondwires to the PCB as shown in Fig. 3.38.

The parameters of the wire-bonded SRA ICs as part of the SRT, including phase coherent sampling are also characterized independently by giving RF input using a Keysight® E8257D signal generator, and analyzing the output frequency spectrum in a R&S® FSW67 spectrum analyzer. The corresponding results are summarized in Table 3.2.

The 1 mm thick 4 layer PCB is built as a stack of flame retardant-4 (FR4) dielectric layer sandwiched between two Rogers RO4350B® dielectric layers on the top and bottom. In addition to the SRA, SRT contains voltage regulators for power supply and bias voltage generation, and a reference current source. An off-the-shelf voltage controlled pulse width modulator IC [Anab] is used for generating the pulses required as input to the quench pulse shaping circuit. The frequency and duty cycle of the quench pulses are current controlled. This is done using current DACs inside an off-the-shelf programmable system on chip (PSoC®) [Cyp]. The state machine implemented in the firmware of the chip generates control signals required for data transfer. Also, a temperature sensor having a inter-integrated

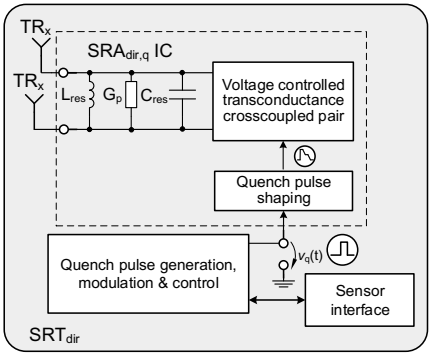

Figure 3.35: Block diagram of the $\mathrm{SRA_{dir,q}}$ based $\mathrm{SRT_{dir}}$.

circuit ($\mathrm{I^2C}$) serial interface is used to obtain real time temperature data to be transferred from the SRT to the interrogator.

Bandwidth enhanced microstrip patch antennas decribed in Section 3.3.1.1 are connected to the RF pads using microstrip transmission lines built over the top RO4350B® layer. RO4350B® has an $\epsilon_\mathrm{r} \approx 3.66$ and dissipation factor $\tan\delta$ of 0.0037 at 10 GHz. The copper metal layers are gold plated using electroless nickel electroless palladium immersion gold (ENEPIG) to facilitate good bonding of the IC to the PCB. The $\mathrm{SRT_{dir}}$ operates from two 1.5 V AAA batteries, and has a lifetime of more than one day when operated continuously.

Table 3.2: Performance summary of SRA ICs post wirebonding

	$\mathrm{SRA_{dir,q}}$	$\mathrm{SRA_{buf,q}}$
f_res (GHz)	24.25	24.25
$P_\mathrm{out,dBm}$ (dBm)	5.6[a]	3.2[a,b]
$P_\mathrm{min,dBm}$ (dBm)	-100	-80
$P_\mathrm{i,N,dBm}$ (dBm)	-75	-57
$A_\mathrm{SRA,dB}$ (dB)	68	51
f_BW (GHz)	0.25	0.5
P_DC (mW)	65/124[c]	44/87[c]
Tech.	130 nm SiGe BiCMOS	130 nm SiGe BiCMOS

[a] Incl. bondwire losses. [b] Per T_x channel. [c] Quenched / DC.

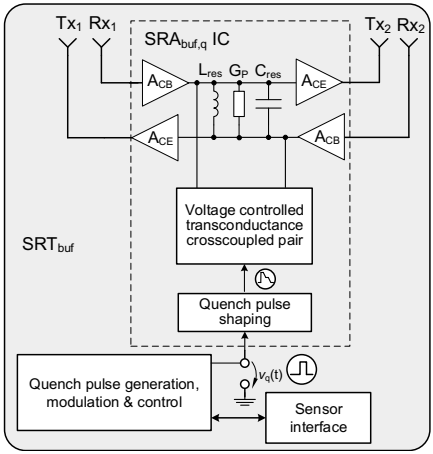

Figure 3.36: Block diagram of the $\mathrm{SRA_{buf,q}}$ based $\mathrm{SRT_{buf}}$ (Adapted from *[TJE20] © 2020 IEEE).

3.3.1.1 Bandwidth Enhanced Microstrip Patch Antennas

Fig. 3.39(a) shows the geometry of the bandwidth enhanced single antenna element ($\mathrm{ANT_{MB1x}}$) used in the presented SRTs. $\mathrm{ANT_{MB1x}}$ has a modified inset-fed rectangular microstrip patch structure and is designed for a resonant center frequency $f_{\mathrm{ant}} = 24.5\,\mathrm{GHz}$. The initial dimensions of L and W are determined using the conventional inset-fed microstrip patch antenna design method from [Bal05]. Taking into account the effect of dielectric-air interface, the dimension L corresponds to the half wavelength at f_{ant} determined as,

$$L = \lambda_{\mathrm{ant}}/2 = c_{\mathrm{o}}/(2 f_{\mathrm{ant}} \sqrt{\epsilon_{\mathrm{r,eff}}}) \approx 3.8\,\mathrm{mm}\,, \tag{3.117}$$

where c_{o} is the speed of light in vacuum and $\epsilon_{\mathrm{r,eff}}$ is the effective dielectric constant determined as

$$\epsilon_{\mathrm{r,eff}} = P(\epsilon_{\mathrm{r}} - 1) + 1 \approx 2.6\,. \tag{3.118}$$

Here $\epsilon_{\mathrm{r}} = 3.66$ is the relative permittivity of the used Rogers®4350 dielectric, and $P \approx 0.6$ is the filling factor [KJ82]. In order to avoid cross polarization [Bal05], the ratio W/L is taken as 1.5, and W is calculated as $W = 5.7\,\mathrm{mm}$. The input impedance of $\mathrm{ANT_{MB1x}}$ is a function of the feed position with a shifted cosine

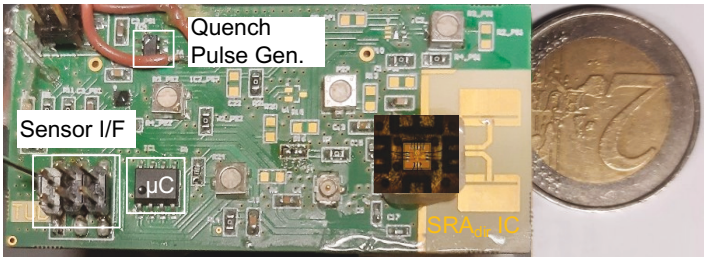

(a)

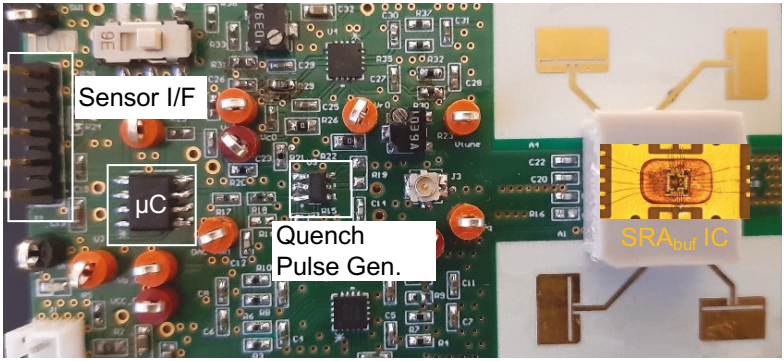

(b)

Figure 3.37: Active reflector tags with bonded SRA ICs shown in inset above chip cap (a) $\mathrm{SRT_{dir}}$ with $\mathrm{SRA_{dir,q}}$ measuring 50 mm × 35 mm. (b) $\mathrm{SRT_{dir}}$ with $\mathrm{SRA_{buf,q}}$ measuring 70 mm × 50 mm. (Reused from *[TFJE23] ©2023 IET).

squared relationship. The input impedance is maximum at the edge of the patch and minimum at the center. The feed dimension Y is estimated from curve fitting as 725 µm for $\underline{Z}_{in} = 50\,\Omega$. A microstrip transmission line with a width $D = 500\,\mu\mathrm{m}$ corresponding to a characteristic impedance of $50\,\Omega$ is used to extend the feedline to SRA RF ports. The simulated and measured input reflection coefficients of the $\mathrm{ANT_{MB1x}}$ without any slots are shown with legend $\mathrm{ANT_{MN}}$ in Fig. 3.39(c).

The introduction of the slot with width $W_\mathrm{s} = 6\,\mathrm{mm}$ and length $L_\mathrm{s} = 300\,\mu\mathrm{m}$ results in an effective volume increase. This in turn increases the bandwidth by 4 times from 0.5 GHz to 2 GHz as shown in the simulation and measurement results with legends $\mathrm{ANT_{MB1x}}$ in Fig. 3.39(c). Other dimensions are determined as $X = 2W/5 = 2.6\,\mu\mathrm{m}$ and $S = W/5 = 1.3\,\mathrm{mm}$ from [Bal05]. The optimized

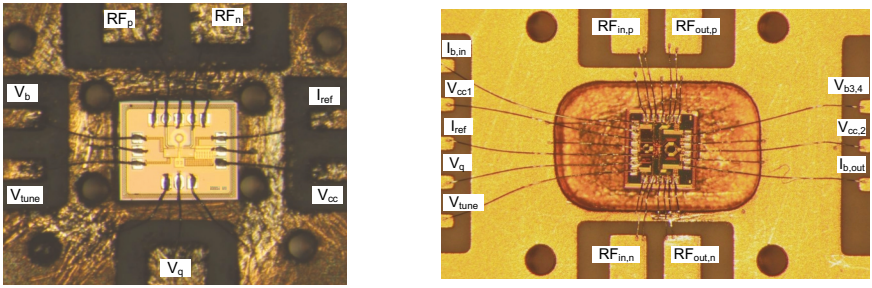

(a) (b)

Figure 3.38: Fabricated SRA ICs with quench pulse shaping in 130 nm SiGe BiCMOS technology (a) Direct antenna interface SRA occupying an area of 875 µm × 725 µm. (b) Buffered antenna interface SRA, occupying an area of 990 µm × 895 µm. (Reused from *[TFJE23] ©2023 IET).

dimensions of $\mathrm{ANT_{MB1x}}$ using EM simulation results are higher than than the calculations with $L = 4.1\,\mathrm{mm}$ and $W = 6.6\,\mathrm{mm}$. This is mainly because the simplified calculations ignore the effects due to the slot, and conductor thickness.

The $\mathrm{ANT_{MB1x}}$ geometry is optimized with the help of an equivalent circuit model shown in Fig. 3.39(b). Here, the antenna is modeled as two LC resonators coupled to each other using a parallel LC model of the gap. The model also enables the investigation of frequency response and input impedance of the structure. The first resonator is formed by $L_{\mathrm{R1}} \approx 120\,\mathrm{pH}$ and $C_{\mathrm{R1}} \approx 220\,\mathrm{fF}$ corresponding to a resonant frequency

$$f_{\mathrm{R1}} = \frac{1}{2\pi\sqrt{L_{\mathrm{R1}}C_{\mathrm{R1}}}} \approx 32\,\mathrm{GHz}. \tag{3.119}$$

The second resonator is formed by $L_{\mathrm{R2}} \approx 350\,\mathrm{pH}$ and $C_{\mathrm{R2}} \approx 300\,\mathrm{fF}$, corresponding to a resonant frequency $f_{\mathrm{R2}} \approx 17\,\mathrm{GHz}$. The coupling elements $L_{\mathrm{G}} \approx 50\,\mathrm{pH}$ and $C_{\mathrm{G}} \approx 600\,\mathrm{fF}$ model the coupling due to the gap in the structure. This also results in an effective resonant frequency corresponding to the geometric mean of the individual resonant frequencies as

$$f_{\mathrm{R}} = \sqrt{f_{\mathrm{R1}} f_{\mathrm{R2}}} \approx 24\,\mathrm{GHz}. \tag{3.120}$$

Fig. 3.39(c) shows that the model aligns closely with simulation and measurement results.

The single element $\mathrm{ANT_{MB1x}}$ has a simulated gain of 5.2 dBi. In the range optimized $\mathrm{SRT_{dir}}$, a high antenna gain is preferred. So two $\mathrm{ANT_{MB1x}}$ elements

are arranged with a spacing of 3 mm between them as shown in Fig. 3.40(a). Referred to as $\mathrm{ANT_{MB2x}}$, the two elements are fed with each of the differential RF ports from $\mathrm{SRA_{dir,q}}$. The simulated radiation pattern with differential excitation, resulting in a peak gain of 9.17 dBi is shown in Fig. 3.40(a).

Though $\mathrm{ANT_{MB2x}}$ has a high gain, the antenna is linearly polarized with a −50 dB lower vertical component as shown in the polar plot of Fig. 3.40(c). This results in two nulls at $\phi = 90°$ and $\phi = 270°$ as seen in Fig. 3.40(a). In order to make the antenna radiate and receive in both horizontal and vertical polarization to achieve roll invariance in the horizontal plane, four $\mathrm{ANT_{MB1x}}$ elements are oriented orthogonal to each other, referred to as $\mathrm{ANT_{MB4x}}$ in Fig. 3.40(d). $\mathrm{ANT_{MB4x}}$ is used in $\mathrm{SRT_{buf}}$ with two $\mathrm{T_x}$ and $\mathrm{R_x}$ ports. The radiation pattern simulated by differential excitation of orthogonal elements shows that $\mathrm{ANT_{MB4x}}$ has a lower peak gain of 6.63 dBi, but is roll invariant in the horizontal plane.

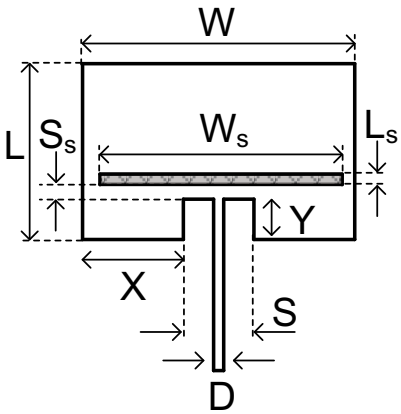

W	6.6 mm
L	4.1 mm
X	2.8 mm
S	1 mm
Y	725 µm
D	500 µm
W_s	6 mm
L_s	300 µm
S_s	125 µm

(a)

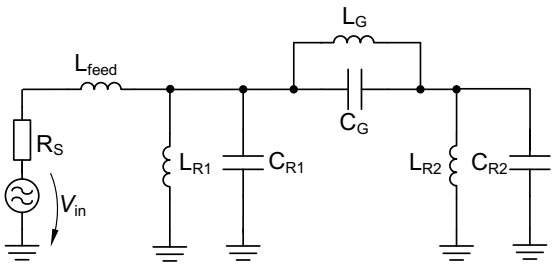

(b)

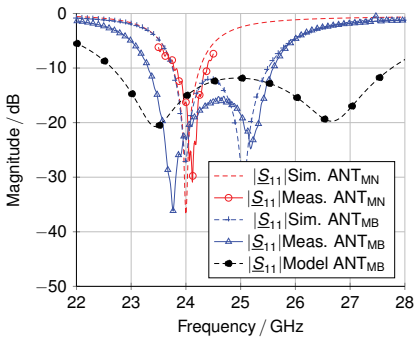

(c)

Figure 3.39: (a) Geometry of the bandwidth enhanced patch antenna $\mathrm{ANT_{MB1x}}$; (b) Equivalent circuit model used to determine frequency response; (c) Measured, simulated and modeled input reflection coefficients for conventional microstrip patch antenna $\mathrm{ANT_{MN1x}}$ and bandwidth enhanced $\mathrm{ANT_{MB1x}}$. (Reused from *[TFJE23] ©2023 IET).

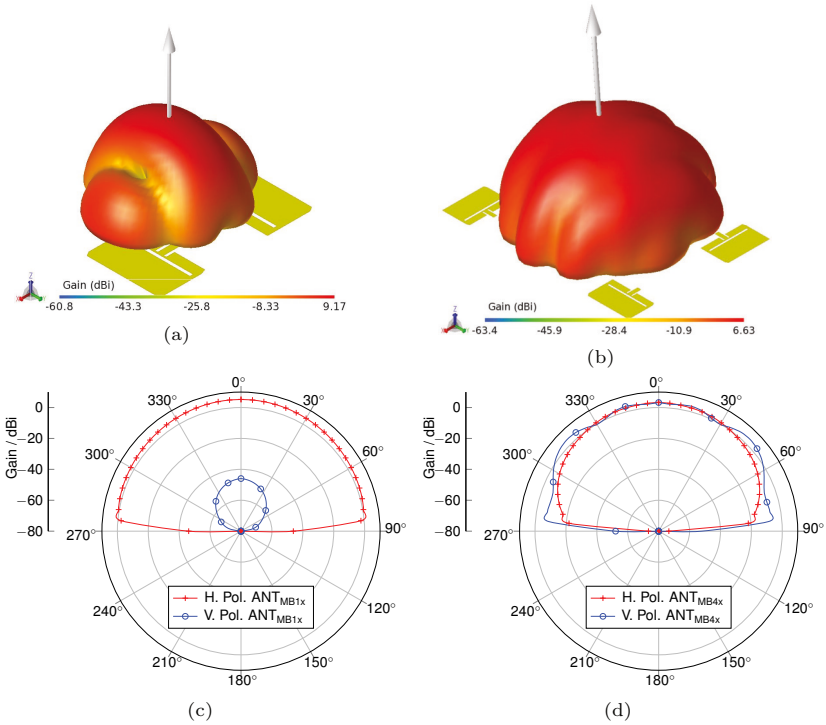

Figure 3.40: (a) Simulated radiation pattern of $\mathrm{ANT_{MB2x}}$ and (b) $\mathrm{ANT_{MB4x}}$; (c) Simulated gain vs. θ cut at $\phi = 90°$ for horizontal and vertical polarization of $\mathrm{ANT_{MB2x}}$ and (d) $\mathrm{ANT_{MB4x}}$. (Reused from *[TFJE23] ©2023 IET).

3.3.2 FMCW Radar Interrogator

The LFMCW chirps to interrogate the SRTs are generated using the chirp sequence LFMCW radar shown in Fig. 3.41(a) and Fig. 3.42(a). The 24 GHz radar interrogator is implemented as a stack of an RF PCB (PCB_{RF}) and a digital PCB (PCB_{dig}). PCB_{RF} has the same layer stack-up as the SRT_{dir}. The main component is the off-the-shelf MMIC [Inf] consisting of a 24 GHz to 26 GHz VCO, a low noise amplifier, a down converting mixer, a differential power amplifier and frequency dividers. As shown in Fig. 3.41(a), the LFMCW frequency chirp is generated giving the divide by 16 output of the MMIC to the RF input of a PLL [Anaa], a 6.1 GHz fractional - N PLL with frequency ramp generation capability.

A PCB balun using design principles from [DSCE13] is implemented to convert the differential output of the PA to a single ended output. The single ended input of the LNA and balun output is then fed to two horn antennas with 14 dBi gain through a custom designed coupled line bandpass filter designed based on [Poz12] with a bandwidth less than 800 MHz. In order to reduce on-chip PA to LNA leakage and internal frequency pulling, the PA is operated with an output power of around 0 dBm. In order to increase the output power for the desired EIRP to maximize the range, a custom designed PA *[TLJE19] is used externally. With the output of the balun of around −1 dBm, an EIRP of 20 dBm is obtained for the radar transmit frontend. The transmitted FMCW chirp is reflected back, and amplified by the receive front end LNA. The LNA output is downconverted and the mixer IF output is bandpass filtered with $f_{q,min} = 300\,kHz$ and $f_{q,max} = 3\,MHz$. The IF signal is digitized using a ADC with number of bits $N_{adc} = 12$ and sampling rate $f_{samp} = 10\,MSps$, with a maximum possible signal to noise ratio (SNR) from the well known equation [Kes04],

$$SNR_{adc,dB} = 6.02\,dB N_{adc} + 1.76\,dB \approx 74\,dB. \tag{3.121}$$

PCB_{dig} includes voltage regulators to generate the required bias voltages, clock references, and a microcontroller to acquire handle sequencing and control. The microcontroller also facilitates the ADC data transfer to a 32 kB external memory using direct memory access (DMA). Another component in PCB_{dig} is the field programmable gate array (FPGA) used to generate various timing signals including the pulses required to trigger the FMCW chirp. An Ethernet interface allows the hardware to be configured, and data to be transferred to a remote PC for analysis.

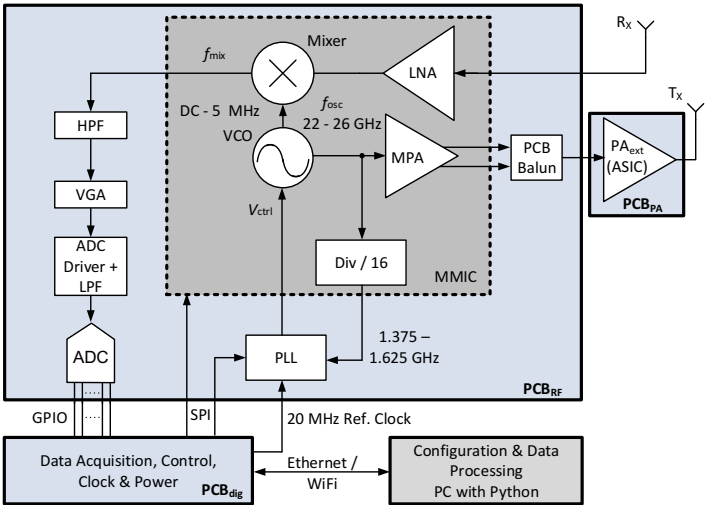

(a)

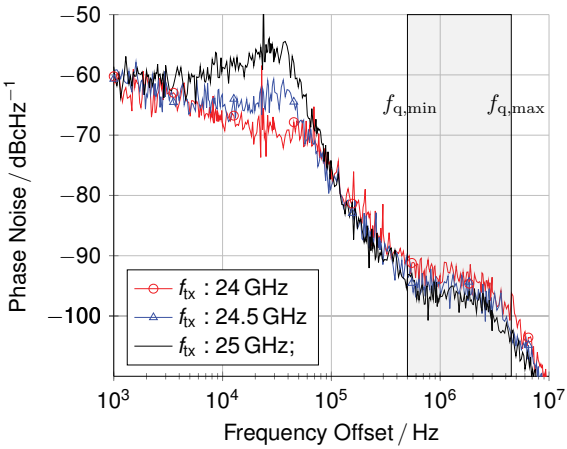

(b)

Figure 3.41: (a) Block diagram of the LFMCW radar interrogator, implemented as a stack of PCB_{dig} and PCB_{RF}; (b) Phase noise profile of the interrogator output in the CW mode for three different frequencies in the band. (Reused from *[TFJE23] ©2023 IET).

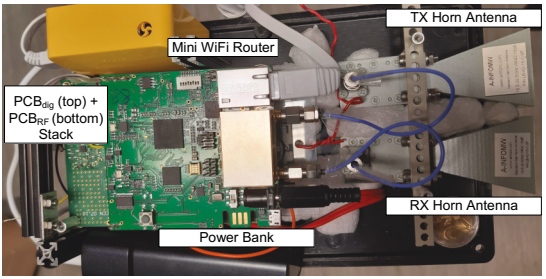

(a)

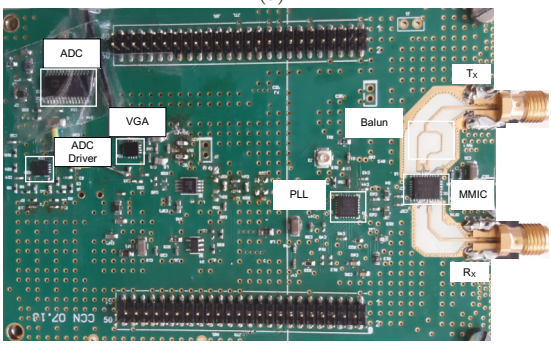

(b)

Figure 3.42: (a) Top view of the hardware with $\mathrm{PCB_{dig}}$ in sight. (b) $\mathrm{PCB_{RF}}$. (Reused from *[TFJE23] ©2023 IET).

3.3.3 Chirp *Z*-transform Based Data Analysis

The distance between the interrogator and SRTs are estimated using the steps shown in Algorithm 1 implemented in Python. For each chirp sent by the LFMCW radar, the the baseband signal is digitized by the ADC and stored as a discrete time series $s_\mathrm{b}[n]$, with $n = 0, ..., N_\mathrm{samp} - 1$. An N_samp point fast Fourier transform (FFT) is computed on the zero padded and windowed $x[n]$. On fixing the distance to SRT, $x[n]$ corresponding to $K = 150$ chirp sequences are collected and the spectral average is calculated. Peak search is then done on a subset of the spectral averaged FFT data between $f_\mathrm{q,min}$ and $f_\mathrm{q,max}$ to determine the upper and lower beat frequencies $f_\mathrm{b,l,FFT}$ and $f_\mathrm{b,u,FFT}$ respectively. The corresponding quench frequency is

$$f_\mathrm{q,FFT} = \frac{f_\mathrm{b,l,FFT} + f_\mathrm{b,u,FFT}}{2}\,, \tag{3.122}$$

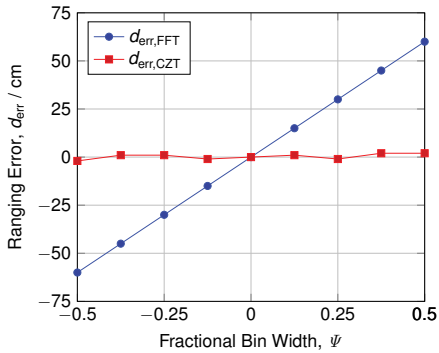

Figure 3.43: Comparison of range estimation error between FFT and CZT based methods. (Reused from *[TFJE23] ©2023 IET).

and the distance to SRT is estimated according to (3.9). The FFT outputs a discrete spectrum with a frequency bin resolution $f_{\text{bin,FFT}} = f_{\text{samp}}/N_{\text{samp}}$. With $f_{\text{samp}} = 10\,\text{MSps}$ and $N_{\text{samp}} = 10\,\text{k}$ samples, $f_{\text{bin,FFT}} = 1\,\text{kHz}$ and the corresponding range per bin $d_{\text{bin,FFT}}$ is

$$d_{\text{bin,FFT}} = \frac{C_{\text{o}} f_{\text{bin,FFT}}}{2\mu} = 60\,\text{cm}. \tag{3.123}$$

A non-zero $d_{\text{bin,FFT}}$ discretizes the measured range d_{FFT}, and the corresponding ranging error is $d_{\text{err,FFT}} = d_{\text{act}} - d_{\text{FFT}}$. Here d_{act} is the actual distance to the SRT with $d_{\text{act}} = (n + \Psi)d_{\text{bin,FFT}}$ and $d_{\text{FFT}} = nd_{\text{bin,FFT}}$ is the distance estimated using FFT. Also Ψ is the fractional bin width which varies from -0.5 to +0.5, and between any two adjacent frequency bins, $d_{\text{err,FFT}}$ varies as a function of Ψ within $\pm d_{\text{bin,FFT}}$ as shown in Fig. 3.43. Therefore, in order to improve ranging accuracy, it is necessary to either minimize $d_{\text{bin,FFT}}$ by increasing N_{samp}, or by using alternate approaches like parabolic or *sinc* interpolation as reported in [Qui94, GG04, KCS08] with up to 20 times accuracy improvement.

In this work, a CZT [RSR69] based approach is used to zoom into each beat frequency peak to obtain a sub-bin frequency estimate, and thereby a more accurate ranging. The CZT computes the z-transform of input data $x[n]$ along spiral contours in the z-plane [RSR69, Blu70] according to

$$S_{\mathrm{b},k} = \sum_{n=0}^{N_{\mathrm{samp}}\text{-}1} s_{\mathrm{b}}[n] \cdot z_k^{-n} \,, \tag{3.124}$$

where k = 0,...,M-1, and $M \leq N_{\mathrm{samp}}$ is the number of data points in the resulting discrete CZT X_k. The CZT evaluation contour is described by z_k and given by,

$$z_k = \mathrm{e}^{\frac{j2\pi f_{\mathrm{start}}}{f_{\mathrm{samp}}}} \cdot \mathrm{e}^{\frac{j2\pi(f_{\mathrm{stop}}-f_{\mathrm{start}})k}{M f_{\mathrm{samp}}}} . \tag{3.125}$$

Here f_{start} and f_{stop} are frequencies corresponding to $m_{\mathrm{bin,FFT}}$ bins below and above the beat frequency peaks $f_{\mathrm{b,l,u,FFT}}$, and are given by,

$$f_{\mathrm{start}} = f_{\mathrm{b,l,u,FFT}} - m_{\mathrm{bin,FFT}} f_{\mathrm{bin,FFT}} \tag{3.126}$$

and

$$f_{\mathrm{stop}} = f_{\mathrm{b,l,u,FFT}} + m_{\mathrm{bin,FFT}} f_{\mathrm{bin,FFT}} . \tag{3.127}$$

With $M = N_{\mathrm{samp}} = 10\,\mathrm{k}$ points, a discrete CZT is computed taking $m_{\mathrm{bin,FFT}} = 2$ bins on both sides around each beat frequency peak. The frequencies $f_{\mathrm{b,l,u,CZT}}$ corresponding to the new peak values are then used to estimate the distance to the SRTs using (3.10). The resulting improved frequency bin resolution is

$$f_{\mathrm{bin,CZT}} = 2 m_{\mathrm{bin,FFT}} f_{\mathrm{bin,FFT}} / M = 0.4\,\mathrm{Hz} \,, \tag{3.128}$$

corresponding to a range per bin evaluated using (3.123) of $d_{\mathrm{bin,CZT}} = 240\,\mu\mathrm{m}$, around 2.5 k times improvement compared to the estimated range using on discrete FFT only method and approximately 125 times improvement when compared to discrete FFT with parabolic interpolation based method. An example scenario with $n = 40$ and $M = 100$ for faster computation is considered for the plot in Fig. 3.43. Fig. 3.43 shows that, though the magnitude of ranging error from FFT and CZT methods $d_{\mathrm{err,FFT,CZT}}$ are close to zero at multiples of $d_{\mathrm{bin,FFT}}$ where $\Psi = 0$, with an increasing Ψ, CZT shows orders of magnitude improvement. The maximum ranging error from the FFT method is $d_{\mathrm{err,FFT,max}} \approx 60\,\mathrm{cm}$, and from the CZT method is $d_{\mathrm{err,CZT,max}} \approx 2.4\,\mathrm{cm}$, a 25 times lower error as confirmed by experimental tests in Section 5.1.1.

Algorithm 1 Interrogator to SRT Distance estimation. ((Reused from *[TFJE23] ©2023 IET). from *[TFJE23] ©2023 IET).

```
Input: Digitized chirp sequence samples x[n]
Output: Distance estimate d_{SRT,c} in (3.10)
function DistanceToSRT(x[n])
    for each chirp c in the FMCW chirp sequence do
        Compute N_samp point FFT on time series data x[n]
        rss ← Sum up squared magnitude spectra
    end for
    Calculate spectral average from rss
    Call function for FFT peak search from f_{q,min} to f_{q,max}
    if atleast two peaks found then
        for each peak i do
            Determine f_start from (3.126) and f_stop from (3.127)
            Compute M point discrete CZT using (3.124)
            CZT peak search from f_start to f_stop
            if multiple CZT peak values then
                Calculate mean peak index
            end if
            Calculate f_peak from mean peak index
            f_b[i] ← f_peak
        end for
        f_{b,l,CZT} ← f_b[0]
        f_{b,u,CZT} ← f_b[1]
        if f_{b,l,CZT} + f_{b,u,CZT} equals 2f_q then
            Calculate distance d_{SRT,c} using (3.10)
        end if
    end if
end function
```

4 60 GHz Single Antenna RFID Interrogator based Identification System

This chapter begins with a discussion on the system design principles of passive RFID transponder detection using a CW single antenna interrogator. The system is based on a cooperative architecture where the detected tag has to give a specific response to allow detection. The focus is on the analysis, design, experimental characterization outcomes and knowledge acquired from the RFICs designed for the interrogator frontend. The last section of the chapter presents the details of the proof of concept system implemented using a custom designed passive RFID transponder for testing the important characteristics of the interrogator frontend.

4.1 System Design

The functional block diagram of the designed 60 GHz CW interrogator using a single antenna and one PLM based PBT is illustrated Fig. 4.1. In this system, a 60 GHz CW signal generated by an external signal source is split using a power divider and is fed as input to a PA in the $\mathrm{T_x}$ path and as LO input to a down-conversion mixer in the $\mathrm{R_x}$ path. The PA amplifies the input signal, and drives it to $\mathrm{ANT_{TR_x}}$ through the $\mathrm{T_x}$ port of a QC. QCs, are 3-port 2-way non-magnetic devices which provide transmission path between $\mathrm{T_x}$ port and $\mathrm{ANT_{TR_x}}$, and $\mathrm{ANT_{TR_x}}$ and $\mathrm{R_x}$ port, but isolation between $\mathrm{T_x}$ and $\mathrm{R_x}$ ports. The transmitted signal $s_{\mathrm{T_x}}$ with amplitude $A_{\mathrm{T_x}}$and frequency $f_{\mathrm{T_x}}$ is given by

$$s_{\mathrm{T_x}} = A_{\mathrm{T_x}} \cos 2\pi f_{\mathrm{T_x}} t. \tag{4.1}$$

From Fig. 4.1, we can see that $s_{\mathrm{T_x}}$ is received by the PBT which consists of an antenna $\mathrm{ANT_{PBT}}$ that is terminated with two different impedance values Z_1 and Z_2, controlled by a periodic signal. The PBT modulates s_{TX} by a subcarrier signal $m_{\mathrm{b}}(t)$ using ASK as illustrated in Fig. 4.2(a). $m_{\mathrm{b}}(t)$ encodes data corresponding to bits $b = 0$ or 1 within the symbol duration T_{s} given by $0 \leq t \leq T_{\mathrm{s}}$. The symbol rate $1/T_{\mathrm{s}}$ is relatively low compared to the carried frequency $f_{\mathrm{T_x}}$. The resulting backscatter signal s_{bs} is

$$s_{\mathrm{bs}}(t) = \alpha_{\mathrm{bs}} s_{\mathrm{T_x}} m_{\mathrm{b}}(t) \tag{4.2}$$

where $m_{\mathrm{b}}(t) = A_{\mathrm{b}}$, and A_{b} is one among two possible amplitude levels represented by data bit $b = 0$ or 1. α_{bs} determines the amplitude of s_{bs} and is a function of the RCS σ_{PBT} of the PBT.

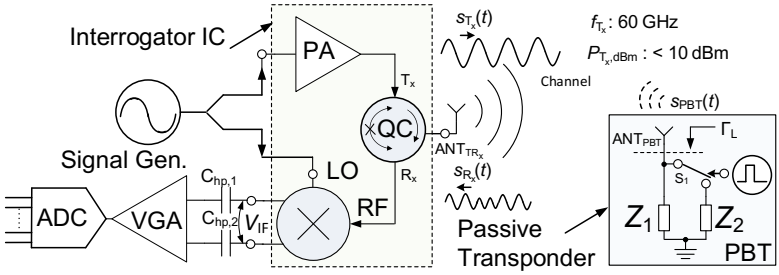

Figure 4.1: 60 GHz CW interrogator and passive backscatter transponder based identification system.

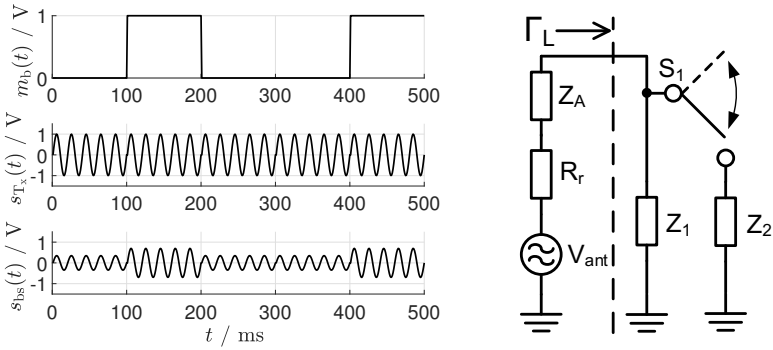

Figure 4.2: Passive load modulation: (a) ASK modulated PBT signals corresponding to a data of 5'b01001. (b) PBT equivalent circuit with antenna source impedance.

The impedance and thereby the $|\Gamma_L|$ presented by the PBT changes due to the periodic closing and opening of the switch S_1, and results in modulation of the reflected wave from the transponder. The equivalent circuit of the periodic switching of the RFID transponder antenna between two termination impedances $\underline{Z}_{1,2}$ can be represented as shown in Fig. 4.2. This impedance modulation results in a variation in the power scattered by the antenna due to changing RCS σ_{PBT} given by [Han89, NR06]

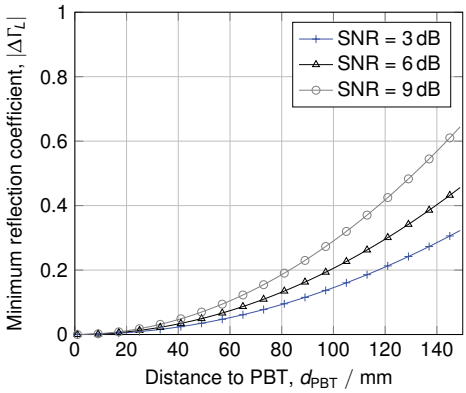

Figure 4.3: Minimum magnitude of load reflection coefficient to detect the PBT at a particular distance at different SNR values.

$$\sigma_{\mathrm{PBT}} = \frac{P_{\mathrm{bs,PBT}}}{P_{\mathrm{av,PBT}}} = \frac{V_{\mathrm{ant}}^2 R_{\mathrm{r}}}{P_{\mathrm{av,PBT}}[(R_{\mathrm{r}} + R_{1,2} + R_{\mathrm{ant}})^2 + (X_{1,2} + X_{\mathrm{ant}})^2]} \tag{4.3}$$

where $P_{\mathrm{av,PBT}}$ is the power incident on the PBT, $P_{\mathrm{bs,PBT}}$ is the power backscattered from the PBT, V_{ant} is the voltage across the antenna and R_{r} is the radiation resistance. $R_{1/2}$ and $X_{1,2}$ are the real and imaginary parts respectively of the termination impedance $Z_{1,2}$ and R_{ant} and X_{ant} are the real and imaginary parts respectively of the loss impedance of the antenna Z_{ant}.

The fraction of $s_{\mathrm{bs}}(t)$ radiated in the direction of the interrogator is received by the same interrogator antenna $\mathrm{ANT}_{\mathrm{TR_x}}$ and circulated to the $\mathrm{R_x}$ port of the QC with an integrated loss compensation amplifier (LCA). The direct conversion receiver front end downconverts $s_{\mathrm{R_x}}$ to $s_{\mathrm{R_x,bb}}$ and amplifies $s_{\mathrm{R_x,bb}}$ for retrieving the modulated signal and decoding data bits b.

Power Link Analysis

As shown in Fig. 4.1, the signal power from the signal generator P_{in} is divided with a loss of L_{PD} and given as input to the PA with gain G_{PA}. The signal power encounters loss $L_{\mathrm{QC,T_x}}$ through the $\mathrm{T_x}$ path of the QC, before being radiated

using $\mathrm{ANT_{TRx}}$ with gain $G_{\mathrm{TR_x}}$. The corresponding EIRP from the interrogator can be written as

$$\mathrm{EIRP}_{\mathrm{T_{R_x}}} = \frac{P_{\mathrm{in}} G_{\mathrm{PA}}}{L_{\mathrm{PD}} L_{\mathrm{QC,T_X}}}. \tag{4.4}$$

Using (4.4), the power received and available at the PBT, $P_{\mathrm{av,PBT}}$ can then be written as

$$P_{\mathrm{av,PBT}} = \mathrm{EIRP}_{\mathrm{T_{R_x}}} \cdot G_{\mathrm{T_{R_x}}} \cdot \frac{1}{4\pi d_{\mathrm{PBT}}^2} \cdot \frac{\lambda^2}{4\pi} G_{\mathrm{PBT}}. \tag{4.5}$$

Where G_{PBT} is the PBT antenna gain and d_{PBT} is the distance between PBT and the interrogator. As illustrated in the equivalent circuit of Fig. 4.2(b), the PBT periodically switches its impedance between termination impedances Z_1 and $Z_{\mathrm{p}} = Z_1 || Z_2$. The resultant load reflection coefficients $\Gamma_{\mathrm{L,Z1}}$ are $\Gamma_{\mathrm{L,Z_p}}$ respectively. Hence we can define a difference of reflection coefficients [XKK+09] $\Delta\Gamma_L$ as

$$\Delta\Gamma_L = \Gamma_{\mathrm{L,Z1}} - \Gamma_{\mathrm{L,Z_p}}. \tag{4.6}$$

Using (4.6), the backscattered power of the sidebands from the PBT is given by [XKK+09, KF03]

$$P_{\mathrm{bs,PBT}} = \frac{P_{\mathrm{av,PBT}}}{4} \left|\Delta\Gamma_{\mathrm{L}}\right|^2. \tag{4.7}$$

$P_{\mathrm{bs,PBT}}$ from (4.7) undergoes attenuation by free space path loss (FSPL) and the power received by the interrogator $P_{\mathrm{R_x,PBT}}$ can be determined as

$$P_{\mathrm{R_x,PBT}} = P_{\mathrm{bs,PBT}} \cdot G_{\mathrm{PBT}} \cdot \frac{1}{4\pi d_{\mathrm{PBT}}^2} \cdot \frac{\lambda^2}{4\pi} G_{\mathrm{TR_x}}. \tag{4.8}$$

This received power $P_{\mathrm{R_x,PBT}}$ is amplified in the $\mathrm{R_x}$ path of the QC with $G_{\mathrm{QC,RX}}$ and circulated to the downconversion mixer with a voltage conversion gain of $a_{\mathrm{v,dmix}}$, and is further amplified by a VGA with a gain $a_{\mathrm{v,VGA}}$ and digitized by an ADC. On defining the effective noise figure (NF) as $\mathrm{NF_{R_x}}$, the minimum SNR needed by the interrogator $\mathrm{SNR_{min}}$ and modulation bandwidth as $\mathrm{f_{BW,m}}$, the sensitivity of the interrogator $\mathrm{R_x}$ path, $P_{\mathrm{R_x,PBT,min}}$ can be determined using a similar approach from (3.17) as

$$P_{\mathrm{R_x,PBT,min}} = 10 \log \left(\frac{\mathrm{k_B T} f_{\mathrm{BW,m}}}{1\,\mathrm{mW}} \right) + \mathrm{SNR_{min}}. \tag{4.9}$$

Now based on the definition of FSPL from from (3.13),

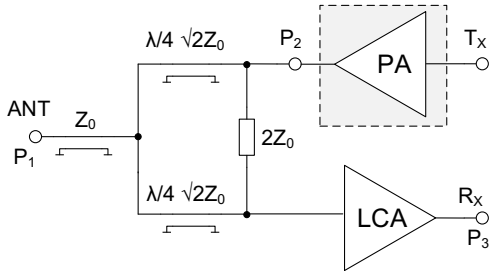

Figure 4.4: Block diagram of the transmission lines based QC_{TL}. (Reused from *[TPC+21]©2021, IEEE)

$$\mathrm{FSPL}_{\mathrm{PBT}} = \left(\frac{4\pi d_{\mathrm{PBT}}}{\lambda}\right)^4. \tag{4.10}$$

Substituting (4.10) and (4.8) in (4.9), $\Delta\Gamma_L$ can be derived as

$$|\Delta\Gamma_L| = \frac{4P_{\mathrm{R_x,PBT,min}}\mathrm{FSPL}_{\mathrm{PBT}}}{G^2_{\mathrm{TR_x}}G^2_{\mathrm{PBT}}\mathrm{EIRP}_{\mathrm{TR_x}}}. \tag{4.11}$$

Since $\mathrm{FSPL}_{\mathrm{PBT}}$ is a function of d_{PBT}, the $|\Delta\Gamma_L|$ can be plotted as a function of distance as shown in Fig. 4.3 and the minimum SNR, min required for system design can be estimated.

4.2 RFIC Designs

The CW interrogator frontend in the system concept envisaged in Fig. 4.1 is realized by designing a combination of QC IC and downconversion mixer IC. QC designs are described in Section 4.2.1 and the downconversion mixer design details are covered in Section 4.2.2.

4.2.1 Quasi-circulator ICs

Analysis, design and characterization of two different QC designs is done. Both QCs are implemented using a Wilkinson power divider (WPD) based passive compensation technique [RNDK19]. A comparative study of the two QCs is done to select the optimum design for the low power interrogator frontend IC.

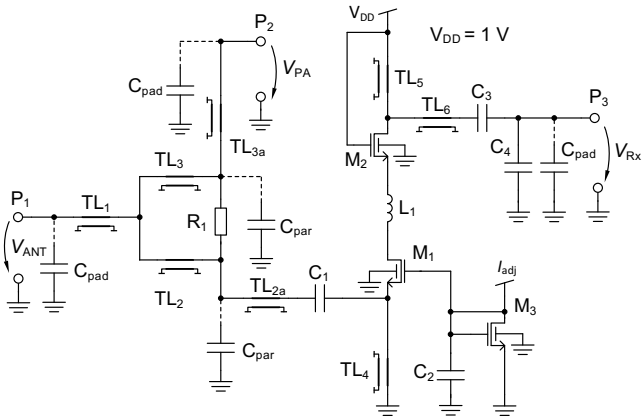

Figure 4.5: Schematic of the transmission line based QC_{TL}. (Reused from *[TPC+21]©2021, IEEE).

4.2.1.1 Transmission Lines based Quasi-Circulator IC

The block diagram of a RF front end interfaced to a single antenna using a 3-port 2-way QC is shown in Fig. 4.4. The design is based on a WPD formed by quarter wavelength ($\lambda_{QC}/4$) transmission lines $TL_{2\text{-}3}$ at the center frequency f_{QC} and resistor R_1. Under impedance matched conditions, the ideal scattering matrix of a WPD can be written from [Poz12] as,

$$[\underline{S}_{\text{WPD}}] = \frac{-j}{\sqrt{2}} \begin{bmatrix} 0 & 1 & 1 \\ 1 & 0 & 0 \\ 1 & 0 & 0 \end{bmatrix}. \tag{4.12}$$

According to (4.12), when a T_x signal with power P_{T_x} is fed directly at P_2, $P_{T_x}/2$ is delivered into the antenna port P_1. Similarly, power received by ANT at port P_1 is divided equally between ports P_2 and P_3. Also inherent to WPD is the bilateral isolation between ports P_2 and P_3, resulting in $\underline{S}_{23} = \underline{S}_{32} = 0$. Now, if two unilateral amplifiers, a PA with gain G_{PA} and a LCA with gain G_{LCA} are added at ports P_2 and P_3, respectively, the scattering matrix of the resulting

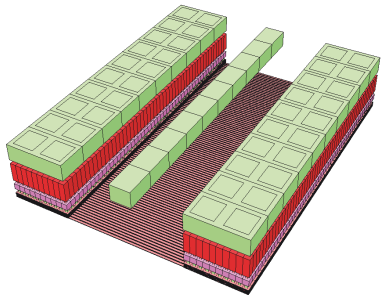

Figure 4.6: Isometric view of the 70 Ω GCPW transmission line used for the WPD. (Reused from *[TPC+21]©2021, IEEE).

network shown in Fig. 4.4 can be written as

$$[\underline{S}_{\mathrm{QC}}] = \frac{-j}{\sqrt{2}} \begin{bmatrix} 0 & G_{\mathrm{PA}} & 0 \\ 0 & 0 & 0 \\ G_{\mathrm{LCA}} & 0 & 0 \end{bmatrix}. \tag{4.13}$$

From (4.13), it can be seen that the reverse isolation of PA and LCA makes the network non-reciprocal, and corresponds to the QC scattering matrix defined in [RNDK19]. The gain of these amplifiers also compensates for the losses introduced by the passive WPD on the relatively small received signal power $P_{\mathrm{R_x}}$, without getting the input saturated by the relatively large signal power $P_{\mathrm{T_x}}$.

Circuit Analysis and Design: The schematic of the designed QC, for use in combination with an external PA is shown in Fig. 4.5. The characteristic impedance of the quarter wave transmission lines $\mathrm{TL_{2\text{-}3}}$, $\underline{Z}_{\mathrm{TL2\text{-}3}}$ is calculated as

$$\underline{Z}_{\mathrm{TL2\text{-}3}} = \sqrt{\underline{Z}_{\mathrm{ANT}} * \underline{Z}_{\mathrm{c}}} \tag{4.14}$$

where $\underline{Z}_{\mathrm{ANT}}$ is the antenna port impedance and the characteristic impedance $\underline{Z}_{\mathrm{c}} = \underline{Z}_{\mathrm{out,PA}} = \underline{Z}_{\mathrm{in,LCA}} = 50\,\Omega$. The WPD is implemented using grounded coplanar waveguide (GCPW) transmission lines with characteristic impedance $\underline{Z}_{\mathrm{TL2\text{-}3}}$, realized in the back end of line (BEOL) of the technology described in [OLC+18]. As shown in Fig. 4.6, the topmost aluminum metal layer is used as the signal layer, and the lowest intermediate layer is used as bottom ground plane. The ground plane is also made patterned to meet the local and global metal density requirements for the technology. EM simulations are used to optimize the bends

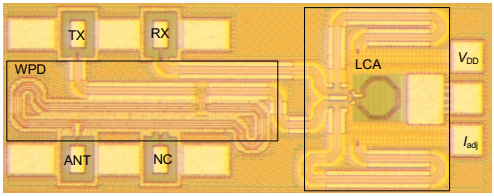

Figure 4.7: Photograph of the fabricated QC measuring 1150 µm × 430 µm. (Reused from *[TPC+21]©2021, IEEE).

and T-junctions to create a compact layout as shown in Fig. 4.7.

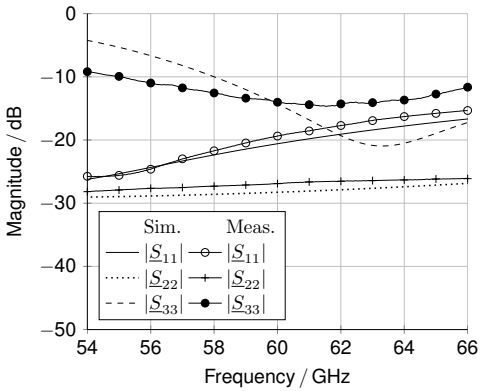

Figure 4.8: Measured and simulated QC_{TL} input reflection coefficients: ANT ($|\underline{S}_{11}|$), T_x ($|\underline{S}_{22}|$) and R_x ($|\underline{S}_{33}|$). (Reused from *[TPC+21]©2021, IEEE).

The value of resistor R_1 is calculated as

$$R_1 = 2 \cdot Z_c \approx 100\,\Omega \tag{4.15}$$

for maximum passive isolation [Poz12]. Unsilicided N+ diffusion resistors used to implement R_1 can have process variations up to 20 %. The implemented structure also has parasitic capacitances C_{par} at each port, which affects the circuit parameters including isolation. The insertion loss from P_1 to P_2, which includes the insertion loss of the WPD, losses due to C_{pad}, C_{par} and R_1 variations, $TL_{1\text{-}3a}$ losses and associated interface mismatch determined by EM simulations, amount

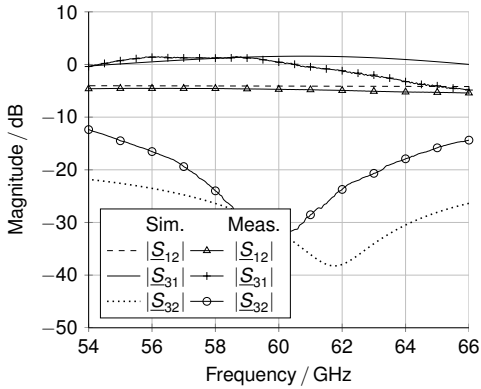

Figure 4.9: Measured and simulated QC_{TL} transmission coefficients: T_x to ANT. ($|\underline{S}_{12}|$), ANT. to R_x ($|\underline{S}_{31}|$) and T_x to R_x ($|\underline{S}_{32}|$). (Reused from *[TPC+21]©2021, IEEE).

to $\approx 5.2\,\text{dB}$. In order to compensate for both the process variations and conductor losses, a two stage common gate (CG) LCA with gain G_{LCA} and tunable input impedance $Z_{\text{in,LCA}}$ is implemented using grounded back-gate nFETs $M_{1\text{-}2}$.

The variations in WPD input impedance at the LCA input is compensated by the first stage CG amplifier implemented using M_1 which is biased using a current mirror with input current I_{adj}. The real part of the input impedance, which is a function of transconductance $g_{\text{m,M1}} \propto \sqrt{kI_{\text{adj}}}$, is calculated as

$$\mathfrak{Re}Re(Z_{\text{in,M1}}) \approx \frac{1}{g_{\text{m,M1}}} + \frac{R_{\text{p,L1}} \parallel 1/g_{\text{m,M2}}}{1 + \frac{g_{\text{m,M1}}}{g_{\text{o,M1}}}} \approx 50\,\Omega, \tag{4.16}$$

where $g_{\text{m,M1-2}}$ is the transconductance of M_{1-2} and $g_{\text{o,M1}}$ is the output conductance of M_1. $R_{\text{p,L1}}$ is the loss of the inductor L_1 and is calculated from the unloaded quality factor $Q_{\text{L1}} \approx 20$ and series resistance $R_{\text{s,L1}}$ as

$$R_{\text{p,L1}} = R_{\text{s,L1}} \cdot (1 + Q_{\text{L1}}^2) \tag{4.17}$$

at $f_{\text{QC}} = 60\,\text{GHz}$. The inductor L_1 is added to optimize gain and noise figure (NF), and together with the gate source capacitances $C_{\text{gd,M1}}$ and $C_{\text{gs,M2}}$ in the decade femtofarad range, form an artificial transmission line, with characteristic impedance,

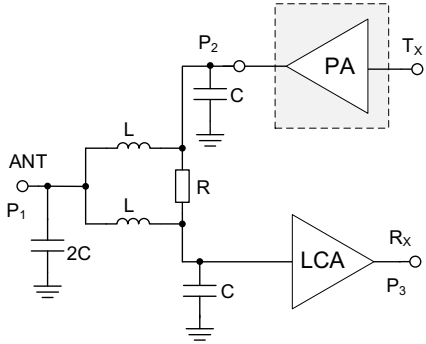

Figure 4.10: Block diagram of the lumped elements based QC_{LC}.

$$Z_{0,\mathrm{LC}} = \sqrt{\frac{L_1}{C_{\mathrm{gd,M1}} + C_{\mathrm{gs,M2}}}}. \tag{4.18}$$

The output impedance transformation network, implemented using transmission lines $TL_{5\text{-}6}$ and capacitors C_3 and the equivalent capacitance of C_4 in the hundred femtofarad range and pad capacitance C_{pad}, with an impedance Z_{out} is used to obtain a cascaded gain CG cascode amplifier, $|\underline{a}_{\mathrm{v,LCA,TL}}|$ according to,

$$\underline{a}_{\mathrm{v,LCA,TL}} = g_{\mathrm{m,M1}} \underline{Z}_{\mathrm{out}} \approx 5 \tag{4.19}$$

4.2.1.2 Lumped Elements WPD based Quasi-Circulator

When the transmission lines in the QC_{TL} of Fig. 4.4 are replaced with equivalent LC networks as shown in Fig. 4.10, a lumped element WPD (LWD) based QC_{LC} can be designed. LWD has the advantage of significantly reducing the area of the QC implementation. The availability of high Q passive elements enable such an implementation in the used FDSOI technology as described in Section 2.7.2.

From Fig. 4.4, we can see that inductor L together with capacitor C form two π-networks. At the center frequency $f_{\mathrm{QC}} = 60\,\mathrm{GHz}$, with a target bandwidth $f_{\mathrm{BW,QC}}$, the unloaded quality factor required for the network can be determined as

$$Q_{\mathrm{LC}} = \frac{f_{\mathrm{QC}}}{f_{\mathrm{BW,QC}}}. \tag{4.20}$$

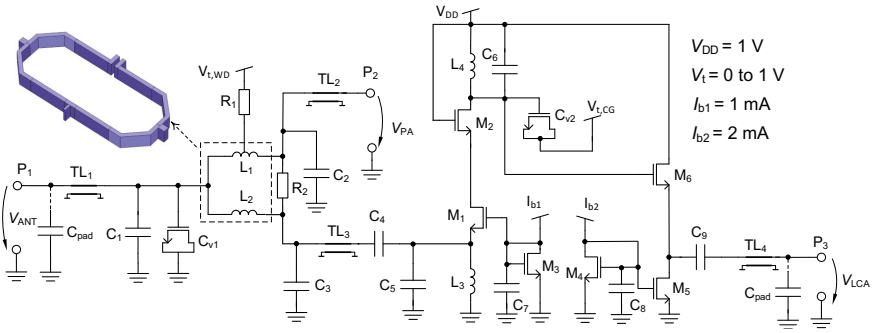

Figure 4.11: Schematic of the lumped elements based $\mathrm{QC_{LC}}$.

Also the characteristic impedance of the LC network is [Poz12]

$$\underline{Z}_{\mathrm{LC}} = \sqrt{\underline{Z}_{\mathrm{ANT}}\underline{Z}_{\mathrm{c}}} \tag{4.21}$$

where Z_{ANT} is the antenna port impedance and Z_{c} the characteristic impedance given by $Z_{\mathrm{c}} = Z_{\mathrm{out,PA}} = Z_{\mathrm{in,LCA}} = 50\,\Omega$.

The real and imaginary parts of $\underline{Z}_{\mathrm{LC}}$ can determined using (4.20) as,

$$\begin{aligned} \mathfrak{Re}(\underline{Z}_{\mathrm{LC}}) &= \sqrt{\frac{|\underline{Z}_{\mathrm{LC}}|^2}{1+Q_{\mathrm{LC}}^2}} \\ \mathfrak{Im}(\underline{Z}_{\mathrm{LC}}) &= Q_{\mathrm{LC}} \cdot \mathfrak{Re}(\underline{Z}_{\mathrm{LC}}). \end{aligned} \tag{4.22}$$

Using (4.22), the inductance and capacitance of the LWD π-network can be written as

$$\begin{aligned} L &= \frac{\mathfrak{Im}(\underline{Z}_{\mathrm{LC}})}{2\pi f_{\mathrm{QC}}} \\ C &= \frac{L}{\mathfrak{Im}(\underline{Z}_{\mathrm{LC}})^2}. \end{aligned} \tag{4.23}$$

Circuit Analysis and Design: The schematic of the designed lumped elements based $\mathrm{QC_{LC}}$ is shown in Fig. 4.11. The inductor is L of the LWD is determined using (4.23) and is implemented as $L_{1,2}$ using the custom inductive structure shown in the inset of Fig. 4.11. The topmost copper metal layer in the BEOL of the technology described in Section 2.7.2 is used as the signal layer, and the lowest

intermediate layer is used as bottom patterned ground plane. EM simulations are used to optimize the structure to create the optimized layout shown in Fig. 4.12.

The capacitance C is implemented using APMOM capacitors in the technology. At port P_1, the parallel combination of C_1 and C_{v1} sets the required equivalent capacitance

$$2C \approx C_1 + C_{v1}(V_{t,WD}) \tag{4.24}$$

where C_{v1} is an NMOS varactor whose capacitance is tuned by the voltage $V_{t.WD}$ to trim phase variations in LWD. $V_{t.WD}$ is supplied through resistor R_1 which interfaces to the fourth port of the inductive structure shown in Fig. 4.11. Resistor R_2 is similar to R_1 in Section 4.2.1.1 and is calculated using (4.15) for maximum passive isolation [Poz12], and has process variations up to 20 %. EM simulations shows that the LWD introduces ≈ 5.6 dB insertion loss.

The LCA of the LWD is implemented as the cascade of a CG input amplifier M_1, CG tuned amplifier M_2 and a common drain (CD) amplifier M_3. When compared to Fig. 4.5, the transmission line TL_4 is replaced by inductor L_1 at the source of the CG cascode amplifier input nFET M_1. M_1 is biased by the current mirror nFET M_3 with input current I_{b1}. The real part of the input impedance, which is a function of transconductance of M_1, $g_{m,M1} \propto \sqrt{kI_{b1}}$,can be derived as

$$\mathfrak{Re}(Z_{in,M1}) \approx \frac{1}{g_{m,M1}(I_{b1})||R_{p,L1}}, \tag{4.25}$$

where $R_{p,L1}$ is the equivalent parallel resistance of L_1 and is determined using (4.17) with the unloaded quality factor Q_{L1} and series resistance $R_{s,L1}$ obtained from EM simulations at $f_{QC} = 60$ GHz.

The voltage gain of the LCA, $a_{v,LCA}$ is the product of the voltage gains of the first stage tuned CG amplifier $a_{v,CG}$ and the second stage CD amplifier $a_{v,CD}$. But since $a_{v,CD} \approx 1$,

$$a_{v,LCA} = \frac{v_{LCA}}{v_{in,CG}} = a_{v,CG}a_{v,CD} \approx g_{m,M1}\underline{Z}_{CG} \tag{4.26}$$

where $\underline{Z}_{CG}$ is the impedance of the tuned load which the parallel combination of the reactance of inductance L_4 and the equivalent capacitance $C_{eq,CG}$, and can be derived as

$$\underline{Z}_{CG} = \frac{j\omega L_4 R_{p,eq}}{R_{p,eq}(1-\omega^2 C_{eq,CG}L_4) + j\omega L_4}. \tag{4.27}$$

$C_{eq,CG}$ is the equivalent capacitance of the tuned load which includes the gate to drain capacitance of $M_{2,6}$, $C_{gd,M2,6}$, a fraction of the gate to source capacitance

of M_6, $C_{gd,6}$, the tuned load capacitor C_6 and the transformed parallel varactor capacitance $C_{v2,P}$ which is controlled by the tuning voltage $V_{t,CG}$, and is given by

$$C_{eq,CG} \approx C_6 + C_{v2,P}(V_{t,CG}) + C_{gd,M2} + C_{gd,M6} + (1 - a_{v,CD})C_{gs,M6}. \quad (4.28)$$

$C_{v2,P}$ is given by

$$C_{v2,P} = C_{v2}\frac{Q_{v2}^2}{1 + Q_{v2}^2}, \quad (4.29)$$

with

$$Q_{v2} = \frac{1}{\omega C_{v2} R_{s,v2}} \quad (4.30)$$

where $R_{s,v2}$ is the series equivalent resistance of C_{v2} obtained from simulations. $R_{p,eq}$ is the equivalent parallel resistance $R_{p,L4}$ of L_4 and the equivalent parallel resistance resulting from the quality factor of the capacitors and varactor C_{v2} $R_{p,C}$ at the drain of M_2. $R_{p,L4}$ is determined from the series resistance and unloaded quality factor calculated in a similar manner as (4.17) as

$$R_{p,L4} = R_{s,L4}(1 + Q_{L4}^2), \quad (4.31)$$

and $R_{p,C}$ is the parallel network of the transformed series resistance of the varactor C_{v2} and the real part of the input impedance looking into M_6.

$$R_{p,C} = \frac{1}{\omega Q_{v2} C_{v2}} || \mathfrak{Re}\underline{Z}_{in,M6}. \quad (4.32)$$

By varying $V_{t,CG}$, the capacitance of the varactor C_{v2} and thereby the center frequency of the bandpass filter formed by the tuned load can be varied to adapt to process variations. I_{b2} is used to set the bias current and tune the output impedance of the M_6 based CD stage which drives a $50\,\Omega$ load, and has an output impedance $\underline{Z}_{out,CD}$ which is also the output impedance of the LCA

$$\underline{Z}_{out,CD} = \underline{Z}_{out,LCA} \approx \frac{1}{g_{m,M6}}. \quad (4.33)$$

By substituting parameters extracted from simulation in (4.26), the resultant cascaded voltage gain is obtained as $|\underline{a}_{v,LCA}| \approx 14.5$. The loss of the LWD reduces the effective gain of the QC_{LC} to around 7.5 as shown in the simulation results of Fig. 4.13(b).

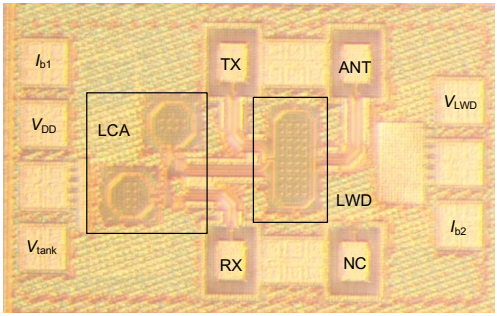

Figure 4.12: Photograph of the fabricated QC_{LC} measuring 755 µm × 450 µm including pads.

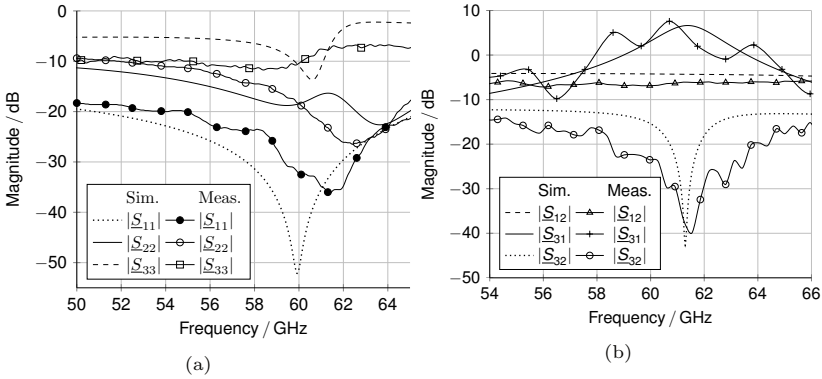

Figure 4.13: Measured and simulated QC_{LC} $\underline{S}$ parameters (a) Input reflection coefficients. (b) Transmission coefficients : T_x to ANT. $|\underline{S}_{12}|$, ANT. to R_x $|\underline{S}_{31}|$ and T_x to R_x $|\underline{S}_{32}|$.

4.2.1.3 Characterization

To prove the design concepts, QC_{TL} and QC_{LC} are implemented in a 22 nm FDSOI technology. The QC_{TL} IC shown in Fig. 4.7 and QC_{LC} shown in Fig. 4.12 are measured on a Süss probe station with 67 GHz Cascade Microtech GSGSG Infinity probes. S-parameter measurements are done using the R & S® ZVA-67 network analyzer with four port hybrid short-open-load-through (SOLT)-short-open-load-reciprocal (SOLR) calibration. Linearity measurements are also done

using the network analyzer, after doing power calibration using the R & S® NRP-Z57 power meter. Also, the R & S® FSW-67 in combination with a Noisecom NC5115 noise source is used for noise figure measurements.

For QC_{TL}, the plot of the characterized magnitude of input reflection coefficients in Fig. 4.8 shows that all three ports are matched to less than −10 dB in the frequency range of 56 GHz to 64 GHz, aligning well with simulation results. Fig. 4.9 shows the measured transmission coefficients and comparisons with simulation. The T_x to ANT insertion loss is around 5.7 dB, ANT to R_x gain is 2 dB and T_x to R_x isolation is better than 20 dB in the 57 GHz to 63 GHz range, and better than 30 dB around 60 GHz, aligning well with the simulation results. A relatively high NF of 14 dB resulting from the combined NF of the WPD and LCA. The circuit draws 5.4 mA from a 1 V power supply.

For QC_{LC}, the magnitude of the reflection coefficients is plotted in Fig. 4.13(a) and shows that ANT port and T_x port are matched to less than −10 dB in the similar frequency range as that of QC_{TL}, from 54 GHz to 64 GHz, while the R_x port is matched in the narrow band of 56 GHz to 60.5 GHz. Fig. 4.13(b) shows the measured transmission coefficients and comparisons with simulations. The T_x to ANT insertion loss is around 6.1 dB, ANT to R_x peak gain is 8.5 dB at 60.9 GHz and T_x to R_x isolation is better than 10 dB in the 54 GHz to 64 GHz range, and better than 27 dB from 58.5 GHz to 64 GHz, aligning well with the simulation results. The measured NF is around 8 dB at 60 GHz and is the combined NF of the LWD, LCA and the interfacing transmission lines. It is tolerable for the targeted application of a close range integrated RFID interrogator. QC_{LC} consumes around 12.2 mW also from a 1 V power supply. The characterization results of both QCs are summarized in Table 4.1.

4.2.1.4 Knowledge Gained

Circulators are 3-port 3-way devices that enables a common ANT to be interfaced simultaneously with the T_x and R_x front ends of the RFID interrogator. They are typically ferrite based off-chip components which are costly and bulky [Poz12]. One approach to achieve similar functionality is to use a rat-race coupler, which occupies a large area making it not suitable for integrated applications, and have a relatively narrow bandwidth [Poz12]. Enabled by advances in semiconductor technology, recently, there has been quite some research interest on non-magnetic silicon based integrated circulators [NK19] and 3-port 2-way non-magnetic QCs [TGX+19, WLW16, TLH+16, FB17, CKLW15, PWJS15]. While many of the integrated active ICs reported in literature are at low frequencies [TGX+19, WLW16, TLH+16, FB17], RF implementations like [TGX+19, WLW16] have relatively low

linearity and transmit power handling capability. They also occupy a large area [NK19] and consume high power [TLH+16].

Both QC_{TL} and QC_{LC} are compact low power 60 GHz QC implementations using a passive cancellation technique [RNDK19], where a WPD in combination with an active LCA is used. The WPD provides passive isolation between T_x and R_x ports, improved T_x to ANT path linearity, and high bandwidth and transmit power handling capacity as is evident from Table 4.1. The LCA in the R_x path compensates the insertion loss in the ANT to R_x path and enables non-reciprocity and tunable isolation. While both QCs occupy relatively low area, the use of lumped elements give QC_{LC} the upper hand. The two stage approach of QC_{LC} employing a tuned first stage load also helps to increase the gain compared to QC_{TL}. But the use of a tuned load results in a relatively narrow bandwidth when compared to QC_{TL}.

Table 4.1: Comparison with state-Of-the-art integrated active quasi-circulators

Ref.	f_{QC} / GHz	T_x to ANT $\lvert S_{21}\rvert$ / dB	ANT to R_x $\lvert S_{32}\rvert$ / dB	T_x to R_x Isolation $-\lvert S_{31}\rvert$ / dB	T_x to ANT $P_{L,OP1dB}$ / dBm	NF / dB	P_{DC} / mW	Area / mm^2	Tech.
[PWJS15]	76-80	-0.3 to -1	-1.5	> 16	1	11[a]	60	0.07[b]	0.18 µm SiGe
[CKLW15]	24.17-24.55	-5.7	-5.7	20	9.5[c]	N.R.	7.2	0.72	0.18 µm CMOS
[WLW16]	9.9	-2 to 7	-2 to 7	> 17.3	-6.1	6.5	18.6	0.72	0.18 µm CMOS
[TLH+16]	10-67	-0.5 to -4.8	-1.1 to -4.3	23.4 to 31.3	7	7.9 to 12.8	67.8	0.51	90 nm SOI
[FB17]	5.3-7.3	10.5	-5	> 30	4.5	N.R.	415	1.57	45 nm SOI
[TGX+19]	1-7	10	9	36	-1.6	16-20	25.2	0.57	0.18 µm CMOS
[NK19]	50-56.8	-3.9	-3.1	> 40	13	3.20	24.14	1.72	45 nm SOI
QC_{TL}	**56-64**	**-5.7**	**2**	**20 to 32**	**10**	**14**	**5.4**	**0.49**	**22 nm FDSOI**
QC_{LC}	**59.5-61.5**	**-6.1**	**8.5**	**20 to 37**	**10**	**8**	**13.2**	**0.34**	**22 nm FDSOI**

[a] Simulations only [b] Area does not include pads [c] Input compression

4.2.2 Folded Switching Stage Downconversion Mixer IC

The downconversion mixer in Fig. 4.2(a) is implemented using the novel FSSDM topology *[TSJE21]. The FSSDM is based on a modified single-balanced Gilbert cell using a classic cascode amplifier input transconductance stage, a pFET based folded switching stage and a tunable load IF stage. The output IF stage transistors make use of the back-gate control of the FDSOI devices for offset, amplitude imbalance correction and conversion gain tuning.

4.2.2.1 FSSDM Circuit Design

The schematic of the FSSDM is shown in Fig. 4.14 and the comprehensive small signal model of the FSSDM excluding balun and the output load tuning circuit is depicted in Fig. 4.15. The RF input is single-ended while the IF output is differential. A single-ended LO input in combination with an integrated transformer balun generates the differential LO switching signals.

4.2.2.2 Cascode Transconductance Stage

The RF input voltage V_{RF} is converted to RF current I_{RF} by the transconductance stage formed by nFETs $\mathrm{M}_{1,2}$, biased at an optimum minimum NF current density $J_{\mathrm{M1,2,opt}}$. nFETs $\mathrm{M}_{1,2}$ are dimensioned with a channel width $W_{\mathrm{M1,2}}$, and the bias current $I_{\mathrm{b,RF}}$ is set as $I_{\mathrm{b,RF}} \approx 5.2\,\mathrm{mA}$ resulting in corresponding transconductance $g_{\mathrm{m,M1}}$. The biasing is done using $\mathrm{M_m}$, which mirrors the reference current set using $V_{\mathrm{b,RF}} \approx 1.4\,\mathrm{V}$ in combination with resistor R_{m}. The corresponding input impedance of M_1 is $\underline{Z}_{\mathrm{in,M1}} = R_{\mathrm{in,M1}} + jX_{\mathrm{Cin,M1}}\,\Omega$ and is capacitive at 60 GHz.

The RF input port with a source impedance of $50\,\Omega$ is conjugate matched to the input of M_1 using transmission line TL_1, capacitor C_1 and inductance L_1. L_1 also functions as a DC feed to bias M_1 and has an unloaded quality factor Q_{L1}. TL_1 is a GCPW based transmission line, having a signal conductor width W_{TL} and spacing to ground walls S_{TL}, implemented in the thickest copper layer of the technology. M_2 is the CG stage of the cascode amplifier. In addition to reducing the Miller effect [Ell07, Voi13], which causes high frequency gain roll off, and reverse transmission to facilitate better input matching, M_2 also helps to improve LO to RF isolation in the mixer, and provides a high output impedance at the folding node $\mathrm{N_{fold}}$.

The transcoductance of the RF input stage is defined as

$$\underline{G}_{\mathrm{m,RF}} = \frac{\underline{I}_{\mathrm{RF}}}{\underline{V}_{\mathrm{RF}}}. \tag{4.34}$$

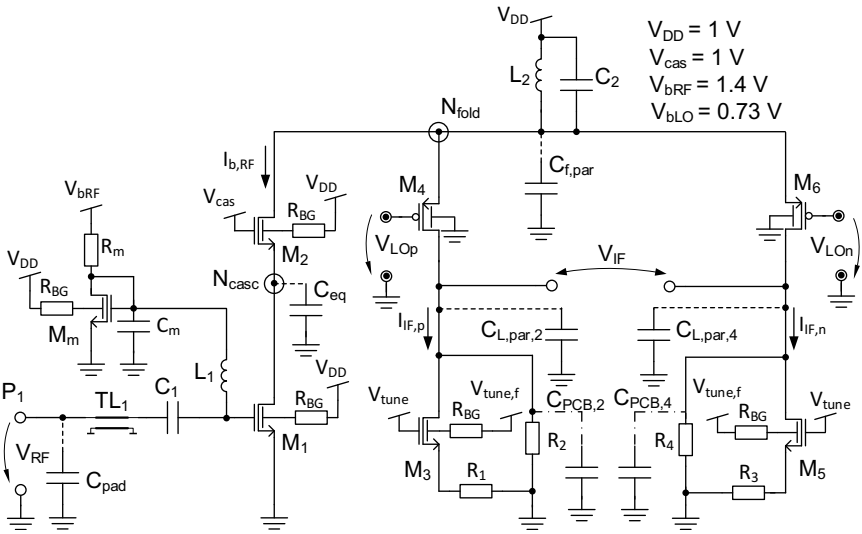

Figure 4.14: Circuit schematic of the designed 60 GHz FSSDM (Reused from *[TSJE21] © 2021 IEEE).

In order to analyze $\underline{G}_{\mathrm{m,RF}}$ and other small signal parameters, the simplified high frequency equivalent circuit in Fig. 4.16 and Fig. 4.17 is considered. To enable hand calculation, parameters [Voi13] in the comprehensive model illustrated in Fig. 4.15 like the transconductance delay τ, the channel access resistance R_{i}, the series resistive parasitics R_{g}, R_{d} and R_{s} at the gain, drain and source respectively of the metal oxide semiconductor FETs (MOSFETs) are not considered. Though these parameters affect the performance of the circuit at 60 GHz operating frequency of the FSSDM, the compact model simulations are relied for optimization based on the contribution from each parameter.

From Fig. 4.16 we can see that the input transconductance stage is the cascade of a common source (CS) amplifier formed by M_1 and CG amplifier formed by M_2. The RF input voltage $\underline{V}_{\mathrm{RF}}$ is applied across the input capacitance $C_{\mathrm{in,1}}$ and equals the gate to source voltage of M_1, $\underline{V}_{\mathrm{gs,1}}$. $C_{\mathrm{in,1}}$ is the equivalent parallel combination of the gate to source capacitance $C_{\mathrm{gs,1}}$ and the gate to drain capacitance $C_{\mathrm{gd,1}}$ scaled by the voltage gain according to Miller's theorem with

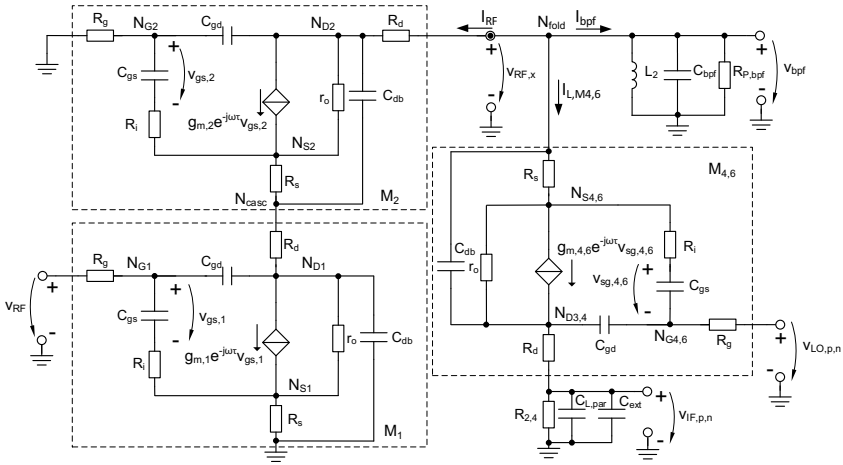

Figure 4.15: The complete small signal equivalent circuit of FSSDM core excluding balun and the output load tuning circuit.

$$C_{\mathrm{in},1} = C_{\mathrm{gs},1} + (1 - \underline{a}_{\mathrm{v},1}(0))C_{\mathrm{gd},1}. \tag{4.35}$$

which controls the output current of M_1 as $g_{\mathrm{m},1}$ driven into node N_{casc} given by,

$$\underline{I}_1 = -g_{\mathrm{m},1}\underline{V}_{\mathrm{gs},1} = -g_{\mathrm{m},1}\underline{V}_{\mathrm{RF}}. \tag{4.36}$$

At node N_{casc}, I_1 is split into three branches. The dominant one being the input current of the CG amplifier based on M_2. Of the other two components, the current through the equivalent capacitance C_{eq} leads to losses at 60 GHz. C_{eq} is the parallel combination of drain to source capacitance $C_{\mathrm{ds},1}$, drain to body capacitance $C_{\mathrm{db},1}$, and gate to drain capacitance $C_{\mathrm{gd},1}$ of M_1, together with the gate to source capacitance $C_{\mathrm{gs},2}$ and source to body capacitance $C_{\mathrm{sb},2}$ of M_2, and is given by,

$$C_{\mathrm{eq}} = C_{\mathrm{ds},1} + C_{\mathrm{db},1} + (1 - \frac{1}{\underline{a}_{\mathrm{v},1}(0)})C_{\mathrm{gd},1} + C_{\mathrm{gs},2} + C_{\mathrm{sb},2}. \tag{4.37}$$

With reference to Fig. 4.16 and applying Kirchhoff's current law (KCL) at node $\mathrm{N}_{\mathrm{mid}}$, the current $\underline{I}_2$ is determined according to

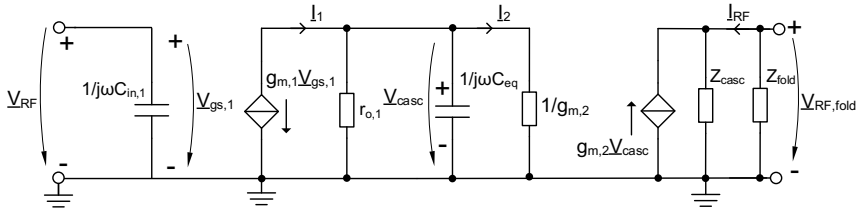

Figure 4.16: The simplified high frequency small signal equivalent circuit used for the analysis of the cascode transconductance amplifier based RF input stage of the FSSDM.

$$\underline{I}_2 = \frac{-g_{\mathrm{m},1}\underline{V}_{\mathrm{RF}}(r_{\mathrm{o},1}||\frac{1}{j\omega C_{\mathrm{eq}}})}{\frac{1}{g_{\mathrm{m},2}} + (r_{\mathrm{o},1}||\frac{1}{j\omega C_{\mathrm{eq}}})}. \tag{4.38}$$

When substituting model parameters in (4.38) we can see that C_{eq} shunts around 5 % of $\underline{I}_1$ at node Ncasc, and a 50 % reduction in $r_{\mathrm{o},1}$ reduces $\underline{I}_1$ by another 10 %. An inductor based matching network would significantly reduce $\underline{I}_1$ shunting due to C_{eq} at the cost of chip area. So as a trade off, narrow inductive interconnects are used between drain of M_1 and source of M_2. To increase $r_{\mathrm{o},1}$, M_1 is biased near weak inversion region. Also since

$$\underline{V}_{\mathrm{casc}} = \frac{\underline{I}_2}{g_{\mathrm{m},2}}, \tag{4.39}$$

the output current $\underline{I}_{\mathrm{RF}}$ can be determined using (4.39) with respect to Fig. 4.16 as,

$$\underline{I}_{\mathrm{RF}} = -\underline{I}_2 \frac{\underline{Z}_{\mathrm{casc}}}{\underline{Z}_{\mathrm{casc}} + \underline{Z}_{\mathrm{fold}}}. \tag{4.40}$$

$\underline{Z}_{\mathrm{casc}}$ is the output impedance of the cascode transconductance stage determined according to,

$$\begin{aligned}\underline{Z}_{\mathrm{casc}} = \left.\frac{\underline{V}_{\mathrm{RF,fold}}}{\underline{I}_{\mathrm{RF}}}\right|_{V_{\mathrm{RF}}=0} &= (r_{\mathrm{o},2}||\frac{1}{j\omega C_{\mathrm{gd},2}})[1 + g_{\mathrm{m},2}(r_{\mathrm{o},1}||\frac{1}{j\omega C_{\mathrm{eq}}})] \\ &\approx g_{\mathrm{m},2} r_{\mathrm{o}}^2,\end{aligned} \tag{4.41}$$

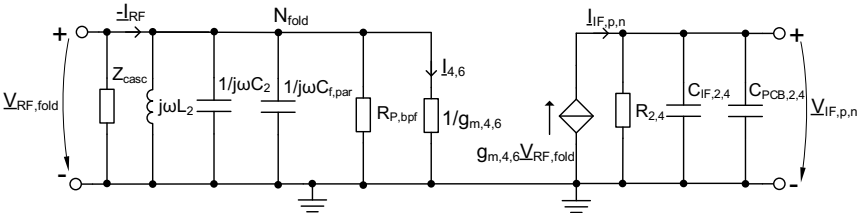

Figure 4.17: Small signal equivalent circuit used for the analysis of the LC band-pass filter load of the FSSDM.

assuming identical devices with $r_{\mathrm{o}} = r_{\mathrm{o},1} = r_{\mathrm{o},2}$.

Substituting (4.38) and (4.34) in (4.40) gives $G_{\mathrm{m,RF}}$,

$$\underline{G}_{\mathrm{m,RF}} = \frac{g_{\mathrm{m},1}\left(r_{\mathrm{o},1}\|\frac{1}{j\omega C_{\mathrm{eq}}}\right)}{\left[\frac{1}{g_{\mathrm{m},2}} + \left(r_{\mathrm{o},1}\|\frac{1}{j\omega C_{\mathrm{eq}}}\right)\right]} \cdot \frac{\underline{Z}_{\mathrm{casc}}}{\underline{Z}_{\mathrm{casc}} + \underline{Z}_{\mathrm{fold}}}. \tag{4.42}$$

$\underline{Z}_{\mathrm{fold}}$ is the equivalent impedance from the parallel combination of the band pass filter (BPF) and the folded switching stage given by,

$$\underline{Z}_{\mathrm{fold}} = \underline{Z}_{\mathrm{bpf}}\|\frac{1}{g_{\mathrm{m},4,6}}, \tag{4.43}$$

and is described in Section 4.2.2.3.

4.2.2.3 Folded Switching Stage with *LC* DC Feed

The RF output current from the transconductance stage is directly coupled to the switching stage current commutation pFETs $\mathrm{M}_{4,6}$. The pFETs not only enable folding to reduce DC power consumption, but also have lower flicker noise compared to nFETs and enables the switching stage to be biased at an independent lower current density, which also helps in reducing the output offset voltage (V_{os}).

Both the transconductance stage and switching stage transistors are biased through the inductor L_2 with value less than the hundred picohenry range. L_2 is designed such that it resonates with C_{bpf} with a value less than the hundred femto Farad range at node N_{fold},

$$L_2 = \frac{1}{(2\pi f_{\mathrm{mix}})^2 C_{\mathrm{bpf}}}. \tag{4.44}$$

$f_{\mathrm{mix}} = 60\,\mathrm{GHz}$ is the center frequency of the bandpass filter from by the combination of L_2C_{bpf} as shown in Fig. 4.17. Here C_{bpf} is the equivalent parallel combination of APMOM capacitance C_2 and the parasitic capacitances to ground given by

$$C_{\mathrm{bpf}} = C_2 + C_{\mathrm{f,par}}. \tag{4.45}$$

Where $C_{\mathrm{f,par}} \approx 0.8C_2$ is defined as the effective parasitic capacitance including the drain to gate and and drain to body capacitances of M_2 and the gate to source and source to body capacitances of $\mathrm{M}_{4,6}$ given by

$$C_{\mathrm{f,par}} = C_{\mathrm{ds,M2}} + C_{\mathrm{db,M2}} + C_{\mathrm{gs,M4}} + C_{\mathrm{sb,M4}} + C_{\mathrm{gs,M6}} + C_{\mathrm{sb,M6}}. \tag{4.46}$$

The L_2C_{bpf} BPF also presents a high effective parallel resistance $R_{\mathrm{p,L2}}$ at N_{fold} given by

$$R_{\mathrm{p,L2}} = Q_{\mathrm{L2}}\omega_{\mathrm{mix}}L_2. \tag{4.47}$$

Q_{L2} is the unloaded quality factor of the inductance L_2. The BPF also shunts the unwanted harmonics including the second harmonics and intermodulation products as a result of LO switching. A high value of $R_{\mathrm{p,L2}}$ is desired because it prevents loss of $\underline{I}_{\mathrm{RF}}$ at node N_{fold} and results in better conversion efficiency and gain, trading off with bandwidth at N_{fold}.

pFETs $\mathrm{M}_{4,6}$ are dimensioned for efficient switching and to minimize the current division losses at node N_{fold} and biased near subthreshold region using bias voltage $V_{\mathrm{b,LO}} \approx 0.72\,\mathrm{V}$. The corresponding source to gate input impedance of $\mathrm{M}_{4,6}$, $Z_{\mathrm{in,4\text{-}6}}$, with reference to Fig. 4.17 is is around 13 times lower than $R_{\mathrm{p,L2}}$ from simulations and is given by,

$$Z_{\mathrm{in,4\text{-}6}} \approx \frac{1}{g_{\mathrm{m,4,6}}}. \tag{4.48}$$

The schematic of Fig. 4.17 also helps to deduce the expression for the impedance of the bandpass filter $\underline{Z}_{\mathrm{bpf}}$ constituted by the parallel combination of L_2, C_{bpf} and $R_{\mathrm{p,L2}}$ according to

$$\underline{Z}_{\mathrm{bpf}} = \frac{j\omega L_2 R_{\mathrm{p,L2}}}{R_{\mathrm{p,L2}}(1-\omega^2 C_{\mathrm{bpf}}L_2) + j\omega L_2}. \tag{4.49}$$

Now using (4.49), the current commuted $\mathrm{M}_{4,6}$ in each LO half period can be determined from Fig. 4.17 as

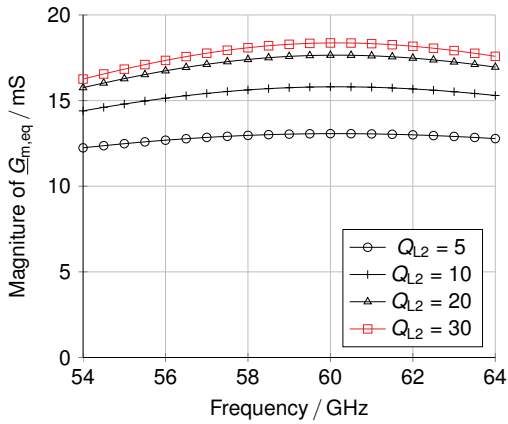

Figure 4.18: Plot of the magnitude of transcondutance $\underline{G}_{\mathrm{m,eq}}$ versus frequency for different inductor L_2 quality factor values.

$$\underline{I}_{4,6} = \underline{I}_{\mathrm{RF}} \frac{\underline{Z}_{\mathrm{bpf}}}{\frac{1}{g_{\mathrm{m},4,6}} + \underline{Z}_{\mathrm{bpf}}}. \tag{4.50}$$

Also,

$$\underline{I}_{4,6} = g_{\mathrm{m},4,6}\underline{V}_{\mathrm{fold}} = \underline{I}_{\mathrm{IF,p,n}}. \tag{4.51}$$

After substituting (4.49), (4.40) and (4.38) in (4.51), a modified expression of the transconductance is obtained using the definition as

$$\begin{aligned} \underline{G}_{\mathrm{m,eq}} &= \frac{\underline{I}_{\mathrm{IF,p,n}}}{\underline{V}_{\mathrm{RF}}} \\ &= \frac{g_{\mathrm{m},1}(r_{\mathrm{o},1}||\frac{1}{j\omega C_{\mathrm{eq}}})}{\frac{1}{g_{\mathrm{m},2}} + (r_{\mathrm{o},1}||\frac{1}{j\omega C_{\mathrm{eq}}})} \cdot \frac{\underline{Z}_{\mathrm{bpf}}||\underline{Z}_{\mathrm{casc}}}{\frac{1}{g_{\mathrm{m},4,6}} + \underline{Z}_{\mathrm{bpf}}||\underline{Z}_{\mathrm{casc}}}. \end{aligned} \tag{4.52}$$

It can be deduced from (4.52) that in order to maximize the transconductance $\underline{G}_{\mathrm{m,eq}}$, in addition to maximizing $g_{\mathrm{m},1}$ and $g_{\mathrm{m},4,6}$, $\underline{Z}_{\mathrm{bpf}}$ around ω_{mix} should also be maximized. The first term of (4.52) is a low pass filtering term with a cut off frequency set by $g_{\mathrm{m},4,6}$, $r_{\mathrm{o},1}$and C_{eq}. The second term of (4.52) describes the bandpass characteristics of the L_2C_{eq} DC feed stage. Fig. 4.18 shows the combined effect of both terms and the corresponding dependence of transcondutance $\underline{G}_{\mathrm{m,eq}}$

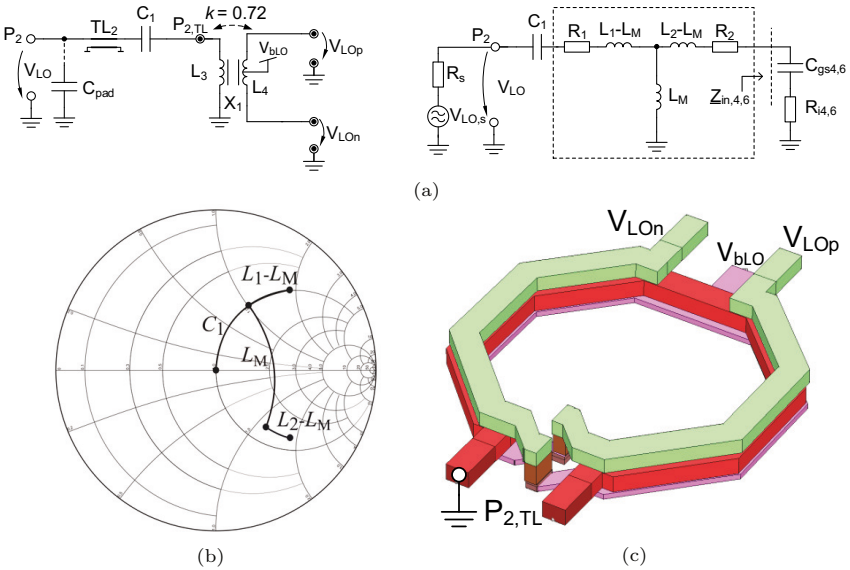

Figure 4.19: LO balun design: (a) schematic and equivalent circuit. (b) LO input matching (c) stacked balun implementation (Reused from *[TSJE21] ©2021 IEEE).

on the quality factor of inductance L_2.

4.2.2.4 LO Balun

The differential LO signals $V_{\mathrm{LO,p,n}}$ required to drive pFETs $\mathrm{M}_{4,6}$ in Fig. 4.14 are generated using a balun X_1 as shown in the schematic of Fig. 4.19(a). The single ended primary input inductor L_3 receives power from an external source $V_{\mathrm{LO,s}}$ through transmission line TL_2 and capacitor C_1 and couples it to secondary inductor L_4 and the corresponding coupling factor k. The gate bias voltage of $\mathrm{M}_{4,6}$, $V_{\mathrm{b,LO}}$, is fed through the center tap of L_4. As depicted in right half of Fig. 4.19(a), $L_{3,4}$ are transformed using the equivalent circuit with an addition of inductor L_{M} to model the mutual coupling [Voi13], and combined with the gate to source input impedance of the pFETs given by, $\underline{Z}_{\mathrm{in,gs,M4,6}} = R_{\mathrm{i,4,6}} + jX_{\mathrm{Cgs,4,6}}\Omega$ to transfer maximum LO power from the $50\,\Omega$ $V_{\mathrm{LO,s}}$ port to the differential $V_{\mathrm{LO,p,n}}$ signals with minimum insertion loss. The corresponding impedance matching trajectory

is shown in Fig. 4.19(b). The LO balun implementation is done as the stack of octagonal inductors using overlapped thickest copper metal layers from the technology and the corresponding layout is shown in Fig. 4.19(c). A mutual coupling factor of $k \approx 0.72$ is determined using EM simulations.

4.2.2.5 Backgate Tunable IF Stage and Offset Correction

The FSSDM IF output stage converts the current commuted by pFETs $M_{4,6}$ to the IF output voltage. This stage is implemented using the fixed resistors $R_{1\text{-}4}$ in parallel to the nFETs $M_{3,5}$ in series with $R_{1,3}$ respectively as depicted in Fig. 4.20. $R_{1,3} \approx 10\,\Omega$ sets the minimum load and $R_{2,4} \approx 600\,\Omega$ sets the maximum load, while $M_{3,5}$ functions as a voltage variable resistor. The effective resistance presented by $M_{3,5}$ varies as a coarse function of the gate bias voltage $\underline{V}_{\text{tune}}$ and as a fine function of the backgate bias voltage $\underline{V}_{\text{tune,f}}$. The equivalent output load resistance R_{load} seen by the IF node can then be derived as

$$\begin{aligned} R_{\text{load}} &= \left[\frac{V_{\text{DS,3,5}}}{I_{\text{D,3,5}}} + R_{1,3}\right] || R_{2,4} \\ &= \left[\frac{V_{\text{DS,3,5}}}{\frac{\beta_{\text{n}}}{2}(V_{\text{tune}} - V_{\text{th,n}}(V_{\text{tune,f}}))^2(1 + \frac{V_{\text{DS,3,5}}}{V_{\text{A}}})} + R_{1,3}\right] || R_{2,4}. \end{aligned} \tag{4.53}$$

$I_{\text{D,3,5}}$ is the drain current in the saturation region of $M_{3,5}$ [Voi13]. $V_{\text{th,n}}(V_{\text{tune,f}})$ is the threshold voltage of $M_{3,5}$ which varies as a function of $V_{\text{tune,f}}$. V_{A} is the Early voltage and β_{n} is the transistor dimension constant given by

$$\beta_{\text{n}} = \mu_{\text{n}} C_{\text{ox}} \frac{W_{3,5}}{L_{3,5}}, \tag{4.54}$$

where μ_{n} is the electron mobility, C_{ox} is the gate oxide capacitance, $W_{3,5}$ is the gate width and $L_{3,5}$ is the gate length of $M_{3,5}$.

Fig. 4.21(b) shows the variation of R_{load} when V_{tune} is varied and Fig. 4.21(b) shows R_{load} change with respect to $V_{\text{tune,f}}$. A effective linear resistance variation in the range of $\approx 33\%$ is obtained using this method.

The total output capacitance at the IF output C_{load} is the parallel combination of the parasitic capacitances internal to the IC, $C_{\text{L,par}}$ and the external capacitances on the PCB used for characterization, C_{PCB}, given by

$$C_{\text{load}} = C_{\text{L,par}} + C_{\text{PCB}}. \tag{4.55}$$

The IF output parasitic capacitance $C_{\text{L,par}}$ is relatively small, the external

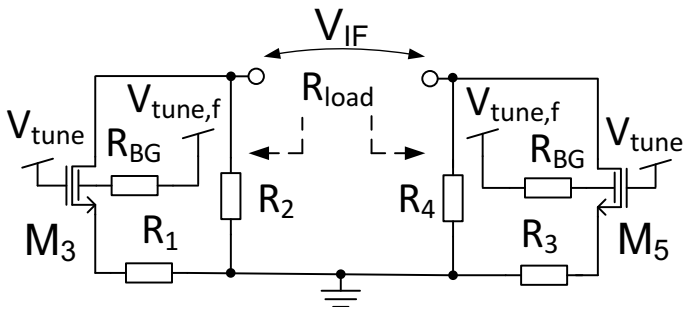

Figure 4.20: Schematic of the backgate tunable output stage of the FSSDM.

capacitance when the FSSDM is wirebonded for measurements on a PCB, C_{ext}, sets the 3 dB IF bandwidth $f_{\text{IF,BW}}$ according to,

$$f_{\text{IF,BW}} = \frac{1}{2\pi R_{\text{load}} C_{\text{load}}} \approx 30\,\text{MHz}. \tag{4.56}$$

The IF stage DC output offset voltage V_{os} is dependent on the mismatch between $R_{2,4}$ due to process variations. The independent control of $R_{2,4}$ using separate $\underline{V}_{\text{tune}}$ and $\underline{V}_{\text{tune,f}}$ enables the correction of V_{os} within $\pm 500\,\mu\text{V}$ to account for the process mismatch. It is observed from mismatch simulations that a lower I_{L} results in lower V_{os}, but this decreases the output common mode voltage. To account for this trade off, an optimum $I_{\text{L}} \approx 375\,\mu\text{A}$ is used to obtain a lower V_{os} while maintaining mid-rail output common mode voltage.

4.2.2.6 Voltage Conversion Gain

The voltage conversion gain of the FSSDM $a_{\text{v,FSSDM}}$ can be determined by considering the time domain signal based definition [Raz12],

$$a_{\text{v,FSSDM}} = \frac{\hat{V}_{\text{IF}}(t)}{\hat{V}_{\text{RF}}(t)}. \tag{4.57}$$

When the LO signal power level is large enough to emulate square wave like switching $i_{\text{IF,p}}(t)$ is commuted between M_4 and M_6 in every cycle of LO signal. The resulting differential $v_{\text{IF,t}}$ can be written as,

$$\begin{aligned} v_{\mathrm{IF,t}} &= Z_{\mathrm{L,p}} i_{\mathrm{IF,p}}(t) - Z_{\mathrm{L,n}} i_{\mathrm{IF,n}}(t) \\ &= Z_{\mathrm{L}} i_{\mathrm{IF,p,n}}(t) \left(s(t) - s(t - \frac{1}{2f_{\mathrm{LO}}}) \right) \end{aligned} \tag{4.58}$$

where $i_{\mathrm{IF,p}}(t)$ and $i_{\mathrm{IF,n}}(t)$ are 180° out of phase IF signals, commuting the RF current $i_{\mathrm{RF}}(t)$ for half LO period [Raz12]. $Z_{\mathrm{L,p}} = Z_{\mathrm{L,n}} = Z_{\mathrm{L,p}}$ is the effective load impedance at the IF output node constituted by the parallel combination of $R_{4,6}$ and C_{L}. Using the Fourier series expansion of a square wave switching between +1 and -1, it can be seen that [Raz12],

$$s(t) - s(t - \frac{1}{2f_{\mathrm{LO}}}) = \frac{4}{\pi}(\cos \omega_{\mathrm{LO}} t + \frac{1}{3} \cos 3\omega_{\mathrm{LO}} t + \frac{1}{5} \cos 5\omega_{\mathrm{LO}} t + ...). \tag{4.59}$$

substituting (4.59) in (4.58), and truncating all the higher order harmonics and intermodulation products at the IF output as the result of low pass filtering effect of Z_{L}, $v_{\mathrm{IF,t}}$ can be written as,

$$v_{\mathrm{IF}}(t) = \frac{2}{\pi} z_{\mathrm{L}} g_{\mathrm{m,eq}} \hat{V}_{\mathrm{RF}} \cos(\omega_{\mathrm{RF}} - \omega_{\mathrm{LO}}) t \tag{4.60}$$

and using the definition (4.57), the conversion gain can be written as [Ell07, Raz12],

$$a_{\mathrm{v,FSSDM}} = \frac{2}{\pi} g_{\mathrm{m,eq}} Z_{\mathrm{L}}. \tag{4.61}$$

Applying approximations, $g_{\mathrm{m,2}}(r_{\mathrm{o,1}} || \frac{1}{j\omega C_{\mathrm{eq}}}) \gg 1$, and $\underline{Z}_{\mathrm{bpf}} \gg \underline{Z}_{\mathrm{casc}}$, to (4.52), the expression for conversion gain can then be derived as the convolution (defined in Appendix B) of the frequency domain equivalent transconductance from (4.52) and load impedance contributed by R_{load} and C_{load} as,

$$\underline{a}_{\mathrm{v,FSSDM}} \approx \frac{2}{\pi} g_{\mathrm{m1}} \left| \frac{g_{\mathrm{m4,6}}}{g_{\mathrm{m4,6}} + \underline{Z}_{\mathrm{bpf}}} \right| * \left| \frac{R_{\mathrm{load}}}{1 + j\omega R_{\mathrm{load}} C_{\mathrm{load}}} \right|. \tag{4.62}$$

When FSSDM operates at the resonant center frequency of the bandpass filter $\omega_{\mathrm{mix}} = 1/\sqrt{L_2 C_{\mathrm{bpf}}}$, and $\underline{Z}_{\mathrm{bpf}}$ defined in (4.49) reduces to $R_{\mathrm{P,L2}}$ and the corresponding voltage conversion gain becomes,

$$\underline{a}_{\mathrm{v,FSSDM,max}} \approx \frac{2}{\pi} g_{\mathrm{m1}} R_{\mathrm{load}} \left| \frac{g_{\mathrm{m4,6}}}{g_{\mathrm{m4,6}} + R_{\mathrm{P,L2}}} \right|. \tag{4.63}$$

The control of R_{load} using V_{tune} and $V_{\mathrm{tune,f}}$ can also be used to tune the voltage

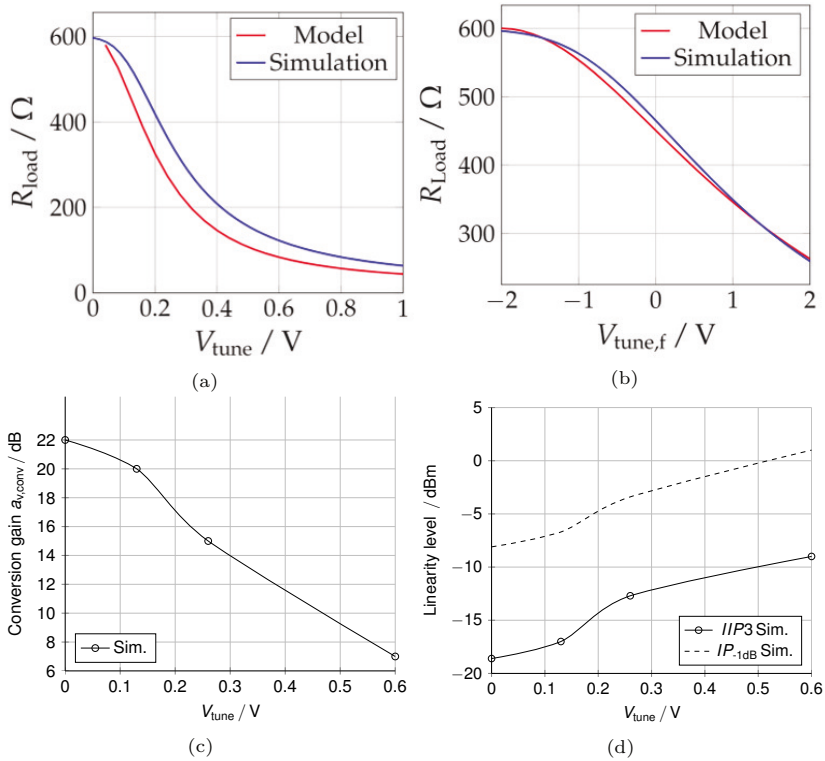

Figure 4.21: Variation of FSSDM load resistance versus tuning voltages (a) Coarse tuning. (b) fine tuning using backgate. (c) Corresponding variation of conversion gain and (d) linearity.

conversion gain and linearity. A coarse tuning is achieved by varying the gate voltage V_{tune} from 0 to 0.8 V and fine tuning is done by varying the backgate voltage $V_{\text{tune,f}}$ from 0 to 2V. As depicted in Fig. 4.21(c), the conversion gain can be varied from a maximum of 22 dB to around 7 dB, and the resulting $IP_{\text{-1dB}}$ varies from −19 dBm to −9 dBm and corresponding IIP_3 varies from around −9 dBm to 1 dBm as depicted in Fig. 4.21(d).

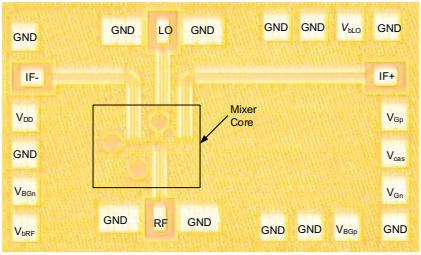

Figure 4.22: Die micrograph of the FSSDM measuring 1090 µm x 620 µm inlcuding pads, and a core area of 260 µm x 250 µm (Reused from *[TSJE21] ©2021 IEEE).

4.2.2.7 Characterization

To prove the design concept, the FSSDM IC is implemented in the FDSOI technology discussed in Section 2.7.2. The IC shown in Fig. 4.22 is characterized on a wafer prober using 67 GHz GSG Infinity probes for RF and LO signals. All DC signals and IF outputs are wire-bonded to a PCB. Since the FSSDM has a high ohmic IF output impedance, an off-the-shelf operational amplifier is used as an external buffer to drive equipments with 50 Ω input impedance. The R&S® ZVA67 vector network analyzer (VNA) is used for most of the small signal and large signal characterization.

Characterization of RF parameters are done after output offset calibration is done to bring V_{os} below 500 uV, and setting an $f_{\mathrm{IF}} = 1\,\mathrm{MHz}$. The magnitude of input reflection coefficients at the RF port, $|\underline{S}_{11}|$, and LO port, $|\underline{S}_{22}|$, are shown in Fig. 4.23(a). Both ports have a return loss better than 10 dB over the 54 GHz to 64 GHz frequency range, aligning with simulations to within ±5 dB. The minimum LO power required for peak G_{conv} is obtained as $\approx -3\,\mathrm{dBm}$ from Fig. 4.23(b). The secondary axis of Fig. 4.23(b) also shows the corresponding current drawn of $\approx 5.25\,\mathrm{mA}$ from a power supply forcing $V_{\mathrm{dd}} = 1\,\mathrm{V}$, less than 2 % deviation from simulated values. Fig. 4.23(c) shows that $G_{\mathrm{conv,dB}}$ of FSSDM is within 3 dB of peak conversion gain across the frequency range of 53 GHz to 64 GHz, a 11 GHz 3 dB RF bandwidth.

The plot of $G_{\mathrm{conv,dB}}$ with a fixed IF frequency of 1 MHz, while sweeping the RF input power $P_{\mathrm{RF,dBm}}$ is shown in Fig. 4.23(d). With $I_{\mathrm{b,RF}}$ varying from 0.3 mA to 0.6 mA, the input referred 1 dB compression points vary from −16.2 dBm for $G_{\mathrm{conv,dB}} = 21.5\,\mathrm{dB}$, to −10 dBm for $G_{\mathrm{conv,dB}} = 16\,\mathrm{dB}$. The measured maximum IF bandwidth $f_{\mathrm{IF,BW}} \approx 30\,\mathrm{MHz}$. $f_{\mathrm{IF,BW}}$ is limited by the effective external capac-

itance $C_{\text{ext}} \approx 8\,\text{pF}$. C_{ext} is the sum of PCB trace capacitance and external buffer input capacitance.

Using the combination of voltages forced at $V_{\text{Gp,n}}$ and $V_{\text{BGp,n}}$, the amplitude imbalance at the IF outputs are also corrected to within 50 µV, whereas the IF output phase imbalance is much less than 5°. The single sideband noise figure (NF_{SSB}) with a minimum of 11.2 dB of the FSSDM is measured using the Y factor method with the R&S® FSW67 spectrum analyzer, in combination with Noisecomm noise sources NC5115 for RF frequency range and NC346D for IF frequency range. The FSSDM also has measured LO to RF isolation better than 38 dB, and an LO to IF isolation better than 50 dB, aligning closely with simulation results.

4.2.2.8 Knowledge Gained

Compared to other folded designs like [SK05], the classic cascode input stage in this work is the key differentiator which enables to simultaneously achieve a high G_{conv} and isolation, while consuming a low P_{DC} at frequencies around 60 GHz. As shown in Table 4.2 comparing this work with state-of-the-art 60 GHz CMOS downconversion mixers, this design has one of the highest reported conversion gain, tunable from 16 dB to 21 dB with a moderate LO power of -3 dBm and NF_{SSB} of 11.2 dB. To the knowledge of the authors, the mixer also has one of the best reported figures of merit (FoM) resulting from the high conversion gain to DC power consumption ratio.

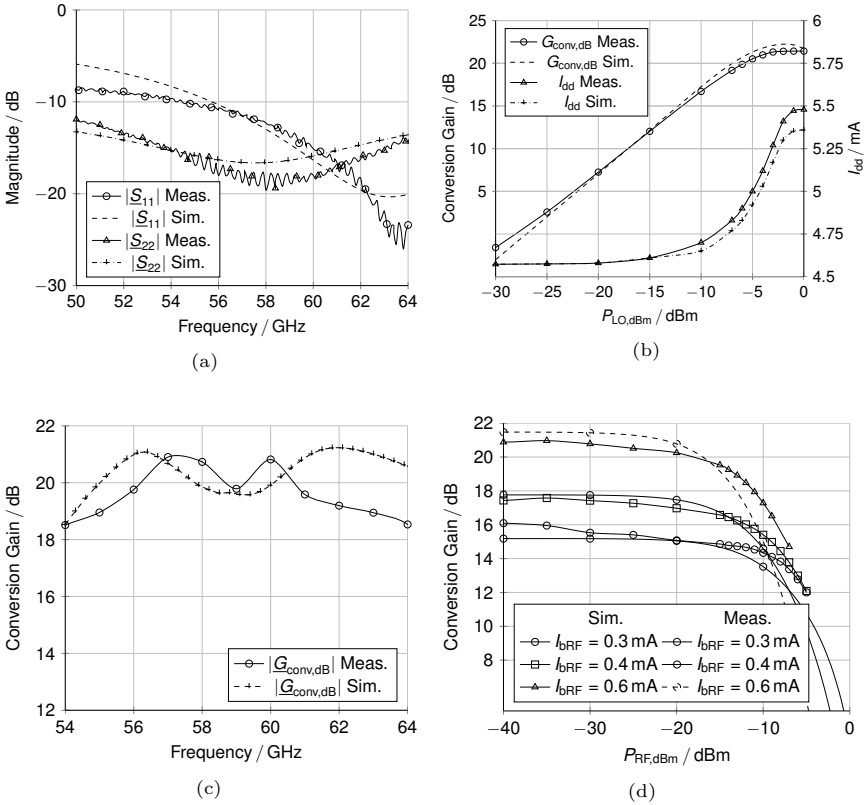

Figure 4.23: Comparison of characterization results with simulation. (a) Magnitude of input reflection for RF port $|\underline{S}_{11}|$ and LO port $|\underline{S}_{22}|$; (b) G_{conv} versus and I_{dd} as a function of $P_{\mathrm{LO,dBm}}$; (c) G_{conv} versus f_{RF} for a fixed IF frequency of 1 MHz; (d) G_{conv} as function of $P_{\mathrm{RF,dBm}}$ for different bias currents, demonstrating tunable linearity (Reused from *[TSJE21] ©2021 IEEE).

Table 4.2: Comparison with state-Of-the-art 60 GHz CMOS active downconversion mixers (Reused from *[TSJE21] ©2021 IEEE.)

Ref.	f_{RF} (GHz)	$P_{\mathrm{LO,dBm}}$ (dBm)	$G_{\mathrm{conv,dB}}$ (dB)	$P_{\mathrm{1dB,\ dBm}}$ (dBm)	NF_{SSB} (dB)	P_{DC} (mW)	LO to RF Iso. (dB)	$f_{\mathrm{IF,BW}}$ GHz	$OIP3$ dBm	Area (mm^2)	FoM[a] (GHz/mW)	CMOS Tech.
[LCC+13]	52-66	0	6.5	-3.0	10.1[b]	4.2	> 30	0.1	7	0.138	1.5	90 nm
[SVL+13]	60	-2	-15-+11	-18.9	17.0	19.0	> 43	3.5-7	1.49-13.3	1.38[c]	1.3	32 nm SOI
[KP15]	45-66	0	13.8	-11.0	8.5[b]	6.4	> 45[d]	1.2	-	0.225	0.5	45 nm SOI
[LDC+18]	62-90	-3	9.5	-3.8	12.2[b]	15	> 48	-	10.6	0.53	1.5	65 nm
[CWHI19]	60	-5	2.0	-4.0	14.0	11.7	> 25	0.05	-	0.47	0.7	28 nm
[CSLN17]	57-66	0	5.6	-7.0	11.0	18	> 35	2	12.4	0.14	1.9	65 nm
This	**54-64**	**-3**	**16-21.5**	**-16- -10**	**11.2**	**5.25-4.25**	**> 38**	**0.03**	**-5-0[e]**	**0.675/0.065[f]**	**2.1**	**22 nm FDSOI**

[a] $FoM = \frac{f_{\mathrm{RF}} G_{\mathrm{conv}} P_{\mathrm{1dB}}}{P_{\mathrm{DC}} F_{\mathrm{SSB}} P_{\mathrm{LO}}}$ [b] Calculated from DSB [c] Area incl. VGA+ADC+Serializer [d] incl. LNA
[e] Sim. [f] FSSDM core

4.3 Proof of Principle System Implementation

To prove the system principle, an interrogator frontend integrating QC_{TL}, FSSDM and a PA [CTCE21] is implemented according to the system block diagram illustrated in Fig. 4.1. The corresponding IC is shown in Fig. 4.24(b). An external off-the-shelf VGA and ADC is used to amplify and digitize the FSSDM output signal V_{IF}. A horn antenna is used at the PA output to radiate power in the direction of the PBT.

The schematic of the implemented PBT is shown in Fig. 4.25. The source and drain of an nFET M_1 available in the FDSOI technology discussed in Section 2.7.2 are connected together to form a diode using bond wires with inductance $L_{b,1\text{-}3}$. The antenna ANT_{PBT} is interfaced using microstrip transmission line TL_1 to the drain of M_1. Microstrip transmission line TL_2 and capacitor C_2 forms a quarter stub, which presents a high impedance to the 60 GHz signals at node NT, and enables to bias M_1 with low frequency switchable modulation signal V_m.

When $V_m = 0\,V$ corresponding to a data bit '0', nFET M_1 is in cut-off region and presents only parasitic capacitances to the equivalent circuit. The ANT_{PBT} which presents a relatively inductive impedance is conjugate matched to the relatively capacitive impedance presented by TL_1 and capacitor C_1. The corresponding impedance $Z_{T,1}$ is given by

$$\underline{Z}_{T,1} \approx \frac{1}{j\omega C_1}. \tag{4.64}$$

When $V_m \approx 800\,mV$ corresponding to a data bit '1', M_1 operates in the saturation region and presents an inductive load in parallel with C_1, and an impedance

$$\underline{Z}_P \approx \frac{j\omega L_{b,eq}}{1 - \omega^2 L_{b,eq} C_1}, \tag{4.65}$$

where $L_{b,eq}$ is the effective inductance at node NT. This change in impedance shifts the reflection coefficient $|\Gamma|$ as shown in Fig. 4.26(d). This change in $|\Gamma|$ changes the RCS of the transponder and thereby the backscatter signal amplitude. This change is then demodulated by the interrogator, digitized and processed.

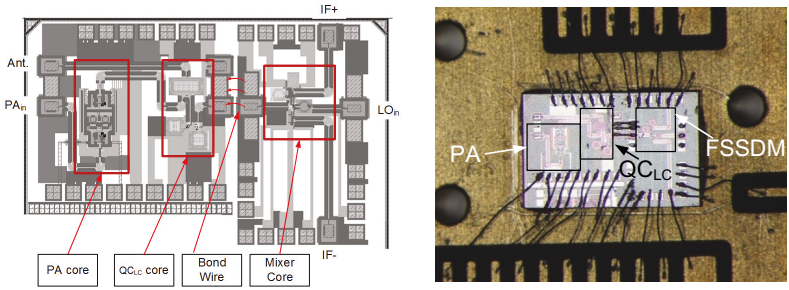

(a) (b)

Figure 4.24: Fabricated interrogator frontend. (a) Layout of the integrated designs. (b) The implemented IC occupying an area of 1300 µm × 1090 µm wire-bonded to a PCB for characterization.

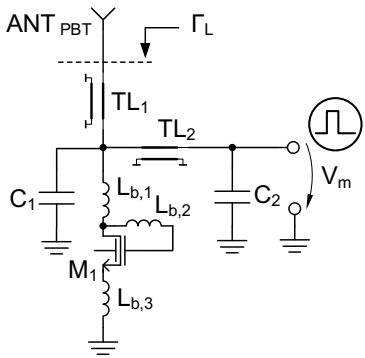

Figure 4.25: Schematic of the designed passive backscatter transponder.

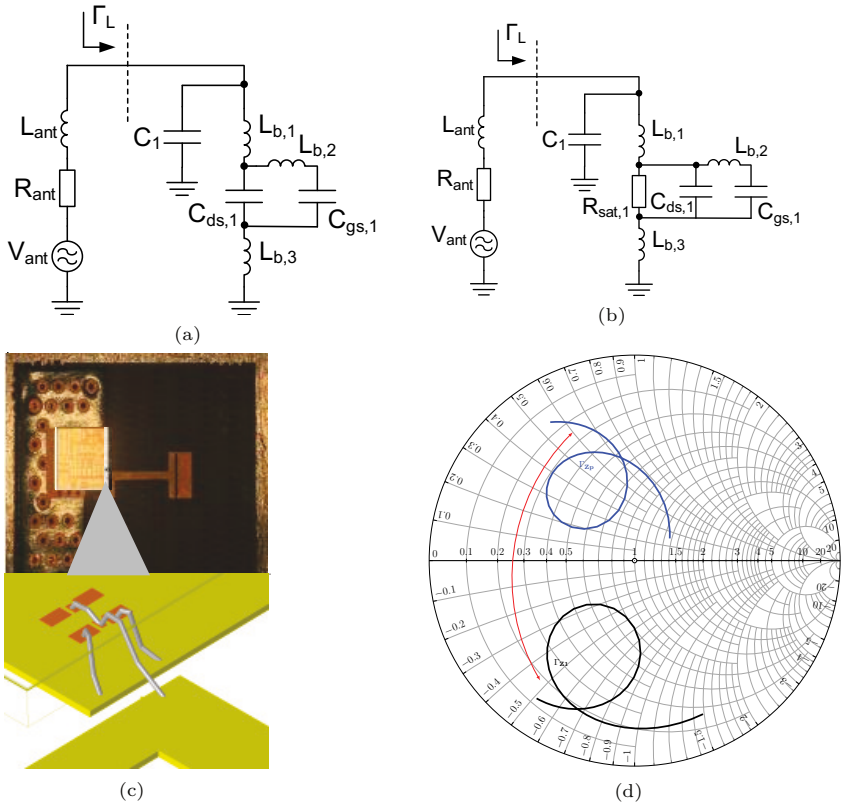

Figure 4.26: Equivalent circuit of the PBT (a) M_1 is in cut off (b) M_1 is in saturation. (c) PBT and view of the bondwires used in EM simulation. (d) Shows the impedance trajectories for PBT switching.

5 Experimental Tests

In order to prove the proposed 24 GHz and 60 GHz system concepts described in Section 3.3 and Section 4.3, experimental characterization in the laboratory were done. For the 24 GHz SRT based system, the outcomes from indoor ranging experiments and SQ-FSK based data transfer experiments are presented in Section 5.1.1 and Section 5.1.3 respectively. For the 60 GHz passive transponder based system, the results from identification experiments are presented in Section 5.2.

5.1 24 GHz System

System level experiments are done to characterize ranging error and data transfer functionality using both $\mathrm{SRT_{dir}}$ and $\mathrm{SRT_{buf}}$ described in Section 3.3.1 as transponders and with the LFMCW secondary radar from Section 3.3.2 as interrogator. Initially the functionality of the standalone LFMCW radar without antenna is carried out by loop back of cascaded RF cables of various lengths between the $\mathrm{T_x}$ output and $\mathrm{R_x}$ input. The relatively shorter cable lengths result in lower baseband frequencies when compared to SRT based ranging according to (3.4) and (3.5). In order to account for this, the lower cut off frequency of the interrogator baseband filter, $f_{\mathrm{l,bpf}}$ is also lowered to 3 kHz from the 300 kHz for SRTs based ranging from Section 3.3.2.

5.1.1 Ranging Experiments

Ranging experiments in a laboratory environment are carried out using both the $\mathrm{SRT_{dir}}$ and $\mathrm{SRT_{buf}}$. The experiment setup is shown in Fig. C.5. The LFMCW interrogator is configured to transmit chirps with a duration of $T_{\mathrm{c}} = 1\,\mathrm{ms}$ and a bandwidth $f_{\mathrm{BW}} = 250\,\mathrm{MHz}$. The distance to SRTs are then calculated from the baseband beat frequencies using (3.10). Fig. 5.1(a) and Fig. 5.1(b) shows the peaks from baseband spectrum for short range measurements starting at 0.7 m, and up to 10 m for $\mathrm{SRT_{dir}}$ and 5 m for $\mathrm{SRT_{buf}}$ respectively. Fig. 5.1(c) and Fig. 5.1(d) plots the baseband spectrum for long range measurements, and shows that the envelope of the spectral peaks at constant baseband gain closely matches the results from the model based on (3.20). The maximum measured range for $\mathrm{SRT_{dir}}$ and $\mathrm{SRT_{buf}}$ are 77 m and 25 m respectively.

In order to determine key statistics and insights from the measurements, ranging is done by sending a sequence of 150 chirps at each distance. A laser-based distance measurement device with ±1 mm accuracy, Bosch GLM 250 VF®, is used

to measure the actual distance d_{laser} to determine the accuracy of the measurements according to [Kay93] as

$$d_{\text{err}} = \sqrt{\frac{1}{K-1}\sum_{c=1}^{K}(d_{\text{SRT,c}} - d_{\text{laser}})^2}. \tag{5.1}$$

The distance measurement error plots showing mean and standard deviation error bars for the interrogator ART system is depicted in Fig. 5.2(a) and Fig. 5.2(b). The worsening of standard deviation as the distance increases correlates well with the inference using (3.27) described in Section 3.1.3. The SRT_{dir} based system has a measured accuracy better than 5 cm for a range less than 5 m, 11 cm for a range less than 10 m, and 94 cm for the entire range as shown in Fig. 5.2(a). The measured precision is less than 1.5 cm for a range less than 5 m as shown in the cumulative density function (CDF) of Fig. 5.2(c) and less than 24.4 cm for the entire range. The measured close range precision is around 3.8 times better in comparison with the state-of-the-art reported in Table 5.1. For SRT_{buf}, the measured precision of less than 1.96 cm for a range less than 5 m shown in the CDF of Fig. 5.2(d) is around 1.3 times higher than that for SRT_{dir}. For the entire range, the precision is better than 32.2 cm.

5.1.2 Roll Invariance Experiments

The effectiveness of roll invariance resulting from the use of antennas ANT_{MB2x} and ANT_{MB4x} described in Section 3.3.1.1 are characterized using a custom measurement setup where the SRTs at a fixed distance from the interrogator are mounted on a stepper motor shaft shown in Fig. C.4. The corresponding range measurements are recorded at every 10° step rotation in the horizontal plane of the ARTs. The peak power at the beat frequencies are then plotted at each step angle as shown in Fig. 5.3. It is also seen from Fig. 5.3 that SRT_{buf} with four antennas show 360° roll invariance, while SRT_{dir} using ANT_{MB2x} has two nulls around at ±90°, aligning closely with simulation results.

5.1.3 Joint Ranging and Data Transfer Experiments

Now, the concept for simultaneous ranging and data transmission described in Section 3.1.4 is proved by experimental characterization in the laboratory. The SRTs shifts the quench modulation frequency based on the data to be transmitted. The interrogator sends the chirps and acquires the data for the duration of at least two full data frames. Although the SRTs are designed to send data in any of the

common number systems, in this experiment, the number of digits including a start bit, $N = 5$, and the quaternary number system with $M = 4$ is used. The spectrogram of Fig. 5.4 plots the quench frequency against the chirp sequence number, and color grading intensity shows the relative spectral magnitude.

As discussed in Section 3.1.4, each digit received by the interrogator is represented by a quench frequency f_q. For the start bit, $f_q \approx 450\,\text{kHz}$. For subsequent digits $b_{0\text{-}3}$, the corresponding fixed quench frequencies are 950 kHz, 820 kHz, 710 kHz and 590 kHz respectively. So from Fig. 5.4, the captured data "0123" represents decimal "27" in quaternary numeral system. The data corresponds to the integer part of the temperature reading, 27 °C read by SRT_{buf} from an I^2C based temperature sensor, positioned at a distance of 5 m from the interrogator.

Though the chirp duration of $T_c = 1\,\text{ms}$ implies a theoretical maximum possible chirp rate of $1/T_c = 1\,\text{k}$ chirps per second, in our experiments, the maximum chirp rate is limited to 50 chirps per second. This is due to a throughput bottleneck in the Ethernet based data acquisition system employed. So with $K = 100$ chirps per symbol, the achieved symbol rate is 0.5 symbols per second. Fig. 5.5 shows the spectrogram frequencies measured at distances of 1.5 m, 2.5 m, 15 m and 25 m, clearly showing an increase in separation between beat frequency peaks, and decrease in magnitude as the distance to SRT from the interrogator is increased.

A summary of parameters from the two SRTs are tabulated and are compared against the state-of-the-art in Table 5.1. As shown, the maximum range of 77 m for SRT_{dir} is around 2.5 times higher than the second highest reported in [Weh10]. The corresponding maximum range of 25 m for SRT_{buf} is also double when compared to those reported in works at comparable frequencies like [SCW+13b]. This results from the combination of high output power and low minimum detectable input power of the integrated SRAs with integrated quench pulse shaping. For distances less than 10 m, the measured accuracy for SRT_{dir} is better than 11 cm, and precision is better than 2.4 cm while the accuracy for SRT_{buf} is better than 16.6 cm, and precision is better than 2.5 cm. The combination of the maximum range, precision and accuracy are one of the best reported among similar works in literature to the authors' knowledge. While both ARTs feature simultaneous ranging and data transfer, battery powered operation and on-PCB antenna, SRT_{buf} also features 360° roll invariance in the horizontal plane. The knowledge gained from this experimental study is fruitful for the conception of future systems employing secondary radar and low power, low data rate, locatable wireless sensor nodes for civilian automotive applications.

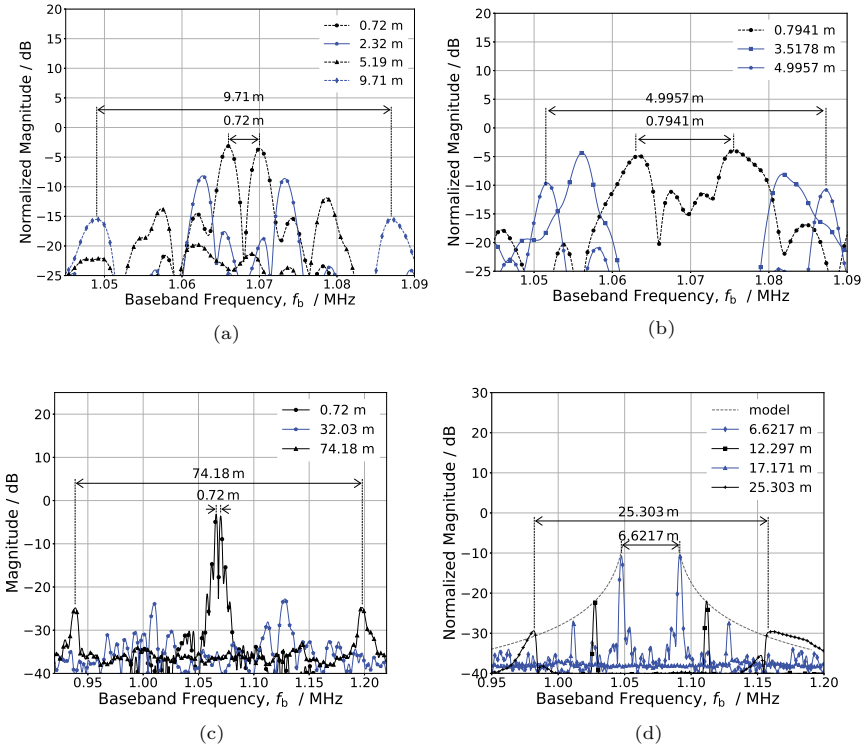

Figure 5.1: Normalized baseband spectrum corresponding to short range distance measurements using (a) $\mathrm{SRT_{dir}}$; (b) $\mathrm{SRT_{buf}}$, and long range measurements using (c) $\mathrm{SRT_{dir}}$; (d) $\mathrm{SRT_{buf}}$. (Reused from *[TFJE23] ©2023 IET).

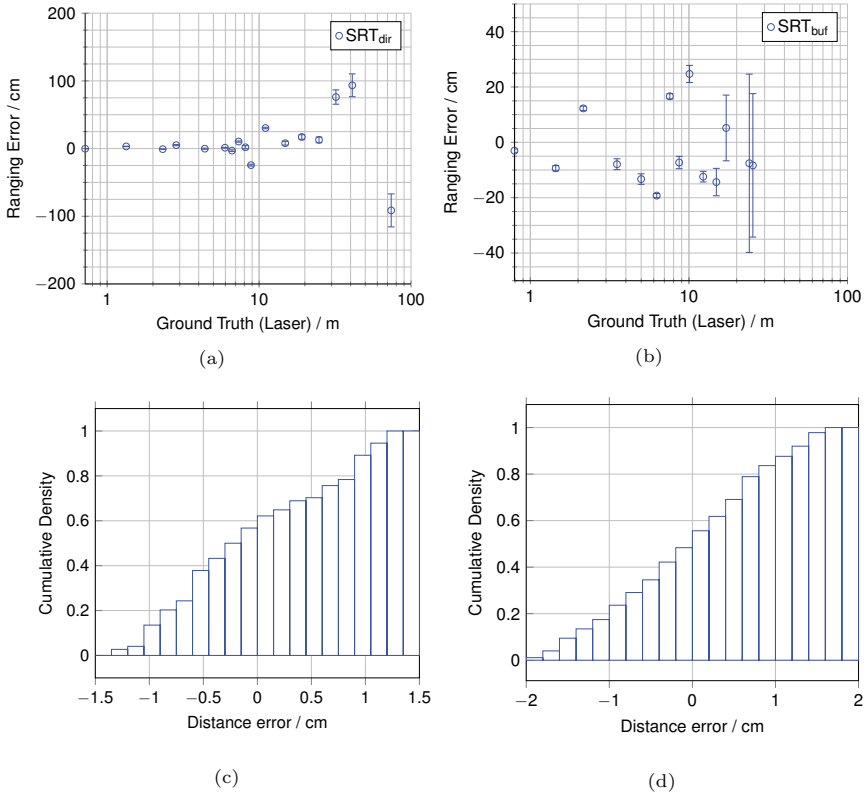

Figure 5.2: Indoor distance measurement error versus ground truth from a laser based device. (a) $\mathrm{SRT_{dir}}$; (b) for $\mathrm{SRT_{buf}}$. Measured cumulative density function at 2.5 m for (c) $\mathrm{SRT_{dir}}$; (d) $\mathrm{SRT_{buf}}$. (Adapted from *[TFJE23] ©2023 IET). (Adapted from *[TFJE23] ©2023 IET).

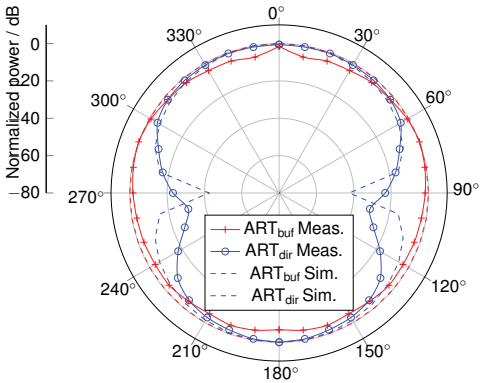

Figure 5.3: Polar plots showing measured and simulated normalized baseband power variation for different angles when the SRTs are rotated in the horizontal plane. (Reused from *[TFJE23] ©2023 IET).

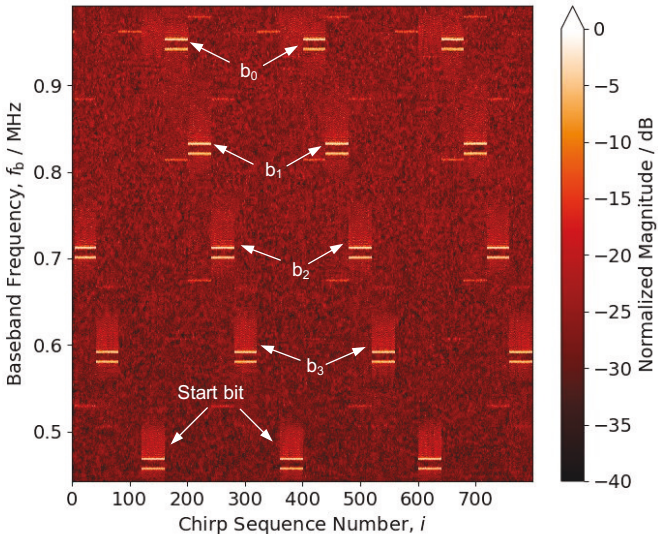

Figure 5.4: Measured baseband frequency spectrogram showing simultaneous ranging and data transfer at a distance of 5 m. (Adapted from *[TFJE23] ©2023 IET).

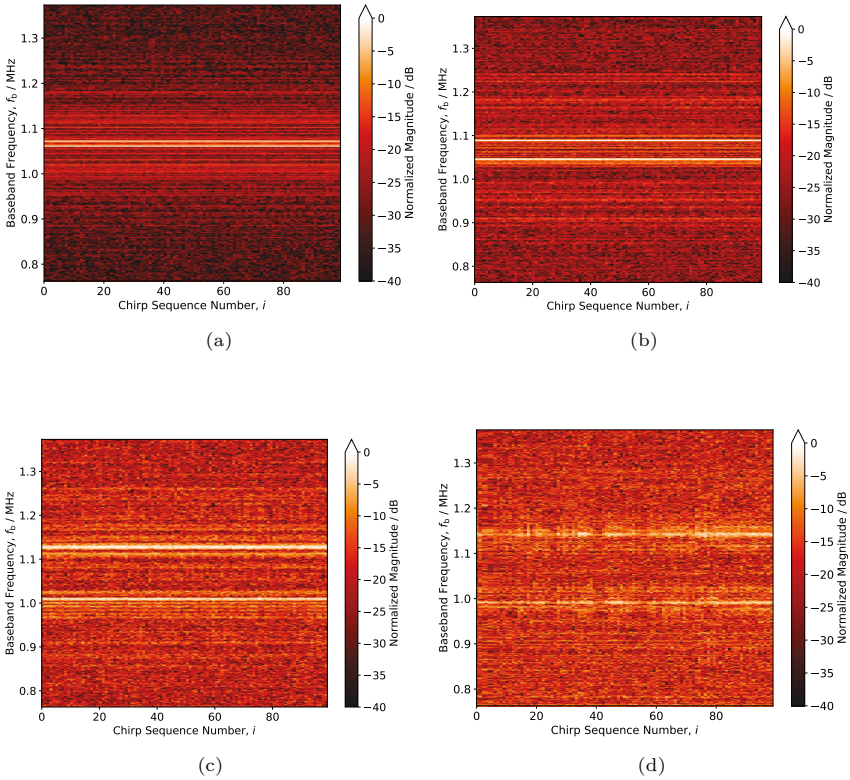

Figure 5.5: Spectrogram showing baseband frequencies for a single bit at different measured distances: (a) 1.5 m (b) 2.5 m (c) 15 m (d) 25 m. (Adapted from *[TFJE23] ©2023 IET).

Table 5.1: Comparison with state-of-the-art FMCW radar based ranging systems employing integrated circuits based active transponders. (Reused from *[TFJE23] ©2023 IET).

	[Weh10]	[NEAE18]	[SCW+13b]	[SFS11]	[DHV17b]	$\mathbf{SRT_{dir}}$	$\mathbf{SRT_{buf}}$
Frequency (GHz)	5.8	24 / 2.4	34	76	77	24	24
Precision (cm)	26	5.8	10	0.016	-	< 5 m range: 1.5 10 m range: 2.4 Full range: 24.4	< 5 m range: 1.96 10 m range: 2.5 Full range: 32.2
Accuracy (cm)	33	22.3	7	-	-	< 5 m range: 5 < 10 m range: 11 Full range: 94	< 5 m range: 12.3 10 m range: 16.6 Full range: 24.7
Range (m)	30	5	11.5	8	5	0.5 to 77	0.5 to 25
Power cons. (mW)	54	7.4	122	-	25	65	44
Sensitivity (dBm)	-64	-50	-53	-	-62	< -66	< -58
Architecture	Pulsed	Sub-harmonic	SILO	Phase mod.	BPSK	SRA	SRA
Ranging	Yes	Yes	Yes	Yes	No	Yes	Yes
Battery powered	No	No	No	No	No	Yes	Yes
PCB antenna	No	No	No	No	No	Yes	Yes
Data transfer	No	No	No	No	Yes	Yes	Yes

5.2 60 GHz System Detection Experiments

A very basic detection experiment to prove the system concept is done. The interrogator IC is mounted on a wafer probe station and contacted using Infinity probes®. An external signal source, Keysight® E8167D supplies the input signal to the PA. A power divider sources signal the LO port of the mixer. An antenna similar to the design in [SQC13] is connected to the TR_x port of the QC, and is mounted at the fixed end of the adhoc guide rail. The PBT is mounted on the mobile end of the guide rail, which is used to vary the distance between the interrogator antenna and the PBT. The IF output FSSDM is band pass filtered, amplified and digitized to obtain an output signal as shown in Fig. 5.7.

An output voltage V_{PBT} with a peak to peak amplitude of around 5.2 mV is measured when the PBT is placed at close proximity of approximaely 5 mm to the interrogator antenna. V_{PBT} is extremely lower than modeled paramters due to the impact of multiples losses.

The losses in the PBT is mainly due to the modeling inaccuracies for the bondwires used. For the interrogator, there are multiple loss components. These include probe losses and cable losses which results in reduced output power delivered to the interrogator antenna. Losses originate in the very short bondwires between QC and the FSSDM RF input, and also the relatively longer transmission lines used in the full chip routing for the PA input to the pads and the QC TR_x port to the pads. Also, distance measurements were extremely difficult due to alignment issues and the occurrence of nulls, which only an IQ mixer can reliably detect albeit at the cost of increased power consumption.

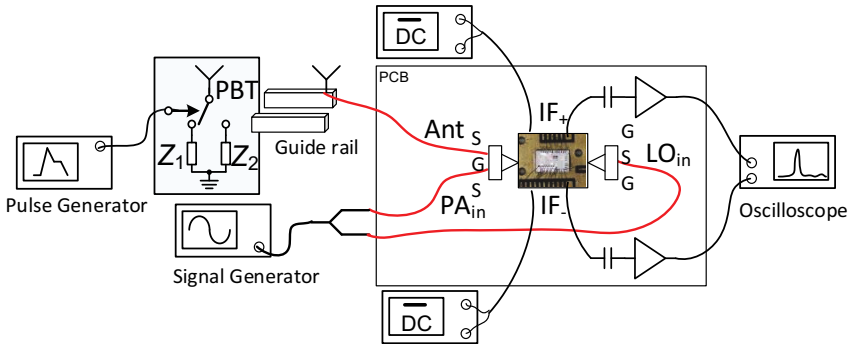

Figure 5.6: PBT system level testing setup.

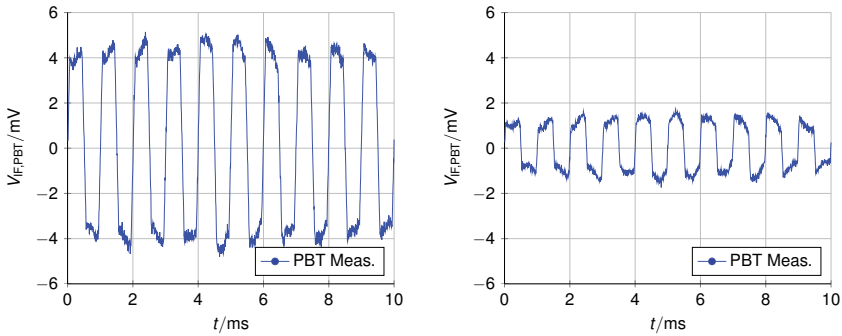

Figure 5.7: Amplified, filtered and digitized output voltage from the PBT for $d_{\mathrm{PBT}} \approx 5\,\mathrm{mm}$ and $d_{\mathrm{PBT}} \approx 10\,\mathrm{mm}$ after post processing.

6 Summary and Future Work

This scientific work presented the analysis, design and characterization of RFICs for radio frequency identification, ranging and communication. System concepts are hypothesized and experiments devised to prove them.

The key questions posed at the beginning of this thesis are answered:

Is it possible to reduce energy consumption of integrated microwave RFID transponders that are jointly identifiable and localizable at long ranges? Are such transponders analyzable and implementable using superregenerative amplifier theory?: Yes, it was proven by the novel 24 GHz SRT topologies analyzed and designed.

Are monolithic IC based components consuming very low power at mmWave frequency bands feasible for implementing single antenna RFID interrogators? Is it possible to analyze and understand the characteristics of these components?: Yes, but more research is needed to optimize the performance as proven by the 60 GHz PBT based designs.

Examples of key scientific contributions from this work which push the research state-of-the-art are:

- A novel quench pulse shaping method to simultaneously improve the output power and minimum detectable input power of SRAs is envisaged *[TLJE18]. 24 GHz SRA ICs are designed with an integrated quench pulse shaping circuit to prove the theoretical considerations. At the system level, this resulted in a maximum range of 77 m for $\mathrm{SRT_{dir}}$ *[TLJE18] which is around 2.5 times higher than the second highest reported in [Weh10]. The corresponding maximum range of 25 m for $\mathrm{SRT_{buf}}$ *[TJE20] is also double when compared to those reported in works at comparable frequencies like [SCW+13b]. For distances less than 10 m, the measured accuracy for $\mathrm{SRT_{dir}}$ is better than 11 cm, and precision is better than 2.4 cm while the accuracy for $\mathrm{SRT_{buf}}$ is better than 16.6 cm, and precision is better than 2.5 cm. The combination of the maximum range, precision and accuracy are one of the best reported among similar works in literature to the author's knowledge.

- Devised a methodology and theory for using SRA based active reflectors for a novel joint ranging and quench frequency shift based simplex communication. Two ARTs are designed to prove this concept. ARTs feature simultaneous ranging and data transfer, battery powered operation and custom bandwidth enhanced on-PCB antenna, $\mathrm{SRT_{buf}}$ also features 360° roll invariance in the horizontal plane *[TFJE23].

- Analytic expressions including minimum SRA gain required for achieving a particular maximum range. Equation for the maximum number of symbols that can be transmitted in data transfer mode is derived as a function of system parameters. This also corresponds to the maximum number of tags that can be interrogated simultaneously in a multi-tag ranging scenario. A formula was derived for output voltage swing incorporating bond-wire losses in a direct drive SRA with integrated quench pulse shaping.

- A low power single antenna interrogator system concept is also tested using a passive transponder. The interrogator is based on a 60 GHz downconversion mixer *[TSJE21], which uses a novel folded switching stage topology which results in a high conversion gain to DC power consumption ratio, and a low power quasi circulator *[TPC+21] occupying very low area.

Open questions for future research

Optimization of the multi-disciplinary building blocks including antennas, algorithms, RFICs, and digital signal processing for identification and localization of cooperative targets is an evolving topic and many exciting unsolved research problems including the following remain for the future:

- One of the key challenges encountered is the losses from the bond-wires, especially as frequencies move towards 60 GHz. Leveraging on technologies like Antenna in Package (AiP) or Antenna in Semiconductor (AiS) to build fully integrated systems from bits to antenna on the same die is an interesting research problem for the future.

- Exploring ways to augment such systems with energy harvesting to make the tags self sustainable would align well with green technology initiatives for the future.

- From preliminary investigations, utilizing the phase information of the SRA baseband signal, along with the use of an in-phase/quadrature (I/Q) downconversion mixer is shown to improve the distance estimation accuracy significantly. This looks like a research problem with very good potential.

- In the current system, the optimum duty cycle where the SRA functions best is done using manually controlling the duty cycle of the quench signal source. Automating this calibration procedure can improve performance using machine learning (ML) techniques with SRA in the loop.

- An SRA based automatic gain control (AGC) where the quench signal slope is controlled in a feedback loop is an interesting research problem that would also result in better localization accuracy.
- Three dimensional (3D) integration of SRAs and antennas to include spatial diversity in all direction and not just in the horizontal plane as implemented in this work.
- Extending experimental characterization of both SRT and PBT by including bit error rate measurements.

Appendices

A Derivation of Parameters for CB Amplifier with Base Feedback Capacitance

To determine $\underline{Z}_{\mathrm{in},2}$, KCL is applied at the emitter node $\mathrm{N_{E2}}$ to obtain the relationship,

$$\underline{I}_{\mathrm{in}} - \frac{\underline{V}_{\mathrm{in}}}{\underline{X}_{\mathrm{Ceq}}} - \frac{\underline{V}_{\mathrm{in}}}{\underline{X}_{\mathrm{Co},2}} + g_{\mathrm{m},2}\underline{V}_{\mathrm{be},2} = 0. \tag{A.1}$$

Where $\underline{X}_{\mathrm{Ceq}}$ is the equivalent capacitive reactance of the branch where $C_{\pi,2}$ is in series with the parallel network of C_{B} and $C_{\mu,2}$ calculated as

$$\underline{X}_{\mathrm{Ceq}} = \frac{C_{\pi,2} + C'_{\mathrm{B}}}{j\omega C_{\pi,2} C'_{\mathrm{B}}}, \tag{A.2}$$

where C'_{B} is defined as,

$$C'_{\mathrm{B}} = C_{\mathrm{B}} + C_{\mu,2}. \tag{A.3}$$

$\underline{X}_{\mathrm{Co},2}$ is the capacitive reactance of the output capacitance $C_{\mathrm{o},2}$ given by

$$\underline{X}_{\mathrm{Co},2} = \frac{1}{j\omega C_{\mathrm{o},2}}. \tag{A.4}$$

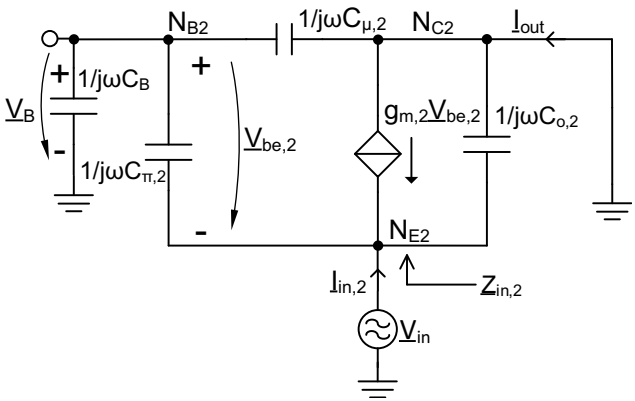

Figure A.1: Simplified small signal equivalent circuit of the stacked transistor CCO half cell for high frequency analysis.

The relationship involving base emitter voltage $\underline{V}_{\mathrm{be},2}$ as a function of $\underline{V}_{\mathrm{in}}$ is determined by applying Kirchhoff's voltage law (KVL) as,

$$\underline{V}_{\mathrm{be},2} = \underline{V}_{\mathrm{B}} - \underline{V}_{\mathrm{in}}, \tag{A.5}$$

where

$$\underline{V}_{\mathrm{B}} = \frac{\underline{V}_{\mathrm{in}}}{j\omega C'_{\mathrm{B}} \underline{X}_{\mathrm{Ceq}}}. \tag{A.6}$$

On substituting (A.2), (A.3) and (A.6) in (A.5) and solving,

$$\underline{V}_{\mathrm{be},2} = \underline{V}_{\mathrm{in}} \frac{-C'_{\mathrm{B}}}{C_{\pi,2} + C'_{\mathrm{B}}}. \tag{A.7}$$

Substituting (A.2), (A.4) and (A.7) in (A.1) and solving, the input admittance $\underline{Y}_{\mathrm{in},2}$ of the CB amplifier with base feedback capacitor can be written as,

$$\underline{Y}_{\mathrm{in},2} = \left.\frac{\underline{I}_{\mathrm{in}}}{\underline{V}_{\mathrm{in}}}\right|_{\underline{V}_{\mathrm{out}}=0} = g_{\mathrm{m},2} \frac{C'_{\mathrm{B}}}{C_{\pi,2} + C'_{\mathrm{B}}} + j\omega \frac{C_{\pi,2} C'_{\mathrm{B}} + C_{\mathrm{o},2}(C_{\pi,2} + C'_{\mathrm{B}})}{C_{\pi,2} + C'_{\mathrm{B}}}. \tag{A.8}$$

Taking the reciprocal of admittance, expanding C'_{B} and rearranging terms, the input impedance $\underline{Z}_{\mathrm{in},2}$ can be written as,

$$\underline{Z}_{\mathrm{in},2} = \frac{1}{\underline{Y}_{\mathrm{in},2}} = \left(1 + \frac{C_{\pi,2}}{C_{\mathrm{B}} + C_{\mu,2}}\right) \frac{1}{g_{\mathrm{m},2} + j\omega \left[C_{\pi,2} + C_{\mathrm{o},2}\left(1 + \frac{C_{\pi,2}}{C_{\mathrm{B}} + C_{\mu,2}}\right)\right]}. \tag{A.9}$$

The transconductance of the CB amplifier with base capacitor feedback, $\underline{G}_{\mathrm{m},2}$ can be determined using a similar method. At first, KCL is applied at the collector node $\mathrm{N}_{\mathrm{C}2}$ to obtain the relationship

$$\underline{I}_{\mathrm{out}} + \frac{\underline{V}_{\mathrm{B}}}{\underline{X}_{\mathrm{C}\mu,2}} + \frac{\underline{V}_{\mathrm{in}}}{\underline{X}_{\mathrm{Co},2}} - g_{\mathrm{m},2} \underline{V}_{\mathrm{be},2} = 0, \tag{A.10}$$

where

$$\underline{X}_{\mathrm{C}\mu,2} = \frac{1}{j\omega C_{\mu,2}}, \tag{A.11}$$

is the capacitive reactance of the base-collector capacitance $C_{\mu,2}$.

Substituting for $\underline{V}_{\mathrm{B}}$ from (A.6) and from $\underline{V}_{\mathrm{be},2}$ (A.7) in (A.10) and rearranging,

$$\frac{\underline{I}_{\mathrm{out}}}{\underline{V}_{\mathrm{in}}} = \frac{-C'_{\mathrm{B}}}{C_{\pi,2} + C'_{\mathrm{B}}}(g_{\mathrm{m},2} - \frac{1}{j\omega C_{\mu,2}}) - (\frac{1}{j\omega C_{\mu,2}} + \frac{1}{j\omega C_{\mathrm{o},2}}). \tag{A.12}$$

On defining the base feedback factor $\mathrm{K}_{\mathrm{B,fb}}$ as,

$$\mathrm{K}_{\mathrm{B,fb}} = \frac{C_{\pi,2}}{C'_{\mathrm{B}}} = \frac{C_{\pi,2}}{C_{\mathrm{B}} + C_{\mu,2}}, \tag{A.13}$$

(A.12) can again be solved to obtain the maximum transconductance,

$$\underline{G}_{\mathrm{m},2} = \left.\frac{\underline{I}_{\mathrm{out}}}{\underline{V}_{\mathrm{in}}}\right|_{\underline{V}_{\mathrm{out}}=0} = -\frac{g_{\mathrm{m},2}}{1 + \mathrm{K}_{\mathrm{B,fb}}} - j\omega\frac{C_{\mu,2}\mathrm{K}_{\mathrm{B,fb}} + (1 + \mathrm{K}_{\mathrm{B,fb}})C_{\mathrm{o},2}}{(1 + \mathrm{K}_{\mathrm{B,fb}})}. \tag{A.14}$$

The negative sign indicates that since $\underline{I}_{\mathrm{out}}$ is flowing into the collector node, $\underline{V}_{\mathrm{in}}$ and $\underline{I}_{\mathrm{out}}$ are 180° out of phase.

B Definitions

Special Functions

Rectangular function

The time domain rectangular function $\mathrm{rect}(t)$ is defined as:

$$\mathrm{rect}(t) = \begin{cases} 0 & \text{for } |t| > \frac{1}{2} \\ \frac{1}{2} & \text{for } |t| = \frac{1}{2} \\ 1 & \text{for } |t| < \frac{1}{2} \end{cases} \tag{B.1}$$

Dirac Delta function

Properties of Dirac Delta function:

$$\begin{aligned} \sum_{n=-\infty}^{\infty} e^{-j2\pi f n b} =& \frac{1}{b} \sum_{n=-\infty}^{\infty} \delta\left(f - \frac{n}{b}\right) = \frac{1}{b} \mathrm{III}_{\frac{1}{b}}(f) \\ G(f) * \delta(f-a) =& G(f-a) \end{aligned} \tag{B.2}$$

sinc function

The $\mathrm{sinc}(f)$ is defined as:

$$\mathrm{sinc}(f) = \frac{\sin(\pi f)}{\pi f} \tag{B.3}$$

Fourier transform

Some key properties of the Fourier transform:

$$\begin{aligned} \mathfrak{F}\{a \cdot g(t) + b \cdot h(t)\} &= a \cdot \mathfrak{F}\{g(t)\} + b \cdot \mathfrak{F}\{h(t)\} \\ \mathfrak{F}\{g(t) \cdot h(t)\} &= \mathfrak{F}\{g(t)\} * \mathfrak{F}\{h(t)\} \\ \mathfrak{F}\{\cos(a(t-b))\} &= \frac{1}{2} e^{-jab} \delta\left(f - \frac{a}{2\pi}\right) + \frac{1}{2} e^{jab} \delta\left(f + \frac{a}{2\pi}\right) \\ \mathfrak{F}\{\sin(a(t-b))\} &= \frac{1}{2j} e^{-jab} \delta\left(f - \frac{a}{2\pi}\right) - \frac{1}{2j} e^{jab} \delta\left(f + \frac{a}{2\pi}\right) \\ \mathfrak{F}\{\mathrm{rect}(a(t-b))\} &= \frac{1}{a} \cdot \mathrm{sinc}\left(\frac{f}{a}\right) e^{-j2\pi f b} \end{aligned} \tag{B.4}$$

High frequency small signal models

Common emitter amplifier

$$[y_{\mathrm{CE}}] = \begin{bmatrix} g_\pi + j\omega(C_{\mathrm{be}} + C_{\mathrm{bc}}) & -j\omega C_{\mathrm{bc}} \\ g_{\mathrm{m}} - j\omega C_{\mathrm{bc}} & g_{\mathrm{o}} + j\omega(C_{\mathrm{ce}} + C_{\mathrm{bc}}) \end{bmatrix}. \tag{B.5}$$

Common base amplifier

$$[y_{\mathrm{CB}}] = \begin{bmatrix} g_{\mathrm{m}} + g_{\mathrm{o}} + g_\pi + j\omega C_{\mathrm{be}} & -g_{\mathrm{o}} \\ g_{\mathrm{m}} - g_{\mathrm{o}} & g_{\mathrm{o}} + j\omega(C_{\mathrm{ce}} + C_{\mathrm{bc}}) \end{bmatrix}. \tag{B.6}$$

C 24 GHz Experiment Setups

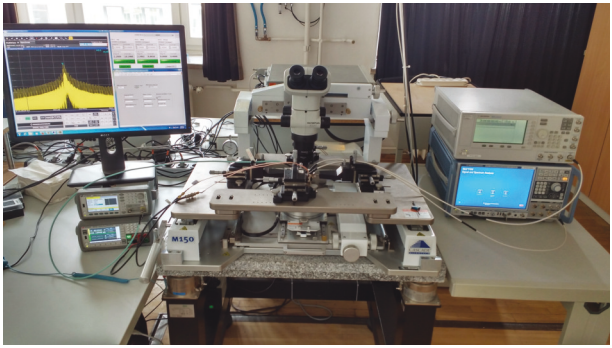

Figure C.1: Frequency domain SRA measurement on probe station, with the characteristic Dirac delta function peaks clearly visible.

(a)

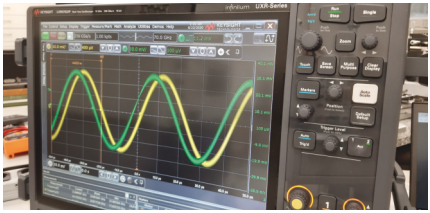

(b)

Figure C.2: Time domain measurement of SRA output using a real time oscilloscope (a) SRA in action (b) Phase coherence observation.

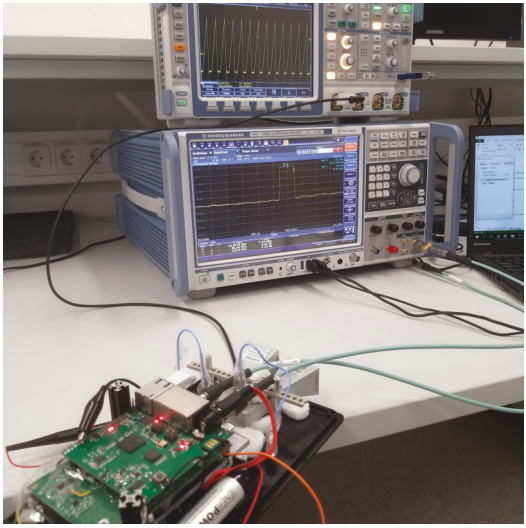

Figure C.3: Time and frequency domain characterization of LFMCW interrogator chirp sequence.

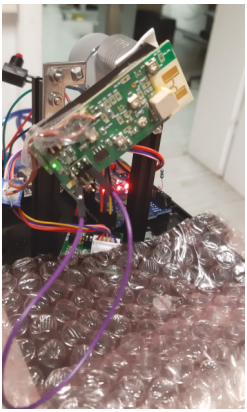

(a)

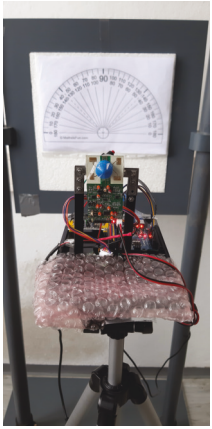

(b)

Figure C.4: SRTs mounted on a stepper motor shaft for roll-invariance experiments (a) $\mathrm{SRT}_{\mathrm{dir}}$ (b) $\mathrm{SRT}_{\mathrm{buf}}$.

Figure C.5: SRT laboratory testing setup.

D 60 GHz Experiment Setups

Figure D.1: Setup used to characterize FSSDM.

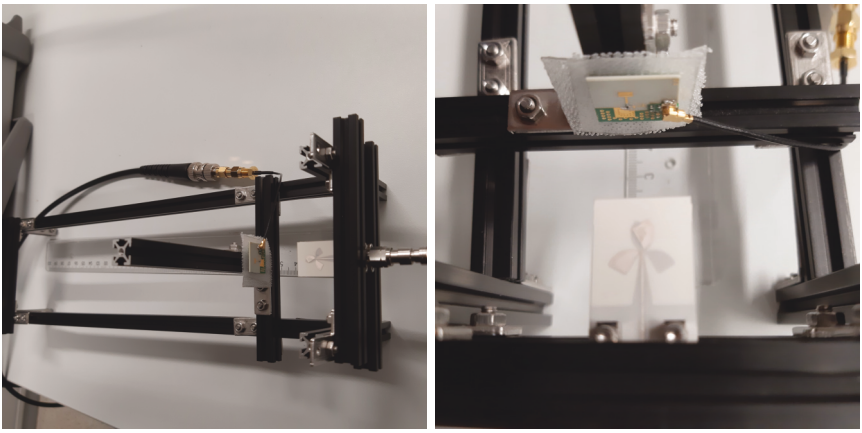

(a) (b)

Figure D.2: 60 GHz passive transponder mounted on a linear guide rail.

References

[AD19] M. Alhassoun and G. D. Durgin, "A comparative study of coupler-based retrodirective arrays for next-generation rfid tags," in *2019 IEEE International Conference on RFID Technology and Applications (RFID-TA)*, 2019, pp. 439–443.

[Anaa] Analog Devices. Direct Modulation/Waveform Generating, 6.1 GHz Fractional-N Frequency Synthesizer. [Online]. Available: https://www.analog.com/media/en/technical-documentation/data-sheets/ADF4158.pdf

[Anab] ——. TimerBlox: Voltage-Controlled Pulse Width Modulator (PWM). [Online]. Available: https://www.analog.com/media/en/technical-documentation/data-sheets/LTC6992-1-6992-2-6992-3-6992-4.pdf

[Arm22] E. Armstrong, "Some recent developments of regenerative circuits," *Proceedings of the Institute of Radio Engineers*, vol. 10, no. 4, pp. 244–260, 1922.

[AWM09] D. Arnitz, K. Witrisal, and U. Muehlmann, "Multifrequency continuous-wave radar approach to ranging in passive uhf rfid," *IEEE Transactions on Microwave Theory and Techniques*, vol. 57, no. 5, pp. 1398–1405, 2009.

[AWVF05] P. Andreani, X. Wang, L. Vandi, and A. Fard, "A study of phase noise in colpitts and lc-tank cmos oscillators," *IEEE Journal of Solid-State Circuits*, vol. 40, no. 5, pp. 1107–1118, 2005.

[Bal05] C. A. Balanis, "Antenna theory: analysis and design," *Microstrip Antennas, third edition, John wiley & sons*, 2005.

[Bid02] P. Bidigare, "The Shannon channel capacity of a radar system," in *Conference Record of the Thirty-Sixth Asilomar Conference on Signals, Systems and Computers, 2002.*, vol. 1, 2002, pp. 113–117 vol.1.

[Blu70] L. Bluestein, "A linear filtering approach to the computation of discrete Fourier transform," *IEEE Transactions on Audio and Electroacoustics*, vol. 18, no. 4, pp. 451–455, 1970.

[BMCD09] J. L. Bohorquez, S. Member, A. P. Chandrakasan, and J. L. Dawson, "Frequency-Domain Analysis of Super-Regenerative Amplifiers," *IEEE Trans. Microw. Theory Tech.*, vol. 57, no. 12, pp. 2882–2894, 2009.

[BMM12] J. Bousquet, S. Magierowski, and G. G. Messier, “A 4 GHz active scatterer in 130 nm CMOS for phase sweep amplify-and-forward,” *IEEE Transactions on Circuits and Systems I: Regular Papers*, vol. 59, no. 3, pp. 529–540, March 2012.

[BMN+19] A. Buffi, A. Motroni, P. Nepa, B. Tellini, and R. Cioni, “A sar-based measurement method for passive-tag positioning with a flying uhf-rfid reader,” *IEEE Transactions on Instrumentation and Measurement*, vol. 68, no. 3, pp. 845–853, 2019.

[Bon98] P. Bondyopadhyay, “Sir J.C. Bose diode detector received Marconi’s first transatlantic wireless signal of December 1901 (the "Italian Navy Coherer" Scandal Revisited),” *Proceedings of the IEEE*, vol. 86, no. 1, pp. 259–285, 1998.

[BSRS10] M. Bolic, D. Simplot-Ryl, and I. Stojmenovic, *Principles and Techniques of RFID Positioning*, 2010, pp. 389–415.

[CCL03] S.-J. Chung, S.-M. Chen, and Y.-C. Lee, “A novel bi-directional amplifier with applications in active van atta retrodirective arrays,” *IEEE Transactions on Microwave Theory and Techniques*, vol. 51, no. 2, pp. 542–547, 2003.

[CF06] H. I. Cantu and V. F. Fusco, “A 21 GHZ Reflection Amplifier MMIC for Retro-Directive Antenna and RFID Applications,” in *2006 IET Seminar on MM-Wave Products and Technologies*, 2006, pp. 66–70.

[CF11] P. Chan and V. Fusco, “Bi-static 5.8GHz RFID range enhancement using retrodirective techniques,” in *2011 41st European Microwave Conference*, 2011, pp. 976–979.

[CKLW15] J. Chang, J. Kao, Y. Lin, and H. Wang, “Design and analysis of 24-ghz active isolator and quasi-circulator,” *IEEE Transactions on Microwave Theory and Techniques*, vol. 63, no. 8, pp. 2638–2649, 2015.

[CL05] T. S. D. Cheung and J. R. Long, “A 21-26-GHz SiGe bipolar power amplifier MMIC,” *IEEE Journal of Solid-State Circuits*, vol. 40, no. 12, pp. 2583–2597, Dec 2005.

[Cri66] E. Cristal, “Analysis and exact synthesis of cascaded commensurate transmission-line c-section all-pass networks,” *IEEE Transactions on Microwave Theory and Techniques*, vol. 14, no. 6, pp. 285–291, 1966.

[CSLN17] C. Choi, J. H. Son, O. Lee, and I. Nam, "A +12-dBm OIP3 60-GHz RF Downconversion Mixer With an Output-Matching, Noise- and Distortion-Canceling Active Balun for 5G Applications," *IEEE Microwave and Wireless Components Letters*, vol. 27, no. 3, pp. 284–286, 2017.

[CTCE21] M. Cui, Z. Tibenszky, C. Carta, and F. Ellinger, "Design of a Compact Power Amplifier with 18.6 dBm 60 GHz 20.5% PAE in 22 nm FD-SOI," in *2020 15th European Microwave Integrated Circuits Conference (EuMIC)*, 2021, pp. 141–144.

[CWHI19] R. Ciocoveanu, R. Weigel, A. Hagelauer, and V. Issakov, "Modified Gilbert-Cell Mixer With an LO Waveform Shaper and Switched Gate-Biasing for 1/f Noise Reduction in 28-nm CMOS," *IEEE Transactions on Circuits and Systems II: Express Briefs*, vol. 66, no. 10, pp. 1688–1692, 2019.

[Cyp] Cypress Semiconductor. PSoC® 4: PSoC 4000 Family Datasheet. [Online]. Available: https://www.cypress.com/file/138646/download

[DDR+10] D. Dardari, R. D'Errico, C. Roblin, A. Sibille, and M. Z. Win, "Ultrawide bandwidth rfid: The next generation?" *Proceedings of the IEEE*, vol. 98, no. 9, pp. 1570–1582, 2010.

[DHV17a] M. S. Dadash, J. Hasch, and S. P. Voinigescu, "A 77-ghz active millimeter-wave reflector for fmcw radar," in *2017 IEEE Radio Frequency Integrated Circuits Symposium (RFIC)*, 2017, pp. 312–315.

[DHV17b] ——, "A 77-GHz Active Millimeter-Wave Reflector for FMCW Radar," *Radio Freq. Integr. Circuits Symp.*, pp. 312–315, 2017.

[DSCE13] J. Dirk Leufker, A. Strobel, C. Carta, and F. Ellinger, "A wideband planar microstrip to coplanar stripline transition (balun) at 35 ghz," in *Proceedings of the 2013 9th Conference on Ph.D. Research in Microelectronics and Electronics (PRIME)*, June 2013, pp. 305–308.

[Ell07] F. Ellinger, *Radio Frequency Integrated Circuits and Technologies*, 1st ed. Berlin Heidelberg: Springer Verlag Berlin Heidelberg, 2007.

[Eme97] D. T. Emerson, “The work of Jagadis Chandra Bose: 100 years of millimeter-wave research,” *IEEE Transactions on Microwave Theory and Techniques*, vol. 45, no. 12, pp. 2267–2273, 1997.

[EWU+13] A. Esswein, R. Weigel, T. Ussmueller, C. Carlowitz, and M. Vossiek, “An Improved Switched Injection-Locked Oscillator for Ranging and Communication Systems,” *Proc. 8th Eur. Microw. Integrated Circuits Conf.*, pp. 592–595, 2013.

[FB17] K. Fang and J. F. Buckwalter, “A tunable 5â€“7 GHz distributed active quasi-circulator with 18 dBm output power in CMOS SOI,” *IEEE Microwave and Wireless Components Letters*, vol. 27, no. 11, pp. 998–1000, 2017.

[FHB+21] D. A. Funke, S. Hansen, C. Bredendiek, T. Grenter, G. vom Bögel, A. Harutyunyan, R. Fiedler, A. Heinig, and N. Pohl, “A 61-GHz RFID Frontend with SiGe Transceiver MMIC and SIW Coupling Network,” in *2020 50th European Microwave Conference (EuMC)*, 2021, pp. 165–168.

[Fin11] K. Finkenzeller, “Battery powered tags for iso/iec 14443, actively emulating load modulation,” in *RFID SysTech 2011 7th European Workshop on Smart Objects: Systems, Technologies and Applications*, 2011, pp. 1–8.

[FK15] M. Forouzandeh and N. C. Karmakar, “Chipless rfid tags and sensors: a review on time-domain techniques,” *Wireless Power Transfer*, vol. 2, no. 2, p. 62â€“77, 2015.

[FKSE17] F. Farzami, S. Khaledian, B. Smida, and D. Erricolo, “Reconfigurable dual-band bidirectional reflection amplifier with applications in van atta array,” *IEEE Transactions on Microwave Theory and Techniques*, vol. 65, no. 11, pp. 4198–4207, 2017.

[FM10] K. Finkenzeller and D. Müller, *RFID Handbook: Fundamentals and Applications in Contactless Smart Cards, Radio Frequency Identification and Near-Field Communication.* Wiley, 2010.

[FWE12] D. Fritsche, R. Wolf, and F. Ellinger, “Analysis and Design of a Stacked Power Amplifier With Very High Bandwidth,” *IEEE Trans. Microw. Theory Tech.*, vol. 60, no. 10, pp. 3223–3231, 2012.

[Gal14] G. Galati, “On the italian contribution to radar,” in *2014 11th European Radar Conference*, 2014, pp. 37–40.

[GG04] M. Gasior and J. L. Gonzalez, "Improving FFT frequency measurement resolution by parabolic and gaussian spectrum interpolation," *AIP Conference Proceedings*, vol. 732, no. 1, pp. 276–285, 2004. [Online]. Available: https://aip.scitation.org/doi/abs/10.1063/1.1831158

[GHZ+11] R. Gierlich, J. Huettner, A. Ziroff, R. Weigel, and M. Huemer, "A reconfigurable mimo system for high-precision fmcw local positioning," *IEEE Transactions on Microwave Theory and Techniques*, vol. 59, no. 12, pp. 3228–3238, 2011.

[GJE22] H. Ghaleb, N. Joram, and F. Ellinger, "A 60-ghz super-regenerative oscillator with 80 db gain in sige bicmos for fmcw radar active reflectors," in *2022 IEEE 22nd Topical Meeting on Silicon Monolithic Integrated Circuits in RF Systems (SiRF)*, 2022, pp. 31–34.

[GK83] D. D. Gajski and R. H. Kuhn, "Guest Editors' Introduction: New VLSI Tools," *Computer*, vol. 16, no. 12, pp. 11–14, 1983.

[GNC10] S. Gupta, B. Nikfal, and C. Caloz, "Rfid system based on pulse-position modulation using group delay engineered microwave c-sections," in *2010 Asia-Pacific Microwave Conference*, 2010, pp. 203–206.

[GPSH19] M. Garbati, E. Perret, R. Siragusa, and C. Halope, "Ultrawideband chipless rfid: Reader technology from sfcw to ir-uwb," *IEEE Microwave Magazine*, vol. 20, no. 6, pp. 74–88, 2019.

[GRB+00] J. Godin, M. Riet, S. Blayac, P. Berdaguer, J.-L. Benchimol, A. Konczykowska, A. Kasbari, P. Andre, and N. Kauffmann, "Improved InGaAs/InP DHBT technology for 40 Gbit/s optical communication circuits," in *GaAs IC Symposium. IEEE Gallium Arsenide Integrated Circuits Symposium. 22nd Annual Technical Digest 2000*, 2000, pp. 77–80.

[GSP+15] M. Garbati, R. Siragusa, E. Perret, A. Vena, and C. HalopÃ©, "High performance chipless rfid reader based on ir-uwb technology," in *2015 9th European Conference on Antennas and Propagation (EuCAP)*, 2015, pp. 1–5.

[GWMC12] M. Gebhart, M. Wobak, E. Merlin, and C. Chlestil, "Active load modulation for contactless near-field communication," in *2012 IEEE International Conference on RFID-Technologies and Applications (RFID-TA)*, 2012, pp. 228–233.

[Han89] R. Hansen, "Relationships between antennas as scatterers and as radiators," *Proceedings of the IEEE*, vol. 77, no. 5, pp. 659–662, 1989.

[Har64] R. F. Harrington, "Theory of loaded scatterers," *Proceedings of the Institution of Electrical Engineers*, vol. 111, pp. 617–623(6), April 1964. [Online]. Available: https://digital-library.theiet.org/content/journals/10.1049/piee.1964.0111

[HEKS10] S. Hauptmann, F. Ellinger, F. Korndoerfer, and C. Scheytt, "V-band variable gain amplifier applying efficient design methodology with scalable transmission lines," *IET Circuits, Devices Systems*, vol. 4, no. 1, pp. 24–29, January 2010.

[HES+13] A. Hamidian, R. Ebelt, D. Shmakov, M. Vossiek, T. Zhang, V. Subramanian, and G. Boeck, "24 GHz CMOS Transceiver with Novel T/R Switching Concept for Indoor Localization," *Radio Freq. Integr. Circuits Symp.*, pp. 293–296, 2013.

[HPMC+17] C. Herrojo, F. Paredes, J. Mata-Contreras, S. Zuffanelli, and F. MartÃn, "Multistate multiresonator spectral signature barcodes implemented by means of s-shaped split ring resonators (s-srrs)," *IEEE Transactions on Microwave Theory and Techniques*, vol. 65, no. 7, pp. 2341–2352, 2017.

[HPMCM19] C. Herrojo, F. Paredes, J. Mata-Contreras, and F. MartÃn, "Chipless-rfid: A review and recent developments," *Sensors*, vol. 19, no. 15, 2019. [Online]. Available: https://www.mdpi.com/1424-8220/19/15/3385

[IF83] K. Iizuka and A. Freundorfer, "Detection of nonmetallic buried objects by a step frequency radar," *Proceedings of the IEEE*, vol. 71, no. 2, pp. 276–279, 1983.

[IMU+14] O. Inac, S. Member, M. Uzunkol, S. Member, and G. M. Rebeiz, "45-nm CMOS SOI Technology Characterization for Millimeter-Wave Applications," *IEEE Trans. Microw. Theory Tech.*, vol. 62, no. 6, pp. 1301–1311, 2014.

[Inf] Infineon Technologies. Silicon Germanium 24 GHz Transceiver MMIC. [Online]. Available: https://www.infineon.com/cms/en/product/sensor/radar-sensors/radar-sensors-for-iot/24ghz-radar/bgt24mtr11/

[JAW+13] N. Joram, B. Al-Qudsi, J. Wagner, A. Strobel, and F. Ellinger, "Design of a multi-band FMCW radar module," in *2013 10th Workshop on Positioning, Navigation and Communication (WPNC)*, March 2013, pp. 1–6.

[JR05] I. Jalaly and I. Robertson, "Capacitively-tuned split microstrip resonators for rfid barcodes," in *2005 European Microwave Conference*, vol. 2, 2005, pp. 4 pp.–1164.

[JWSE12] N. Joram, J. Wagner, A. Strobel, and F. Ellinger, "5.8 GHz demonstration system for evaluation of FMCW ranging," in *2012 9th Workshop on Positioning, Navigation and Communication*, 2012, pp. 137–141.

[Kay93] S. M. Kay, *Fundamentals of statistical signal processing: estimation theory.* Taylor & Francis Group, 1993, vol. 37, no. 4.

[KCS08] H.-H. Ko, K.-W. Cheng, and H.-J. Su, "Range resolution improvement for fmcw radars," in *2008 European Radar Conference*, 2008, pp. 352–355.

[KDF75] A. Koelle, S. Depp, and R. Freyman, "Short-range radio-telemetry for electronic identification, using modulated RF backscatter," *Proceedings of the IEEE*, vol. 63, no. 8, pp. 1260–1261, 1975.

[Kes04] W. Kester, *Data Conversion Handbook (Analog Devices), 1st edition.* Newnes, 2004.

[KF03] U. Karthaus and M. Fischer, "Fully integrated passive uhf rfid transponder ic with 16.7-Î¼w minimum rf input power," *IEEE Journal of Solid-State Circuits*, vol. 38, no. 10, pp. 1602–1608, 2003.

[KG95] K. S. Kundert and P. Gray, *The Designer's Guide to Spice and Spectre.* USA: Kluwer Academic Publishers, 1995.

[KGCT14] J. Kimionis, A. T. Georgiadis, A. Collado, and M. M. Tentzeris, "Enhancement of rf tag backscatter efficiency with low-power reflection amplifiers," *IEEE Transactions on Microwave Theory and Techniques*, vol. 62, pp. 3562–3571, 2014.

[KJ82] M. Kirschning and R. Jansen, "Accurate model for effective dielectric constant of microstrip with validity up to millimetre-wave frequencies," *Electronics Letters*, vol. 18, pp. 272–273(1), March 1982.

[KP15] S. Kundu and J. Paramesh, “A Compact, Supply-Voltage Scalable 45-66 GHz Baseband-Combining CMOS Phased-Array Receiver,” *IEEE Journal of Solid-State Circuits*, vol. 50, no. 2, pp. 527–542, 2015.

[KPRVH13] T. Kiuru, P. Pursula, J. RajamÃ¤ki, and T. VÃ¤hÃ¤-HeikkilÃ¤, “A 60-GHz semipassive MMID transponder for backscattering communications,” in *2013 IEEE MTT-S International Microwave Symposium Digest (MTT)*, 2013, pp. 1–3.

[LAE+11] G. Li, D. Arnitz, R. Ebelt, U. Muehlmann, K. Witrisal, and M. Vossiek, “Bandwidth dependence of cw ranging to uhf rfid tags in severe multipath environments,” in *2011 IEEE International Conference on RFID*, 2011, pp. 19–25.

[Lan05] J. Landt, “The history of RFID,” *IEEE Potentials*, vol. 24, no. 4, pp. 8–11, 2005.

[LCC+13] K. Lin, H. Chiou, K. Chien, T. Yang, P. Wu, C. Ko, and Y. Juang, “A 4.2-mW 6-dB Gain 5-65-GHz Gate-Pumped Down-Conversion Mixer Using Darlington Cell for 60-GHz CMOS Receiver,” *IEEE Transactions on Microwave Theory and Techniques*, vol. 61, no. 4, pp. 1516–1522, 2013.

[LDBI96] A. Langman, S. Dimaio, B. Burns, and M. Inggs, “Development of a low cost sfcw ground penetrating radar,” in *IGARSS ’96. 1996 International Geoscience and Remote Sensing Symposium*, vol. 4, 1996, pp. 2020–2022 vol.4.

[LDBL07] H. Liu, H. Darabi, P. Banerjee, and J. Liu, “Survey of wireless indoor positioning techniques and systems,” *IEEE Transactions on Systems, Man, and Cybernetics, Part C (Applications and Reviews)*, vol. 37, no. 6, pp. 1067–1080, 2007.

[LDC+18] Z. Liu, J. Dong, Z. Chen, Z. Jiang, P. Liu, Y. Wu, C. Zhao, and K. Kang, “A 62-90 GHz High Linearity and Low Noise CMOS Mixer Using Transformer-Coupling Cascode Topology,” *IEEE Access*, vol. 6, pp. 19 338–19 344, 2018.

[Lee03] T. H. Lee, *The Design of CMOS Radio-Frequency Integrated Circuits*, 2nd ed. Cambridge University Press, 2003.

[LS20] J. Lienig and J. Scheible, *Fundamentals of Layout Design for Electronic Circuits*, 1st ed. Springer Nature Switzerland AG, 2020.

[LZA09] X. Li, Y. Zhang, and M. G. Amin, "Multifrequency-based range estimation of rfid tags," in *2009 IEEE International Conference on RFID*, 2009, pp. 147–154.

[Mac48] G. MacFarlane, "The theory of the super-regenerative receiver operated in the linear mode," *Journal of the Institution of Electrical Engineers - Part III: Radio and Communication Engineering*, vol. 95, pp. 143–157(14), May 1948. [Online]. Available: https://digital-library.theiet.org/content/journals/10.1049/ji-3-2.1948.0032

[Max65] J. C. Maxwell, "A dynamical theory of the electromagnetic field," *Philosophical Transactions of the Royal Society of London*, vol. 155, pp. 459–512, 1865. [Online]. Available: http://rstl.royalsocietypublishing.org/content/155/459.short

[MBG+96] J.-E. Muller, A. Bangert, T. Grave, M. Karner, H. Riechert, A. Schafer, H. Siweris, L. Schleicher, H. Tischer, L. Verweyen, W. Kellner, and T. Meier, "A gaas hemt mmic chip set for automotive radar systems fabricated by optical stepper lithography," in *GaAs IC Symposium IEEE Gallium Arsenide Integrated Circuit Symposium. 18th Annual Technical Digest 1996*, 1996, pp. 189–192.

[MBN21] A. Motroni, A. Buffi, and P. Nepa, "A survey on indoor vehicle localization through rfid technology," *IEEE Access*, vol. 9, pp. 17 921–17 942, 2021.

[MDG12] J. Meyer, Q. H. Dao, and B. Geck, "Design of an analog frontend for a 5.8 ghz rfid transponder," in *2012 Asia Pacific Microwave Conference Proceedings*, 2012, pp. 1043–1045.

[MDW15] D. Murphy, H. Darabi, and H. Wu, "25.3 a vco with implicit common-mode resonance," in *2015 IEEE International Solid-State Circuits Conference - (ISSCC) Digest of Technical Papers*, 2015, pp. 1–3.

[MEK+11] R. Miesen, R. Ebelt, F. Kirsch, T. Schäfer, G. Li, H. Wang, and M. Vossiek, "Where is the tag?" *IEEE Microwave Magazine*, vol. 12, no. 7, pp. S49–S63, 2011.

[MGAC19] K. Mc Gee, P. Anandarajah, and D. Collins, "A review of chipless remote sensing solutions based on rfid technology," *Sensors*, vol. 19, no. 22, 2019. [Online]. Available: https://www.mdpi.com/1424-8220/19/22/4829

[MMKN16] V. Marotta, G. Macera, M. P. Kennedy, and E. Napoli, "Comparative analysis of differential colpitts and cross-coupled vcos in 180 nm si-ge hbt technology," in *2016 IEEE International Symposium on Circuits and Systems (ISCAS)*, 2016, pp. 1650–1653.

[MMW+19] A. Mishra, W. McDonnell, J. Wang, D. Rodriguez, and C. Li, "Intermodulation-Based Nonlinear Smart Health Sensing of Human Vital Signs and Location," *IEEE Access*, vol. 7, pp. 158 284–158 295, 2019.

[MNM+18] A. Motroni, P. Nepa, V. Magnago, A. Buffi, B. Tellini, D. Fontanelli, and D. Macii, "Sar-based indoor localization of uhf-rfid tags via mobile robot," in *2018 International Conference on Indoor Positioning and Indoor Navigation (IPIN)*, 2018, pp. 1–8.

[MPM05] F. X. Moncunill-Geniz, P. Pala-Schonwalder, and O. Mas-Casals, "A generic approach to the theory of superregenerative reception," *IEEE Transactions on Circuits and Systems I: Regular Papers*, vol. 52, no. 1, pp. 54–70, Jan 2005.

[MSU+11] L. Marcaccioli, E. Sbarra, L. Urbani, R. V. Gatti, and R. Sorrentino, "An accurate indoor ranging system based on fmcw radar," in *2011 IEEE Intelligent Vehicles Symposium (IV)*, 2011, pp. 981–986.

[NEAE18] N. J. Naglaa El-Agroudy, Mohammed El-Shennawy and F. Ellinger, "Design of a 24GHz FMCW radar system based on sub-harmonic generation," *IET Radar, Sonar & Navigation*, vol. 12, pp. 1052–1057(5), September 2018.

[NK19] A. Nagulu and H. Krishnaswamy, "28.5 Non-Magnetic 60GHz SOI CMOS Circulator Based on Loss/Dispersion-Engineered Switched Bandpass Filters," in *2019 IEEE International Solid-State Circuits Conference - (ISSCC)*, 2019, pp. 446–448.

[NMR+10] P. V. Nikitin, R. Martinez, S. Ramamurthy, H. Leland, G. Spiess, and K. V. S. Rao, "Phase based spatial identification of uhf rfid tags," in *2010 IEEE International Conference on RFID (IEEE RFID 2010)*, 2010, pp. 102–109.

[NR06] P. V. Nikitin and K. V. S. Rao, "Theory and measurement of backscattering from RFID tags," *IEEE Antennas and Propagation Magazine*, vol. 48, no. 6, pp. 212–218, 2006.

[NR08] P. V. Nikitin and K. V. S. Rao, "Antennas and propagation in uhf rfid systems," in *2008 IEEE International Conference on RFID*, 2008, pp. 277–288.

[OLC+18] S. N. Ong, S. Lehmann, W. H. Chow, C. Zhang, C. Schippel, L. H. K. Chan, Y. Andee, M. Hauschildt, K. K. S. Tan, J. Watts, C. K. Lim, A. Divay, J. S. Wong, Z. Zhao, M. Govindarajan, C. Schwan, A. Huschka, A. Bcllaouar, W. LOo, J. Mazurier, C. Grass, R. Taylor, K. W. J. Chew, S. Embabi, G. Workman, A. Pakfar, S. Morvan, K. Sundaram, M. T. Lau, B. Rice, and D. Harame, "A 22 nm FDSOI Technology Optimized for RF/mmWave Applications," in *2018 IEEE Radio Frequency Integrated Circuits Symposium (RFIC)*, 2018, pp. 72–75.

[Par10] D. Paret, *RFID at Ultra and Super High Frequencies: Theory and Application*. Wiley Publishing, 2010.

[PBKS08] S. Preradovic, I. Balbin, N. C. Karmakar, and G. Swiegers, "A novel chipless rfid system based on planar multiresonators for barcode replacement," in *2008 IEEE International Conference on RFID*, 2008, pp. 289–296.

[PD11] P. Pursula and F. Donzelli, "Transponders for millimeter wave identification," in *2011 IEEE-APS Topical Conference on Antennas and Propagation in Wireless Communications*, 2011, pp. 1221–1224.

[PK10] S. Preradovic and N. C. Karmakar, "Chipless rfid: Bar code of the future," *IEEE Microwave Magazine*, vol. 11, no. 7, pp. 87–97, 2010.

[PKK+11] P. Pursula, T. Karttaavi, M. Kantanen, A. Lamminen, J. Holmberg, M. Lahdes, I. Marttila, M. Lahti, A. Luukanen, and T. Vähä-Heikkilä, "60-GHz Millimeter-Wave Identification Reader on 90-nm CMOS and LTCC," *IEEE Transactions on Microwave Theory and Techniques*, vol. 59, no. 4, pp. 1166–1173, 2011.

[PMFT+17] Z. Peng, J. M. Munoz-Ferreras, Y. Tang, C. Liu, R. Gomez-Garcia, L. Ran, and C. Li, "A portable fmcw interferometry radar with programmable low-if architecture for localization, isar imaging, and vital sign tracking," *IEEE Transactions on Microwave Theory and Techniques*, vol. 65, no. 4, pp. 1334–1344, 2017.

[PMvD+20] B. W. Parkinson, Y. J. Morton, van Diggelen, S. J. Frank, and J. J., *Introduction, Early History, and Assuring PNT (PTA)*, 2020. [Online]. Available: https://onlinelibrary.wiley.com/doi/abs/10.1002/9781119458449.ch1

[Poz12] D. Pozar, *Microwave Engineering.* Springer, ISBN: 978-0-470-63155-3, pp. 616, 2012.

[PSBDdAL+20] P. Pala-Schonwalder, J. Bonet-Dalmau, F. del Aguila-Lopez, F. X. Moncunill-Geniz, and R. Giralt-Mas, "Superregeneration revisited: From principles to current applications," *IEEE Microwave Magazine*, vol. 21, no. 2, pp. 35–47, 2020.

[PWJS15] M. Porranzl, C. Wagner, H. Jaeger, and A. Stelzer, "An active quasi-circulator for 77 GHz automotive FMCW radar systems in sige technology," *IEEE Microwave and Wireless Components Letters*, vol. 25, no. 5, pp. 313–315, 2015.

[Qui94] B. G. Quinn, "Estimating frequency by interpolation using fourier coefficients," *IEEE Transactions on Signal Processing*, vol. 42, no. 5, pp. 1264–1268, May 1994.

[Raz12] B. Razavi, *RF microelectronics.* Prentice hall New York, 2012, vol. 2.

[RBK+19] F. Roos, J. Bechter, C. Knill, B. Schweizer, and C. Waldschmidt, "Radar Sensors for Autonomous Driving: Modulation Schemes and Interference Mitigation," *IEEE Microwave Magazine*, vol. 20, no. 9, pp. 58–72, 2019.

[RHW+10a] H. Rücker, B. Heinemann, W. Winkler, R. Barth, J. Borngraber, J. Drews, G. G. Fischer, A. Fox, T. Grabolla, U. Haak, D. Knoll, F. Korndörfer, A. Mai, S. Marschmeyer, P. Schley, D. Schmidt, J. Schmidt, M. A. Schubert, K. Schulz, B. Tillack, D. Wolansky, and Y. Yamamoto, "A 0.13 μm SiGe BiCMOS Technology Featuring f_T/f_{max} of 240/330 GHz and Gate Delays Below 3 ps," *IEEE Journal of Solid-State Circuits*, vol. 45, no. 9, pp. 1678–1686, 2010.

[RHW+10b] ——, "A 0.13 μm SiGe BiCMOS Technology Featuring f_T/f_{max} of 240/330 GHz and Gate Delays Below 3 ps," *IEEE Journal of Solid-State Circuits*, vol. 45, no. 9, pp. 1678–1686, 2010.

[Rie49] L. Riebman, "Theory of the superregenerative amplifier," *Proceedings of the IRE*, vol. 37, no. 1, pp. 29–33, Jan 1949.

[RLG13] A. Ramos, A. Lazaro, and D. Girbau, "Semi-passive time-domain uwb rfid system," *IEEE Transactions on Microwave Theory and Techniques*, vol. 61, no. 4, pp. 1700–1708, 2013.

[RNDK19] N. Reiskarimian, A. Nagulu, T. Dinc, and H. Krishnaswamy, "Nonreciprocal electronic devices: A hypothesis turned into reality," *IEEE Microwave Magazine*, vol. 20, no. 4, pp. 94–111, 2019.

[Ros14] L. Roselli, *Green RFID Systems*, ser. EuMA High Frequency Technologies Series. Cambridge University Press, 2014.

[RS18] N. Rinaldi and M. Schröter, *Silicon-germanium heterojunction bipolar transistors for mm-wave systems technology, modeling and circuit applications*, ser. Silicon-Germanium Heterojunction Bipolar Transistors for mm-Wave Systems Technology, Modeling and Circuit Applications, 2018, pp. 1–328, cited By :2. [Online]. Available: www.scopus.com

[RSR69] L. Rabiner, R. Schafer, and C. Rader, "The chirp z-transform algorithm," *IEEE Transactions on Audio and Electroacoustics*, vol. 17, no. 2, pp. 86–92, 1969.

[Sch11] H. Schantz, "On the origins of rf-based location," in *Wireless Sensors and Sensor Networks (WiSNet), 2011 IEEE Topical Conference on*, Jan 2011, pp. 21–24.

[SCW+13a] A. Strobel, C. Carlowitz, R. Wolf, F. Ellinger, and M. Vossiek, "A millimeter-wave low-power active backscatter tag for FMCW radar systems," *IEEE Transactions on Microwave Theory and Techniques*, vol. 61, no. 5, pp. 1964–1972, 2013.

[SCW+13b] ——, "A millimeter-wave low-power active backscatter tag for FMCW radar systems," *IEEE Trans. Microw. Theory Tech.*, vol. 61, pp. 1964–1972, 2013.

[Sey05] *Electromagnetics and RF Propagation*. John Wiley & Sons, Ltd, 2005, ch. 2, pp. 14–37. [Online]. Available: https://onlinelibrary.wiley.com/doi/abs/10.1002/0471743690.ch2

[SFS11] C. M. Schmid, R. Feger, and A. Stelzer, "Millimeter-wave phase-modulated backscatter transponder for FMCW radar applications," in *2011 IEEE MTT-S International Microwave Symposium*, 2011, pp. 1–4.

[SK05] E. Shevchuk and Kyusun Choi, “Folded Cascode CMOS Mixer Design and Optimization in 70 nm Technology,” in *48th Midwest Symposium on Circuits and Systems, 2005.*, 2005, pp. 943–946 Vol. 2.

[SK08] T. Sanpechuda and L. Kovavisaruch, “A review of rfid localization: Applications and techniques,” in *2008 5th International Conference on Electrical Engineering/Electronics, Computer, Telecommunications and Information Technology*, vol. 2, 2008, pp. 769–772.

[Sko80] M. I. Skolnik, *Introduction to radar systems /2nd edition/*, 1980.

[Sko88] M. Skolnik, “Radar: From Hertz to the 21st century,” *IEEE Antennas and Propagation Society Newsletter*, vol. 30, no. 5, pp. 13–18, 1988.

[SPB+21] E. Soltanaghaei, A. Prabhakara, A. Balanuta, M. Anderson, J. M. Rabaey, S. Kumar, and A. Rowe, *Millimetro: MmWave Retro-Reflective Tags for Accurate, Long Range Localization.* New York, NY, USA: Association for Computing Machinery, 2021, p. 69â€“82. [Online]. Available: https://doi.org/10.1145/3447993.3448627

[SQC13] M. Sun, X. Qing, and Z. N. Chen, “60-ghz end-fire fan-like antennas with wide beamwidth,” *IEEE Transactions on Antennas and Propagation*, vol. 61, no. 4, pp. 1616–1622, 2013.

[SR92] S. Seidel and T. Rappaport, “914 mhz path loss prediction models for indoor wireless communications in multifloored buildings,” *IEEE Transactions on Antennas and Propagation*, vol. 40, no. 2, pp. 207–217, 1992.

[SRS+21] N. Suhadolnik, J. Rozman, T. Svete, Z. Korosak, M. Atanasijevic-Kunc, and A. Pletersek, “Phase detection and modulation improvement for active load modulation during continuous transmission,” *Sensors (Basel, Switzerland)*, vol. 21, 2021.

[SSE+14] A. Strobel, M. Schulz, F. Ellinger, C. Carlowitz, and M. Vossiek, “Analysis of phase sampling noise of switched injection-locked oscillators,” in *2014 IEEE Topical Conference on Wireless Sensors and Sensor Networks (WiSNet)*, 2014, pp. 43–45.

[SSP14] T. Sarkar and M. Salazar Palma, "A history of the evolution of radar," in *Microwave Conference (EuMC), 2014 44th European*, Oct 2014, pp. 734–737.

[Sto48] H. Stockman, "Communication by Means of Reflected Power," *Proceedings of the IRE*, vol. 36, no. 10, pp. 1196–1204, 1948.

[Str14] A. Strobel, *Geschaltete Oszillatoren für Hochfrequenz-Entfernungsmesssysteme*, ser. Dissertation an TU Dresden. Vogt Verlag, 2014.

[SVL+13] M. A. T. Sanduleanu, A. Valdes-Garcia, Y. Liu, B. Parker, S. Shlafman, B. Sheinman, D. Elad, S. Reynolds, and D. Friedman, "A 60GHz, linear, direct down-conversion mixer with mm-Wave tunability in 32nm CMOS SOI," in *Proceedings of the IEEE 2013 Custom Integrated Circuits Conference*, 2013, pp. 1–4.

[TFJE23] M. V. Thayyil, A. Figueroa, N. Joram, and F. Ellinger, "Integrated superregenerative amplifier based 24 ghz frequency modulated continuous wave radar active reflector tags for joint ranging and communication," *IET Radar Sonar Navig.*, pp. 1–17, 2023. [Online]. Available: https://ietresearch.onlinelibrary.wiley.com/doi/abs/10.1049/rsn2.12412

[TFL+15] G. Tretter, D. Fritsche, J. D. Leufker, C. Carta, and F. Ellinger, "Zero-Ohm transmission lines for millimetre- wave circuits in 28 nm digital CMOS," *Electron. Lett.*, vol. 51, no. 11, 2015.

[TGJE18] M. V. Thayyil, H. Ghaleb, N. Joram, and F. Ellinger, "A 28 GHz superregenerative amplifier for FMCW radar reflector applications in 45 nm SOI CMOS," in *2018 Asia-Pacific Microwave Conference (APMC)*, Nov 2018, pp. 630–632.

[TGX+19] B. Tang, X. Gui, J. Xu, Q. Xia, and L. Geng, "A Dual Interference-Canceling Active Quasi-Circulator Achieving 36 dB Isolation Over 6 GHz Bandwidth," *IEEE Microwave and Wireless Components Letters*, vol. 29, no. 6, pp. 409–411, 2019.

[TJE20] M. V. Thayyil, N. Joram, and F. Ellinger, "A 22 to 28 GHz SiGe Superregenerative Amplifier with Integrated Quench Pulse Shaping for FMCW Radar Active Reflector Tags," in *2020 IEEE 20th Topical Meeting on Silicon Monolithic Integrated Circuits in RF Systems (SiRF)*, Jan 2020, pp. 84–87.

[TLH+16] S. Tang, C. Lin, S. Hung, K. Cheng, and Y. Wang, "Ultra-wideband quasi-circulator implemented by cascading distributed balun with phase cancelation technique," *IEEE Transactions on Microwave Theory and Techniques*, vol. 64, no. 7, pp. 2104–2112, 2016.

[TLJE18] M. V. Thayyil, S. Li, N. Joram, and F. Ellinger, "A K-Band SiGe Superregenerative Amplifier for FMCW Radar Active Reflector Applications," *IEEE Microwave and Wireless Components Letters*, vol. 28, no. 7, pp. 603–605, July 2018.

[TLJE19] ——, "A 4-32 GHz SiGe Multi-Octave Power Amplifier With 20 dBm Peak Power, 18.6 dB Peak Gain and 156% Power Fractional Bandwidth," *IEEE Microwave and Wireless Components Letters*, vol. 29, no. 11, pp. 745–748, Oct. 2019.

[TMS+19] A. Tzitzis, S. Megalou, S. Siachalou, T. G. Emmanouil, A. Kehagias, T. V. Yioultsis, and A. G. Dimitriou, "Localization of rfid tags by a moving robot, via phase unwrapping and non-linear optimization," *IEEE Journal of Radio Frequency Identification*, vol. 3, no. 4, pp. 216–226, 2019.

[TPC+21] M. V. Thayyil, J. Pliva, M. Cui, N. Joram, and F. Ellinger, "A 60 ghz low power integrated quasi-circulator in 22 nm fdsoi technology," in *2021 IEEE 20th Topical Meeting on Silicon Monolithic Integrated Circuits in RF Systems (SiRF)*, 2021, pp. 15–18.

[TSJE21] M. V. Thayyil, S. Seyyedrezaei, N. Joram, and F. Ellinger, "A 60 GHz Folded Switching Stage Down-Conversion Mixer with 21 dB Conversion Gain in 22 nm FDSOI Technology," in *2021 IEEE MTT-S International Microwave Symposium (IMS)*, 2021, pp. 286–289.

[TTCE18] M. V. Thayyil, P. V. Testa, C. Carta, and F. Ellinger, "A 190 GHz Inset-Fed Patch Antenna in SiGe BEOL for On-Chip Integration," in *2018 IEEE Radio and Antenna Days of the Indian Ocean (RADIO)*, 2018, pp. 1–2.

[VG08] M. Vossiek and P. Gulden, "The Switched Injection-Locked Oscillator : A Novel Versatile Concept for Wireless Transponder and Localization Systems," *IEEE Trans. Microw. Theory Tech.*, vol. 56, no. 4, pp. 859–866, 2008.

[VHPM+08] T. Vähä-Heikkilä, P. Pursula, A. Müller, D. Neculoiu, G. Konstantinidis, and J. Tuovinen, "Millimeter wave identification: concept, applications, and demonstrations," in *Nanosensors and Microsensors for Bio-Systems 2008*, V. K. Varadan, Ed., vol. 6931, International Society for Optics and Photonics. SPIE, 2008, pp. 163 – 168. [Online]. Available: https://doi.org/10.1117/12.776354

[VMCV02] A. P. Venguer, J. L. Medina, R. Chávez, and A. Velázquez, "Low-noise one-port microwave transistor amplifier," *Microwave and Optical Technology Letters*, vol. 33, no. 2, pp. 100–104, 2002. [Online]. Available: https://onlinelibrary.wiley.com/doi/abs/10.1002/mop.10236

[Voi13] S. Voinigescu, *High-frequency and high-data-rate communication systems*, ser. The Cambridge RF and Microwave Engineering Series. Cambridge University Press, 2013, pp. 14–76.

[VPT11] A. Vena, E. Perret, and S. Tedjini, "Chipless rfid tag using hybrid coding technique," *IEEE Transactions on Microwave Theory and Techniques*, vol. 59, no. 12, pp. 3356–3364, 2011.

[VPT12a] ——, "A compact chipless rfid tag using polarization diversity for encoding and sensing," in *2012 IEEE International Conference on RFID (RFID)*, 2012, pp. 191–197.

[VPT12b] ——, "High-capacity chipless rfid tag insensitive to the polarization," *IEEE Transactions on Antennas and Propagation*, vol. 60, no. 10, pp. 4509–4515, 2012.

[WC95] W. Wlesbeck and D. J. Clchon, "The link from Heinrich Hertz to modern communication," in *1995 25th European Microwave Conference*, vol. 2, 1995, pp. 886–894.

[Weh10] Wehrli, Silvan and Gierlich, Roland and Hüttner, Jörg and Barras, David and Ellinger, Frank and Jäckel, Heinz, "Integrated active pulsed reflector for an indoor local positioning system," *IEEE Trans. Microw. Theory Tech.*, vol. 58, no. 2, pp. 267–276, 2010.

[Whi50] J. Whitehead, *Super-regenerative receivers*, ser. Modern radio technique. Cambridge University Press, 1950.

[WLW16] S. Wang, C. Lee, and Y. Wu, "Fully integrated 10-ghz active circulator and quasi-circulator using bridged-t networks in standard cmos," *IEEE Transactions on Very Large Scale Integration (VLSI) Systems*, vol. 24, no. 10, pp. 3184–3192, 2016.

[WS98] M. Win and R. Scholtz, "Impulse radio: how it works," *IEEE Communications Letters*, vol. 2, no. 2, pp. 36–38, 1998.

[WTLH18] L. Wang, K. H. Teng, Y. Lian, and C. H. Heng, "A 4×4 ir uwb timed-array radar based on 16-channel transmitter and sampling capacitor reused receiver," *IEEE Transactions on Circuits and Systems II: Express Briefs*, vol. 65, no. 7, pp. 878–882, 2018.

[WV65] R. M. White and F. W. Voltmer, "Direct piezoelectric coupling to surface elastic waves," *Applied Physics Letters*, vol. 7, no. 12, pp. 314–316, 1965. [Online]. Available: https://doi.org/10.1063/1.1754276

[XKK+09] Y. Xi, S. Kwon, H. Kim, H. Cho, M. Kim, S. Jung, C.-S. Park, J. Kim, and Y. Yang, "Optimum ask modulation scheme for passive rfid tags under antenna mismatch conditions," *IEEE Transactions on Microwave Theory and Techniques*, vol. 57, no. 10, pp. 2337–2343, 2009.

[Xue08] L. Xue, *IET Microwaves, Antennas & Propagation*, vol. 2, pp. 109–114(5), March 2008. [Online]. Available: https://digital-library.theiet.org/content/journals/10.1049/iet-map_20070146

[YZL13] Z. Yang, Z. Zhou, and Y. Liu, "From rssi to csi: Indoor localization via channel response," *ACM Comput. Surv.*, vol. 46, no. 2, dec 2013. [Online]. Available: https://doi.org/10.1145/2543581.2543592

[ZGL19] F. Zafari, A. Gkelias, and K. K. Leung, "A survey of indoor localization systems and technologies," *IEEE Communications Surveys Tutorials*, vol. 21, no. 3, pp. 2568–2599, 2019.

[ZXLW04] J. Zhang, Z. Xie, S. Lai, and Z. Wu, "A design of RF receiving circuit of RFID reader," in *ICMMT 4th International Conference on, Proceedings Microwave and Millimeter Wave Technology, 2004.*, 2004, pp. 406–409.

List of Original Publications

1. **M. V. Thayyil**, S. Li, N. Joram, and F. Ellinger, “A *k*-band SiGe superregenerative amplifier for FMCW radar active reflector applications,” in *IEEE Microwave and Wireless Components Letters*, vol. 28, no. 7, pp. 603–605, July 2018.

2. **M. V. Thayyil**, S. Li, N. Joram, and F. Ellinger, “A 4-32 GHz SiGe multi-octave power amplifier with 20 dBm peak power, 18.6 dB peak gain and 156 % power fractional bandwidth,” in *IEEE Microwave and Wireless Components Letters*, vol. 29, no. 11, pp. 745–748, Oct. 2019.

3. **M. V. Thayyil**, A. Figueroa, N. Joram, and F. Ellinger, “Integrated superregenerative amplifier based 24 GHz frequency modulated continuous wave radar active reflector tags for joint ranging and communication,” in *IET Radar Sonar Navig.* , 1-17 (2023). https://doi.org/10.1049/rsn2.12412

4. **M. V. Thayyil**, S. Seyyedrezaei, N. Joram and F. Ellinger, "A 60 GHz Folded Switching Stage Down-Conversion Mixer with 21 dB Conversion Gain in 22 nm FDSOI Technology," in *2021 IEEE International Microwave Symposium (IMS), Atlanta*, GA, USA, June 2021.

5. **M. V. Thayyil**, N. Joram, and F. Ellinger, “A 22 to 28 GHz SiGe superregenerative amplifier with integrated quench pulse shaping for FMCW radar active reflector tags,” in *2020 IEEE 20th Topical Meeting on Silicon Monolithic Integrated Circuits in RF Systems (SiRF)*, Jan 2020, pp. 84–87.

6. **M. V. Thayyil**, J. Pliva, M. Cui, N. Joram, and F. Ellinger, “A 60 GHz Quasi-Circulator in 22 nm FDSOI Technology,” in *2021 IEEE 21th Topical Meeting on Silicon Monolithic Integrated Circuits in RF Systems (SiRF)*, Jan 2021, pp. 84–87.

7. **M. V. Thayyil**, H. Ghaleb, N. Joram, and F. Ellinger, “A 28 GHz superregenerative amplifier for FMCW radar reflector applications in 45 nm SOI CMOS,” in *2018 Asia-Pacific Microwave Conference (APMC)*, Nov 2018, pp. 630–632.

8. **M. V. Thayyil**, P. V. Testa, C. Carta, and F. Ellinger, “A 190 GHz inset-fed patch antenna in SiGe beol for on-chip integration,” in *2018 IEEE Radio and Antenna Days of the Indian Ocean (RADIO)*, 2018, pp. 1–2.

9. S. Seyyedrezaei, **M. V. Thayyil**, C. Carta, and F. Ellinger, “A DC to 20 GHz Variable Gain Amplifier with Tunable Input Matching in 22 nm FDSOI Technology,” in *51st European Microwave Integrated Circuits Conference (EuMIC)*, 2022, pp. 181-184.

10. S. Li, **M. V. Thayyil**, C. Carta, and F. Ellinger, "A 12 GHz to 46 GHz fully integrated SiGe distributed power amplifier with 20.9 dBm output power and 18.3 dB gain," in *2020 IEEE Topical Conference on RF/Microwave Power Amplifiers for Radio and Wireless Applications (PAWR)*, 2020, pp. 30–33.

11. P. V. Testa,**M. V. Thayyil**, G. Belfiore, C. Carta, and F. Ellinger, "High-impedance multi-conductor transmission-lines for integrated applications at millimeter-wave frequency," in *2017 30th Symposium on Integrated Circuits and Systems Design (SBCCI)*, 2017, pp. 129–135.

12. R. F. Riaz, **M. V. Thayyil**, J. Wagner, L. Wetzel, D. Prousalis and F. Ellinger, "A Multiple Input and Gain Adjustable Phase Detector in 130 nm BiCMOS Technology," in *2022 IEEE BiCMOS and Compound Semiconductor Integrated Circuits and Technology Symposium (BCICTS)*, Phoenix, AZ, USA, 2022, pp. 45–48.

List of Abbreviations

ADC	analog to digital Converter
ADE	analog design environment
AGC	automatic gain control
AM	amplitude modulation
APMOM	alternate polarity metal-oxide-metal
ART	active RFID transponder
ASIC	application specific intergrated circuit
ASK	amplitude shift keying
AWGN	additive white Gaussian noise
BAW	bulk acoustic wave
BEOL	back end of line
BLE	Bluetooth® low energy
BPF	band pass filter
BPSK	binary phase shift keying
μC	microcontrollers
CB	common base
CC	common collector
CCO	cross coupled oscillator
CD	common drain
CDF	cumulative density function
CE	common emitter
CG	common gate
CMOS	complementary metal oxide semiconductor
COTS	commercial off-the-shelf
CS	common source
CW	unmodulated continuous wave
CZT	chirp z-transform
DAC	digital to analog converter
DDS	direct digital synthesizer
DFT	discrete Fourier transform
DR	dynamic range
DSB	double side band
EIRP	effective isotropic radiated power
EM	electromagnetic

f_t	transit frequency
FD-PDoA	frequency domain phase differene of arrival
FDSOI	fully depleted silicon on insulator
FET	field effect transistor
FFT	fast Fourier transform
FoM	figures of merit
FPGA	field programmable gate array
FR4	flame retardant-4
FSK	freqeuncy shift keying
FSPL	free space path loss
FSSDM	folded switching stage down-conversion mixer
GCPW	grounded coplanar waveguide
GF	Global Foundries
GFSK	Gaussian frequency shift keying
HBT	heterojunction bipolar transistor
HF	high frequency
HG	high gain
HP	hybrid parameters
I^2C	inter-integrated circuit
IC	integrated circuit
IDT	inter digital transducer
IF	intermediate frequency
IFF	identify friend or foe
IIP_{1dB}	input referred third order intercept point
IoT	internet of things
IP_{1dB}	input referred 1dB compression point
IQ	in-phase and quadrature
ISM	industry scientific medical
ISO	international standards organisation
KCL	Kirchhoff's current law
KVL	Kirchhoff's voltage law
LCA	loss compensation amplifier
LF	low frequency
LFMCW	linear frequency modulated continuous wave
LG	low gain
LHS	left hand side
LNA	low noise amplifier

LO	local oscillator
LoS	line of sight
LPTV	linear periodically time invariant
LTI	linear time invariant
LWD	lumped element WPD
MIM	metal insulator metal
MMIC	monolithic microwave integrated circuit
MMID	millimeter-wave identification
mmWave	millimeter-wave
MOM	alternate polarity metal oxide metal
MOS	metal oxide semiconductor
MOSFET	metal oxide semiconductor FET
NF	noise figure
NF_{SSB}	single sideband noise figure
nFET	N-channel field effect transistor
NMOS	N-channel metal oxide semiconductor
NTF	noise transfer function
OOK	on-off keying
OTS	off-the-shelf
PA	power amplifier
PBT	passive backscatter transponder
PCB	printed circuit board
PDF	probability density function
PDK	process design kit
PDoA	phase differene of arrival
PDSOI	partially depleted silicon on insulator
pFET	P-channel field effect transistor
PLL	phase locked loop
PLM	passive load modulation
PM	power mode
PMOS	P-channel metal oxide semiconductor
PPM	pulse position modulation
PSP	periodic S-parameter
PSS	periodic steady state
PSTAB	periodic stability
QC	quasi circulator
QPAC	quasi-periodic AC

QPSS	quasi-periodic steady state
R_x	receive
RA	reflection amplifier
RCS	radar cross section
RF	radio frequency
RFIC	radio frequency integrated circuit
RFID	radio frequency identification
RHS	right hand side
RSS	received signal strength
RSSI	received signal strength indicator
RToF	round trip time of flight
SAW	surface acoustic wave
SFCW	stepped frequency continuous wave
SiGe-BiCMOS	silicon-germanium bipolar complementary metal oxide semiconductor
SILO	switched injection locked oscillator
SNR	signal to noise ratio
SOA	safe operating area
SOI	silicon on insulator
SOLR	short-open-load-reciprocal
SOLT	short-open-load-through
SP	scatter matrix parameters
SQ-FSK	SRA quench frequency shift keying
SRA	superregenerative amplifier
$SRA_{buf,q}$	buffered antenna drive SiGe SRA with integrated quench pulse shaping
SRA_{dir}	direct antenna drive SiGe SRA
SRA_{SOI}	direct antenna drive CMOS SRA
SRT	superregenerative transponder
SSB	single sideband
STCCO	stacked transistor cross-coupled quenchable oscillator
T_x	transmit
TAS	trans-admittance amplifier Stage
TDoA	time difference of arrival
TDR	time domain reflectometry
TIA	time interval of arrival
TIS	trans-impedance amplifier Stage
ToA	time of arrival

ToF	time of flight
UHF	ultra high frequency
UWB	ultra-wideband
UWB-IR	ultra-wideband impulse radio
VCO	voltage controlled oscillator
VCVS	voltage controlled voltage source
VGA	variable gain amplifier
VNA	vector network analyzer
WPD	Wilkinson power divider
WSN	wireless sensor node
YP	admittance parameters

List of symbols

$A_{\mathrm{T_x},i}$	voltage amplitude of the transmitted FMCW chirp
C_{p}	arbitrary parallel capacitance
$C_{\mathrm{p,in}}$	equivalent parallel input capacitance of MOPA
i	chirp sequence number
c_0	speed of light in free space
D_{q}	duty cycle of the SRA quench signal
f_{chirp}	FMCW chirp bandwidth
f_{max}	maximum frequeny of oscillation of a transistor
f_{t}	Transit frequency of a transistor
G_{conv}	conversion gain of the FSSDM
g_{ds}	Channel conductance of a MOSFET
g_{m}	Trans-conductance of a MOSFET
I_{D}	Total current consumed by a circuit
$\mathrm{IIP}_{\mathrm{3dB}}$	input-referred third order intermodulation intercept point
$\mathrm{IP}_{\mathrm{1dB}}$	input-referred 1 dB compression point
K	number of chirps in each data symbol
$\mathrm{k_B}$	Boltzmann constant $\approx 1.380649 \cdot 10^{-23} JK^{-1}$
k_{q}	slope of quench waveform
M	number of symbols in the tranmitted digital data
μ	gradient of FMCW chirp
n	index of discretized baseband signal at ADC output
N_{c}	number of chirp sequences in one interrogation
N_{samp}	number of discrete samples in the entire chirp sequence
ω_{min}	angular starting frequency of the FMCW chirp

P_{min}	minimum detectable input power
Q	quality factor
$\lvert\Gamma\rvert$	magnitude of reflection coefficient
$\lvert\Gamma_{\mathrm{L}}\rvert$	magnitude of load reflection coefficient
R_{f}	feedback resistance of MOPA
$R_{\mathrm{f,eq}}$	equivalent feedback resistance of MOPA
$R_{\mathrm{in,fb}}$	input resistance of MOPA with feedback
R_{p}	arbitrary parallel resistance
$R_{\mathrm{p,in}}$	equivalent parallel input resistance of MOPA without resistive feedback
$R_{\mathrm{p,in,fb}}$	equivalent parallel input resistance of MOPA with resistive feedback
$s_{\mathrm{b},i}(t)$	low pass filtered baseband output of the interrogator
$S_{\mathrm{b},i}(f)$	low pass filtered baseband output of the interrogator
$s_{\mathrm{bs}}(t)$	backscattered signa from a passive transponder
$s_{\mathrm{mix},i}(t)$	mixer output of the interrogator
$s_{\mathrm{R_x},i}(t)$	signal received by interrogator
a_{v}	Small signal gain of an LTI system
$s_{\mathrm{T_x},i}(t)$	signal transmitted by interrogator
t	arbitary independent variable denoting time
τ_i	round trip time of flight
T_{chirp}	FMCW chirp duration
$T_{\mathrm{q,on}}$	duration for which the SRA quench signal damping is negative
T_{q}	SRA quenching time period
T_{rep}	FMCW chirp sequence repetition interval
T_{samp}	instant at which phase sampling occurs in an SRA
V_{CC}	TThe supply voltage used for HBT based circuits
V_{DD}	The supply voltage used for CMOS transistor based circuits
$\zeta(t)$	instantaneous damping or quench function
$Z_{\mathrm{in,fb}}$	input impedance of MOPA with feedback

List of Figures

1.1 System overview showing the components of an RFID system, including an interrogator, antennas and passive or active transponders interfacing sensors. 3

2.1 Classification of relevant RFID transponder technologies and interrogator architectures. The areas covered by this work are highlighted in gray. 10
2.2 Schematic of a typical semiconductor based passive transponder. . 11
2.3 Illustration of a active transponder functionality. 13
2.4 (a) Schematic of a unilateral reflection amplifier based ART. (b) Corresponding small signal model. 14
2.5 Schematic of (a) active retrodirective Van Atta array. (b) Bidirectional reflection amplifier. 14
2.6 Schematic of (a) active load modulation transponder. (b) illustration of corresponding amplitude spectrum. 16
2.7 Schematic of pulsed oscillator based transponder (a) The implementation from [Weh10] and (b) [SCW+13b]. 17
2.8 Illustration of (a) Monostatic interrogation and (b) bistatic interrogation principle. 18
2.9 Illustration of an interferometer based interrogator. 19
2.10 Illustration of a IR-UWB interrogator. 20
2.11 Generic architecture of bistatic CW radar interrogators. 21
2.12 Illustration of the frequency domain representation of CW transmit signals. (a) single-carrier CW (b) SFCW and (c) FMCW. 23
2.13 Illustration of frequency domain phase difference of arrival technique. 29
2.14 (a) Circuit model for illustrating the superregeneration principle. (b) Feedback loop based system model used for analysis. 36
2.15 (a), (b) and (c) shows the SRA quenching function. (d), (e) and (f) shows the SRA linear quench mode in which the output voltage amplitude build up is directly proportional to the input current signal. (g),(h) and (i) shows the SRA logarithmic quench mode output in which the time dependent output voltage signal area is proportional to the input current signal. (Partly reused from *[TFJE23] ©2023 IET). 41
2.16 (a) SRA output power level versus input power level for different resonator quality factor values (b) SRA minimum input power level required for phase coherent amplification at different resonator quality factor values, T=290K and $D_{\mathrm{q}} = 0.1$. 44

2.17 (a) Time domain characteristics of SRA operating in the step controlled mode. (b) Phase coherence of the SRA output signal when input signal phase is varied. 45
2.18 Modeled frequency domain characteristics of SRA with normalized amplitude plotted as a function of frequency normalized to f_{in}: (a) shows the spectral lines and peak of envelope align when $f_{\mathrm{in}} = f_{\mathrm{res}}$, (b) shows that the spectral line corresponding to f_{in} is greater the peak of the envelope corresponding to f_{res} by 2.5 times f_{q} and (c) shows the effect of AWGN corresponding to 20 dB SNR in (a). . . 47

3.1 LFMCW radar based ranging using passive reflector and a SRT. (Partly adapted from *[TFJE23] © 2023 IET). 52
3.2 Illustration of interrogating chirp sequence sent by the LFMCW radar. 52
3.3 SRT baseband signal magnitude spectrum: (a) The plot of (3.8) for a distance of 0.1 m. (b) shows the variation of the baseband frequency for different values of distance between interrogator and static transponder. (Reused from *[TFJE23] © 2023 IET). 53
3.4 Baseband magnitude spectrum showing the frequency signature of a SRT in the presence of static clutter. (Reused from *[TFJE23] © 2023 IET). 55
3.5 Minimum SRA gain required for covering a particular range at different SNR values. (Reused from *[TFJE23] © 2023 IET). . . . 56
3.6 Level diagram showing the power levels at different stages in the forward link and return link of the system level implementation, with d_{SRT} of 75 m. 58
3.7 Illustration of the characteristics of a single chirp backscscattered by a corner reflector and a SRT. (Adapted from *[TFJE23] © 2023 IET). 59
3.8 Plot of modeled baseband magnitude spectrum for different chirp sequence numbers corresponding to transfer of binary data 4'b1010 using quench frequency shift keying at a distance of (a) 10 m and (b) 100 m. In this example, $K = 2$, binary zero is represented by $f_{\mathrm{q}}/f_{\mathrm{samp}} = 0.1$ and binary one represented by $f_{\mathrm{q}}/f_{\mathrm{samp}} = 0.3$. (Reused from *[TFJE23] © 2023 IET). 61
3.9 Plot of baseband frequency f_{b} against chirp sequence number i illustrating data transfer using quench frequency shift keying. The properties of the carrier chirp remains constant. (Adapted from *[TFJE23] © 2023 IET). 62
3.10 Schematic of the CMOS cross-coupled oscillator based $\mathrm{SRA}_{\mathrm{SOI}}$ (Adapted from *[TGJE18] © 2018 IEEE). 65

3.11 Small signal equivalent circuit of the CMOS cross-coupled oscillator based $\mathrm{SRA_{SOI}}$. 66
3.12 Illustration of the common centroid layout and corresponding transistor interconnection for $\mathrm{SRA_{SOI}}$: (a) top view (b) perspective view showing via stack. 68
3.13 (a) Schematic of the zero-ohm transmission line unit cell used for DC bias routing. (b) Corresponding layout. 69
3.14 Illustration of the measurement setup around the chip micrograph of $\mathrm{SRA_{SOI}}$ measuring 820 µm × 820 µm including pads (Adapted from *[TGJE18] ©2018 IEEE). 70
3.15 (a) Simulated and measured differential tuning range of $\mathrm{SRA_{SOI}}$ in free-running mode, showing frequency tuning from 24.1 GHz to 25.4 GHz. (b) Measured peak output power spectral density vs. input power, with marking of linear mode to logarithmic mode transition points for sinusoidal and pulsed quenching. . . . 71
3.16 (a) Measured power spectral density with $P_{\mathrm{in,dBm}} = -70\,\mathrm{dBm}$ at $f_{\mathrm{res}} = 24.148\,\mathrm{GHz}$. (b) Measured normalized frequency response for various input power levels, showing an increase in bandwidth with increase in input power from −85 dBm to −60 dBm. 72
3.17 Schematic of the direct antenna interface $\mathrm{SRA_{dir}}$ (Adapted from *[TLJE18] ©2018 IEEE) 73
3.18 Small signal equivalent circuit of the $\mathrm{SRA_{dir}}$ resonator and output network transformation used to derive f_{res} and V_{res}. 74
3.19 The comprehensive HBT small signal equivalent circuit of the stacked transistor CCO half cell. 76
3.20 Simplified high frequency small signal equivalent circuit of the stacked transistor CCO half cell for loop gain analysis and determining the value of C_{B}. 78
3.21 (a) The magnitude of loop gain $|\underline{a}_{\mathrm{v,loop}}(j\omega)|$ and (b) phase of loop gain $\angle\underline{a}_{\mathrm{v,loop}}(j\omega)$ versus frequency for different inductor L_{eff} quality factor values. 82
3.22 Modeled signal characteristics: (a) quench signal $V_{\mathrm{q,w1}}(t)$, (c) normalized sensitivity curve $\mu_{\mathrm{w1}}(t)$, (e) SRA output voltage $V_{\mathrm{res,w1}}$ and (g) bias current $I_{\mathrm{b,w1}}$. (b) quench signal $V_{\mathrm{q,w2}}$, (d) normalized sensitivity curve $\mu_{\mathrm{w2}}(t)$, (f) SRA output oscillations $V_{\mathrm{res,w2}}$ and (h) bias current $I_{\mathrm{b,w2}}$. (Adapted from *[TLJE18] ©2018 IEEE) 84
3.23 Schematic of the direct antenna interface $\mathrm{SRA_{dir,q}}$ with integrated quench pulse shaping. (Adapted from *[TFJE23] ©2023 IET). . . . 87
3.24 Implemented direct drive SRA ICs in a 130 nm SiGe BiCMOS technology measuring 875 µm × 725 µm including pads, and having the same footprint: (a) $\mathrm{SRA_{dir}}$ (reused from [TLJE18] ©2018 IEEE) (b) $\mathrm{SRA_{dir,q}}$ with integrated quench pulse shaping 88

3.25 (a) Illustration of the characterization setup. (b) Resonator frequency versus tuning voltage. (reused from [TLJE18] © 2018 IEEE) 88
3.26 (a) Measured power spectral density with $P_{\mathrm{in,dBm}} = -100\,\mathrm{dBm}$ at $f_{\mathrm{res}} = 25.3\,\mathrm{GHz}$. (b) Plot of $P_{\mathrm{out,dBm}}$ against $P_{\mathrm{in,dBm}}$ for quench signals $V_{\mathrm{q,w1}}$ and $V_{\mathrm{q,w2}}$. (reused from *[TLJE18] © 2018 IEEE) . . 89
3.27 Normalized frequency response: (a) Comparison of measurement and model. (b) Characterization results at different input power levels. (reused from [TLJE18] © 2018 IEEE) 90
3.28 Schematic of buffered antenna interface $\mathrm{SRA_{buf,q}}$ including quench pulse shaping circuit (Adapted from *[TJE20] © 2020 IEEE). . . . 91
3.29 $\mathrm{SRA_{buf,q}}$ small signal equivalent circuits used for analysis. 92
3.30 Plot of $I_{\mathrm{b,samp}}$ and $V_{\mathrm{q,x,samp}}$ as a function of varactor tuning voltage V_{tune}. 94
3.31 Monte Carlo simulation results for 200 iterations showing the variation of $V_{\mathrm{th,M1}}$. 95
3.32 Model and simulation of shaped quench signal (reused from *[TJE20] © 2020 IEEE). 97
3.33 Illustration of the characterization setup around the chip micrograph of the $\mathrm{SRA_{buf,q}}$ occupying an area of $990\,\mu\mathrm{m} \times 895\,\mu\mathrm{m}$. including pads (Adapted from *[TJE20] © 2020 IEEE). 100
3.34 $\mathrm{SRA_{buf,q}}$ characterization results: (a) Measured magnitude of input reflection coefficient versus frequency for different V_{tune} values for $\mathrm{SRA_{buf}}$. (b) Measured and modeled peak of the envelope of output power density versus input power level for $\mathrm{SRA_{buf}}$. (c) Measured envelope of power spectral density showing the Dirac delta peaks when an input signal is applied within the bandwidth of the resonator. (d) Normalized frequency response measurements used to determine bandwidth (Adapted from *[TJE20] © 2020 IEEE). . . . 101
3.35 Block diagram of the $\mathrm{SRA_{dir,q}}$ based $\mathrm{SRT_{dir}}$. 107
3.36 Block diagram of the $\mathrm{SRA_{buf,q}}$ based $\mathrm{SRT_{buf}}$ (Adapted from *[TJE20] © 2020 IEEE). 108
3.37 Active reflector tags with bonded SRA ICs shown in inset above chip cap (a) $\mathrm{SRT_{dir}}$ with $\mathrm{SRA_{dir,q}}$ measuring $50\,\mathrm{mm} \times 35\,\mathrm{mm}$. (b) $\mathrm{SRT_{dir}}$ with $\mathrm{SRA_{buf,q}}$ measuring $70\,\mathrm{mm} \times 50\,\mathrm{mm}$. (Reused from *[TFJE23] © 2023 IET). 109
3.38 Fabricated SRA ICs with quench pulse shaping in 130 nm SiGe BiCMOS technology (a) Direct antenna interface SRA occupying an area of $875\,\mu\mathrm{m} \times 725\,\mu\mathrm{m}$. (b) Buffered antenna interface SRA, occupying an area of $990\,\mu\mathrm{m} \times 895\,\mu\mathrm{m}$. (Reused from *[TFJE23] © 2023 IET). 110

3.39 (a) Geometry of the bandwidth enhanced patch antenna ANT_{MB1x}; (b) Equivalent circuit model used to determine frequency response; (c) Measured, simulated and modeled input reflection coefficients for conventional microstrip patch antenna ANT_{MN1x} and bandwidth enhanced ANT_{MB1x}. (Reused from *[TFJE23] © 2023 IET). 112
3.40 (a) Simulated radiation pattern of ANT_{MB2x} and (b) ANT_{MB4x}; (c) Simulated gain vs. θ cut at $\phi = 90°$ for horizontal and vertical polarization of ANT_{MB2x} and (d) ANT_{MB4x}. (Reused from *[TFJE23] © 2023 IET). 113
3.41 (a) Block diagram of the LFMCW radar interrogator, implemented as a stack of PCB_{dig} and PCB_{RF}; (b) Phase noise profile of the interrogator output in the CW mode for three different frequencies in the band. (Reused from *[TFJE23] © 2023 IET). 115
3.42 (a) Top view of the hardware with PCB_{dig} in sight. (b) PCB_{RF}. (Reused from *[TFJE23] © 2023 IET). 116
3.43 Comparison of range estimation error between FFT and CZT based methods. (Reused from *[TFJE23] © 2023 IET). 117

4.1 60 GHz CW interrogator and passive backscatter transponder based identification system. 122
4.2 Passive load modulation: (a) ASK modulated PBT signals corresponding to a data of 5'b01001. (b) PBT equivalent circuit with antenna source impedance. 122
4.3 Minimum magnitude of load reflection coefficient to detect the PBT at a particular distance at different SNR values. 123
4.4 Block diagram of the transmission lines based QC_{TL}. (Reused from *[TPC+21]©2021, IEEE) 125
4.5 Schematic of the transmission line based QC_{TL}. (Reused from *[TPC+21]©2021, IEEE). 126
4.6 Isometric view of the 70 Ω GCPW transmission line used for the WPD. (Reused from *[TPC+21]©2021, IEEE). 127
4.7 Photograph of the fabricated QC measuring 1150 µm × 430 µm. (Reused from *[TPC+21]©2021, IEEE). 128
4.8 Measured and simulated QC_{TL} input reflection coefficients: ANT ($|\underline{S}_{11}|$), T_x ($|\underline{S}_{22}|$) and R_x ($|\underline{S}_{33}|$). (Reused from *[TPC+21]©2021, IEEE). 128
4.9 Measured and simulated QC_{TL} transmission coefficients: T_x to ANT. ($|\underline{S}_{12}|$), ANT. to R_x ($|\underline{S}_{31}|$) and T_x to R_x ($|\underline{S}_{32}|$). (Reused from *[TPC+21]©2021, IEEE). 129
4.10 Block diagram of the lumped elements based QC_{LC}. 130
4.11 Schematic of the lumped elements based QC_{LC}. 131

4.12 Photograph of the fabricated QC_{LC} measuring 755 µm × 450 µm including pads. 134
4.13 Measured and simulated QC_{LC} $\underline{S}$ parameters (a) Input reflection coefficients. (b) Transmission coefficients : T_x to ANT. $|\underline{S}_{12}|$, ANT. to R_x $|\underline{S}_{31}|$ and T_x to R_x $|\underline{S}_{32}|$. 134
4.14 Circuit schematic of the designed 60 GHz FSSDM (Reused from *[TSJE21] © 2021 IEEE). 139
4.15 The complete small signal equivalent circuit of FSSDM core excluding balun and the output load tuning circuit. 140
4.16 The simplified high frequency small signal equivalent circuit used for the analysis of the cascode transconductance amplifier based RF input stage of the FSSDM. 141
4.17 Small signal equivalent circuit used for the analysis of the *LC* bandpass filter load of the FSSDM. 142
4.18 Plot of the magnitude of transcondutance $\underline{G}_{m,eq}$ versus frequency for different inductor L_2 quality factor values. 144
4.19 LO balun design: (a) schematic and equivalent circuit. (b) LO input matching (c) stacked balun implementation (Reused from *[TSJE21] © 2021 IEEE). 145
4.20 Schematic of the backgate tunable output stage of the FSSDM. . . 147
4.21 Variation of FSSDM load resistance versus tuning voltages (a) Coarse tuning. (b) fine tuning using backgate. (c) Corresponding variation of conversion gain and (d) linearity. 149
4.22 Die micrograph of the FSSDM measuring 1090 µm x 620 µm inlcuding pads, and a core area of 260 µm x 250 µm (Reused from *[TSJE21] © 2021 IEEE). 150
4.23 Comparison of characterization results with simulation. (a) Magnitude of input reflection for RF port $|\underline{S}_{11}|$ and LO port $|\underline{S}_{22}|$; (b) G_{conv} versus and I_{dd} as a function of $P_{LO,dBm}$; (c) G_{conv} versus f_{RF} for a fixed IF frequency of 1 MHz; (d) G_{conv} as function of $P_{RF,dBm}$ for different bias currents, demonstrating tunable linearity (Reused from *[TSJE21] © 2021 IEEE). 152
4.24 Fabricated interrogator frontend. (a) Layout of the integrated designs. (b) The implemented IC occupying an area of 1300 µm × 1090 µm wire-bonded to a PCB for characterization. 155
4.25 Schematic of the designed passive backscatter transponder. 155
4.26 Equivalent circuit of the PBT (a) M_1 is in cut off (b) M_1 is in saturation. (c) PBT and view of the bondwires used in EM simulation. (d) Shows the impedance trajectories for PBT switching. 156

5.1 Normalized baseband spectrum corresponding to short range distance measurements using (a) SRT_{dir}; (b) SRT_{buf}, and long range measurements using (c) SRT_{dir}; (d) SRT_{buf}. (Reused from *[TFJE23] © 2023 IET). 160
5.2 Indoor distance measurement error versus ground truth from a laser based device. (a) SRT_{dir}; (b) for SRT_{buf}. Measured cumulative density function at 2.5 m for (c) SRT_{dir}; (d) SRT_{buf}. (Adapted from *[TFJE23] © 2023 IET). (Adapted from *[TFJE23] © 2023 IET). . 161
5.3 Polar plots showing measured and simulated normalized baseband power variation for different angles when the SRTs are rotated in the horizontal plane. (Reused from *[TFJE23] © 2023 IET). 162
5.4 Measured baseband frequency spectrogram showing simultaneous ranging and data transfer at a distance of 5 m. (Adapted from *[TFJE23] © 2023 IET). 162
5.5 Spectrogram showing baseband frequencies for a single bit at different measured distances: (a) 1.5 m (b) 2.5 m (c) 15 m (d) 25 m. (Adapted from *[TFJE23] © 2023 IET). 163
5.6 PBT system level testing setup. 166
5.7 Amplified, filtered and digitized output voltage from the PBT for $d_{PBT} \approx 5$ mm and $d_{PBT} \approx 10$ mm after post processing. 166

A.1 Simplified small signal equivalent circuit of the stacked transistor CCO half cell for high frequency analysis. 173
C.1 Frequency domain SRA measurement on probe station, with the characteristic Dirac delta function peaks clearly visible. 179
C.2 Time domain measurement of SRA output using a real time oscilloscope (a) SRA in action (b) Phase coherence observation. 179
C.3 Time and frequency domain characterization of LFMCW interrogator chirp sequence. 180
C.4 SRTs mounted on a stepper motor shaft for roll-invariance experiments (a) SRT_{dir} (b) SRT_{buf}. 180
C.5 SRT laboratory testing setup. 181
D.1 Setup used to characterize FSSDM. 183
D.2 60 GHz passive transponder mounted on a linear guide rail. 183

List of Tables

2.1 RFID transponder frequency bands and coupling methods 27
2.2 Features of state-of-the-art RFID interrogator and transponder systems 34

3.1 Comparison of the designed SRAs with state-of-the-art ICs suitable as RFID Transponders 105
3.2 Performance summary of SRA ICs post wirebonding 107

4.1 Comparison with state-Of-the-art integrated active quasi-circulators 137
4.2 Comparison with state-Of-the-art 60 GHz CMOS active downconversion mixers (Reused from *[TSJE21] © 2021 IEEE.) 153

5.1 Comparison with state-of-the-art FMCW radar based ranging systems employing integrated circuits based active transponders. (Reused from *[TFJE23] © 2023 IET). 164

Curriculum Vitae

Manu Viswambharan Thayyil
Geboren am 15. April 1984 in Kerala, Indien
manuthayyil@ieee.org

Beruflicher Werdegang

11/2021 - present	Celtro GmbH • Principal Design Engineer, • Ultra low power integrated circuit (IC) design
11/2015 - 10/2021	Technische Universität Dresden (TUD) • Wissenschaftlicher Mitarbeiter, • Research on radio frequency ICs for local positioning systems
02/2007 - 10/2012	Cypress Semiconductor Corporation • Staff Product Engineer, • Senior Product Engineer, • Product Engineer, • Pre- and post-silicon characterization of analog and mixed-signal ICs
01/2006 - 02/2007	Indian Space Research Organization (ISRO) • Scientist / Engineer - SC, • Systems engineering and electrical integration of satellite launch vehicles

Ausbildung

09/2018 - present	Dissertation at TUD: • "Analysis and Design of Silicon based ICs for Radio Frequency Identification and Ranging

	at 24 GHz and 60 GHz Frequency Bands”
11/2012 - 08/2015	Masters studies at TUD: • M. Sc. degree in Nanoelectronic Systems • Master thesis: “Area and Noise Optimized Low Noise Amplifer and Mixer Combination in 28 nm CMOS Technology” • Project work: “Design of Carbon Nanotube Field Effect Transistor based RF Oscillators with ESD Protection”
10/2001 - 09/2005	Cochin Uni. of Science and Tech., Kochi, India • Bachelor of Tech. degree (4 year programme) in Electronics and Communication Engineering • Bachelor Thesis: “Digital Signal Processing based Vector Control of Permanent Magnet Synchronous Motors” • Minor project: “Automated Telephone Call Indicator using Powerline Carrier Communication” • First class with Distinction
05/2001	Model Tech. Higher Secondary School, Kochi, India • Technical higher secondary examination (THSE) • First class with Distinction

Auszeichnungen und Stipendien

10/2014 - 12/2014	Deutscher akademischer austauschdienst (DAAD) STIBET II stipendium at TUD
03/2020 - 08/2022	Peer Reviewer at *IEEE Tran. on Circuits and Systems I: Regular Papers*, *IEEE Tran. on Microwave Theory and Techniques*, *IEEE Microwave and Wireless Components Letters*
01/2020	Student paper contest finalist at Radio & Wireless Week, San Antonio, USA 2020
02/2007 - 10/2012	Multiple productivity wins and publications in internal conferences at Cypress Semiconductors
06/2004	Best paper award at IEEE Excel2k4, a south India level technical symposium
01/1995	Kerala state schools science and math fair prize

Dresden, den 06. Januar 2023